DESIGN AND IMPLEMENTATION OF AN IONIC-POLYMER-METAL-COMPOSITE BIOMIMETIC ROBOT

A Dissertation

by

YI-CHU CHANG

Submitted to the Office of Graduate Studies of
Texas A&M University
in partial fulfillment of the requirements for the degree of

DOCTOR OF PHILOSOPHY

Approved by:

Chair of Committee,	Won-jong Kim
Committee Members,	Alan Palazzolo
	Bryan Rasmussen
	Yoonsuck Choe
Head of Department,	Andreas A. Polycarpou

May 2013

Major Subject: Mechanical Engineering

ABSTRACT

Ionic polymer metal composite (IPMC) is used in various bio-inspired systems, such as fish and tadpole-like robots swimming in water. The deflection of this smart material results from several internal and external factors, such as water distribution and surface conductivity. IPMC strips with a variety of water concentration on the surfaces and surface conductivity show various deflection patterns. Even without any external excitation, the strips can bend due to non-uniform water distribution. On the other hand, in order to understand the effects of surface conductivity in an aquatic environment, an IPMC strip with two wires connected to two distinct spots was used to demonstrate the power loss due to the surface resistance. Three types of input signals, sawtooth, sinusoidal, and square waves, were used to compare the difference between the input and output signals measured at the two spots. Thick (1-mm) IPMC strips were fabricated and employed in this research to sustain and drive the robot with sufficient forces.

Furthermore, in order to predict and control the deflection, researchers developed the appropriate mathematical models. The special working principle, related to internal mobile cations with water molecules, however, makes the system complicated to be modeled and simulated. An IPMC strip can be modeled as a cantilever beam with loading distribution on the surface. Nevertheless, the loading distribution is non-uniform due to the non-perfect surface metallic plating, and four different kinds of imaginary loading distribution are employed in this model. On the other hand, a reverse-predicted method is used to find out the transfer function of the IPMC system according to the

measured deflection and the corresponding input voltage. Several system-identification structures, such as autoregressive moving average with exogenous (ARX/ARMAX), output-error (OE), Box-Jenkins (BJ), and prediction-error minimization (PEM) models, are used to model the system with their specific mathematic principles. Finally, a novel linear time-variant (LTV) concept and method is introduced and applied to simulate an IPMC system. This kind of model is different from the previous linear time-invariant (LTI) models because the IPMC internal environment may be unsteady, such as free cations with water molecules. This phenomenon causes the variation of each internal part. In addition, the relationship between the thickness of IPMC strips and the deflection can be obtained by this concept.

Finally, based on the experimental results above, an aquatic walking robot (102 mm × 80 mm × 43 mm, 39 g) with six 2-degree-of-freedom (2-DOF) legs has been designed and implemented. It walked in water at the speed of 0.5 mm/s. The average power consumption is 8 W per leg. Each leg has a thigh and a shank to generate 2-DOF motions. Each set of three legs walked together as a tripod to maintain the stability in operation.

To my parents

ACKNOWLEDGEMENTS

First of all, I would like to express my sincere gratitude to my advisor, Dr. Won-jong Kim, for his advice and encouragement not only throughout my doctoral study but in daily life at Texas A&M University. This dissertation would not have been completed without his help.

In addition, I wish to thank Drs. Alan Palazzolo, Bryan Rasmussen, and Yoonsuck Choe for serving as my advisory committee members. I sincerely appreciate their invaluable guidance and comments for my research.

I would like to thank Youngchul Na, Young Ha Kim, Ho Yu, Pin-chun Hsieh, and Ying-Chin Chao for their kindest help since I joined Precision Mechatronics Lab in 2007. My thanks also go to Min-Hyung Lee, Naveen Kumar Bibinagar, Rohit H. Chintala, Chien-Fan Chen, and Jose C. Silva-Rivas for their friendly discussions and inspiration to my research life in this Lab. Thanks are also given for my friends, Shu-Wei Hsu, Shu-Wei Chang, and Yen-po Ho for making my time at Texas A&M University a wonderful experience by daily chatting. Then I would like to thank my best friends, Jiawei Dong and Jiang Lei, for not only their help at midnight but encouragement.

My special appreciation goes to Dr. Batteas and his students, Yang Chan and Albert Wan, in the Department of Chemistry, Texas A&M University for providing with facilities and instruction for manufacturing IPMC samples. I could not continue my research without the well-plated IPMC samples.

Finally, most importantly, this dissertation is dedicated to my parents, Mr. Ching-Sheng Chang and Ms. Chin-Hua Hsiao, for their endless love and support that have enabled me to complete my Ph.D. degree. Without their unconditional love, encouragement, and support, I could have never come so far.

NOMENCLATURE

ADC	Analog-to-Digital Convertor
ARMAX	Autoregressive Moving Average with Exogenous
ARX	Autoregressive with Exogenous
BJ	Box-Jenkins
CL	Cracks Along
CX	Cracks Across
DAC	Digital-to-Analog Convertor
DI	Deionized
DOF	Degree of Freedom
DSP	Digital Signal Processing
EAP	Electroactive Polymer
EVM	Evaluation Module
GUI	Graphical User Interface
IPCF	Ionic Conducting Polymer Film
IPMC	Ionic Polymer Metal Composite
LL	Left Lower
LTI	Linear Time-Invariant
LTV	Linear Time-Variant
LU	Left Upper
MIMO	Multiple-Input-Multiple-Output

OE	Output-Error
PEM	Prediction-Error Minimization
PWM	Pulse-Width Modulation
RL	Roughness Along
RL	Right Lower
RTI	Real-Time Interface
RU	Right Upper
RX	Roughness Across
SB	Isotropic (Sandblast)
SISO	Single-Input-Single-Output
SMA	Shape Memory Alloy

TABLE OF CONTENTS

LIST OF FIGURES

LIST OF TABLES

CHAPTER I

INTRODUCTION

This chapter serves as an introduction to the entire dissertation, including smart materials and the comparison between smart materials and conventional materials. Each smart material has specific characteristics for applications in various fields. For example, smart materials have different specialties from conventional materials, such as aluminum for their lightweight. In addition, widely used frames with actuators can be replaced by smart materials for their availability to be both structures and actuators in tiny sizes or complex shapes. Smart materials have already been used in various frontier applications such as biomimetic insectile robots. Other than robots, a small gripper with precise position control is another famous application. An IPMC-based aquatic robot is implemented based on the practical tests and design presented in Chapters I, IV, and V.

1.1 History and Background of Smart Materials

Mostly, the materials with high density have been chosen in the application of robotics because they are both physically and chemically stable, and cheap. Robots used to be designed in a large size to do something unachievable by human beings. For

*Part of this chapter is reprinted with permission from "Aquatic ionic-polymer-metal-composite insectile robot with multi-DOF legs," by Y.-C. Chang and W.-J. Kim, *IEEE/ASME Transactions on Mechatronics*, vol. 18, no. 2, pp. 547−555, Apr. 2013. Copyright 2013 by *IEEE/ASME Transactions on Mechatronics*.

example, a crane can lift up and transport heavy stuff in construction; a backhoe can not only dig the rigid ground but also move obstacles away on the road; an AUV (autonomous underwater vehicle) can operate and get the information in a high aquatic-pressure environment where human beings cannot survive. In order to keep the structure firm and operate with supporting structures, actuators, and loading, steel has been an appropriate option for its high Young's modulus. However, it has been changing to use the materials with lower density to save the energy, so aluminum becomes more widely-used except for some special environments, such as in high pressure or temperature [1]. TABLE 1.1 shows the densities and Young's modulus of some typical metals. Aluminum has low density (2.7 g/cm^3) but low Young's modulus (70 GPa) [2], so it has been employed in smaller robots instead of large ones with large force outputs. In contrast, steel can be used in large robots in order to meet the demand of sufficient force outputs.

TABLE 1.1 Properties of typical metals [2]

	Aluminum	Steel	Titainum	Copper	Brass	Lead
Densities (g/cm^3)	2.7	7.85	4.5	8.94	8.4	11.34
Young's modulus (GPa)	70	200	105 | 120	117	100 | 125	16
Poisson ratio	0.35	0.28	0.34	0.33	0.34	0.43

The design of robots has become small, light, and dexterous for not only energy saving but fitting in small or narrow environments. Besides, robotic applications are not limited in only human-like but available in a variety of designs to work in various environments. Smart materials have been attracting researchers' attention not only because they can be customized in various complcated shapes and sizes, but because most of these materials can work as both structures and actuators. These kinds of materials can show various outputs by external stimuli. Smart materials are employed in robotic actuators in lieu of metals and alloys due to the following advantages. (1) Lightweight: Traditionally, steel, aluminum and their alloys are used in robot structures. The heavy weight, however, leads to high power consumption in robot locomotion. Light smart materials do not need large power supplies, which has been used to move heavy devices, such as motors and frames in order to decrease the dissipated energy. (2) Easy actuation: High-power and high-speed motors are commonly used to actuate robots. However, motors and robot frames are structurally separate, so they further increase weight. Smart materials can act as both structures and actuators simultaneously to decrease power consumption and reduce the sizes. In addition, this kind of materials do not need complicated input devices to provide with power but only a set of electrodes or changed environment can activate the materials. (3) Flexible shapes and sizes: In many applications, such as insectile or detective robots, the bodies should be designed to be tiny or in complex shapes. The mininum sizes of robots have been limited due to the conventional actuators in the past. Smart materials, however, can meet the demands for the availability in various shapes and sizes without changing the characteristics.

Smart materials can be excited by various external stimuli, such as temperature, electric field, magnetic field, light and pH value, according to their working principles [1]. Electroactive polymers (EAPs) are a kind of material and can categorize in electronic EAPs and ionic EAPs according to the different external stimuli, electric fileds (electronic EAPs) and movement of ions (ionic EAPs). Dielectric elastomer is a typical electronic EAP and requires a high electric field (about 100 V/μm). Other electronic EAPs, such as electrostatic and piezoelectric, require much higher electric field (greater than 150 V/μm) to be activated [1]. High electric fields distort the structures by breaking ionic bondings, which are extremely stable and have high bonding energy, so electronic EAPs exhibit small deflection but large force in performance in a short time. Ionic EAPs, the other kind of EAPs, can generate large deflection by a low external voltage (about 5 V, depending on the thickness) or changing the environmental temperature. These EAPs exhibit deflection response by deformation of the internal structure, caused by mobility of internal ions, instead of strong ionic bonding breaking [1]. Electronic EAPs exhibit strong force but small output deflection. On the contrary, Ionic EAPs' output force is small but these smart materials exhibit conspicuous deflection. In addition, the former can work in high frequency (>1000 Hz), but the latter have an upper limitation of working frequency (~100 Hz) in operation [1]. Both of the above EAPs have been used in robotic applications because of their own advantages. For example, rapid deflection output can used to flap as a wings; slow and large deflection can imitate a fin's undulation of an aquatic robot. Likely, their weakness constraints the ranges of applications. For example, electronic EAPs need high external voltages that

might not be feasible in a small size in order to realize a tiny and autonomous robot. As for the other one, these ionic EAPs typically cannot produce large force although a large deflection can be exhibited. Therefore, ionic EAPs have been applied in small fish- and tadpole-like robots that do not need a great deal of force for substantial locomotion. TABLE 1.2 lists some typical characteristics of the above smart materials.

TABLE 1.2 Typical characteristics of two typical EAPs [1, 2]

	Electronic EAPs	Ionic EAPs
Working principle	Internal deformation by breaking ionic bondings	Internal deformation by the mobility of ions
Typical external stimuli	High electric fields (~100 V)	Low electric fields (~10 V), pH value, temperature
Deflection responses	> 150 V/μm	10 % to 600 %
Working frequency	> 1000 Hz	< 100 Hz
Advantages	Exhibit large force and work in high frequency	Exhibit conspicuous deflection with low external stimuli
Disadvantages	Small deflection and high energy needed	Insufficient force for large system applications

Shape memory alloys (SMAs) are categorized in ionic EAPs and this kind of material typically exhibit conspicuous output deflection without high voltage or strong external stimuli. For example, the nickel-titanium (Ni-Ti) alloys, applied in actuators and medical devices, present sensitive response via the change in surrounding temperature [1]. These materials may not be appropriate in robotic applications due to the

incapability of repetitive and rapid change in environmental temperature. In addition, SMAs have typical two shapes, permanent and temporary shapes as illustrated in Fig. 1.1, instead of continuous deflection with the corresponding external stimuli. Therefore, according to the above points, SMAs are not one of the options for the robotic application in this study due to inconvenient external stimuli, such as environmental temperature, although they would exhibit excellent output responses.

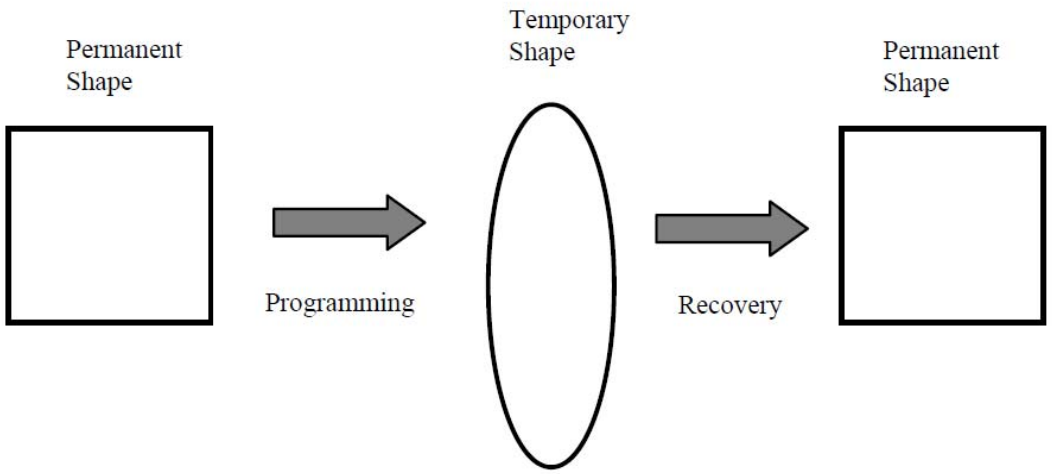

Fig. 1.1 Shape-memory effect produced by thermal activation [1]

1.2 Introduction to IPMC

Ionic polymer-metal composite (IPMC), also called ionic conducting polymer film (ICPF), a kind of ionic EAPs, was firstly reported by Oguro *et al*., Sadeghipour *et al*., and Shahinpoor *et al*. in 1992 [3−5]. This material has the capability of exhibiting conspicuous deflection in response to an external voltage. The structure of IPMC is a

piece of polymeric membrane with a layer of metallic electrodes coated on both sides. Nafion®, a kind basis membrane of IPMC and manufactured by DuPont™, is a polymer and has been used as the cation-exchange film in fuel cells for a long while [6] because only cations can move freely inside. In addition to Nafion®, Flemion®, manufactured by Asahi Glass, Japan, is another chioce as the basis membrane and the IPMCs made of Flemion® have a conspicuous difference in performance [7]. This kind of polymers tend to swell by the internal water molecules [8], so the size is changeable and dependent on the water concentration. Water molecules are bonded with cations, so the deflection of IPMC takes place when there is a difference in water concentration between both sides. The surface metallic electrodes are used to move the cations by attractive and repulsive coulomb forces generated by the surface voltage distribution. When the external power is off, the cations and water molecules are evenly distributed internally. When the power is on, the cations with attached water molecules move to one side by coulumb forces, and the water molecules concentration becomes non-uniform. The swelling and shrinking phenomona make the IPMC bend [9]. The magnitude of the bending angle depends on the stiffness of IPMC strips, and the gradient in the concentration of water molecules, which can be controlled by the external voltage source.

IPMC has attracted much interest in the past decade because of its notable advantages:

(1) Lightweight. The density of IPMC is around 2.25 g/cm^3, much lighter than prevalently used metals such as steel (7.85 g/cm^3) and aluminum (2.70 g/cm^3). It can reduce power consumption if the lighter materials are utilized.

(2) Easy fabrication process. IPMC is fabricated by chemical metallic coating on the surface of Nafion® membrane.

(3) Easy use. Instead of complicated electric circuits or devices, IPMC just needs external voltage between two metallic electrodes on both surfaces. In addition, it can be cut in various sizes and shapes easily in order to apply and fit in a variety of applications.

(4) Low working voltage (1−5 V, depending on the thickness). Unlike other smart materials such as piezoelectric materials, IPMC can work with low external voltage instead of hundreds of Volt [10]. It can not only save the power but also decrease the power loss by providing with lower voltage sources.

(5) Can work in an aquatic environment. IPMC needs water in operation and works in water without being destroyed. In addition, IPMC exhibits the same performance whether the hydraulic pressure is 0.1 MPa or 100 MPa with the same input voltage [11]. Therefore, underwater devices or robots are good applications for IPMC.

(6) No noise and pollution. The working of IPMC is based on the movement of cations with water molecules inside IPMC, so no noise and pollution, which is harmful to the environment and might cause unpredictable effect to responses, is generated in operation.

(7) High working frequency (about 10 Hz, depending on the stiffness). A piece of 7-mil (milli-inch) IPMC strip can exhibit conspicuous vibration in tens of Hertz depending on the input signals.

According to the above properties, an aquatic robot would be an appropriate choice as the application of IPMC because it has the capability of exhibiting the excellent performance in air or water. In addition, IPMC keeps losing internal water via surface evaporization in operation. Therefore, working in an aquatic environment can eliminate the loss of internal water molecules to keep exhibiting good performance.

1.3 Applications of IPMC and Literature Review

IPMC has been used in various applications since the last two decades. One of the popular applications of IPMC is artificial muscles by combinated IPMC strips. The other application is biomimetic robots that can imitate the locomotion of insects and fishes with its repetitive and bi-directional bending. Five categories of biomimetic robots have been implemented by using IPMC according to the various actuation methods. The first one is fish- and tadpole-like robots, which have been developed that could swim in an aquatic environment by undulating an IPMC tail fin [12−14]. Like a real fish or tadpole, it can swim not only straight but also left or right by controling the undulation of the tail fins. Tan *et al*. have developed fish-like robots [14]. By the undulation of the fin, made of an IPMC strip, the robots swam freely in an aquatic environment [15, 16]. Guo *et al*. have improved the direction control by employing two pieces of IPMC strips as tail fins [17]. Both Figs. 1.2 (a) and (b) show two fish-like robots with only one IPMC-strip fin made by Xu *et al*. and Tan *et al*. [17,18]. Yang *et al*. have used four IPMC strips for their robot [19]. By using plenty of IPMC strips operating together, a

jellyfish-like robot can swim freely in an aquatic environment. However, jellyfish-like robots do not move by the undulation of multiple pieces of IPMC strips individually but a group of IPMC strips with the synchronized and asymmetric bending motion [19, 20]. In order to generate sufficient propulsion force to move steadily, IPMC strips do not exhibit an ordinary undulation but a rapid rising followed by a slow decrease repetitively. In addition, the above swimming robots can make a smooth turn by using frequency variation or coordination of the bending motion from different IPMC strips.

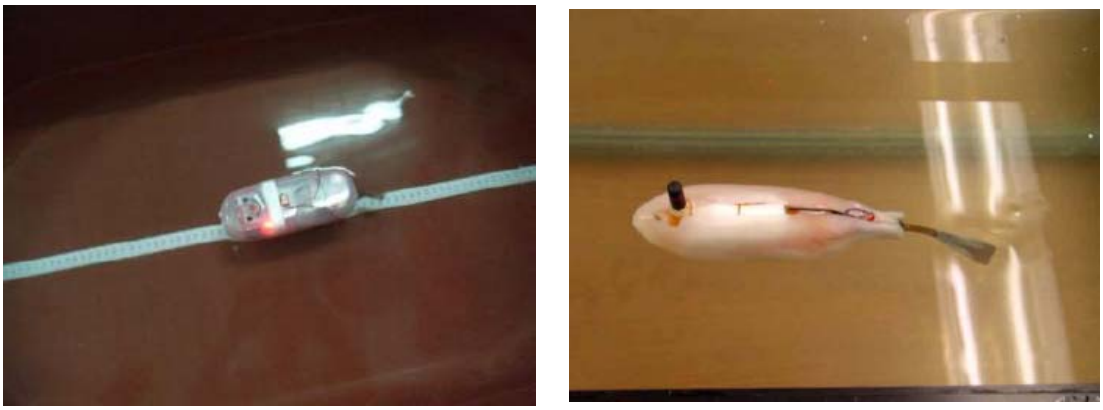

(a) (b)

Fig. 1.2 Two implementations of fish-like swimming robots by using an IPMC strip as a tail fin [17, 18]

Crawling IPMC robots have been also developed and implemented in various styles. A worm-like robot, made of a segmented IPMC strip, crawled with appropriate input signals in different phases for each segment [21]. This robot moves by crawling on the ground with friction segment by segment. Arena *et al.* implemented a wormlike

robot, and this robot crawled on the ground by wriggling as a worm when all segments were provided with the input voltages in various phases in sequence as shown in Fig. 1.3

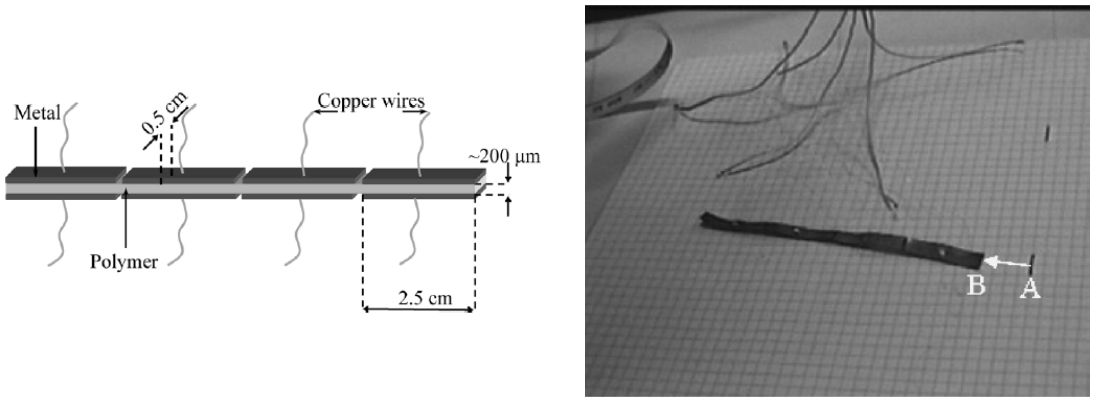

(a) (b)

Fig. 1.3 The structure (a) and implementation (b) of a wormlike IPMC robot [21]

[21]. In Fig. 1.3 (a), this wormlike robot was made of a long IPMC strip and divided into several segments by the gaps of surface electrodes. Figure 1.3 (b) shows the movement of this robot. The application on a series of IPMC strips working in various phases has been reported in other fields. For example, Takagi *et al.* have designed a rajiform swimming robot with two pieces of skate's fins on both sides shown in Fig. 1.4 [22]. Unlike the wormlike robot mentioned above, each fin consists of eight IPMC strips with a thin and transparent cover (in Fig. 1.4 (a)) and works by sequential deflection of all IPMC strips. By activating each piece of IPMC strips sequentially, both fins can move the robot not only forward but freely in an aquatic environment. A biomimetic robot with the combination of the previous two robots has been developed as shown in Fig. 1.5.

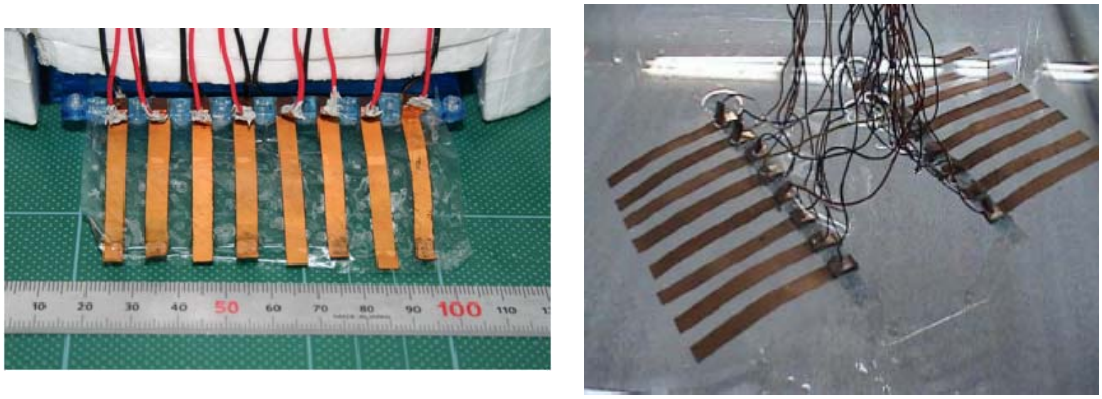

(a) (b)

Fig. 1.4 (a) A fin, made of eight IPMC strips with a thin membrane covered and (b) the entire body of a rajiform IPMC swimming robot [22]

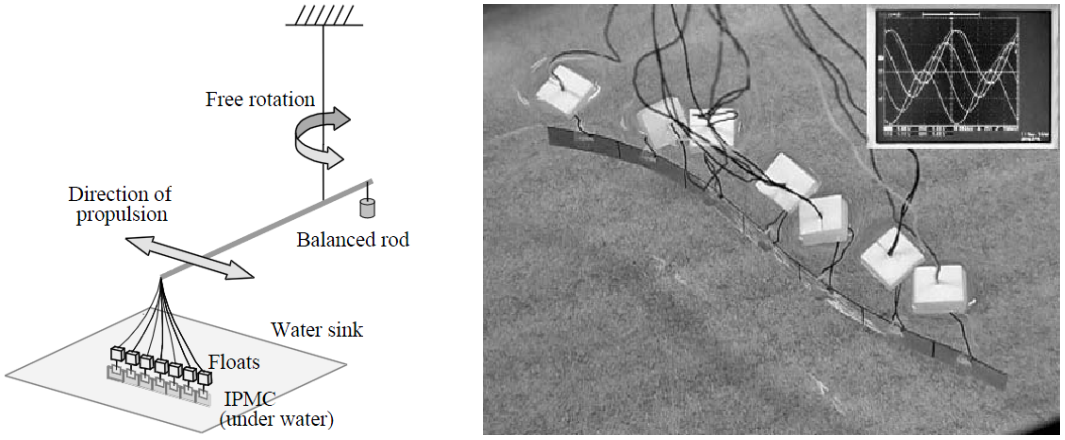

(a) (b)

Fig. 1.5 A swimming snake-like IPMC robot with patterned artificial muscles [1]. (a) Working method and direction and (b) implementation with input signals in various phases

This robot is activated by multiple input signals in different phases (shown in Fig. 1.5 (b)) [1]. Guo *et al*. developed various swimming and walking robots by using IPMC strips [23−29]. Figure 1.6 shows three typical prototypes of the IPMC robots, and all the robots have individual legs as supporters and drivers to lift up and move the body, respectively. In addition to biomimetic robots, the applications of IPMC in other fields have also been

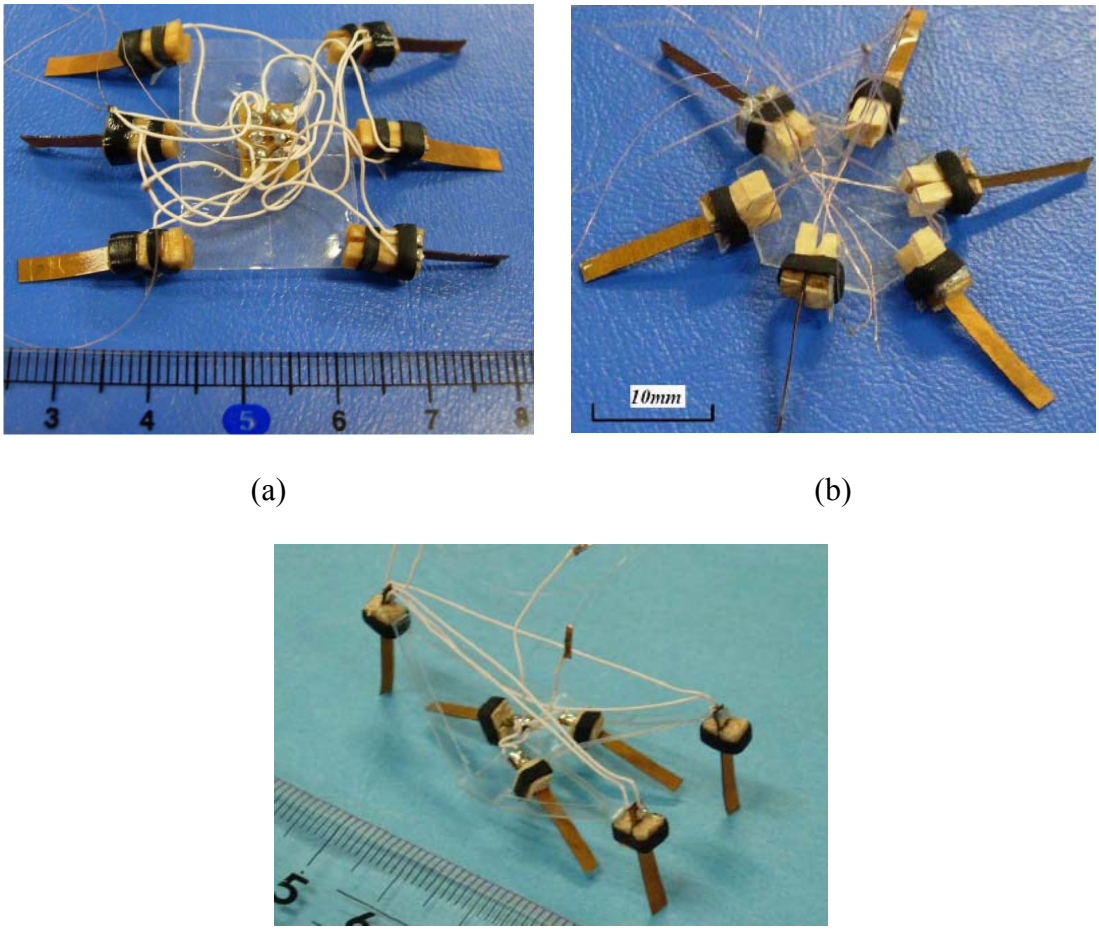

(a) (b)

(c)

Fig. 1.6 Implementation of some typical IPMC walking robots with individual supporters and drivers (one-DOF legs) [25, 26]

developed widely. Chen *et al*. used a piece of IPMC in a specific shape to realize the fin of a manta ray by imitating the working principle of a real ray's fin [30]. A review of various biomimetic underwater robots by using smart materials, such as SMAs, IPMC, and piezoelectric (PZT) materials, is presented in [31]. Furthermore, a robot is not necessary to be insectile but in a versatile style [32]. Kim and Yun implemented a three-finger microgripper of a robotic manipulator with three IPMC strips as shown in Fig. 1.7 [33−35]. Not only the appropriate controllers included, with three laser distance sensors

(a) (b)

Fig. 1.7 Two steps of gripping motion by IPMC three-finger gripper [35]. Three IPMC strips work as fingers with individual laser sensor for precise position control.

on each finger, all strips could be actuated by independent feedback controllers with an anti-windup scheme in order to have both optimal and precise position control for gripping motion.

Besides the applications in the previous paragraph, biomimetic robots were developed in other materials and fields instead of IPMC. However, they could be good choices and ideas for novel IPMC robot designs. Besides a typical hexapod walking robot, Wood *et al*. designed a novel worm robot and implemented a flying robot constructed with piezoelectric ceramics for small size and rapid vibration of wings [36−40]. Figure 1.8 is an insectile robot made in piezoelectric ceramics. Kingsley designed a cockroach robot with six multiple-DOF (degree-of-freedom) legs [41]. His

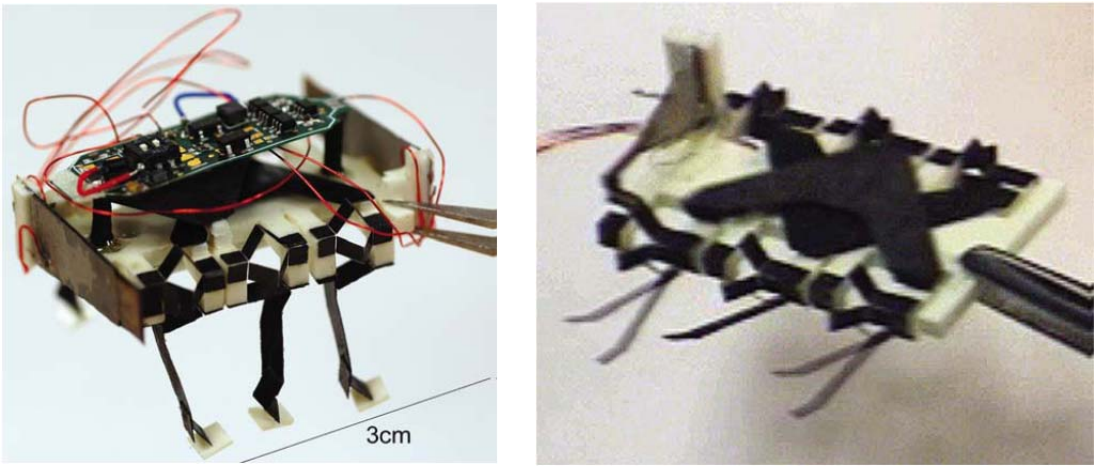

(a) (b)

Fig. 1.8 A tiny six-legged walking robot by using PZT materials [38]

Robot V was different from previous robots in his group so this robot resembled a real-life cockroach as shown in Fig. 1.9. Currie *et al.* developed a hexapod robot with six 3-DOF legs surrounding it [42]. Guo *et al.* proposed a six-legged climbing robot with 5 DOFs in each leg. With a vacuum cap in each leg and a vacuum generator, this robot

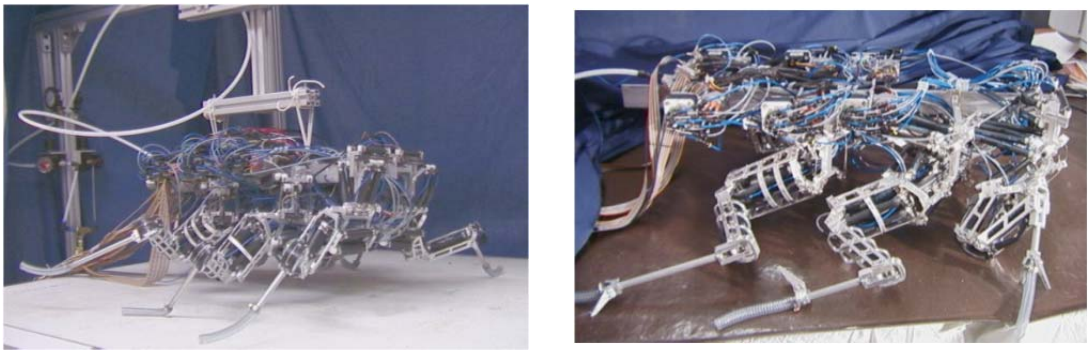

(a) (b)

Fig. 1.9 Robot V, a cockroach robot with six multiple-DOF legs [41]

could climb on the ground, wall, or ceiling [43]. AQUA is a project of hexapod amphibious autonomous robots [44]. These robots have six paddle-like feet as a turtle. Figure 1.10 (a) shows a walking robot, which can be applied in various environments such as aerospace engineering for the capacity of walking on a rugged ground. The robot with six paddles can move freely in an aquatic environment as shown in Fig. 1.10 (b).

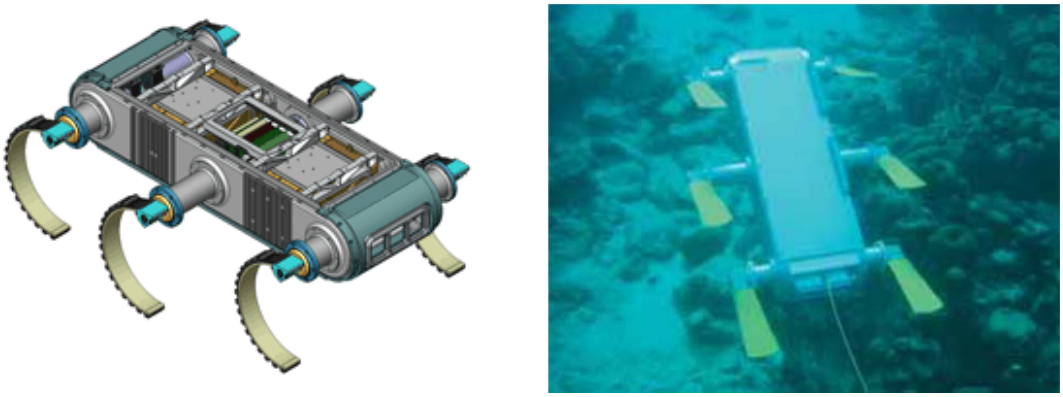

(a) (b)

Fig. 1.10 AQUA robot project. (a) walking on various grounds and (b) aquatic swimming robot with six paddles on the feet [44].

The MEDIC robot as shown in Fig. 1.11 offers a unique solution to the problem of diagnosis and repair of large electronic systems where human inspection is often costly, impractical, or error-prone [45]. The above-mentioned robots emphasized both the applications of smart materials and the agile locomotion that might be accomplished with smart materials.

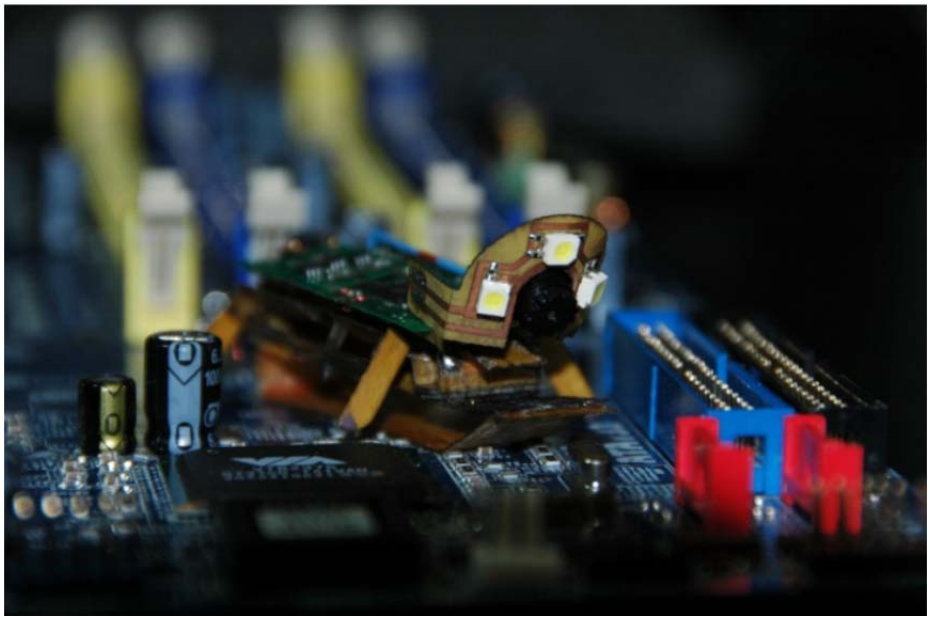

Fig. 1.11 The MEDIC robot walks in an electric environment [43]

1.4 Goals and Contributions of the Research

The objective of this research is to design and implement a novel aquatic walking robot based on our fundamental design principles with the IPMC strips that I fabricated. Most of the robots in the above applications [12−29] were made of thin (about 0.2 mm)

IPMC strips, fabricated with Nafion® 117. These IPMC strips exhibit conspicuous deflection but insufficient force output with low current provision for some specific applications, such as necessarily conspicuous output bending deflection [46]. It is not problematic for fish- and tadpole-like robots because they can swim in water by buoyancy without other supports. In this research, 1-mm-thick Nafion® membranes were used to be the basis membranes in order to generate sufficient force for a walking robot. A simple IPMC strip has only one bending DOF. Walking robots need at least two DOFs for each leg to perform walking locomotion. Therefore, most walking robots have two kinds of legs, a driver and a supporter, to move and support the body [25, 26]. To imitate a real and live insect more closely, one leg with two DOFs will be designed and implemented in this research. In addition, the robot must have firm legs to sustain not only its own body but also the circuitry and battery on itself to realize an autonomous robot walking in an aquatic environment. Thus, this robot can exhibit several innovative applications. For example, with a tiny camera mounted, this robot could be applied to detect a flaw or a crack, and even fix those with tools in a pipeline or an aquatic environment.

An insectile aquatic IPMC-based robot constructed in this research is shown in Fig. 1.12. Unlike the previous IPMC swimming robots, this robot can walk as an insect in an aquatic environment steadily and fast by applying specific walking procedures, which will be introduced in Chapter VI. In addition, this robot can be driven by a convenient circuitry instead of changing environment such as SMAs. Finally, because of the properties of IPMC, the locomotion of this robot is not limited by local aquatic

pressure. Therefore, this robot can be used easily to inspect an unknown aquatic environment such as a pipeline or seabed.

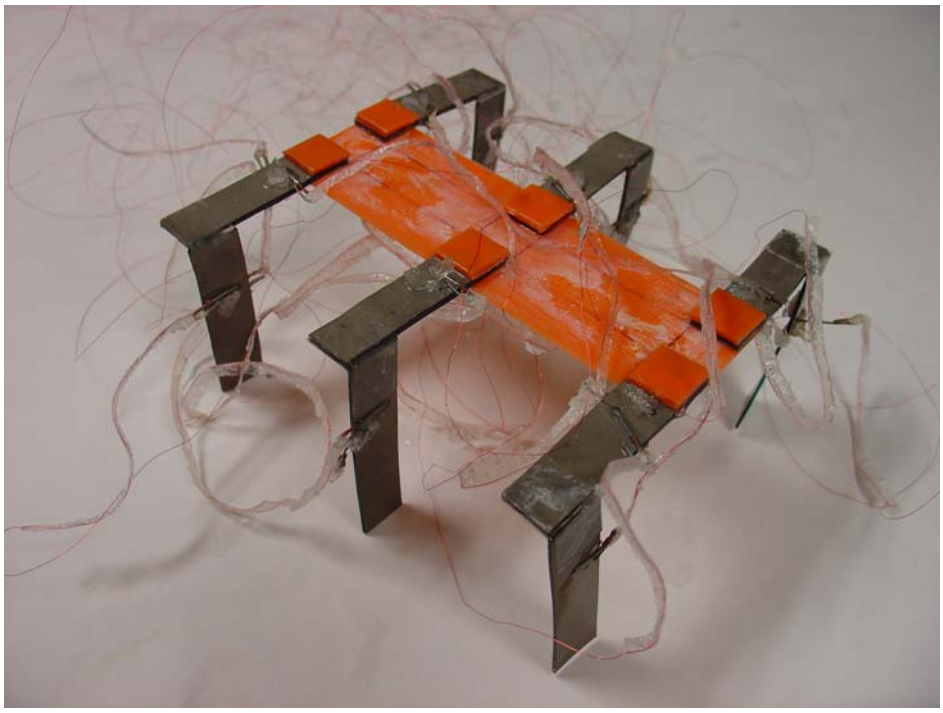

Fig. 1.12 The IPMC-based walking robot

1.5 Overview of Dissertation

This dissertation consists of seven chapters, which cover the fabrication of IPMC strips, the design and the implementation of an IPMC aquatic robot based on fundamental experiments of the IPMC strips. The overview of each chapter is as follows.

Chapter I introduces representative smart materials, including the background, history, and the applications in various fields. In addition, the benefits and weakness of

conventional materials and smart materials are lsited to emphasize the latter. Among the smart materials, a comparison has been made in order to emphasize the advantages of the most appropriate choice for the robot in this research, IPMC.

Chapter II describes the fabrication process and properties of the IPMC fabricated in this research. In addition, the working principle and characteristics of IPMC strips will be explained and illustrated.

Chapter III describes the necessary experimental devices, such as hardware and related interface software. In this research, a DSP (digital signal processing) board is used to both provide simulated signals and process measured signals.

Chapter IV shows the results of fundamental experiments of the fabricated IPMC strips. The experiments include the output deflection in various working environments and input signals. In addition, the importance of IPMC surface condition will be explained in the related experimental results and plots.

Chapter V discusses three modeling methodologies based on the output deflection in Chapter IV. Each model has its specific advantages and disadvantages. In addition, a novel modeling mothod will be introduced.

Chapter VI describes the design and implementation of the aquatic robot in detail including power transmission. In addition, based on the design of 2-DOF legs, a specific walking procedure and the driving signal sequences to generate smooth walking motions in water are also presented. The movement of the implemented walking robot will be shown in a group of sequential figures.

Chapter VII provides the conclusions and future work.

CHAPTER II

INTRODUCTION TO IPMC ACTUATORS

In this chapter, the fabrication, working principle, and characteristics of IPMC will be described and discussed in detail. The IPMC strips in this research were fabricated in the laboratory in order to meet all demands. The working principle and characteristics are closely related to the properties of not only the internal Nafion® membrane but also surface metallic electrodes. For example, the abilities of water absorbing and swelling of Nafion® are the decisive factor of the bending motion IPMC exhibits. Surface metallic electrodes affect the voltage distribution, which attracts and repels internal cations with water molecules to exhibit bending deflection. In this chapter, self-fabricated IPMC strips will be introduced by applying an improved fabrication process to meet all requirements and reduce cost.

2.1 Fabrication of IPMC

Mostly, researchers have obtained IPMC from Environmental Robot, Inc. because this company can provide evenly-plated Nafion®-based IPMC immediately [47]. However, I fabricated IPMC strips in the laboratory, and they could customized to meet

*Part of this chapter is reprinted with permission from "Aquatic ionic-polymer-metal-composite insectile robot with multi-DOF legs," by Y.-C. Chang and W.-J. Kim, *IEEE/ASME Transactions on Mechatronics*, vol. 18, no. 2, pp. 547−555, Apr. 2013. Copyright 2013 by *IEEE/ASME Transactions on Mechatronics*.

the demands, such as the electrical conductivity and the thickness of IPMC strips. In order to fabricate IPMC, Nafion® and platinum were chosen in this research as the membrane and surface metallic electrodes, respectively, because of chemical stability. Gold and platinum are usually used as the surface metallic electrodes because they are both chemically stable and electrically conductive. Other metals, such as sliver and copper, are not suitable to be the metallic electrodes due to being easily-oxidized in spite of high conductivity.

There are a variety of coating methods for various metallic electrodes, but only the electroless plating was selected because the basis membrane, Nafion® in this experiment, is not electrically conductive. The ingredients and reducing agents were chosen depending on plating methods. The following ingredients have to be prepared for our own IPMC, such as Nafion® membranes (manufactured by Dupont™), tetraammineplatinum(II) chloride monohydrate ($Pt(NH_3)_4Cl_2 \bullet H_2O$, manufactured by Alfa Aesar), sulfuric acid (H_2SO_4), sodium borohydride ($NaBH_4$, manufactured by MP Biomedicals) as a reducing agent. The following shows the fabrication procedure based on [48] and improved by us.

(1) Roughening the surface of Nafion® on both sides manually applying sandpapers in the same direction. Roughened surface can easily attach more platinum particles to enhance the surface conductivity because of the enlarged surface area [49]. Not only manual roughening, plasma is prevalently used for fine and uniform roughening. The strips roughened by different plasma such as argon or oxygen show different responses mainly because the etched depth are different [50, 51].

However, according to [49], the IPMC strip showed better performance than those roughened by machine and plasma. Therefore, manual roughening was selected to as a preprocess for IPMC fabrication. Roughening direction must be kept in the same direction to enhance the performance [52, 53]. In Fig. 2.1, five roughening methods are proposed and RX shows the best peformance among all.

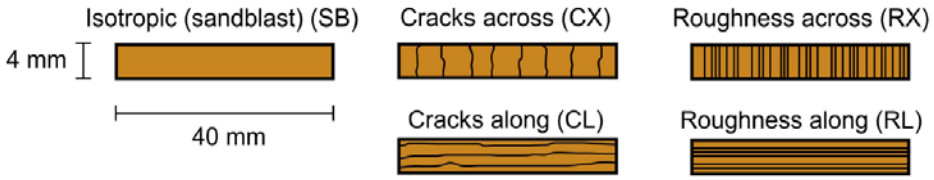

(a)

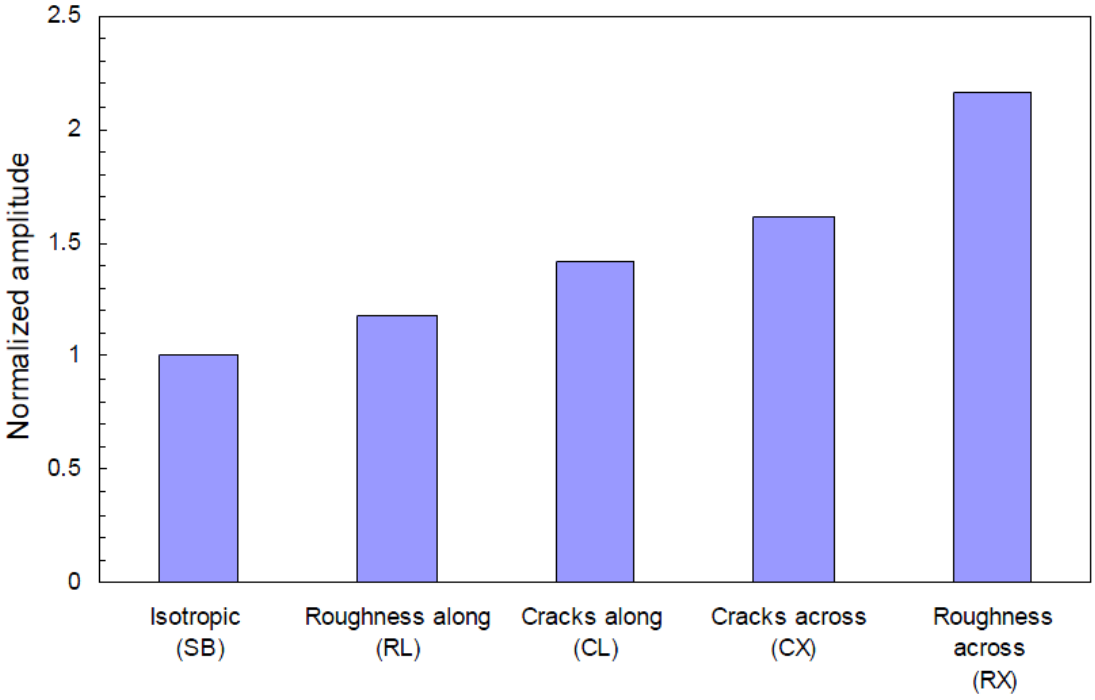

(b)

Fig. 2.1 Relationship between roughening direction and normalized amplitude [52]

(2) Cleaning Nafion® by using deionized (DI) water in an ultrasonic machine for 30 minutes in order to remove the dusts on the surface after roughening and prevent from bad influence on plating [48]. Dusts would attract the reduction of platinum, so it might cause nonuniform distribution if the dusts are uneven.

(3) Removing the organic impurities on the surfaces of Nafion®, which might come from human beings' hands when being roughened, by using 1.0 M boiled sulfuric acid for 30 minutes [48]. Nafion® will swell and be softened in this step, so it must be kept flat to prevent from initial bending, which would influence the performance.

(4) Cleaning the residual sulfuric acid in previous step by using boiled DI water for 30 minutes [48].

(5) Soaking in platinum solution for 48 hours in order to let platinum ions bonded onto the surface of Nafion®. In this research, the surface area of Nafion® was 128 cm^2 and soaked in the solution, consisted of 2 g of platinum powder and 500 ml of DI water, respectively.

(6) Reducing platinum layer by one of strong reducing agents, $NaBH_4$, solution and keeping the temperature of the solution around 40°C for a constant reaction speed [48]. Reaction temperature and speed affect the difference in sizes of surface platinum crystals deeply. More coarse platinum electrodes, caused by fast reducing reaction, makes IPMC stiff and brittle in operation. Not only was the stiffness influenced by coarse crystals, but also the surface conductivity was getting worse due to the huge cracks among platinum crystals [54]. Therefore, after repetitive experiments the IPMC strips could exhibit better performance if the reaction

temperature was kept at around 40ºC. In addition, in order to generate a uniform platinum plating, it is recommended to put a magnet sturbar. However, it must be avoided to damage the IPMC by the sturbar. The reaction equation by using $NaBH_4$ as a reducing agent is:

$$NaBH_4 + 4[Pt(NH_3)_4]^{2+} + 8OH^- \rightarrow 4Pt + 16NH_3 + NaBO_2 + 6H_2O \qquad (2.1)$$

(7) Cleaning residual reducing agent in previous step by using 60−70ºC DI water for an hour.

(8) Repeating Steps (5) to (7) for around five times in order to enhance the thickness of the metallic layers. It has been enhanced up to around 10 μm to improve the surface conductivity in recent research.

(9) Soaking into concentrated saline water (3.5%) for 24 hours and then into DI water for 48 hours to replace counter ions with sodium ions (Na^+) and remove residual sodium ions on the IPMC, respectively. Some characteristics and performance could be different with various counter ions replaced. In this research, sodium ions were selected as the counter ions to enhance the reaction speed.

(10) Soaking into DI water for 48 hours to clean the IPMC thoroughly.

Figure 2.2 illustrates the fabrication process in detail, including pictures in each state. The chemical formula of Nafion® is shown in Fig. 2.3. The cation, H^+, which is called a counter ion, in this chemical formula, can be replaced by alkali-metal, such as Li^+, Na^+, K^+, Rb^+, Cs^+ as well as alkyl-ammonium cations, such as

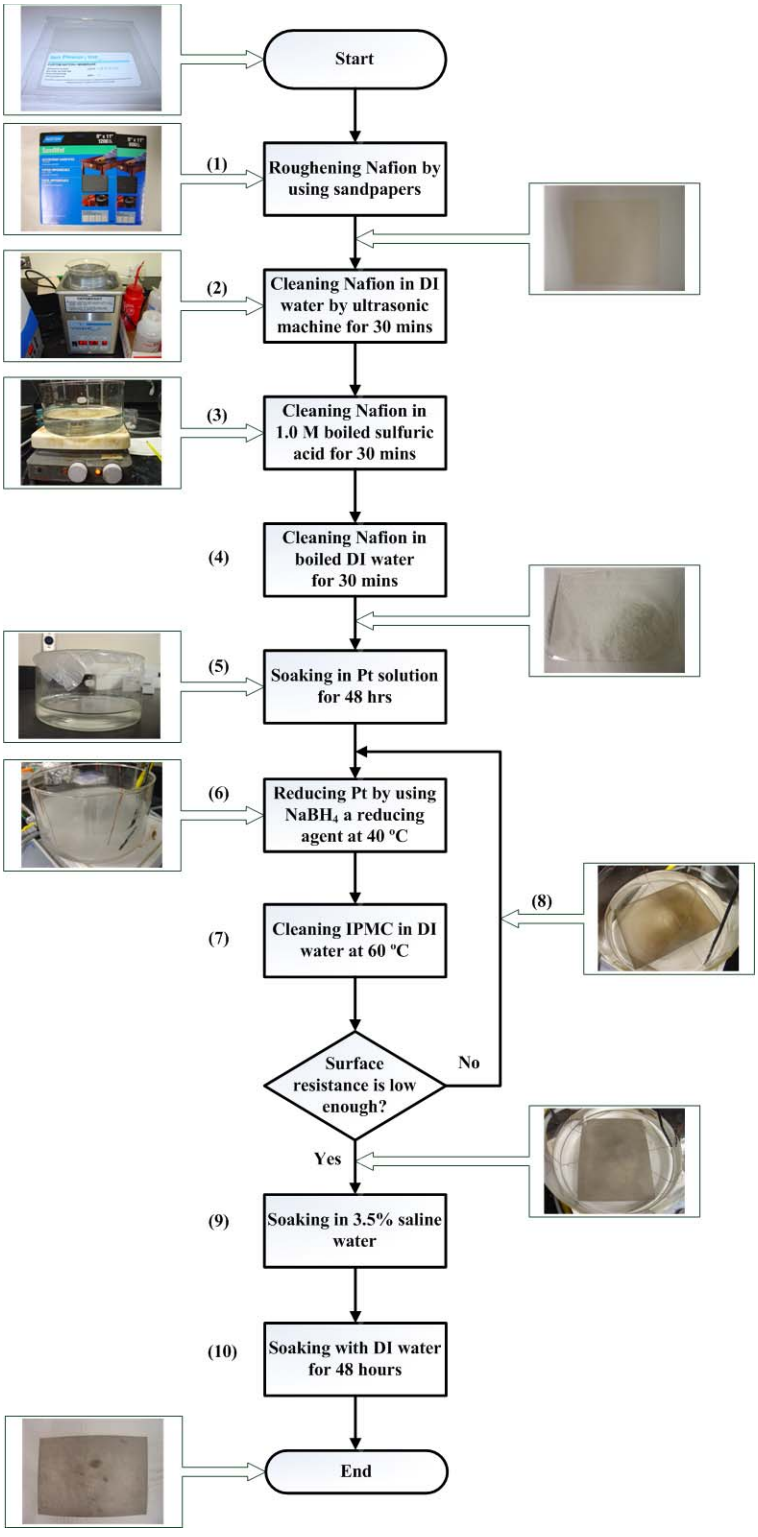

Fig. 2.2 Fabrication process of self-fabricated IPMC

tetramethylammonium (TMA^+) and tetrabutylammonium (TBA^+) [55]. The performance of IPMC such as reaction time and maximal deflection varies with these counter ions.

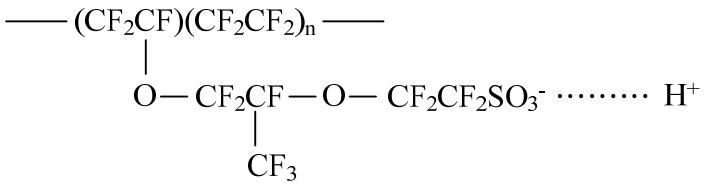

Fig. 2.3 Chemical formula of Nafion®

Internal counter ions cause IPMC strips to exhibit various deflection as shown in Fig 2.4 [55]. In this figure, the IPMC strip with TMA^+ as counter ions exhibits the

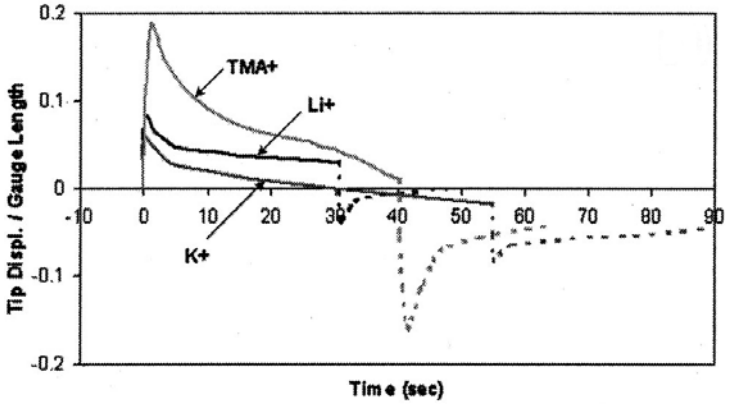

Fig. 2.4 Normalized deflection affected by various counter ions [55]

largest maximum normalized deflection, which is much more conspicuous than those with Li^+ and K^+ as internal counter ions. However, the first IPMC strip has a rapid rising and then it is followed by a rapid decrement. However, the strips with Li^+ and K^+ as

counter ions exhibit smaller deflection but slow decrement, too. Each counter ion has the specific application. For example, the strip with TMA^+ can be used for the first couple seconds because of the instant deflection. For those with Li^+ and K^+, however, they can be applied for a period of time. In this research, Na^+ was used as counter ions and could cause IPMC strips to generate larger and more rapid instant deflection and decrease. However, the decreasing phenomenon could be degraded or eliminated by changing the structure or thickness, which will be discussed in the following paragraph.

Figure 2.5 shows two pieces of fabricated IPMC strips. Nafion® needs to be coated for five or six times of reduction in order to have a sufficiently thick layer of metallic coating, which is used to transmit current more uniformly to the whole surface.

Fig. 2.5 Self-fabricated IPMC strips with burned surface due to external voltage

For metallic electrodes, gold is the best choice for its chemical stability and low resistance. However, it is not easily-coated, so a gold layer has been coated after a layer of nickle coated on in order to enhance the adhersion to gold [56]. In addition, gold has better characteristic of extension, so IPMC strips coated with gold do not crack due to large and repetitive bending motion. For other choices of metallic electrodes, silver and copper are electrically conductive but easily-oxidized [57] and the metal oxides such as AgO and CuO are not electrically conductive, so the surface conductivity will get degraded significantly. Therefore, platinum was selected in this research because it is easily reduced with high chemical stability and electrical conductivity although it is the most expensive.

2.2 Working Principle of IPMC

The basic polymer membrane of IPMC is Nafion®, so the working principle of IPMC results from the properties of Nafion®, which was firstly introduced by DuPont™ in 1969 as a commercial perfluorinated ion-exchange membrane [58]. Nafion® exhibits a decisive property, which is the complete penetrability for protons only, so it has been applied in electrolysis. For example, Nafion® was firstly used in a commercial chloralkali plant in 1975 [59]. Figure 2.6 illustrates an application of a Nafion® membrane. As a proton-exchange membrane in the middle, it prevents the movement of the two anions, Cl^- and OH^-. The equation of this reaction is shown in Eq. (2.2). It generates Chlorine, Hydrogen, and Sodium hydroxide. Another application is fuel cell,

which has been used to provide energy for aircrafts and rockets. In a hydrogen-oxygen proton exchange membrane fuel cell (PEMFC), Nafion® acts as a proton-exchange membrane as the previous example. Nafion® in these two applications exhibits the capacity of being penetrable and movable for protons only. In addition, Nafion® expands by internal water molecules and this phenomenon acts as another factor that is related to the working principle of IPMC.

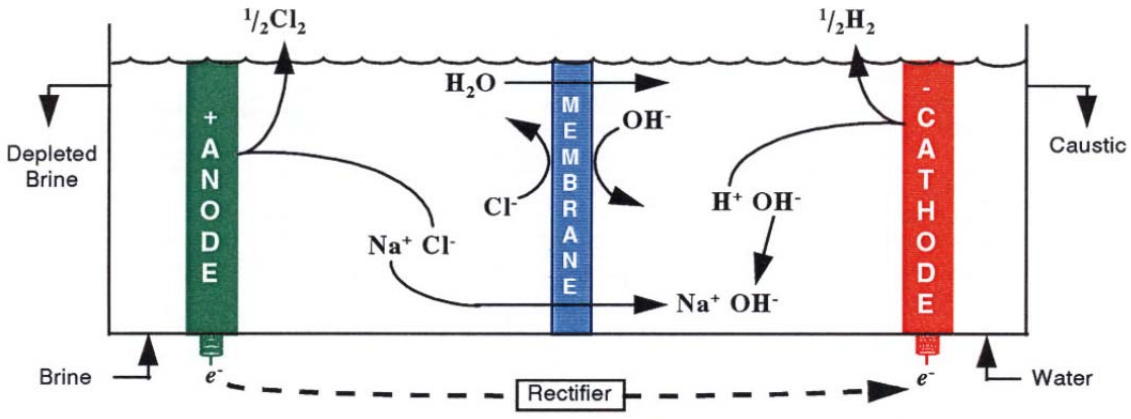

Fig. 2.6 Application of Nafion® membrane [58]

$$NaCl + H_2O \rightarrow \frac{1}{2}Cl_2 + \frac{1}{2}H_2 + NaOH \tag{2.2}$$

Figure 2.7 illustrates the basic structure of IPMC, Nafion® with a layer of metallic electrode coated on both sides, and internal cations with water molecules. Nafion® is the basic membrane of IPMC and has the decisive factors of the deflection of IPMC, swelling by water molecules [58] and movement of cations only. Water

molecules are attached to the cations and move with them. Thus, the deflection of IPMC can be decided according to the concentration of the cations with water molecules, which are movable inside IPMC. In other words, the deflection can be controlled as long as users know how to move the internal water molecules. In this research, water molecules are moved with internal movable cations by surface voltage distribution.

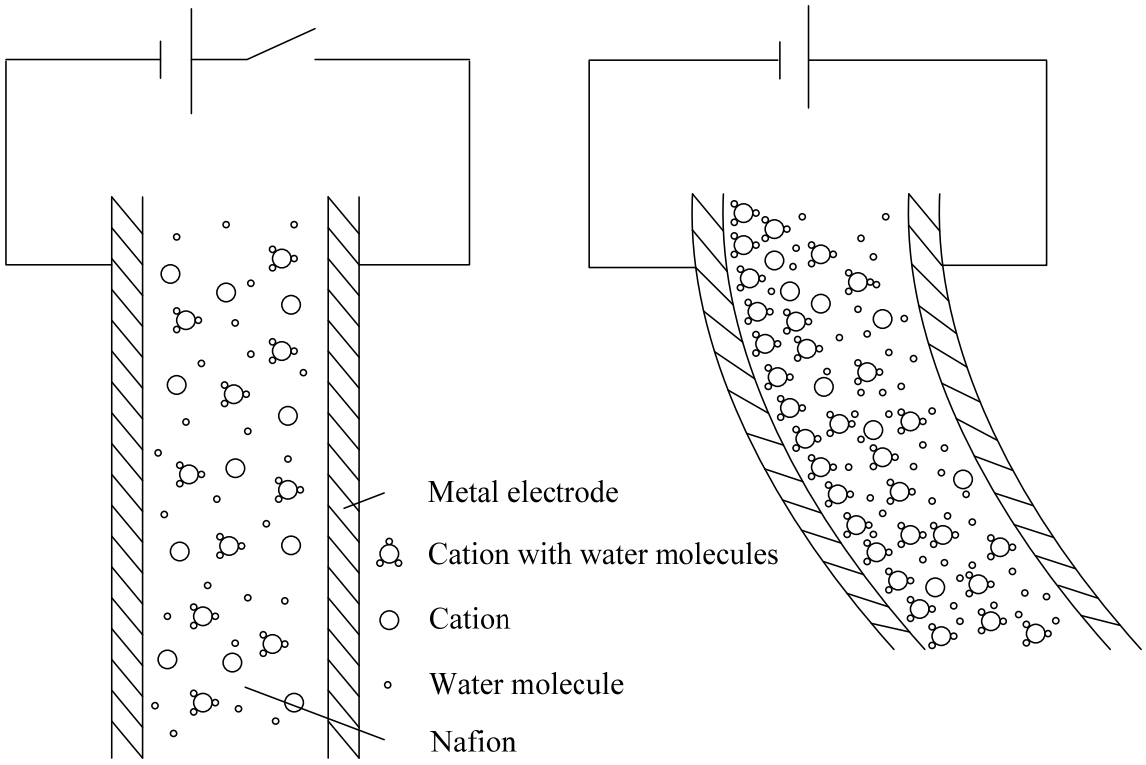

Fig. 2.7 Basic structure and working principle of IPMC strips

It is difficult to move water molecules directly although they are electrically polar. However, with their bonding to cations, which are easily-moved by Coulomb forces, the movement of water molecules becomes under control. Surface metallic

electrodes are used to move the internal cations by attractive and repelling Coulomb forces generated by the surface voltage distribution. Figure 2.7 also illustrates the basic working principle of IPMC. There is a piece of IPMC with an external power to provide with voltage on the surface electrodes. The power is off in the left one, so the cations and water molecules are evenly distributed in the IPMC strip. Without extension or shrinking, both sides have the same length and exhibit no bending motion at all. When the power is on as shown in the right one, however, the cations with the attached water molecules are moved to the cathode side by Coulomb force and cause non-uniform distribution of water molecules. The swelling and shrinking on cathode and anode sides, respectively, makes the IPMC bend toward anode side. The bending angle or curvature depends on the gradient of the water-molecule concentration, which can be controlled by the magnitude of external voltage distribution.

The movement of internal cations comes from the surface voltage distribution, which is greatly affected by conductivity and the thickness of the surface metallic electrodes. An IPMC strip with a layer of highly conductive metallic electrode on each side can exhibit more conspicuous and uniform bending motion. If the thickness of electrodes is insufficient or a large number of cracks or non-uniform metallic coating exists, the strip cannot exhibit a perfect curve with a unique radius of curvature no matter how high the surface voltage is. Surface voltage has been the only medium to move internal water molecules with cations indirectly so far, so the improvement of surface conductivity has acted as an important role although it costs more money and time on IPMC fabrication.

2.3 Characteristics of IPMC

An IPMC actuator is a highly nonlinear system, and its dynamic output responses are affected by a variety of factors as follows:

(1) Driving signals: The deflection angle will increase by a higher input voltage because a higher surface voltage can attract more cations with water moleules to the anode side. However, there is a limitation (about 10 V) because a high voltage may burn and damage the surface electrodes (as shown in Fig. 2.5). In this research, a maximum voltage of 8 V was provided as the input signals to prevent surface-electrode damage. In addition to voltage, the patterns of input signals can also affect the deflection. For example, a rapid and instant increase phenomenon in deflection can exist under square waves instead of triangular and sinusoidal ones because none of them has dramatic change in voltage. The results and comparison will be shown and discussed in Chapter IV. As a consequence, in order to exhibit a rapid and large output deflection, in this research, a series of square waves were provided to activate the robot. Finally, the period of the input signal is another factor to affect the output deflection. An input signal with a longer period can provide more time for IPMC strips to exhibit significant deflection. The fabricated IPMC strips exhibit slower reaction due to the physical structure, so they could show a larger bending curvature by providing with the input signals with a longer period. However, it might not cause apparent difference for thin IPMC strips.

(2) Size/shape: Size can affect the deflection indirectly due to stiffness of IPMC. For the IPMC strips in the same shape, thickness plays an important role in deflection

because of stiffness. Strips with high stiffness can generate large force but small deflection. On the other hand, thin IPMC strips cannot generate sufficient force but rapid and large deflection. Typical illustration of IPMC deflection is shown in Fig. 2.8. A thin IPMC strip exhibits a perfect arc with a uniform radius of curvature as shown in Fig. 2.8 (a). As for a thick IPMC strip, however, the bending strip shows an arc with various radii of curvature, such as $R1$ and $R2$. This phenomenon might

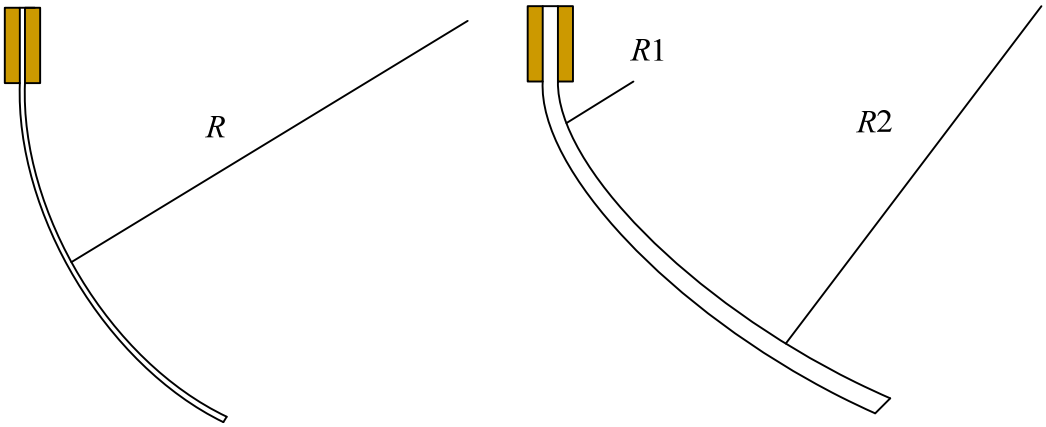

Fig. 2.8 Typical deflection of a thin and a thick pieces of IPMC strips.

be problematic to build a model of this system. Figure 2.9 describes the relationship between output force and length of IPMC strips. It is clear that there is an inversely proportional relationship between each other. Thus, depending on the thickness and size, IPMC can be used in various applications [13−30], and it requires more external power, including voltage and current. As for grippers, IPMC can be cut into various shapes to meet various demands. For example, two thin and fine IPMC

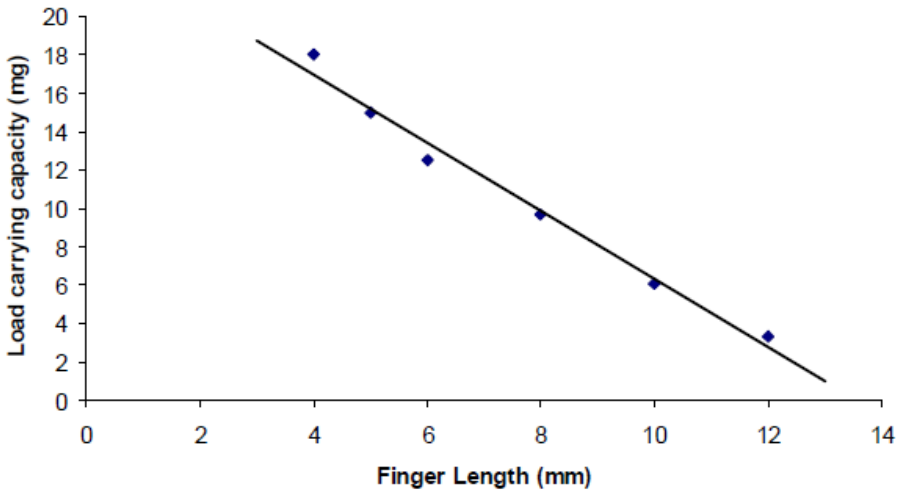

Fig. 2.9 Relationship between force and length of IPMC strips [60]

strips could grip a small ball by providing with precise input signal and controllers as shown in Fig. 2.10 [60]. However, in this research, thick IPMC strips were selected to be the supporters of the robot for their physical structure and to generate sufficient output force. In addition, stiffness might be affected by not only thickness but external environment such as temperature [61].

(3) Surface resistance/conductivity: The deflection of IPMC is generated by cations attracted and repelled by the surface voltage. A conspicuous deflection could be exhibited if there is no power or voltage loss on the surface electrodes. The surface becomes more conductive as the thickness of the metallic layer increases because the surface condition is directly and closely related to the quantities and thickness of metallic layer attached on the surface. Mostly, IPMC strips have been coated with an around 10-μm-thick metallic layer of electrodes on both sides to reduce the resistance by repetitive coating [11]. For the fabricated strips in this research, the

Fig. 2.10 Various shapes of IPMC grippers [60]

thickness of surface metallic layers is also enhanced up to more than 10 μm by five to six times of coating reaction. Furthermore, the surface resistance of our newly fabricated strips is about 0.3 Ω/mm when the width is 10 mm. Voltage decreased by surface resistance will be shown and discussed in Chapter IV.

(4) Water distribution: IPMC needs water to exhibit bending deflection, but the performance might be degraded in some specific conditions instead of water distribution only. In other words, internal water molecules do not mean everything in exhibiting deflection. For example, water molecules in an over-saturated strip might hinder cations from moving freely, so the deflection would be much smaller in an aquatic environment (completely saturated) than that in the air (a dry environment). In addition, water would degrade surface condition such as increasing the surface and internal resistance by expanding IPMC. Surface cracks might exist and become thinner on the expanded IPMC by internal water molecules,

so the surface resistance would be increased greatly. In a practical measuring, it has become from 0.3 Ω/mm up to 1 Ω/mm. Therefore, the water distribution must be set appropriately for the best performance. This comparison will also be shown and explained in Chapter IV.

IPMC exhibits a peculiar phenomenon, back relaxation, which means that IPMC strip bends toward an opposite direction although a constant external voltage is provided. It usually happenes to thin IPMC strips. An illustration of this phenomenon is shown in Fig. 2.11, and it will be described in Chapter IV. It is conspicuous that the normalized deflection is going to the negative although the external voltage and the internal current, given for the entire IPMC system and it comes from the external voltage, are still positive and being provided continuously.

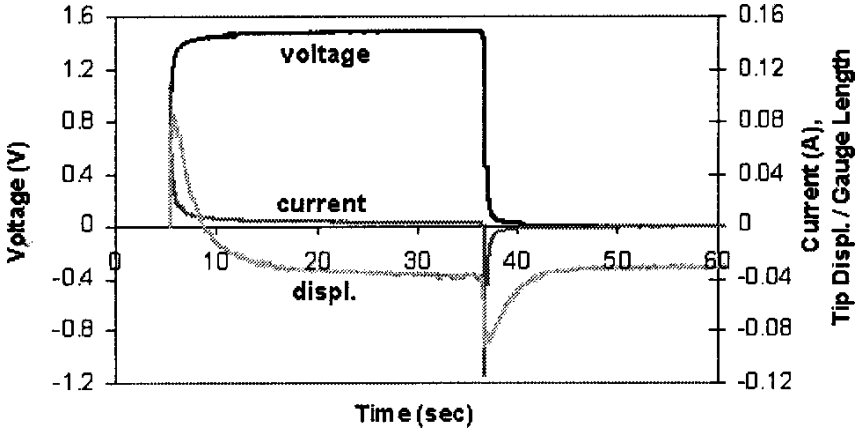

Fig. 2.11 Illustration of back relaxation of IPMC strips [55]

CHAPTER III

SYSTEM ARCHITECTURE

In order to design and implement an IPMC biomimetic robot, a series of hardware and the related interface software have been used in various fundamental experiments and practical robot operation. In this research, a DSP-based dSPACE 1104 board was used as the kernel to generate the signals simulated with Simulink and process digitally the output deflection of IPMC strips. The specific GUI (Graphical User Interface) software makes it possible to use the DSP board more easily. In this chapter, the architectures of the robot, including both the hardware and software, will be introduced and illustrated.

3.1 Architecture of Fundamental Experiments

In order to test the performace of the fabricated IPMC strips, a series of experiments which were decesive to design the robot according to the performance, were employed in this research. For example, the dimension (length and thickness) of the robot and IPMC strips should be decided according to the maximum deflection of IPMC strips in need in order to exhibit higher walking speed and keep the robot stable in operation. A small robot can exhibit high-frequency walking motion but small walking strides by using shorter IPMC strips; a large robot needs more time but makes a big stride in each step. Therefore, the size of IPMC strips and the robot can be decided based

on the experiments. In addition, it is important to make sure of the practical operation in the working environment because in this research the robot is designed to work in an aquatic environment instead of walking in the air. The deflection of IPMC is closely related to the internal water concentration, so the humidity of operation environments affects the performance of IPMC. Therefore, in the fundamental experiments, the IPMC strip was gripped in a small water tank and tested in order to obtain the responses more closely to the practical environment..

In this research, a laser distance sensor (Model ODAM 20I4540/S14C, manufactured by Baumer Electrid, Ltd.) and shown in Fig. 3.1 (a), was applied to measure the deflection of IPMC strips in an aquatic environment. With 12-V input voltage, an analog output from 0 to 10 V corresponding to the distance can be acquired and analyzed. Figure 3.1 (b) illustrates the importance of measuring point. The laser

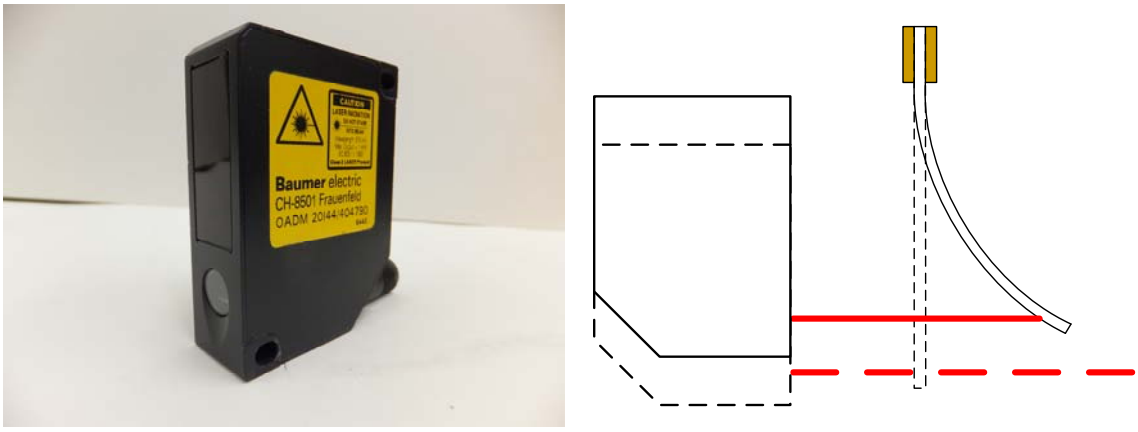

(a) (b)

Fig. 3.1 Deflection measurement using a laser sensor, shown in (a) projecting and receiving laser beam and (b) with and without laser beam received

sensor and the laser beam in dashed lines cannot measure the deflection output after the strip bends beyond a specific extent. For the set-up in solid lines, designed after repetitive experiments, however, the bending deflection at the tip can be derived. Figure 3.2 illustrates the practical architecture of the fundamental experiments. The laser beam is projected to the point 20 mm from the electrodes. In this research, no faulty deflection output is detected due to overbending as shown in Fig. 3.1 (b).

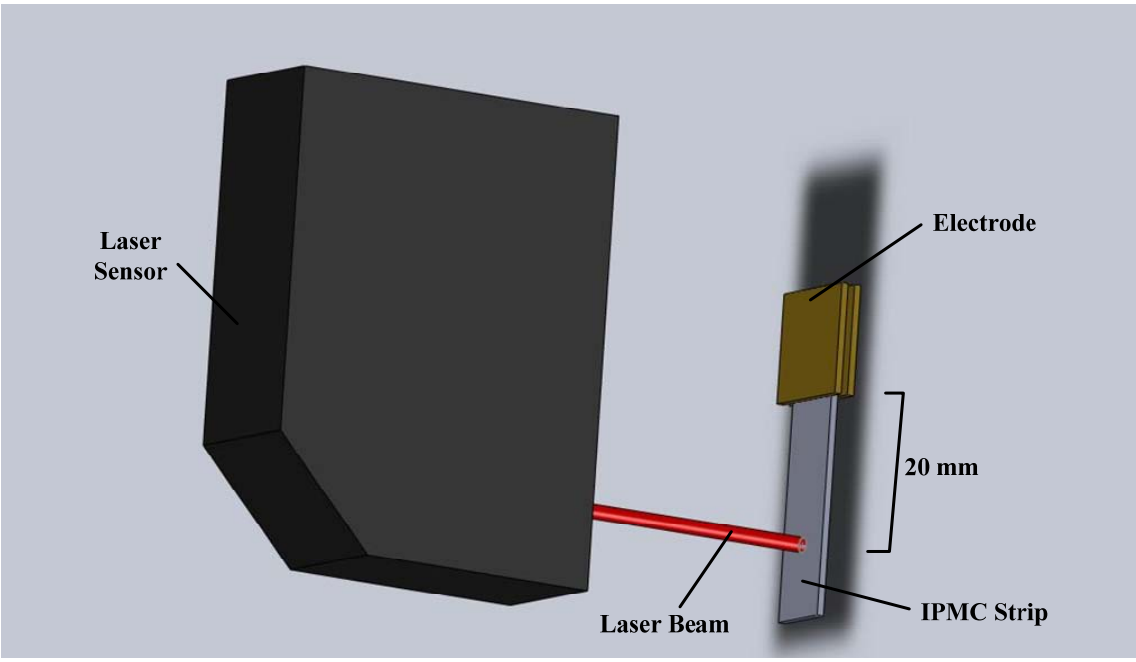

Fig. 3.2 Practical deflection measurement set-up

One of the ends of a piece of IPMC strip was fixed by a clamp (manufactured by McMaster Inc., GA, USA). Two holes were drilled to connect the wires with the external power supply. With the external power via two pieces of copper electrodes (manufactured by Alfa Aesar, Ward Hill, MA, USA) attached to the clamp, the other end

exhibits a conspicuous bending motion that can be measured by a laser sensor. Therefore, the modified clamp becomes both a fixer and an external voltage transmitter as shown in Fig. 3.3.

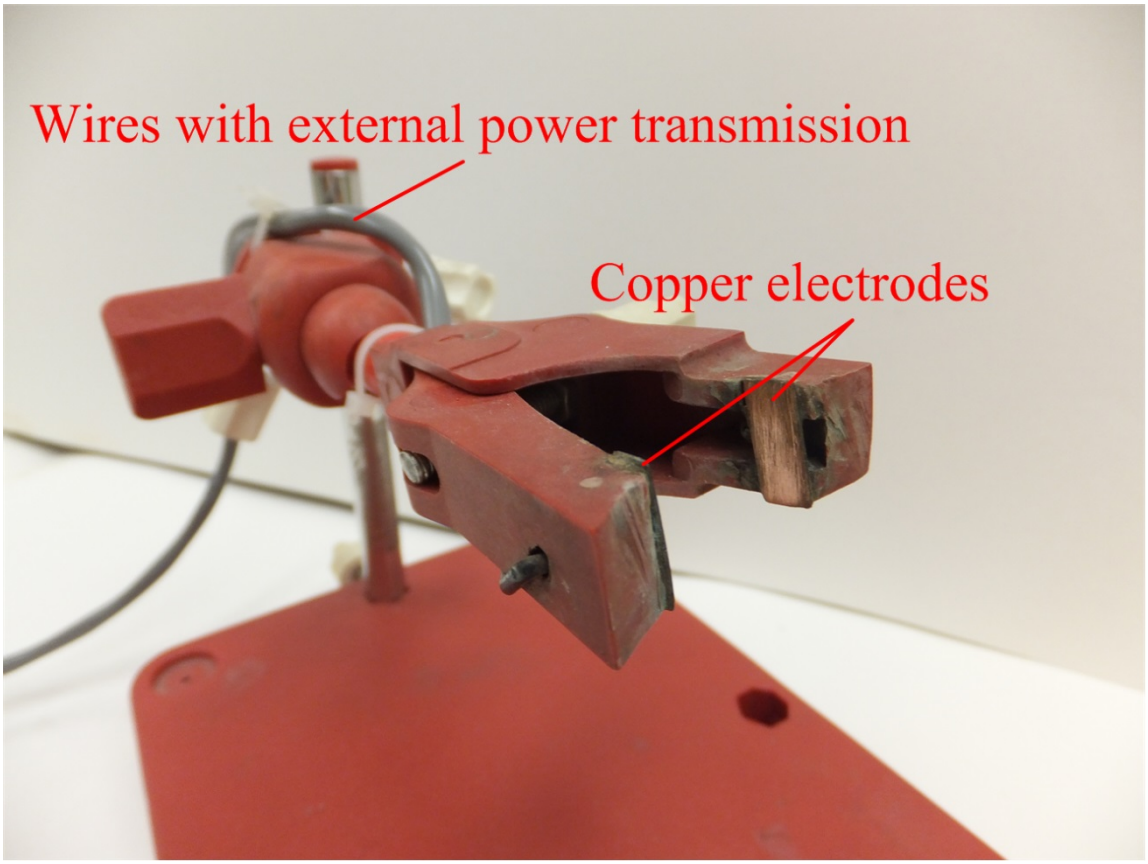

Fig. 3.3 The clamp with two copper electrodes in order to transmit external power and fix one end of an IPMC strip

For the kernel unit in this research, a DS 1104 R&D controller board (shown in Fig. 3.4), which is manufactured by dSPACE with multiple analog and digital input/output channels, is used to do signal processing and communciation with a PC via

a PCI (peripheral component interconnect) slot. In addition, some peripheral devices were used to do signal transmission, process, and acquisition. For example, the analog output signals from a laser sensor go to one of the 8 channels of 16-bit analog-to-digital convertors (ADCs). Output signals can be transmitted via the 16-bit digital-to-analog convertors (DACs) mounted on the board. Then the analog output signals will be amplified in current via a voltage follower before transmitted to IPMC samples. A real-time interface (RTI) software, which will be introduced in next section, provides graphical I/O configuration [56]. Via the specific connector panel, CP1104, a DS1104 board can provide easy-to-use connections between itself and devices to be connected to it.

Fig. 3.4 A DS1104 R&D controller board [60]

Figure 3.5 shows the architecture of an IPMC measurement system in this research. The deflection of an IPMC strip which is stimulated by a specific input signal

is measured by a laser sensor, and an analog output signal from the sensor is acquired via an ADC channel. After a series of processing based on the executable file from a PC, the board transmits an analog signal via a DAC channel to the IPMC strip via two copper electrodes. A voltage follower which amplifies the current with a stable voltage signal is used to meet the lowest current requirement for the activation of an IPMC strip. The corresponding executable file, edited and generated with Simulink®, is downloaded on the DSP board to do complex computing and simulate the necessary output.

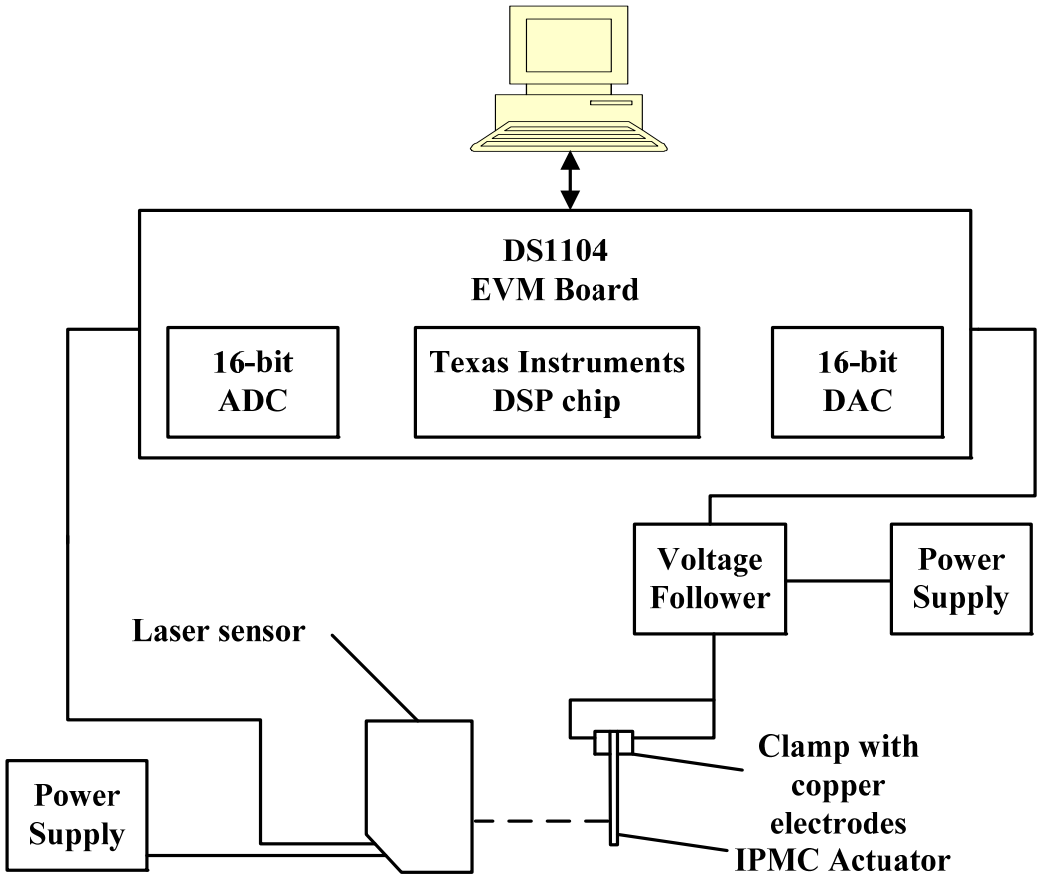

Fig. 3.5 Architecture of an IPMC measurement system

Two groups of external power supplies are used for the laser sensor and the voltage follower. As shown in Fig. 3.5, the laser sensor needs 12-V external power and transmits analog output signals in operation. The voltage follower used in this research can enhance the necessary current and keep the output in the same voltage as the input signal by two external power (8V and −8V). Finally, the IPMC strip is stimulated by the external power via the copper electrodes on both sides uniformly. However, there might be oxidation between the surfaces of IPMC strip and copper electrodes, and can degrade the surface conductivity of IPMC strip, so both of the copper electrodes must be wiped with sandpapers periodically to remove the layer of the non-conductive substance.

3.2 Communication between DS 1104 EVM Board and Users

In addition to the 8 channels of both ADCs and DACs, the dSPACE DS 1104 provides other practical peripheral devices such as digital I/O and pulse-width modulation (PWM) wave generators. Other than the above peripherals devices, DS 1104 board provides a digital incremental encoder interface. As for transmission devices, RS232 and RS422/RS485 transmission connectors are also lined out to the connector panel. dSPACE provides a specific GUI software, ControlDesk, for users to communicate with a DS 1104 board [62]. Users only need to insert the blocks into a Simulink® block diagram and an executable file can be generated and downloaded into the internal synchronous dynamics random access memory (SDRAM) of a DS 1104 board. ControlDesk, a GUI software, can be customized by users and execute the file

generated by Simulink®. In addition, DS 1104 and ControlDesk provide real-time interface, so all parameters in the whole system can be changed in operation. In other words, not only data acquisition, users can also change the processing methods or outputs manually. Figure 3.6 shows an example of Simulink® block diagram for the IPMC measuring system. Original data from sensers are processed by a series of

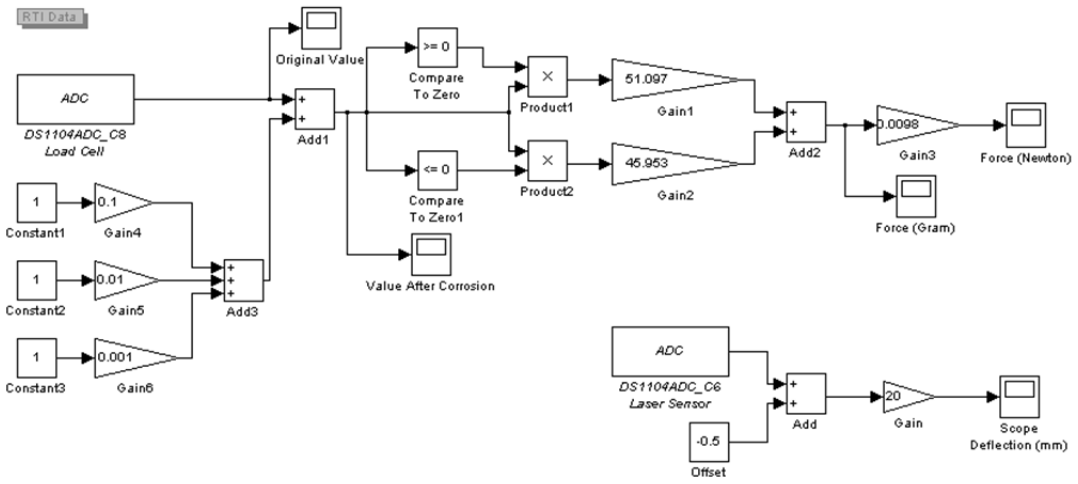

Fig. 3.6 Simulink® block diagram

computing blocks, and then the processed measurement data are shown in the graphical window shown in Fig. 3.7, a working environment of ControlDesk. In this figure, numeric and graphic outputs are displayed, and a gain input box, which is used to change the gain of input signal, is located in the middle. The mark, "RTI Data," on the top left means this program can be tweaked manually in operation to meet the requirements of a real-time control system.

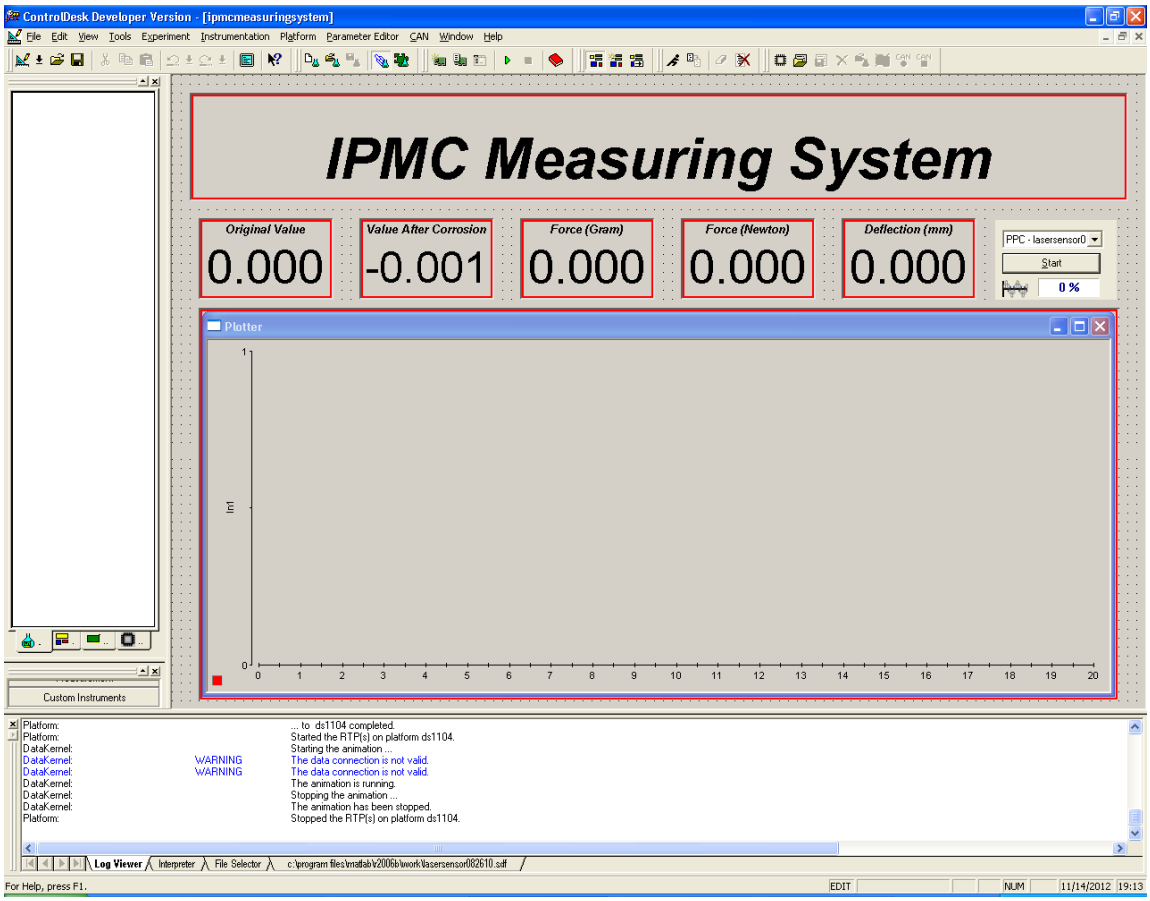

Fig. 3.7 The specific GUI working environment of ControlDesk

CHAPTER IV

FUNDAMENTAL EXPERIMENTS

AND TESTS OF IPMC

In Chapter II, the working principle of IPMC was discussed and described in detail. The deflection, however, may not be perfectly good in practical testing due to the non-uniformity in thickness of surface electrodes in fabrication process, which is one of the decisive factors of the performance of IPMC. Therefore, after IPMC strips are fabricated, some fundamental tests are to be performed to characterize them in practical operation and choose the most appropriate strips and input signals for a robot. The robot needs the IPMC strips with stable and fast deflection in order to exhibit a perfect walking motion. Moreover, the first two experiments can be used to prove that the movement of internal water molecules decides how an IPMC strip exhibits deflection. The results in the fundamental experiments can be used to decide and choose the size of the IPMC strip, the working environment, and the pattern of input signal to activate the IPMC robot in Chapter VI, and prevent unnecessary waste of power.

---

*Part of this chapter is reprinted with permission from "Aquatic ionic-polymer-metal-composite insectile robot with multi-DOF legs," by Y.-C. Chang and W.-J. Kim, *IEEE/ASME Transactions on Mechatronics*, vol. 18, no. 2, pp. 547−555, Apr. 2013. Copyright 2013 by *IEEE/ASME Transactions on Mechatronics*, and "Design and implementation of an ionic-polymer-metal-composite aquatic biomimetic robot," by Y.-C. Chang and W.-J. Kim, in *Proceedings of ASME 2011 Dynamic Systems and Control Conference and Bath/ASME Symposium on Fluid Power and Motion Control*, Oct. 31–Nov. 2, 2011, Arlington, Virginia, USA, pp. 411−418. Copyright 2011 by DSCC.

4.1 Relationship between Internal Water Molecules and IPMC Deflection

The internal membrane of IPMC is the polymer, Nafion®, which swells by water molecules. Non-uniform existence of water molecules causes IPMC to bend. This phenomenon can be applied in practical tests by controlling the movement of water molecules. To prove this relationship, some experiments were proposed and used to show and explain in the following paragraphs because of the characteristics of Nation®, — strong water absorbing and swelling.

In the first fundamental experiment, a piece of dry IPMC sample was fixed and splashed with DI water on one side as shown in Fig. 4.1 (a). Then an apparent bending motion took place immediately without other stimuli. The side with DI water's splashing on would keep swelling, but on the other side IPMC was dried and shrank, lacking in water molecules. The difference of length between two sides resulted in this bending motion. In addition, this bending motion showed a perfect arc, which means that the arc had the same radius of curveature everywhere, owing to uniform distribution of water splishing. Figure 4.1 (b) shows the picture of this experiment.

The deflection is shown in Fig. 4.2. In this experiment, DI water had been splashed after 10 s. The response got increasing abruptly because a bending motion occurred suddenly. Around 50 s, the splashing was stopped, so the slope of the line suddenly changed slightly. After that, the bending speed decreased gradually but deflection still kept increasing owing to the following two reasons: (1) the surface water was evaperated and (2) water molecules moved to the other side by diffusion via the Nafion® membrane. Finally, no large and apparent change in deflection was detected,

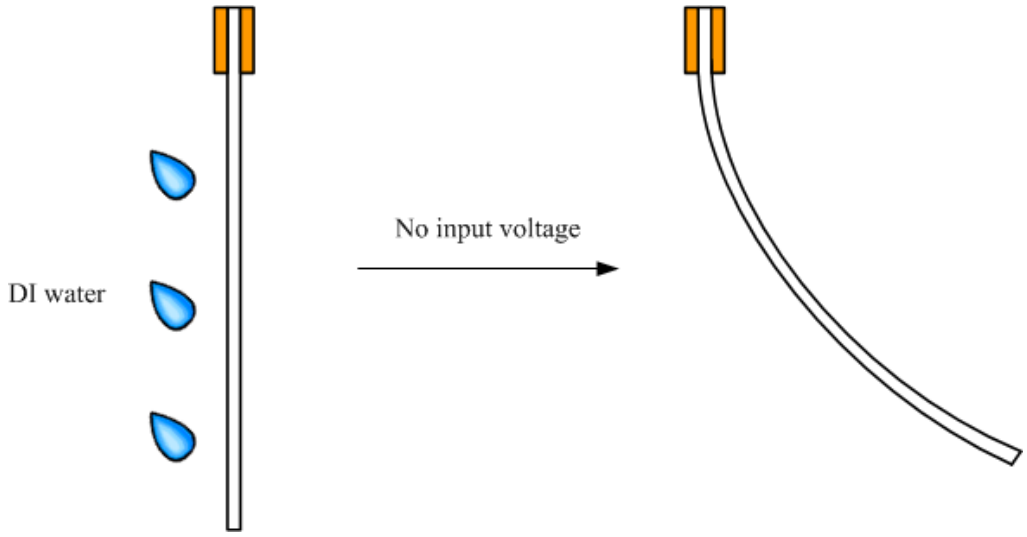

(a)

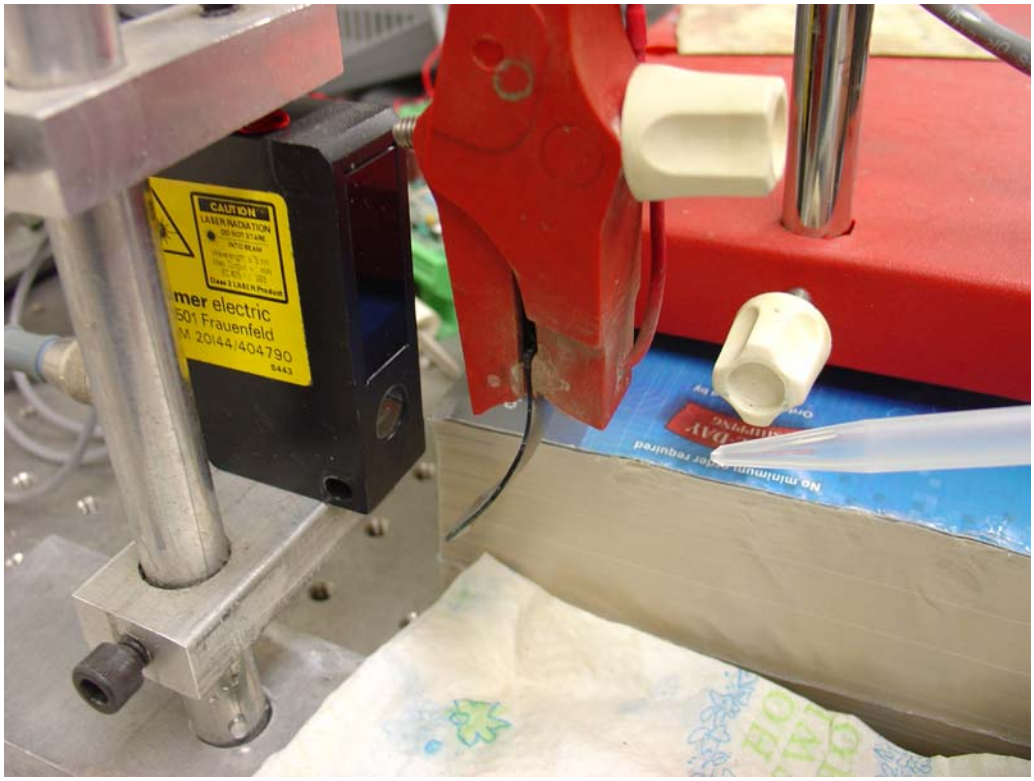

(b)

Fig. 4.1 Splashing DI water on one side without external voltage

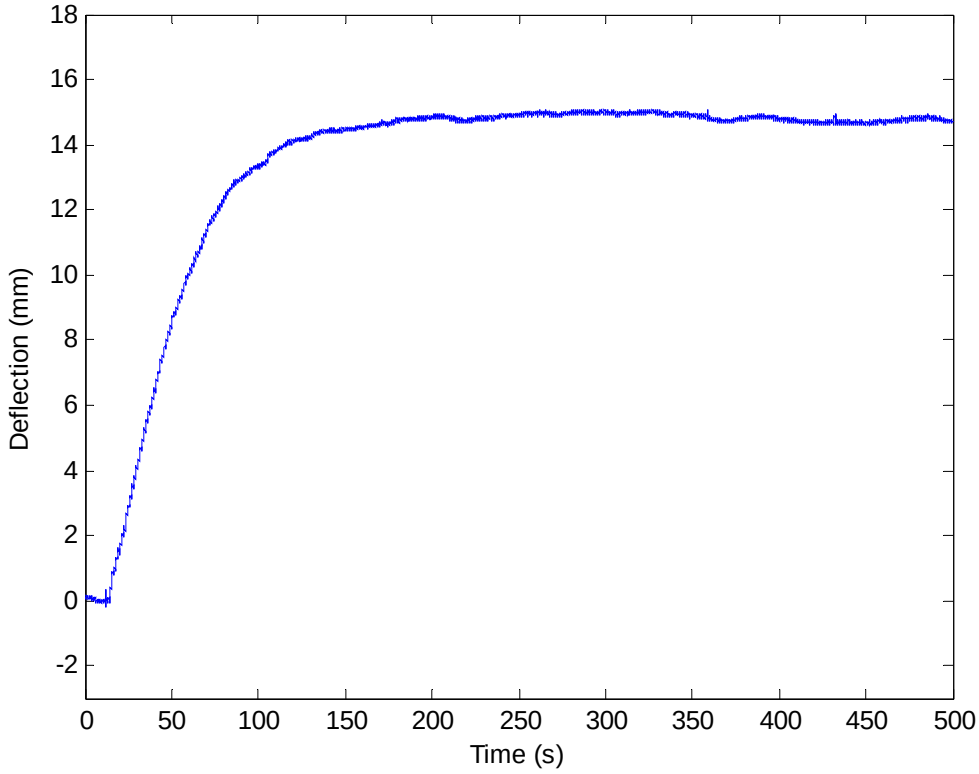

Fig. 4.2 IPMC deflection with one side splashed with DI water

and the deflection was kept in a small range before the strip was dried throughly. This final state indicates the limitation of deflection without any external electrical power. In Fig. 4.2, this state exists after 200 s and still exhibits little change in deflection.

Two reasons might result in the downspeeding bending motion right after stopping splashing DI water in the previous paragraph. The first reason decreased or stopped the swelling speed of the wet side due to insufficient water existence inside the IPMC strip. The second reason caused the other side to swell slightly owing to the moving water molecules to this side by diffusion. Both of them decreased the difference

in length between two sides, so it degraded the speed of the bending motion. The final state came after this phenomenon at 200 s with a vibration-like change in deflection. In this figure, the IPMC sample kept showing small bending motion instead of being exactly stable in this state due to the surrounding noise, such as temperature and humidity fluctuation, which can affect the surface wetness of IPMC.

In Chapter II, an thick IPMC strip could not show a perfect arc in operation due to non-uniform voltage distribution on the surfaces, which causes non-uniform internal water distribution. According to Fig. 4.1 (b), however, it is clear that the IPMC sample shows a perfect arc because of almost uniform water distribution without any external voltage distribution. As a consequence, water molecules, which can be viewed as free particles like cations inside Nafion®, play an important role in IPMC bending motion. In other words, the extent and speed of bending motion can be controlled and determined by moving the internal water molecules instead of free cations, which means the user who can control the distribution of the internal water molecules can determine the deflection of IPMC. However, in this research, distribution was used as a means of water molecules' movement.

The basic concept of IPMC deflection results from the movement of water molecules. In order to focus on the effect of internal water molecules, a drying blower was used to keep the other side dried in this experiment. In other words, this experiment is to measure the deflection of an IPMC strip and keep two surfaces wet and dry, respectively by using DI water and a blower. Moreover, the surface temperature was about 55ºC because of input power consumption in operation. A blower, placed at

around 200 mm in distance in order to keep the surface at this temperature, was used to evaporate the surface water on one side. Simutaneously, DI water was splashed on the other side for a while (around 90 s for this experiment). The dry side could prevent swelling by water molecules, and the other side was used as an activation for bending. Thus, the sample should show a speedy bending motion toward the blower and clear change after stopping splashing DI water and drying. Figure 4.3 shows the experiment setup and the practical picture. DI water and a blower were placed on each side to activate the sample by swelling and shrinking on different sides. With a larger difference in internal humidity between two sides, it should have caused larger bending motion than the previous experiment in theory.

Figure 4.4 shows the result of this experiment. The deflection increased significantly with the conspicuous noise when it began due to the vibration caused by

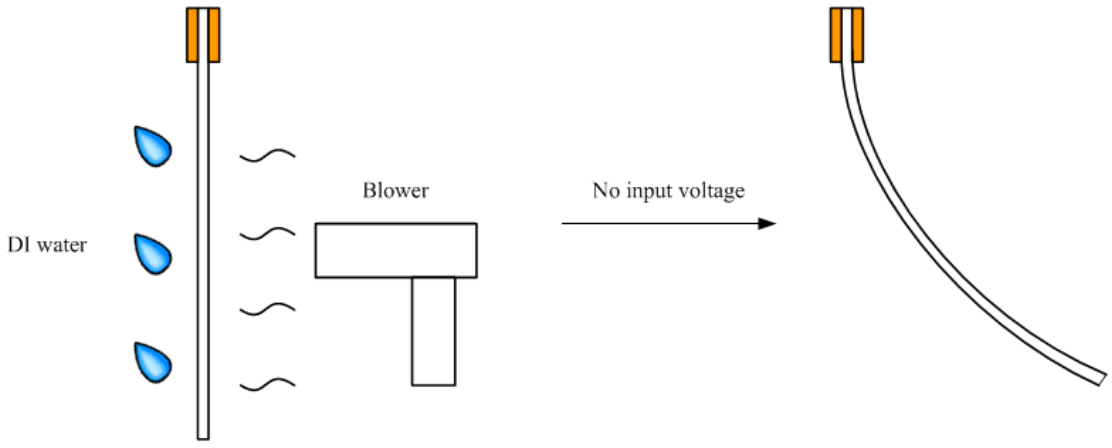

(a)

Fig. 4.3 (a) Splashing DI water and (b) drying on different sides

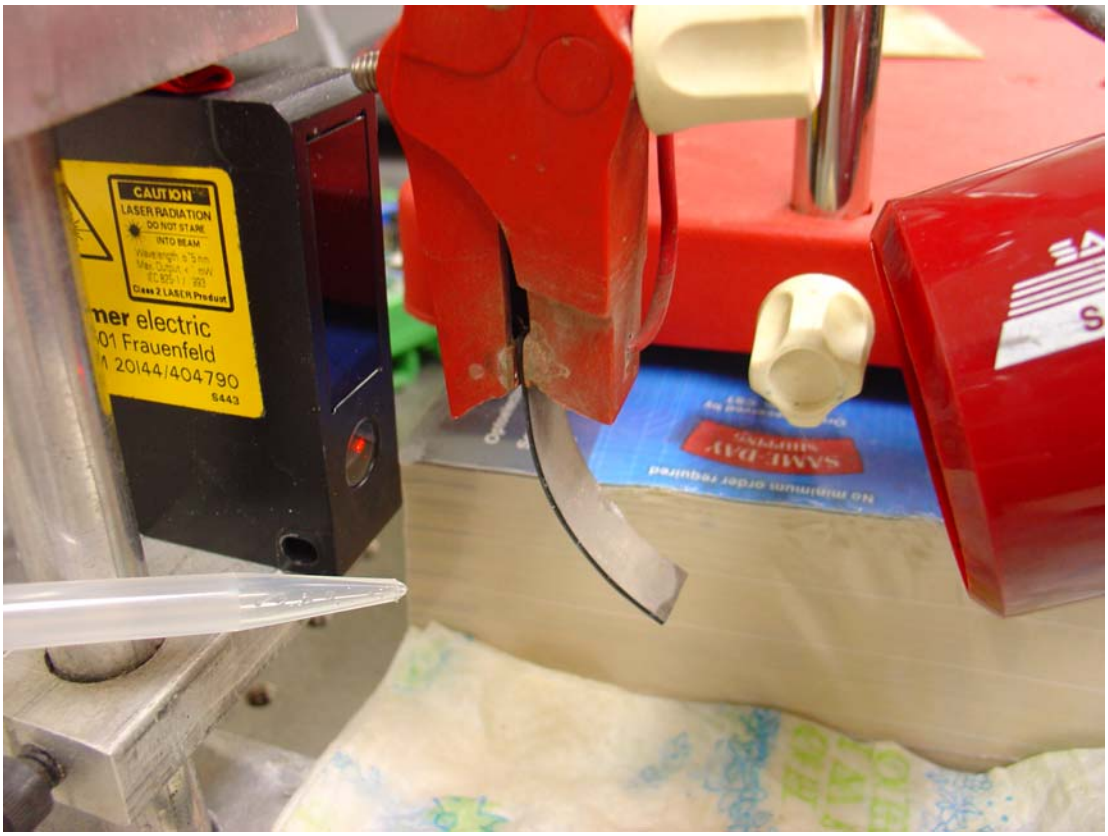

(b)

Fig. 4.3 continued.

powerful wind from the blower. After 100 s, stopping splashing water and drying by the blower, it went down suddenly and then exhibited an unstable phenomenon due to the change of external environment such as temperature and humidity which can affect the water evaporation on the surface. In addition, water molecules might move close to the dry side by diffusion, so the deflection was degraded after 100 s. Eventually, it tended to be stable as a final state when it became an internal and external balance although there were still some vibrations.

The maximal deflection was not greater than that in the previous experiment because the IPMC strip had a powerful wind from the blower. This hinder influenced the results so that these two experiments could not be compared. However, Figs. 4.2 and 4.4 could be used to explain the characteristics and the internal working principle of IPMC.

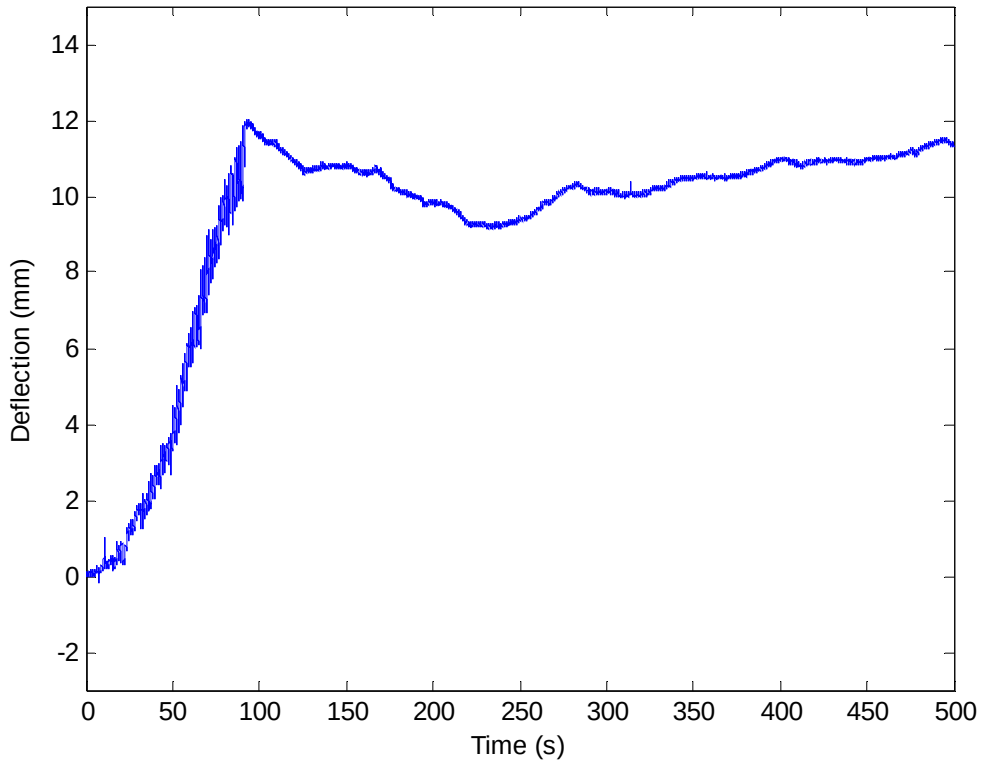

Fig. 4.4 IPMC deflection with each side splashed and dried, respectively

4.2 Back Relaxation and the Effect of Surface Water Concentration

Back relaxation is a typical behavior of IPMC. Theoretically, IPMC strips should bend toward the anode side. However, after a short and rapid positive response, IPMC

strips exhibits a smaller deflection toward the opposite side under the same input signal. This phenomenon is called back relaxation. IPMC strips with different counter ions replaced, such as sodium and potassium ions, show various speeds and extents in not only ordinary responses but also back relaxation [55, 62, 63], and it was discussed in Chapter II. Generally speaking, IPMC strips with a rapid response show a large and instant back relaxation. On the contrary, their back relaxation is small and slow for the IPMC strips with slow responses. Moreover, back relaxation is usual in Nafion®-based IPMC but rare in Flemion®-based IPMC [64]. The following experiment is to measure the back relaxation in four different environments with the same step input signal.

This phenomenon can be described and illustrated in detail by the following plots. Figure 4.5 (a) shows the initial status, when all internal cations with water molecules are uniform. When an input signal was given, most cations are moved to the cathode side by the external voltage. Then the bending motion toward the anode side occurs because of the swelling by the crowded water molecules on the cathode side as shown in Fig. 4.5 (b). The arrows in this figure indicate the imaginary force by the surface voltage distribution. Water on the anode surface is evaporated due to the heat caused by the external power consumption, so this dried surface attracts the internal water molecules continuously by diffusion and decreases the existence of water molecules close to the anode side. Therefore, part of crowded water molecules close to the cathode side move toward the anode side by diffusion, so this phenomenon causes the deflection to be degraded. This case is shown in Fig. 4.5 (c) in detail. Part of the internal cations with water molecules move toward the anode side by diffusion (large

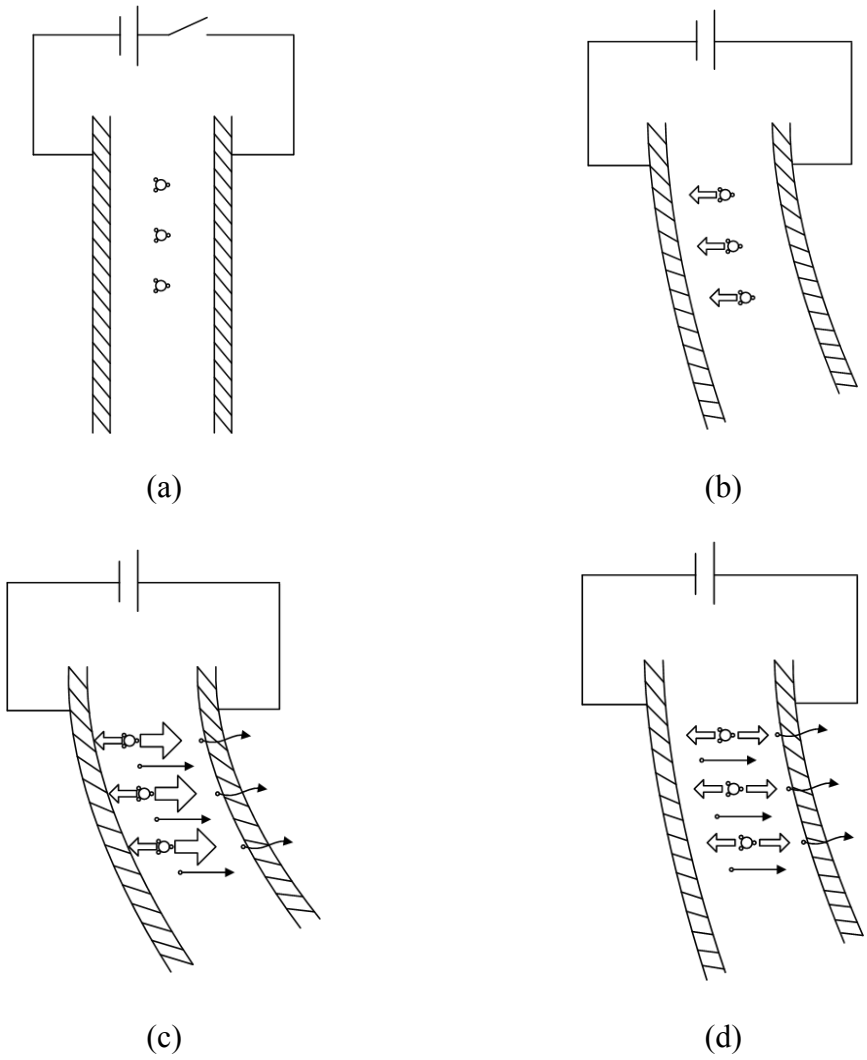

Fig. 4.5 Illustration of back relaxation of IPMC

white arrows) although they are still affected by the surface voltage (smaller white arrows). In addition, water molecules are also moved by diffusion (black arrows).

Finally, the IPMC strips exhibit a stable but smaller deflection than the previous status when the internal part reaches the balance. In Fig. 4.5 (d), the white arrows in the same size meant the cations are in a steady status. Thus, the smaller bending motion

would be held because the water evaporation on the anode side is still ongoing. According to the above description, back relaxation should result from water diffusion and might be more apparent when the sample works in air instead of an aquatic environment.

The following experiment can support the previous hypothesis. In this experiment, an IPMC sample was put in four kinds of environments to measure the deflection with a specific 8-V step input signal generating at 10 s as shown in Fig. 4.6. Figure 4.6 shows the four conditions, which have different surface initial wetness. The wetness was defined by the length, which results from the property of Nafion®. This membrane swells if saturated with water, so the wetness can be attained by the difference in length between two sides. For example, the IPMC strip is 40 mm and 46 mm when thoroughly dry and wet, respectively. It means 50% wet if one side is 43 mm. In the first condition, shown in Fig. 4.6 (a), an IPMC sample was saturated and kept wet thoroughly, but measured in the air. With a step input signal, the anode side would become dried within a short time and then the dry side degraded the surface resistance, so the performance became better in operation. Furthermore, after the evaporation of water molecules, the surface which was not completely wet exhibited larger deflection because overloaded water molecules caused hinders to mobile cations. It means that the IPMC which exhibits the best deflection with neither 100% nor 0% but the specific saturation of internal DI water. In addition, the evaporation of surface water lowers the surface resistance of this side, which can provide more attraction to the cations. As a consequence, in Fig. 4.7 (a), there was a two-stage rising part, initial state, due to this

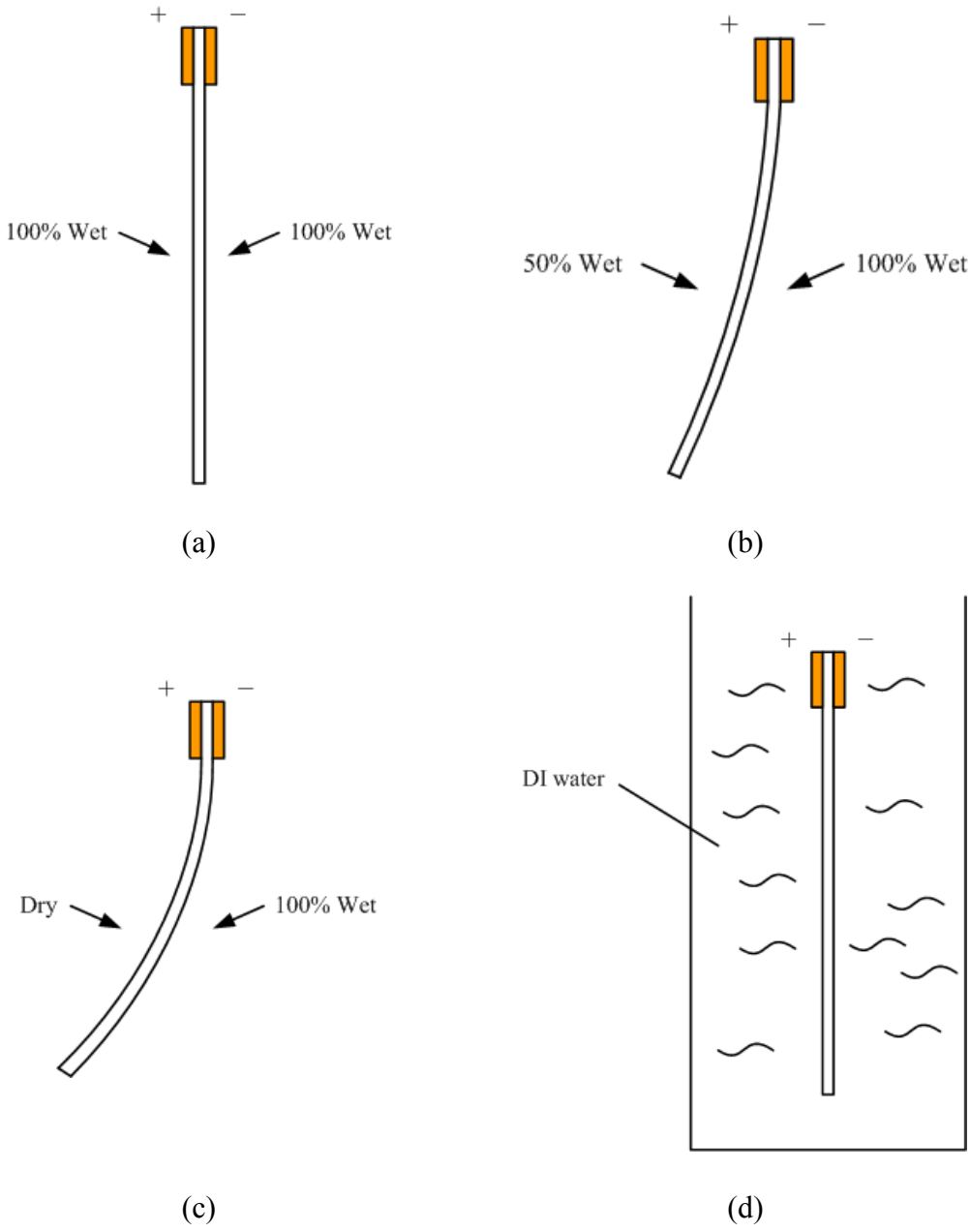

Fig. 4.6 Four testing conditions for IPMC (a) fully wet, (b) half wet, (c) dry on one side, and (d) submerged in DI water

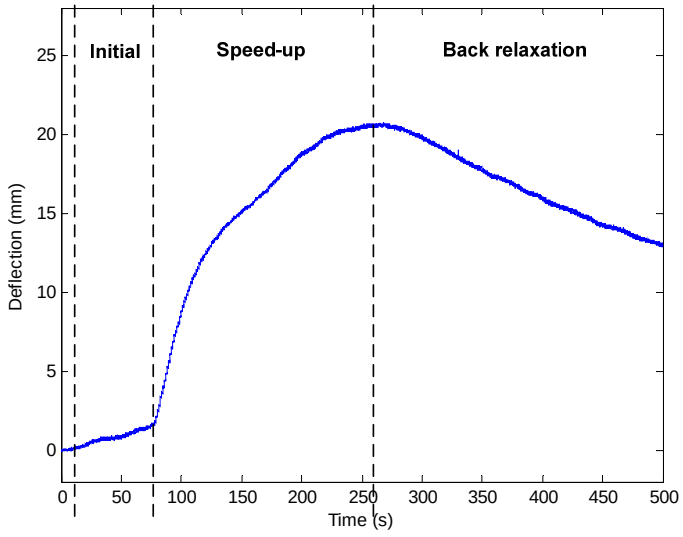

(a)

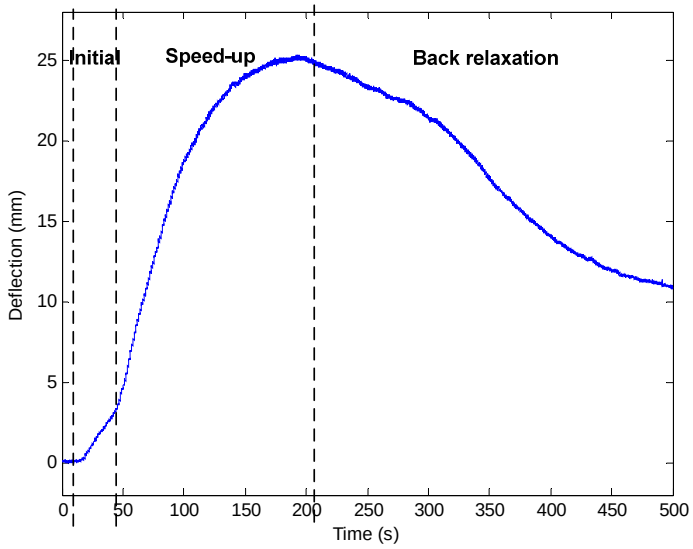

(b)

Fig. 4.7 Responses of IPMC with an 8-V step input in the four environments, (a) fully wet, (b) half wet, (c) dry on one side, and (d) submerged in DI water, corresponding to all in Fig. 4.6

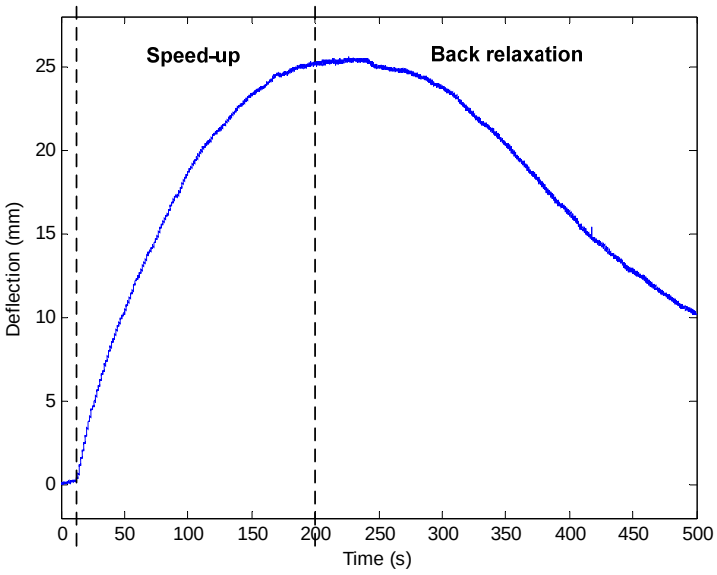

(c)

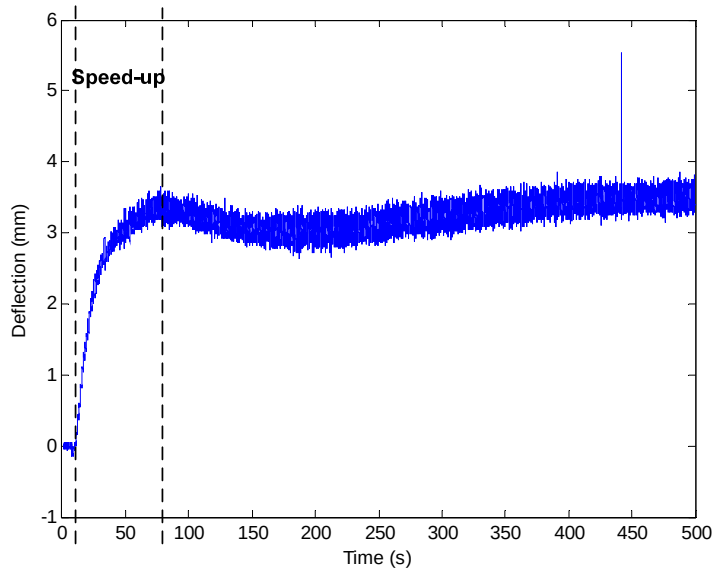

(d)

Fig. 4.7 continued.

phenomenon. In addition to that, several other states, such as speed-up and back relaxation, show up as in Fig. 4.7. The initial state is the time duration before the response increases significantly for dried surfaces. The back-relaxation state, a special phenomenon in IPMC testing, shows a backward bending motion although the positive input signal has been provided continuously. The speed-up state is the time duration between the initial state and back relaxation and it shows up when the anode surface is dried, which causes the surface to shrink and then improve the surface conductivity. This initial state, a gently rising line, has a worse performance due to high surface resistance and too much internal water. After 80 s, the deflection sped up until an upper limitation because the surface conductivity became better than that in the previous state. In this case, the maximum deflection reached around 25 mm at 260 s. After that, the strip exhibited back relaxation and bent toward the cathode side when a positive voltage was applied.

Under Condition 2, the strip was 50% and 100% wet on the anode and cathode sides, respectively. Fig. 4.7 (b) shows that the initial state was shortened because it took less time to dry the anode surface. It showed almost no change for the first 10 s without any input signal. From 10 s, it showed a conspicuous deflection when the external voltage was applied. The speed was faster than the previous one because of the lower water distribution on the anode surface. Then the speed-up state began at 60 s when the anode surface was dried. Finally, the back relaxation toward the cathode side appeared. Compared with the previous result, this showed shorter initial, speed-up, and back-

relaxation states. In addition, the maximum of the deflection was around 25 mm, which is also larger than the previous result.

According to the previous two results, it is obvious that the IPMC sample had a faster and larger response, and back relaxation when the anode side was 50% wet because of the shorter drying time. To prove this theory further, for the third condition as shown in Fig. 4.6 (c), an IPMC sample was kept completely dry and wet on the anode and cathode surfaces, respectively. This strip had a default bending before being provided with the input voltage due to non-uniform distribution of internal water molecules. After the step input was given, it showed a rapid and continuous rising up to the upper limitation without any state change. In other words, there was no initial state in this case because the anode surface was completely dry. From 10 s, the speed-up state appeared for around 200 s to the maximum deflection, 25 mm. This state spent more time than the previous two cases, 180 s and 160 s. The reason is that the lack of water molecules improved the stiffness of the strip and caused it not to bend easily. Therefore, dry surfaces cause the strip to shrink to improve the surface conductivity in general, but the high stiffness is problematic in deflection. The deflection was going back close to zero after the back relaxation happened within a short time. As mentioned in the previous paragraph, back relaxation could result from a large difference in water distribution between the two sides, so it follows that the strip in Condition 3 exhibited higher back relaxation than that in Condition 2. Therefore, it should not be obvious in Condition 4 that a sample was measured in an aquatic environment, which means that an

IPMC strip might not have back relaxation in a 100%-wet working environment based on the hypothesis in Fig. 4.5.

According to the results in the above three conditions, the IPMC samples exhibited transient rising in deflection which could be one or two stages due to the situations of surface wetness. The first stage could endure depending on the water existence on the anode surface. Then a typical back relaxation came after owing to the water diffusion resulting from lacking in water on the anode side. It means that the moving cations with water molecules were affected by the electrical force and the diffusion force, and the former was weaker than the latter. Therefore, in general, the IPMC with larger deflection would be followed by a larger back relaxation. Figures 4.7 (a), (b), and (c) show three examples of back relaxation that happened in practice. Therefore, the internal water molecules would influence the deflection of IPMC, and the self-designed robot will work in an aquatic environment in order to avoid back relaxation.

In order to explain the effect of diffusion, the IPMC sample was tested in an aquatic environment from water evaporation in the last group as shown in Fig. 4.6 (d). The sample was fully soaked into DI water in operation and the result is shown in Fig. 4.7 (d). In this experiment, the sample worked in an aquatic environment without surface water evaporation, so the surface resistance was kept constant in operation. In addition, although the internal water molecules were moved to the cathode side by the surface voltage, the anode side could attract the water outside the sample instead of that from the cathode side. As a consequence, theoretically, the deflection should not be affected by

internal water diffusion. According to Fig. 4.7 (d), the deflection had become increasing since 10 s. Like the strips in the previous environments, it exhibited a transient rising up. However, it was followed by the final state soon due to the aquatic environment. This sample firstly bent toward the other side a little and then went back to the final state gradually. At around 440 s, a sizable bubble was generated and then popped suddenly, leading to an impulse-like noise. The most significant advantage under this submerged condition is that there was no back relaxation that showed in the previous three tests. Moreover, the deflection did not change much after rising up to the maximum but was kept almost steady. Therefore, an aquatic environment is more suitable than the previous three cases because of the steady deflection and no fear of lacking in water molecules. If the voltage is higher than 1.23 V, bubbles will be generated continuously due to water electrolysis.

The specific phenomenon shown in Fig. 4.7 (d) that the deflection went back slightly and then moved back to the maximal value, might not be thought as a back relaxation due to the following reasons. (1) This phenomenon usually happens in aquatic environments. (2) It shows small and transient responses. (3) After that, it still goes back to a stable and saturation value.

This phenomenon often takes place when the sample is working in DI water since the whole piece of sample can obtain sufficient water molecules continuously during the operation. According to the first experiment, however, the performance will not be enhanced if the sample is thoroughly wet. However, back relaxation usually occurs when the sample is measured in the air but not in the water. Therefore, obviously

it is not a typical back relaxation but a specific phenomenon in the water. Moreover, this phenomenon does not endure for a long time. In Fig. 4.7 (d), it has existed around 150 s. Back relaxation, however, will show a large and conspicuous change in deflection instead of going back to the final value. Finally, in this figure, it went back to the saturation value, which is the value before this phenomenon happened.

According to the reasons, this phenomenon, a fake back relaxation, is not the same as a back relaxation. However, they both result from water diffusion. A back relaxation happens due to water diffusion from cathode side to anode side; a fake back relaxation happens because of water diffusion not only from cathode side but also the water outsides an IPMC strip [65]. TABLE 4.1 lists all results, including rise time, peak time and maximum deflection of the IPMC strips in all conditions.

TABLE 4.1 Comparison of the results in all conditions

Condition	Rise time (s)	Peak time (s)	Maximum deflection (mm)
1	230	250	21
2	200	200	23
3	180	180	25
4	40	70	4

4.3 Deflection with Various Input Signals and Deviation

In order to activate the IPMC robot, input signals, closely related to several phenomena, such as back relaxation and bending deflection, should be taken into

consideration carefully. In Chapter II, it was shown in detail that compared with the input voltage, internal current is much more relevant to the extent of the output response. Therefore, the enhancement of input current has more importance than that how to provide with higher input voltage for IPMC strips. Nevertheless, the current generated by the input signal is not only closely depending on the maximal input voltage, but also related to the pattern and frequency of input signals. The samples in the previous experiments were provided with an 8-V step input signal, but they would be stimulated by various signals in the coming experiment.

Three typical signals, sawtooth, sinusoidal, and square waves, were chosen to test the responses of IPMC strips. These input signals were given in three different frequencies to prove that frequencies and the patterns of input signals can affect the output due to slow reaction time. Each input signal increased the internal current in the specific way for its waveform. Sawtooth waves lifted the voltage instantly, went down to the negative both linearly and slowly, and then repeated in the next period. Sinusoidal waves changed the current by slow increase and decrease in voltage. Square waves changed both the voltage and current abruptly, which means the current changed between the positive and negative maximum. Furthermore, the input signals in various frequencies caused the IPMC strip to exhibit various amplitudes due to different reaction time. These three input signals in three frequencies were chosen to test and find out the most appropriate input signal waveform to activate the robot.

Figures 4.8 (a), (b), and (c) show the outputs in response to sawtooth waves with the frequencies of 0.1, 0.2 and 0.3 rad/s, respectively. Sawtooth waves caused a rapid

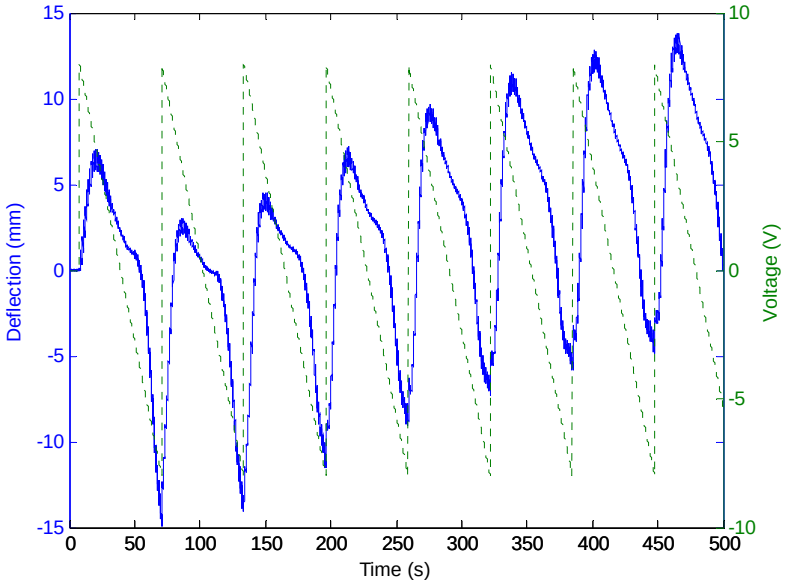

(a)

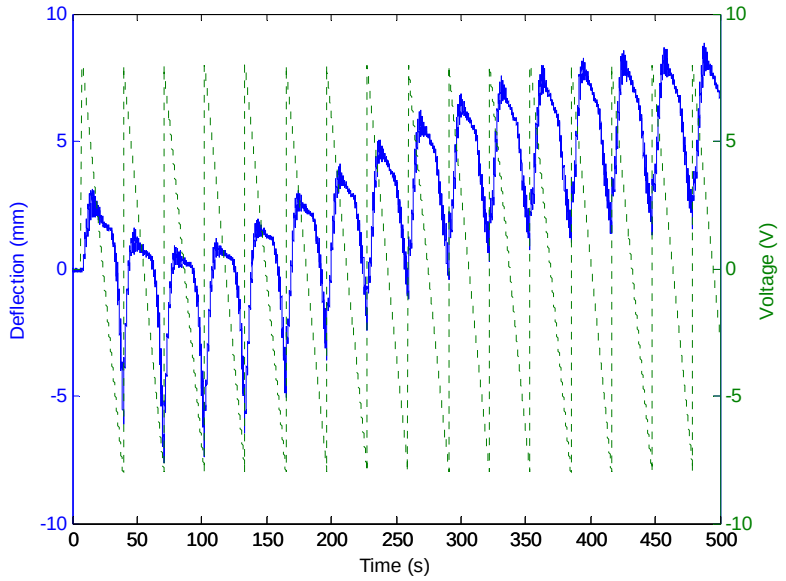

(b)

Fig. 4.8 Output deflection with the providence of sawtooth waves with the frequencies of (a) 0.1 rad/s, (b) 0.2 rad/s, and (c) 0.3 rad/s

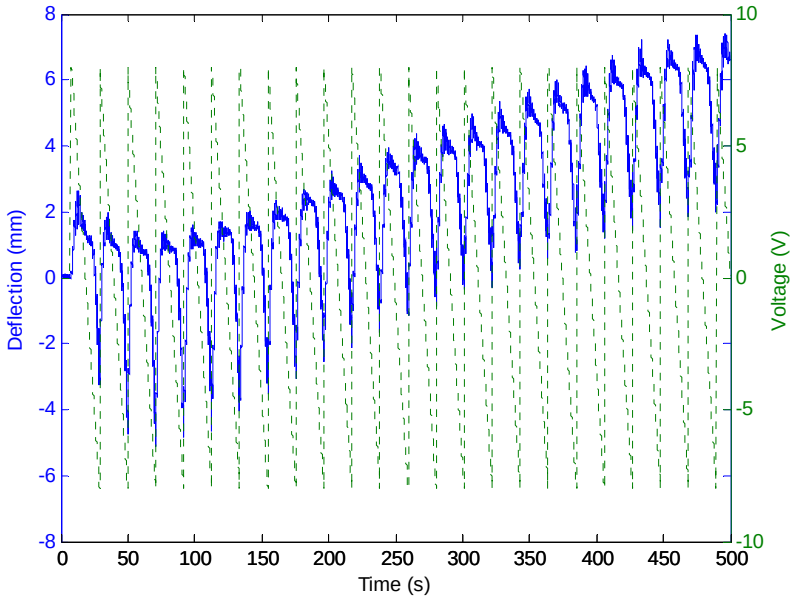

(c)

Fig. 4.8 continued.

rising in voltage and the line went down to the negative gently. According to these three figures, the IPMC sample should bend toward the anode side instantly and then toward the opposite side gradually like the voltage line. In this case, there were two steps in bending toward the anode side. First of all, the IPMC sample showed a bending toward the anode side slowly and smoothly before the input voltage became negative. Afterward, in the second step, a more rapid and larger bending occurred, so this phenomenon not only sped up but also enlarged the bending motion with an more steep slope. Then a new cycle began and the strip bent back to the anode side. Therefore, one-step increase and two-step decrease are the characteristics of the output reponses with sawtooth input signals. By the way, this kind of input signal has been applied in an IPMC fish-like robot

to make a turn due to the asymmetry [14]. This asymmetry in time and deflection could provide unbalanced force for two sides to make a turn.

The deflection amplitude is also related to the frequencies of input signals. In Fig. 4.8 (a), the amplitude was around 10 mm with 0.1-rad/s sawtooth input signals. However, in Figs. 4.8 (b) and (c), it decreased to around 4 and 3 mm with 0.2- and 0.3-rad/s input signals due to insufficient reaction time. The same phenomenon also happened to other tests with different input signals to be described in the following paragraphs. Therefore, both frequency and deflection should be taken into consideration simutaneously in order to activate the robot more efficiently.

Figures 4.9 (a), (b), and (c) are the deflction with the sinusoidal waves with the frequencies of 0.1, 0.2, and 0.3 rad/s, respectively. Slow and smooth change between the maximum and minimum in voltage did not generate a large change in current, so the surface of IPMC samples was not burned by the input current. Nevertheless, the voltage was at the maximum and minimum values for just one moment, so the IPMC samples did not have sufficient current and power to exhibit and keep a good performance. In other words, the IPMC strips could not generate large deflection due to insufficient power and reaction time, so the performance is not as good as expected.

In the previous testing, sawtooth signals caused the samples to show one- and two-step phenomena in the rising and declining, respectively. However, the outputs in this testing showed a two-step rising and then declined with sinusoidal waves because the input signal was symmetric in amplitude. A two-step increasing and decreasing degraded the bending motion speed and deflection, so it took more time and exhibited

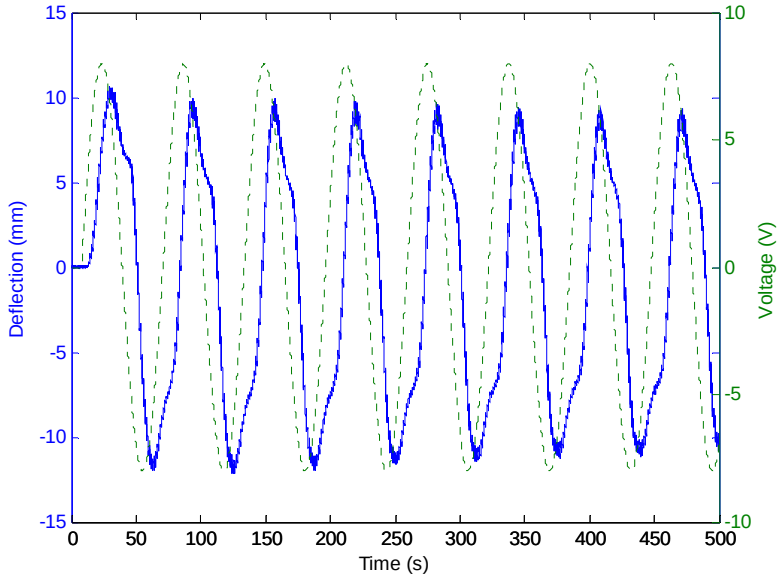

(a)

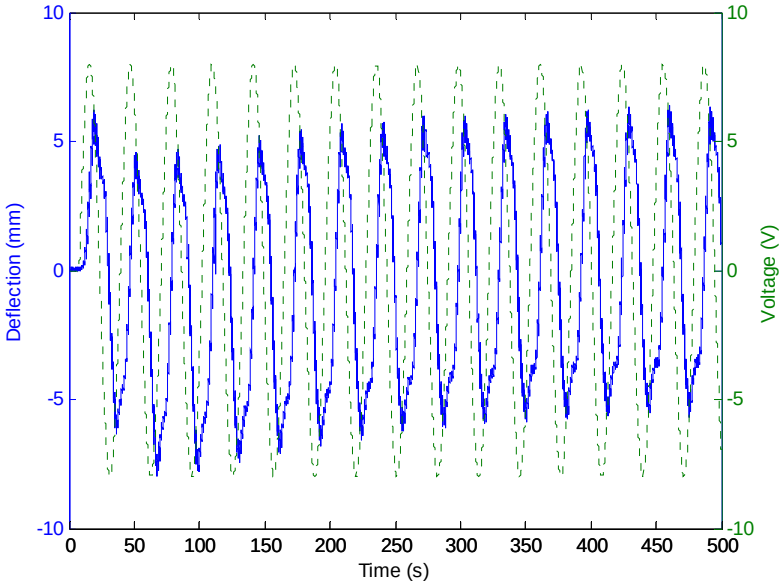

(b)

Fig. 4.9 Output deflection with the providence of sinusoidal waves with the frequencies of (a) 0.1 rad/s, (b) 0.2 rad/s, and (c) 0.3 rad/s

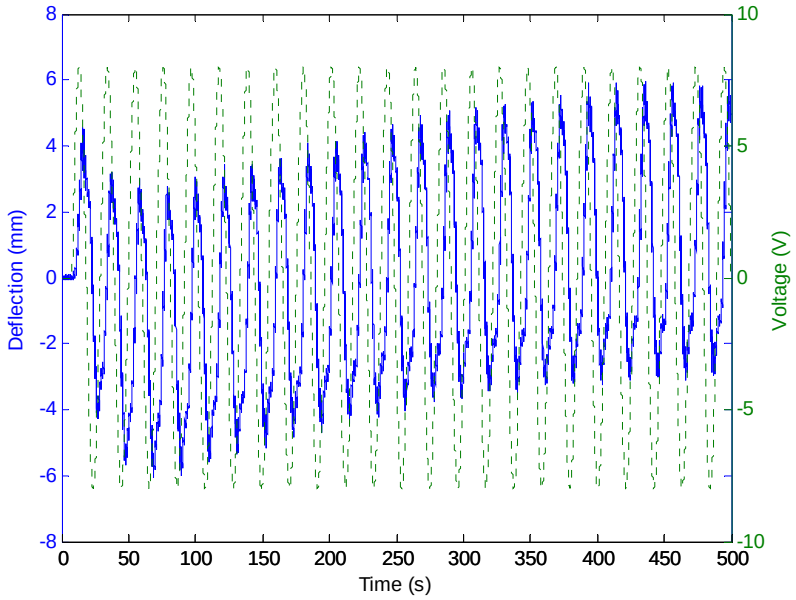

(c)

Fig. 4.9 continued.

smaller extent of bending motion.

The maximum of deflection amplitude was quite close to the previous testing when the frequency was 0.1 rad/s. However, the strip showed better deflection with 0.2 and 0.3 rad/s and the amplitudes were around 6 mm and 4 mm, respectively. Compared with the sawtooth wave, the sinusoidal wave is more appropriate to activate the robot for larger deflection, more symmetric responses, and less damage on IPMC samples. Nevertheless, the next testing, with square waves, would show the best performance among these three input signals, including the deflection and symmetry, so square waves should be the best choice to drive an aquatic robot.

In the last group of testing, square waves, which can generate the highest current periodically, were provided for IPMC strips with the frequencies of 0.1, 0.2, and 0.3 rad/s. Figs. 4.10 (a), (b), and (c) showed the deflection and the corresponding input signals, respectively. All deflection amplitudes were around 10 mm. The following groups are the description and the corresponding output of each input signal.

(1) Sawtooth waves: the transient voltage rising caused IPMC samples to burn easily on the anode side but kept clean on the other side owing to slow decreasing to the negative in voltage. In addition, this input signal showed insufficient reaction time to keep at the maximum, so the positive reaction was smaller than the negative one. In other words, the reaction was asymmetric between the two sides. The asymmetric output would affect the stride and relationship with other IPMC strips if applied in robotic walking lcomotion.

(2) Sinusoidal waves: slow voltage rising and declining did not cause large and instant change in current, so the IPMC sample did not usually burn. However, the sample did not show good deflection for robotic walking motion due to insufficient time under both the highest and the lowest voltages. Besides, according to Fig. 4.9 , all of the outputs were a little bit asymmetric although this sinusoidal signal was completely symmetric. Therefore, this signal might destroy the walking stride and balance of the robot due to the asymmetric deflection.

(3) Square waves: abrupt and repetitive changes between the maximum and minimum caused large changes in current which could make IPMC strips burn severely. However, the IPMC sample exhibited a large deflection, which can provide

sufficient locomotion for the robot, with the square waves. Furthermore, the more symmetric performance than the previous two can make the robot walk more steadily and smoothly.

Generally speaking, the amount of current shows a positive proportion to the voltage although Ohm's Law is not exactly applicable to an IPMC system (It will be discussed in Chapter V). For example, the input current in the sinusoidal wave testing showed a sinusoide-like plot. In the square waves test, the current kept around the maxima in the positive and negative. This is why in the last group the sample exhibited the best deflection but burned easily and severely. The instant maximal current in Groups 1 and 2 could be up to 1.5 A when the voltage was given in 8 V. In Group 1, like a sawtooth wave, the current rose up to the maximum instantly and then declined slowly following the input voltage. Finally, it reached the negative maximum value and then came back to the positive maximum rapidly. The current in Group 2 also showed the similar plot to the sinusoidal waves. The current increased and decreased slowly and periodically. In Group 3, however, the instant highest current could be higher than 2 A with an 8-V input provided and kept for the entire period. Moreover, the current showed a square wave. In other words, the current always kept at the positive and negative maxima due to the square waves, so the power consumption was the largest among these three tests due to the highest input current. The IPMC-strip surface showed the largest defection due to the highest power consumption and input current for a long time.

Furthermore, in these plots, a specific rising-up phenomenon that the average deflection of the wave crests and troughs became increasing gradually occurred and

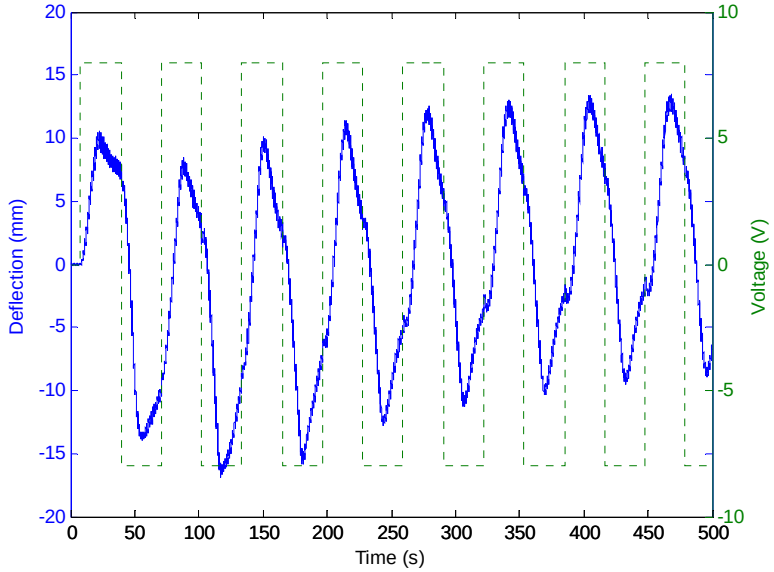

(a)

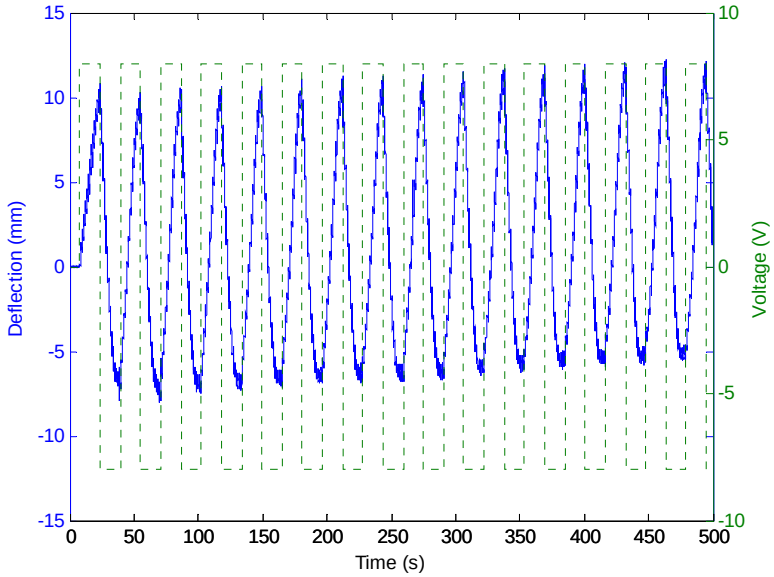

(b)

Fig. 4.10 Output deflection with the providence of square waves with the frequencies of (a) 0.1 rad/s, (b) 0.2 rad/s, and (c) 0.3 rad/s

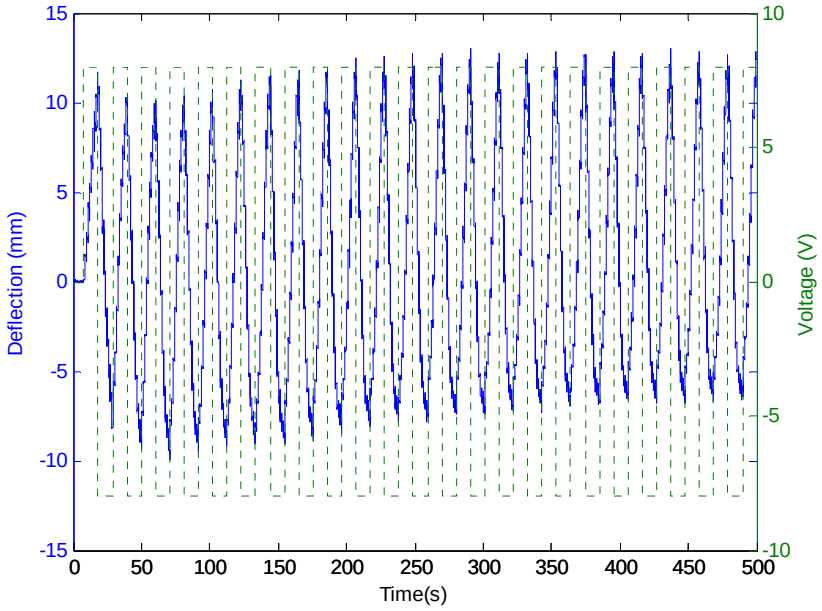

(c)

Fig. 4.10 continued.

endured for the entire testing period. This prevalent phenomenon is called deviation and often exists in IPMC deflection as a specific characterisitc. IPMC exhibits a rising deviation to the positive side after a temporary and short decrease. Figures 4.8, 4.9, and 4.10 show some examples of conpicuous and large deviation and the deviation can be up to 4 mm in Group 1. According to the results, the deflection exhibits various deviation with various input signals, including categories and frequencies. First of all, it seems that the sawtooth wave caused greater deviation than the sinusoidal and square waves in the same frequency due to the asymmetry of sawtooth waves. There is a conspicuously larger deviation in Fig. 4.8 than those in Figs. 4.9 and 4.10 because this kind of asymmetric input signals spend different time reaching to the wave crests and troughs

[66]. This asymmetric input signal shows an instant increasing to the crest but spends the entire period going down to the trough slowly. Nevertheless, it does not mean that no deviation happens with fully symmetric input signals but a little tiny rising shows up in Figs. 4.9 and 4.10, which have around 2-mm and 1-mm deviation, respectively.

In addition to input patterns, as for another factor, frequency, the input signals in higher frequency results in the existence of larger deviation if the input signals have the same characteristics. High-frequency input signals, which provide insufficient time to exhibit an entire reaction, so an asymmetric deflection occurs. For example, in Fig. 4.8, Part (c) (4.5 mm) has larger deviation than Part (a) (4 mm) and Part (b) (4.2 mm), and the same phenomenon is shown in Figs. 4.9 and 4.10 although the deviation phenomena in these two figures are small. As a result, the frequency of input signal plays as an key role in the deviation of IPMC strips. Finally, during the fabrication process, Nafion® become soft and deformed after being cleaned by sulfuric acid. It is difficult to keep the Nafion® fully flat, so IPMC strips have large or tiny default bending. Obviously it tends to bend toward the side the same as the default bending instead of the other side. The default bending status, however, has no significant influence on this phenomenon.

In order to ensure the relationship between default bending and deviation, a specific experiment in three groups was performed, and the results are shown in Figs. 4.11, 4.12, and 4.13. In this experiment, an IPMC strip with default bending (around 10 mm) was given with 6-V square waves. In the first group, the strip was gripped and provided with an ordinary square wave as shown in Fig. 4.11 (a). The direction which the default bending bent toward was set as the positive one. As shown in Fig. 4.11 (b), a

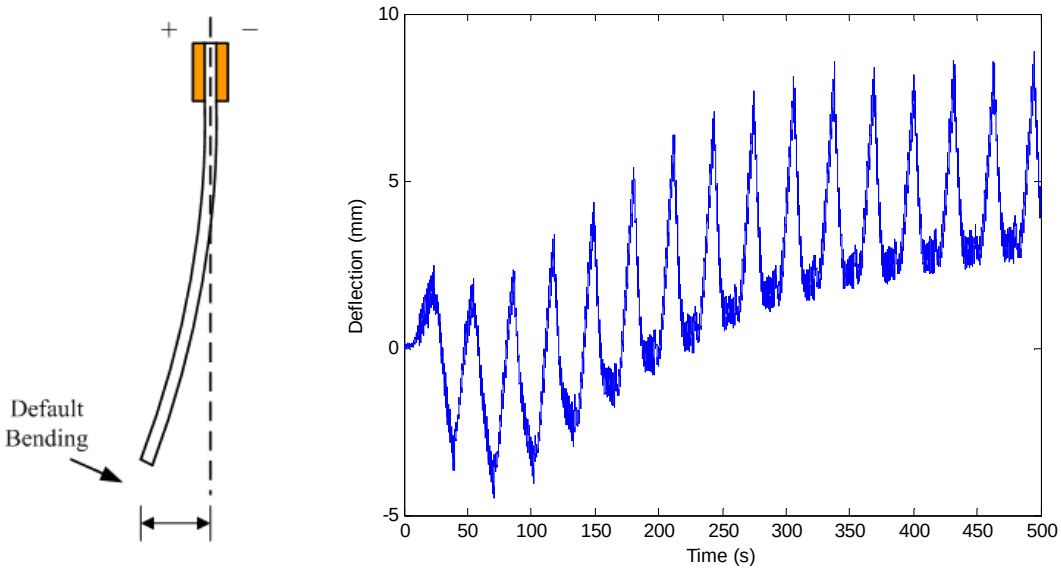

(a) (b)

Fig. 4.11 (a) IPMC strip with a positive default bending and (b) the experimental result

conspicuous and typical deviation (around 5 mm) occurred as expected that the default bending was helpful to the deviation. In the second group, the same square wave was input to the IPMC strip which was gripped toward the opposite direction. In other words, theoretically the default bending might cause an obstable to the deviation. The strip was gripped and the result was shown in Figs. 4.12 (a) and (b), respectively. According to Fig. 4.12 (b), however, a similar deviation toward the positive direction instead of the inverse one. In addition, there was almost no deviation toward the negative direction although the default bending was toward this side. The results in Figs. 4.11 and 4.12 can assure that the direction of default bending did not cause the deviation phenomenon as

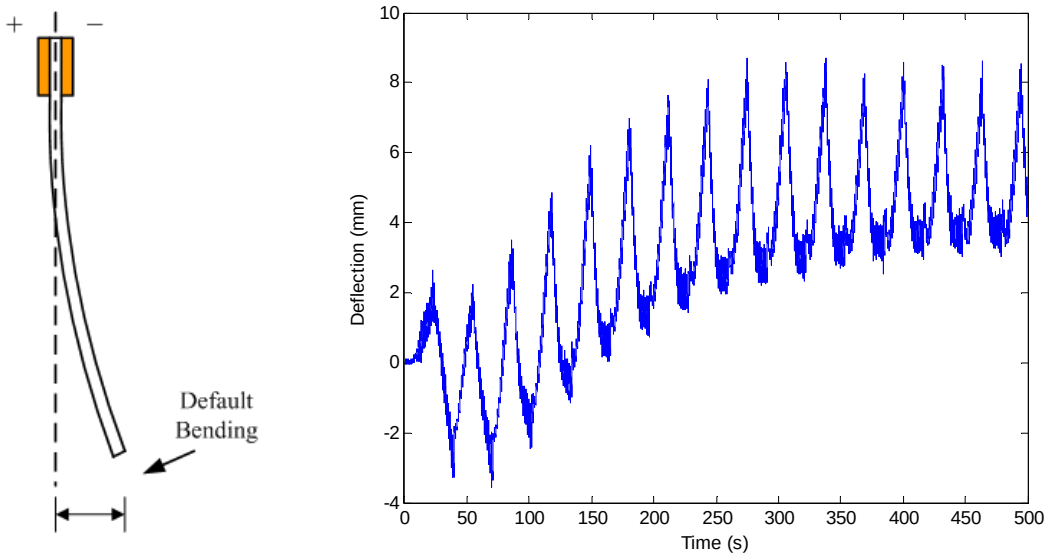

(a) (b)

Fig. 4.12 (a) IPMC strip with a negative default bending and (b) the experimental result

expected, so in the next testing, the input signal was given for the strip fixed as shown in Fig. 4.13 (a) inversely as shown in Fig. 4.13 (b) in order to see if the initial voltage affects the deviation. The input signal was fully opposite to the previous two in phase. In order words, the strip was bending toward the cathode side instead of the anode side initially. Theorectically, the strip in this testing should exhibit a conspicuous deviation toward the cathode side due to the fully opposite input signal in phase. As shown in Fig. 4.13 (b), the strip, however, still exhibited a similar deviation to the previous two, a deviation toward the anode side gradually instead of the cathode side like the input signal. As a consequence, according to the above results, neither the phase of input

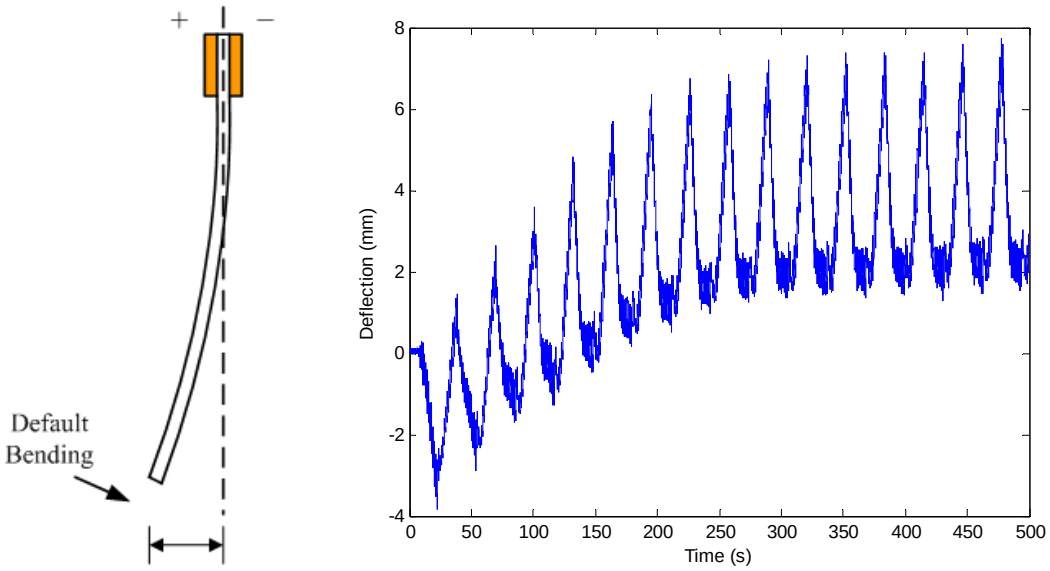

(a) (b)

Fig. 4.13 IPMC strip with a positive default bending and (b) the experimental result with opposite input signals to that in Fig. 4.11 (b)

signals nor the direction of strips is deeply related to the deviation phenomenon of IPMC.

For the robotic walking motion, the deviation phenomena should be avoided due to unstable and constantly positive or negative working range, which might not be able to move the robot. In addition, deviation phenomena might cause a problem to the coordination of two strips. For example, a leg, which is composed of two individual strips, needs well-matched coordination to exhibit the walking locomotion. If they cannot match each other, this phenomenon will cause interference to lose the control of the robot. The deviation causes a strip to keep bending toward one side, so a typical walking motion may not occur because of no reciprocal bending motion. Therefore, in

order to generate well-performed walking motion from the effect by deviation, not only a fully symmetric input signal, but brand-new IPMC strips without any damage on the surface are the appropriate choice to construct a robot.

In addition to the frequencies and patterns of input signals, the voltages (amplitudes) of input signals shows a relationship with deviation. According to Fig. 4.10, a brand-new IPMC strip exhibited various extents of deviation with the 8-V square wave input with various frequencies. In Figs. 4.11, 4.12, and 4.13, all of them exhibited deviation with 6-V square waves. For robotic application, however, 8-V square waves caused not only much smaller deviation, but also larger bending motion in Fig. 4.10, so this signal seems the best choice among these three signals. To explain and prove the relationship between the voltages of input signals and deviation, however, an experiment was used to describe how the voltage of a unique input affect the occurrence of deviation.

According to the previous experiments, a special relationship exists between deviation and the patterns and frequencies of input signals. In this test, however, the relationship between the voltages of input signals and deviation will be found. An IPMC strip was given with 0.2-rad/s square input signals from 1 V to 6 V and then the deflection was recorded as shown in Fig. 4.14. Only the voltage of the input signal changed in this test, but everything else, including the working environment, gripping direction, and the strip, was kept the same. According to Fig. 4.14, the strip did noy exhibit conspicuous deflection or deviation when the input voltage was below 3 V. When the 3-V square wave was given, a small deflection occurred and was followed by the deviation. As the voltage rose up, the deviation became more conspicuous and larger.

In addition, since the voltage was 3 V, the deviation had become twice than the previous one. The maximal deviation in each situation were around 0 mm, 0 mm, 1 mm, 2 mm, 3 mm, and 6 mm, respectively. However, there was just a small deviation when the voltage was 8 V for a brand-new IPMC strip as shown in Fig. 4.10 (b). To drive an IPMC robot, it seems better to employ higher voltage on brand-new IPMC strips to not only exhibit larger bending deflection but also prevent the deviation phenomenon. Therefore, the 8-V, 0.2-rad/s square wave is found to be the best among the all input signals.

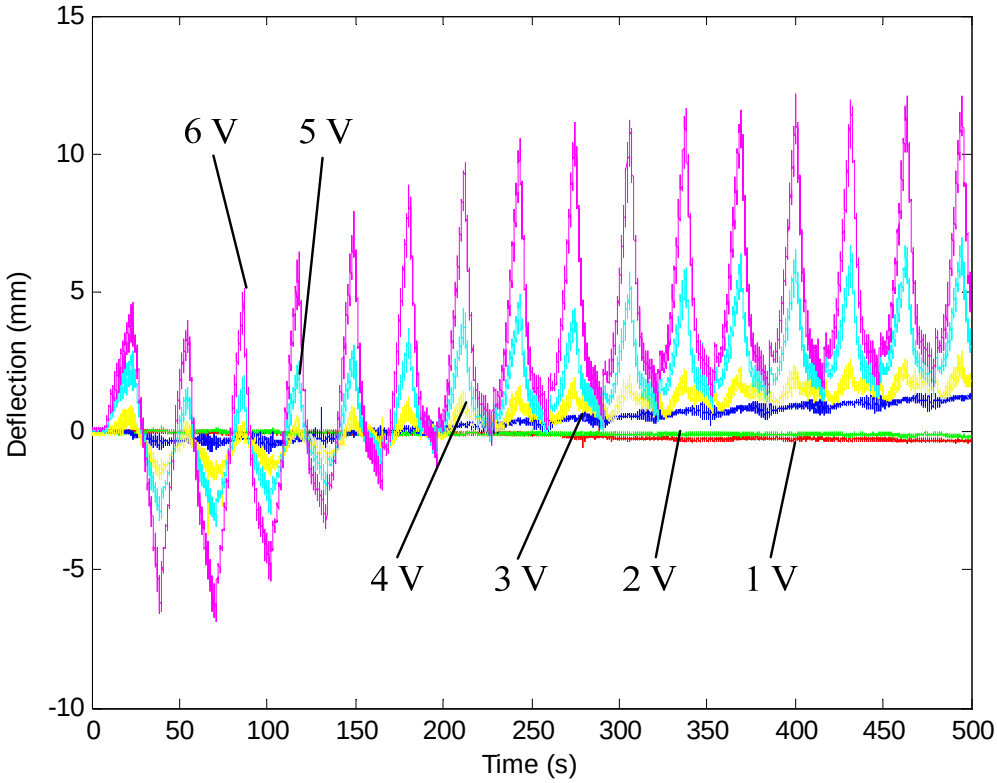

Fig. 4.14 Relationship between the input voltages and deviation

4.4 Effect of Surface Conductivity

Theoretically, the surface resistance of IPMC strips should be zero in order to exhibit uniform voltage distribution on the surface for a bending motion. The internal current, mentioned in Chapter II, can be viewed as a virtual external force, related in the structural model in Chapter V, and the decisive factor is the surface conductivity. For example, a pure signal (around 30 mA) could drive a thin (200-μm-thick) IPMC strip, but a thick (1-mm-thick) IPMC strip could not be stimulated by the voltage providing less than 300 mA. However, a uniform voltage distribution might not exist due to non-zero surface resistance, which might result from the insufficient coating in fabrication or damage in operation. In other words, for an IPMC strip with an external voltage provided via one end, the surface voltage measured everywhere on the surface is not exactly the same. Non-uniform surface voltage might lead to the occurrence of non-uniform radii of curvature. The following testing can illustrate the effect of surface conductivity on the voltage distribution, the relation between surface condition and voltage distribution. This experiment is used to show the voltage distribution decrement due to the flawed surface, and they are related to each other. It means that if the surface condition is better with lower resistance, the voltage distribution can be more uniform, and the bending deflection will still exist even at the end of the strip.

In this testing, an IPMC strip in the same dimension as those in all previous experiments, 40 mm × 10 mm × 1 mm, was drilled two holes to fix two connectors, which were used to measure the surface voltage at these spots. The connector was made of a clip and a thin magnet wire (AWG 38) not to interfere with the motion of the strip,

which will be discussed in Chapter VI because this connector would be used as an option for external power transmission as well. The wires attached to the connectors were linked to the dSPACE EVM board for immediate voltage measurement. Two connectors were fixed at the spots which are 10 mm and 30 mm from the copper electrodes, respectively. This strip was a brand-new one, so the surface resistance should be close to zero (around 0.3 Ω/mm in measurement). The surface resistance between the copper electrodes and these two holes were 3 Ω and 9 Ω, respectively. The experiment setup is shown in Fig. 4.15 (a) and (b). Like the previous tests, the input signals in this

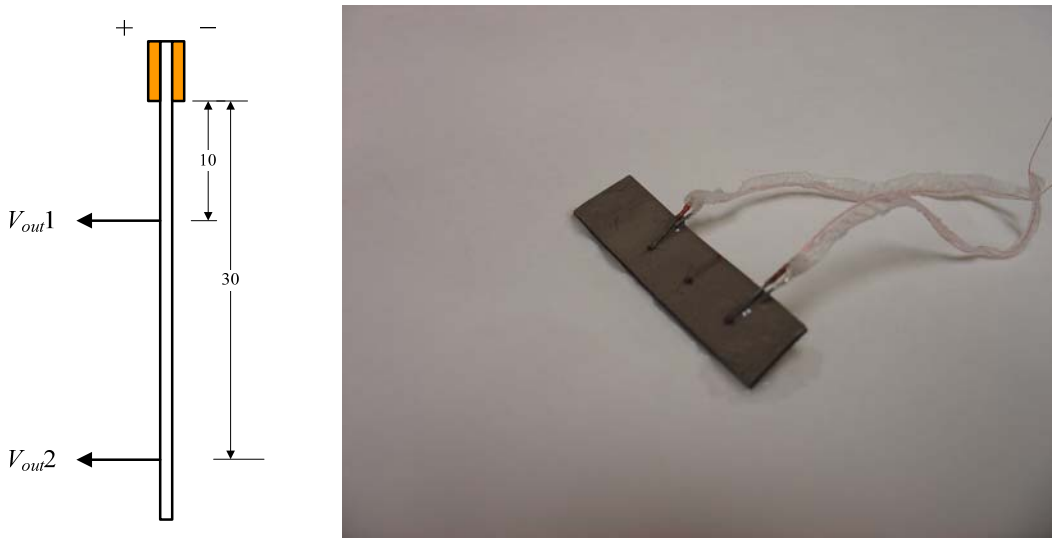

(a) (b)

Fig. 4.15 IPMC strip with two drilled holes to measure the surface voltage distribution. (a) Two holes are located at 10 mm and 30 mm from the copper electrodes. (b) Photograph of this IPMC sample.

experiment were given with sawtooth, sinusoidal and square waves with the frequencies of 0.2 rad/s, and the surface voltage at these two spots were measured by a dSPACE board. The deflection in this experiment, however, could not be measured immediately because the connectors might disturb the laser beam from the distance sensor if it was projected to the connectors.

The input voltage was set at 8 V, but the output voltage measured at the copper electrode was around 7.5 V due to the large output impendence. However, the practical measured voltage on the surface of IPMC is neither 8 nor 7.5 due to other impedances. Figure 4.16 shows a large voltage decrease in each input signal. The two spots for

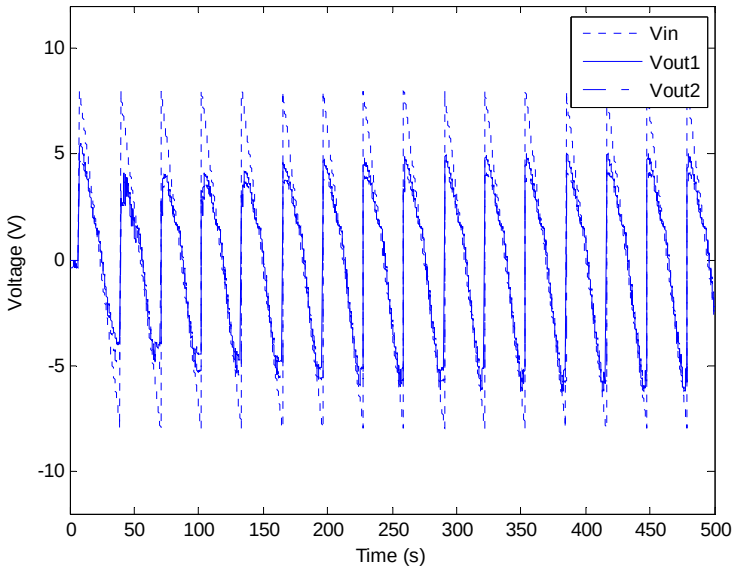

(a)

Fig. 4.16 Difference between the input voltage and measured voltages on IPMC surface. (a) Sawtooth waves, (b) sinusoidal waves, and (c) square waves with the frequencies of 0.2 rad/s

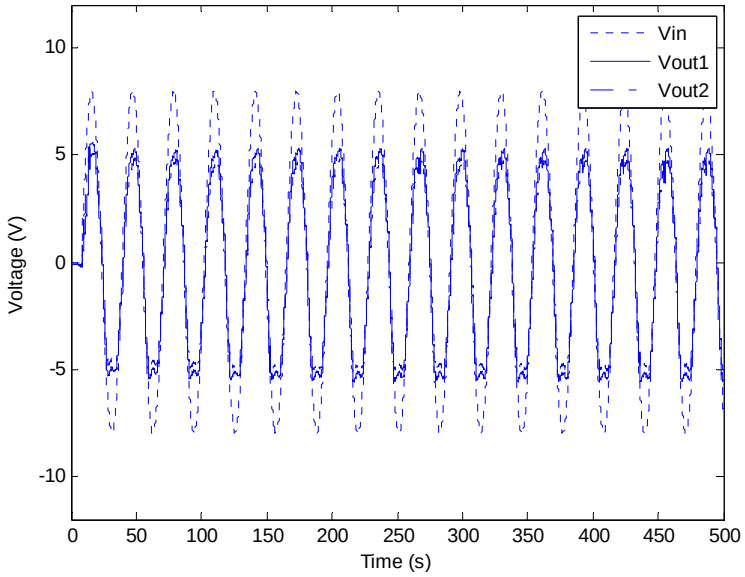

(b)

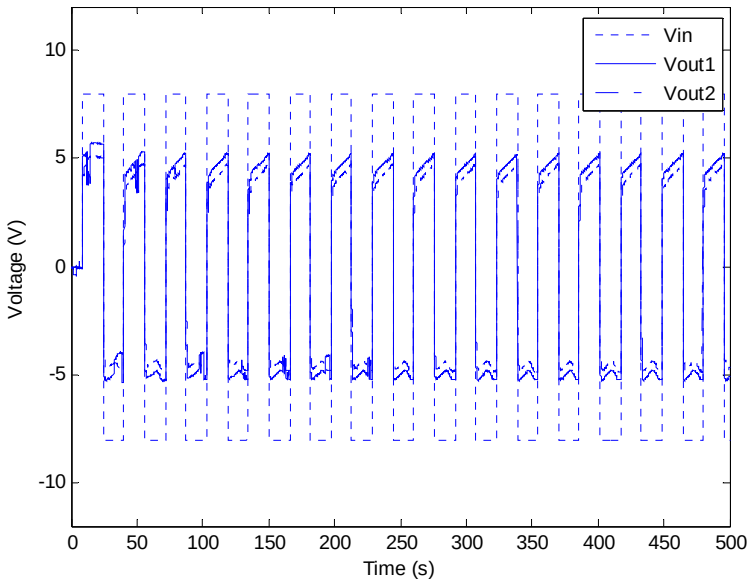

(c)

Fig. 4.16 continued.

voltage measurement are V_{out1} and V_{out2}, respectively, as mentioned in the previous paragraph. In Fig. 4.16, the dashed, solid, and center lines mean the input voltage, and the voltage measured at the first hole and the second hole, respectively. The input signals were sawsooth, sinusoidal, and square waves with the frequencies of 0.2 rad/s in Figs. 4.16 (a), (b), and (c), respectively, and the voltages measured in all spots and input signals are listed in TABLE 4.2. It seems that there is no significant difference among the specific measured voltages in these three types of input signals.

TABLE 4.2 Maximal voltages measured at two separate spots

	Desired (V)	Electrodes (V)	V_{out1} (V)	V_{out2} (V)
Sawtooth	8	7.5	5.5	5
Sinusoidal	8	7.5	5.5	5
Square	8	7.5	5.5	5

According to the above results shown in Fig. 4.16, for the brand-new sample, the voltage measured at the two spots were very close to each other although they had a 20-mm distance between each other. According to Fig. 4.16, the differences in voltage between these two spots were around 0.5 V when provided with these three input signals. After repetitive operation, the surface conductivity would go from bad to worse due to the falling-off of surface electrodes, and the voltages measured at these two spots became degraded extremely. Defected surface electrodes would degrade the range and

extent of bending motion due to the flawed surface conductivity. As discussed in Chapter II, a thick IPMC strip in this research cannot exhibit a perfect arc due to the thickness and non-perfect surface conductivity, which results from non-uniform surface voltage distribution. In this testing, the result showed that even a brand-new IPMC strip suffered from the imperfect surface conductivity instead of a uniform voltage distribution.

Surface conductivity is a key factor of the performance of IPMC because it is related to the distribution of surface voltage used to move the internal free cations and activate the strip. Non-uniform voltage distribution, which can be viewed as non-uniform force loading distribution on the surface, will cause various radii of curveature everywhere on the strip. The surface conductivity of an IPMC strip might be damaged in operation, such as surface cracks, falling-off, or impurities. It is difficult to assure perfectly uniform coating in fabrication even with a continuously rotating magnet stirbar for complete reduction, so each strip has specific surface conductivity different from those of other strips. Therefore, the deflection, comes from the virtual surface loading distribution, is closely related to the surface condition.

On the contrary, surface cracks can be used to change the force distribution. Stoimenov *et al*. utilized the placement of surface gaps to exhibit a complex curve in a single IPMC strip with a step input signal [67, 68]. By making holes and gaps, which are used to connect both surfaces via the holes fully covered with conductive gold powders, and isolate from two portions, respectively, they controlled the bending curve as whatever they expect. The two portions isolated by the gaps exhibited the deflection by

changing the extent of surface voltage distribution. With arbitrary bending motion, this kind of IPMC strips can be used in various applications, such as helping for complex drains or pipes in operation.

Even a tiny surface crack or impurity might damage the bending motion by degrading the surface conductivity greatly. In order to see how the attractive and repelling surface force distributions affect the deflection, it would be appropriate that an IPMC strip with different range of voltage distribution on each side is tested in an aquatic environment. In this experiment, there was a gap used to separate from two portions as shown in Fig. 4.17 (a) on the surface of an IPMC strip. The upper portion

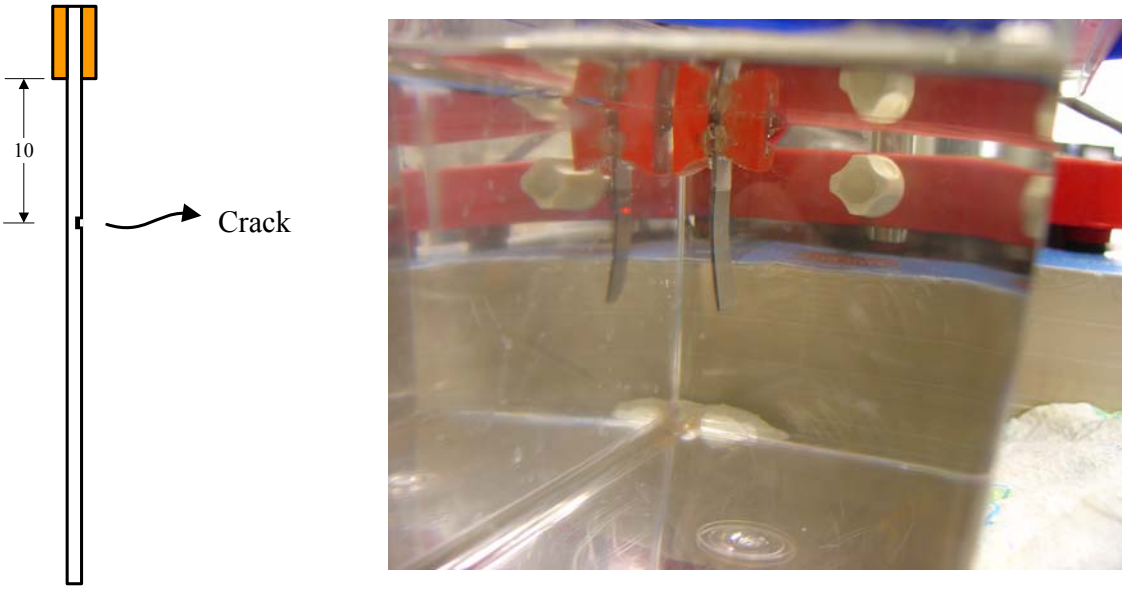

(a) (b)

Fig. 4.17 The experimental setup of an IPMC strip with a long gap. (a) The gap is 10 mm from the electrodes. (b) Testing of this strip in an aquatic environment.

was conductive to the copper electrode, but the lower one was not. Although all metallic coating were separated physically, each of the two was not exactly open-circuited due to the internal Nafion® membrane, which had resistance instead of being fully isulated. Nevertheless, all the voltage distribution will be on the upper portion instead of the lower portion due to the insuficient voltage distribution on this surface. The bubbles generated by water electrolysis could be found if sufficient voltage was distributed on the surface as shown in Fig. 4.17 (b). In this fugure, the surface above the gap had many bubbles by water electrolysis, but nothing happened to the surface below the gap. Therefore, the upper portion should exhibit a conspicuous and normal deflection but only a small bending for the lower one due to the insufficient voltage which did not generate conspicuous bending motion on this portion. The practical testing is shown in Fig. 4.18 and these five parts show a sequence of the practical bending motion in an entire cycle. However, it does not mean that there is no voltage distribution on the lower portion, but it is too low to move the internal cations and generate water electrolysis. Moreover, on the other side, where no crack or gap existed, the surface did not show the reaction of water electrolysis on the entire surface but only a small area as shown in Figs. 4.17 and 4.18. It might result from the interal resistance of IPMC. As a result, the deflection of this IPMC strip will be limited due to insufficient attractive and repelling forces caused by partial reaction in IPMC.

Nafion®, the base polymer of IPMC, has the existence of relatively low internal resistance, so IPMC has not only the capcitance but the resistance (It will be discussed in Chapter V to obtain the model), so the IPMC strip can be modeled as in Fig. 4.19.

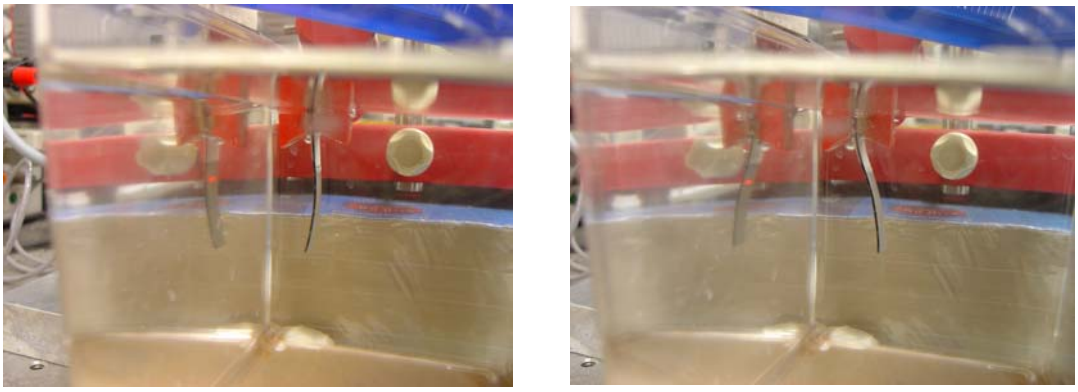

(a)

(b)

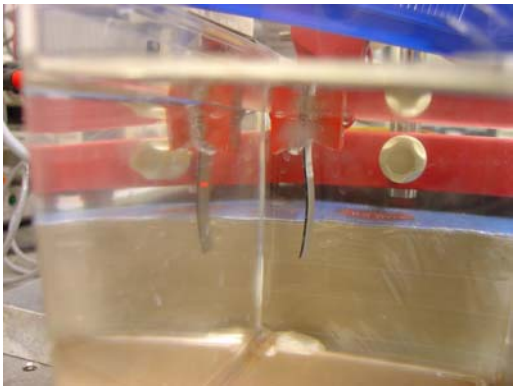

(c)

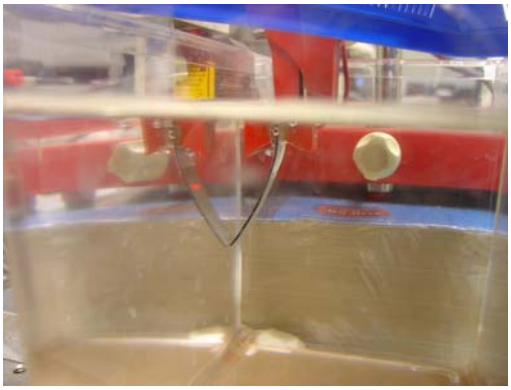

(d)

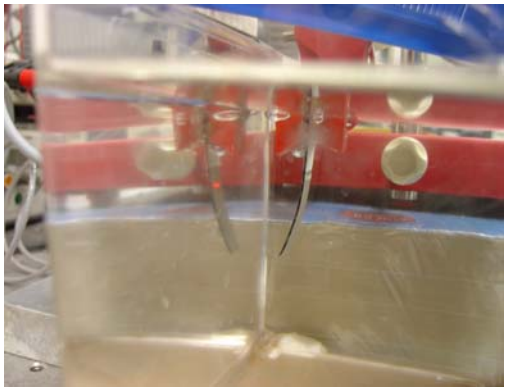

(e)

Fig. 4.18 A sequence of practical operation of the IPMC strip with a gap on one surface

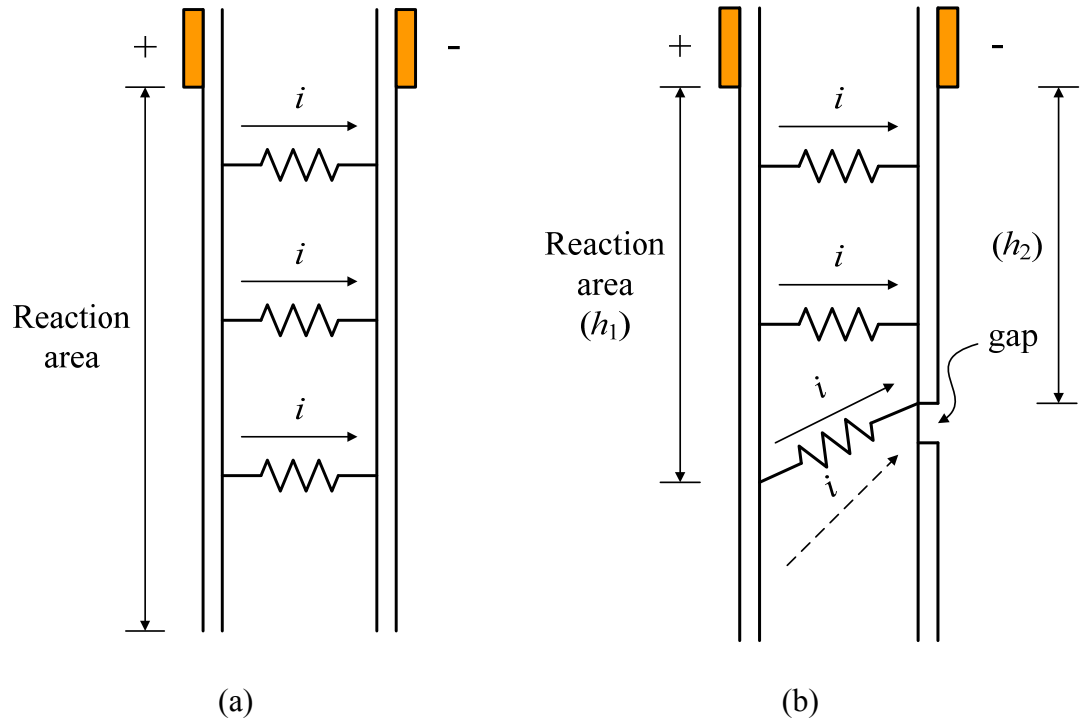

Fig. 4.19 Internal current-loop change of IPMC (a) without a gap and (b) with a gap on one surface. The current drawn in dashed line means this loop is open-circuited.

Internal impedances make numerous loops for currents when no damage or gap exists on the surface as shown in Fig. 4.19 (a). For this IPMC strip, the entire surfaces on both sides can generate conspicuous water electrolysis for their conductive surfaces. In other words, the reaction area in this figure covers the entire anode surface. Once a gap exists as shown in this case, some of the loops may be open-circuited because of the broken internal routes as the dashed line in Fig. 4.19 (b), which result in the higher internal impedance, so the currents cannot exist in the loops. In addition, the reaction areas on two surfaces are different as h_1 and h_2 as depicted in Fig. 4.18. In this figure, some main current loops show up and those in solid and dashed lines mean the available and

unavailable loops, respectively. Therefore, according to this experiment, an IPMC has the characteristics of both a capacitor and a resistor, and these characteristics will be applied to build an electrical model in Chapter V.

To see how a gap influences an IPMC strip further, three types of input signals, sawtooth, sinusoidal, and square waves with the frequencies of 0.2 rad/s, were employed to generate the output deflection in various casess. It is very difficult to fabricate IPMC strips with perfectly uniform metallic electrodes distribution, so small gaps or cracks inevitably exist and have detrimental effect to the surface conductivity. In addition, the falling-off of a platinum layer in operation also degrades the surface conductivity. The above phenomena may destroy the performance due to the decrease of surface voltage distribution. Therefore, in this experiment, the effect of surface flaws will be discussed in both theory and practice.

According to Fig. 4.19, the deflection would be degraded due to the smaller reaction surface areas on the strip with a gap. If the gap is closer to the copper electrode, the distribution area of the deflection might be smaller as the reaction area. Figures 4.20, 4.21, and 4.22 show the deflection of IPMC strip with and without a gap on one surface. With these three input signals, the IPMC strip exhibited various deflection in response to the input signals. Figures 4.20 (a) and (b) show the responses when given with sawtooth signal with the frequencies of 0.2 rad/s with and without a gap. The strip exhibited 6 mm and 5 mm in the maximal output amplitudes before and after making a gap on the surface, respectively. It did not show a large difference on output deflection. The small difference might result from the smaller reaction areas and the damaged structure due to

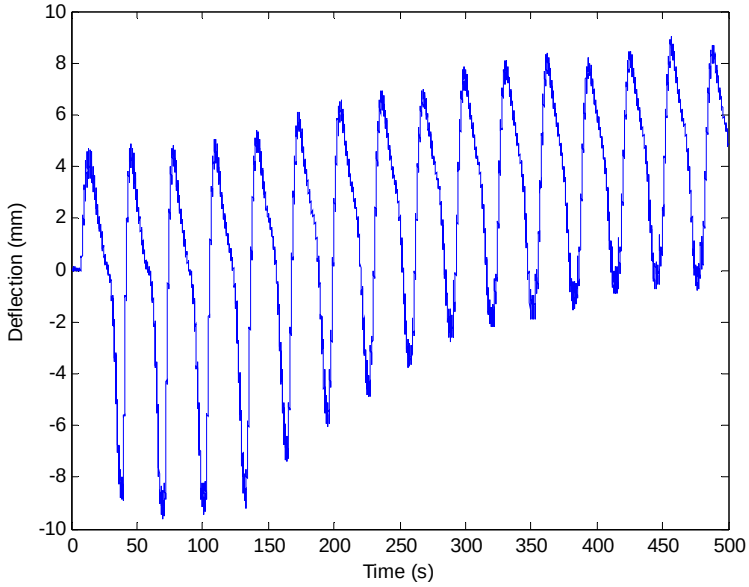

(a)

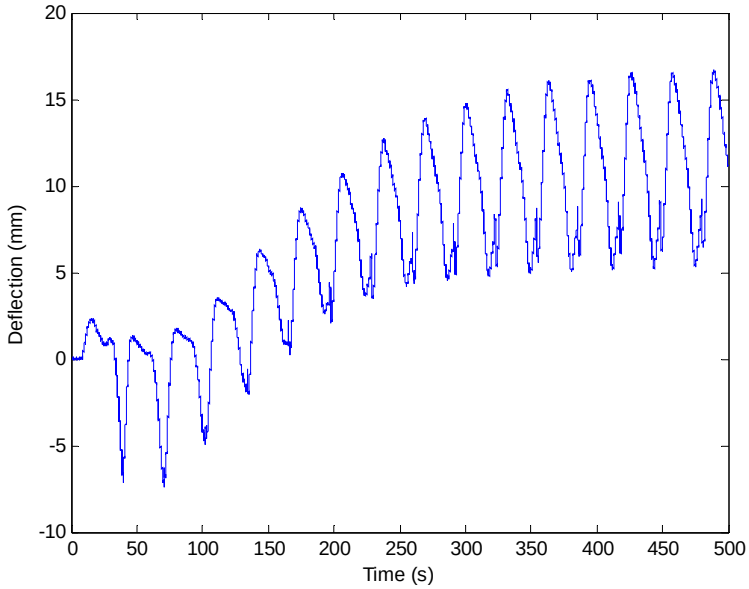

(b)

Fig. 4.20 Responses of the IPMC strips (a) without and (b) with a gap inputted with 0.2-rad/s sawtooth signals

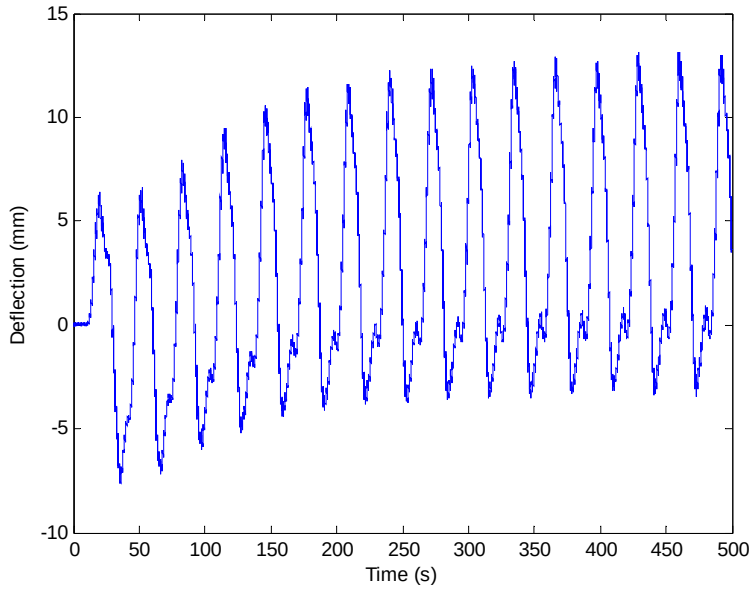

(a)

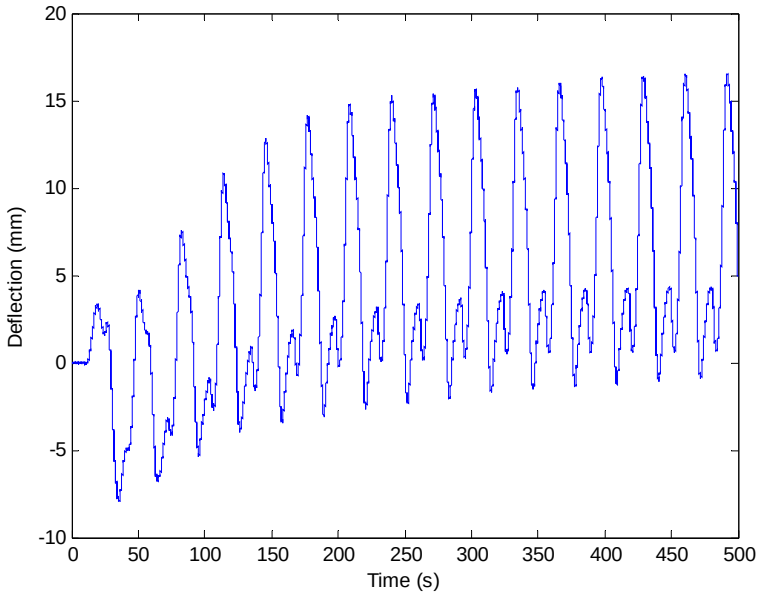

(b)

Fig. 4.21 Responses of the IPMC strips (a) without and (b) with a gap inputted with 0.2-rad/s sinusoidal signals

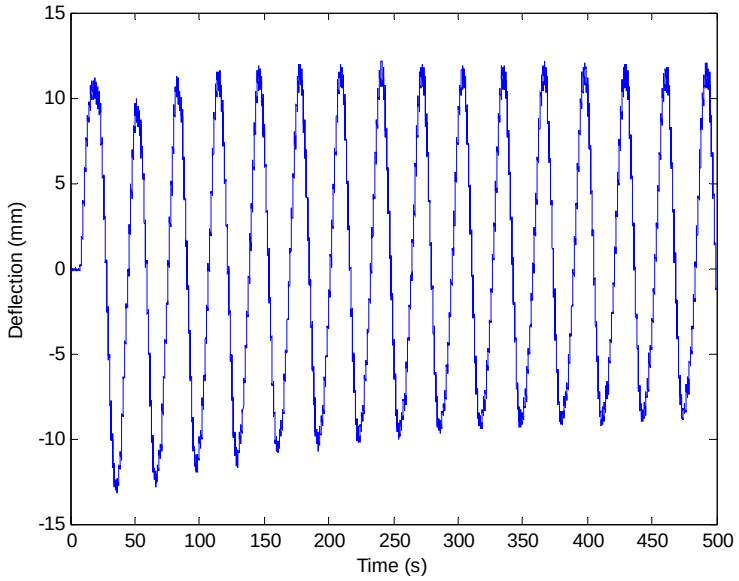

(a)

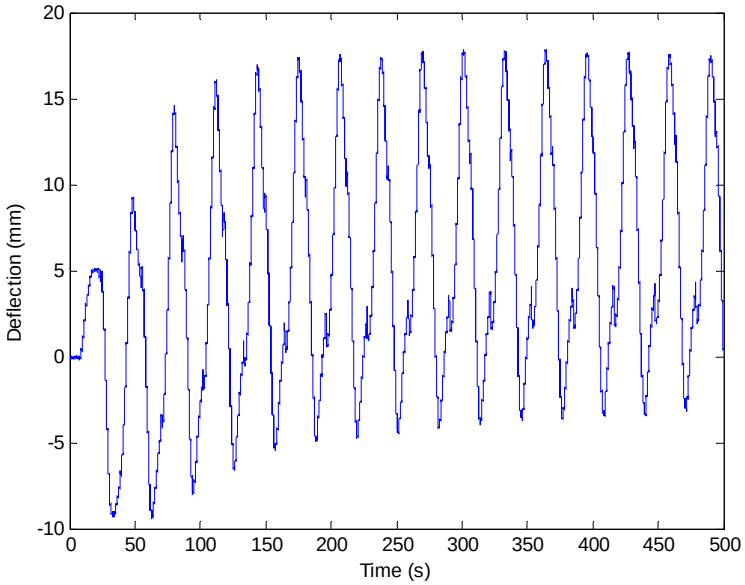

(b)

Fig. 4.22 Responses of the IPMC strips (a) without and (b) with a gap inputted with 0.2-rad/s square signals

the surface gap. As for the deviation, it showed 4 mm and 10 mm in these two cases, respectively, and apparently came from the gap. According to Fig. 4.20 (b), the gap not only enlarged the deviation, but also shortened the deviation showing time. An earlier deviation causes the deflection farther away from the original place.

Figures 4.21 and 4.22 show the same responses but provided with 0.2-rad/s sinusoidal and square signals, respectively. As the result in Fig. 4.20, the gap did not degrade the deflection when provided with the other two signals (8 mm and 11 mm for sinusoidal and square inputs in both cases). Nevertheless, the deviation responses were enlarged greatly. The large deviation will put a significant influence on the walking motion, such as moving the body reciprocally instead of forward, and even the balance of the robot. In addition, the deviation starting time was also accelerated in these two cases as in Fig. 4.20. In other words, the output deflection of the IPMC with a gap exhibited a rapid and large deviation away from the center line. Therefore, sawsooth waves activated an IPMC strip with a gap to exhibit the largest deviation among these three results due to the asymmetry.

Furthermore, a special oscillating phenomenon happened to the IPMC strip with a gap at the trough part of the deflection in this experiment. However, it was not exactly continuous oscillation but a bending motion toward the opposite side. In Figs. 4.20 (b), 4.21 (b), and 4.22 (b), conspicuous and typical oscillation at the trough showed up and this phenomenon became larger and more gradually as operation time went by. It is obvious that this phenomenon occurred at troughs due to insufficient force to bend, and sometimes it bent toward the opposite direction like back relaxation. This special

phenomenon has been usually found in repetitively used IPMC strips, so it might result from low surface conductivity of IPMC strips. Furthermore, deviation might be another factor of the osciallation owing to different need of bending force toward two sides. Therefore, these two phenomena result from flawed or non-perfectly conductive surface condition, and cause a problem to the movement of the robot. In addition, surface condition is greatly related to the performace of IPMC strips, which will be discussed and simulated in Chapter V. The maximal deflection, deviation, and the showing time of deviation in each case are listed in TABLE 4.3. According to TABLE 4.3, square waves could keep the best performance in a flawed IPMC strip.

TABLE 4.3 Comparison of the responses between the IPMC strips without and with gap on one surface

	Deflection (mm)		Deviation (mm)		Deviation showing time (s)	
Gap	Without	With	Without	With	Without	With
Sawtooth	6	5	4	10	100	70
Sinusoidal	8	8	5	8	70	50
Square	11	11	2	7	100	60

To make a comparison, Fig. 4.23 shows the response of an IPMC strip with a gap at the corresponding places on both sides with a 0.2-rad/s square signal. This figure is

used to explain the physical effect of a gap in the response. In the previous experiment, a strip with a gap exhibited the vibration at the trough of the deflection. In this case, however, the strip had a gap on each surface. Theoretically, the strip should exhibit similar oscillation at both peaks and troughs. When provided with the square signals, the strip had not only two oscillation phenomena on both sides but also smaller deviation than that for the strip with only one gap. Therefore, it seems that gap on the surface can not only degrade the deflection but also enhance the deflection damaged by the gap on the other surface.

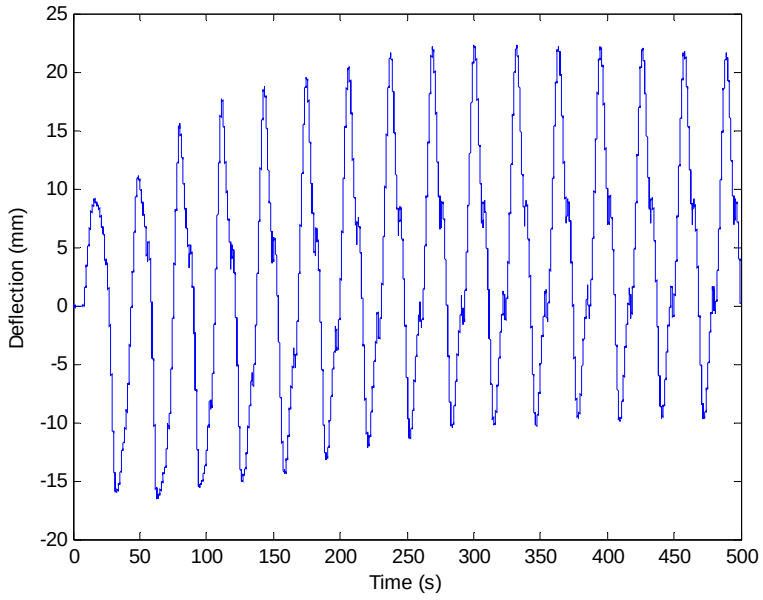

(a)

Fig. 4.23 Responses of the IPMC strip with a gap on each surface inputted with 0.2-rad/s square signals

4.5 Hysteresis Phenomenon and Capacitive Effect

IPMC has two surfaces with sufficient voltage distribution so the capacitive effect shows in operation. With two conductive metallic layers as the plates with voltage distribution on both surfaces, an IPMC strip exhibits not only a resistive performance, but a capacitive response, which is a phase lag. As a resistive response, IPMC strips show a proportional relation between input voltage and internal current; as for the capacitive effect, the phase of internal current has an obvious lag from the corresponding input voltage. Bonomo *et al*. proposed this specific phenomenon and relationship in IPMC systems according to the experimental results, and built an electrical model based on their hypotheses [69]. Two possible factors to influence this phenomenon were proposed, and they are (1) voltage of input signals and (2) frequency of input signals. In the authors' experiments, an IPMC strip was given with a 0.8-V, 100-mHz sinusoidal input, and the relation between *I* (Internal current) and *V* (Input voltage) exhibited an elliptic Lissajous figure. As the voltage increased, however, the ellipse was deformed, but the phase lag did not change much. When a 2.5-V, 50-Hz input signal was given, an almost linear response without phase change was shown clearly. In addition to the previous factors, the distance between two plates in a capacitor, i.e. the thickness of an IPMC strip could be considered. Thus, the fabricated IPMC strips were used as another choice for testing the capacitive response.

In the previous paragraph, IPMC systems showed a phase lag between the internal current and the input voltage. The internal current, however, has a direct proportional relationship with the output deflection, which will be described in Chapter

V in order to develop a precise model. According to the response results in [69], the deflection output has an apparent proportional relationship with the input current, and that relationship will be the basis of the modeling method in Chapter V. Therefore, instead of the internal current as other research papers, in this experiment, the relationship between the output deflection and the corresponding input signal will be described and explained in Figs. 4.24—4.27. All of them were drawn in the first round in IPMC operation.

Figure 4.24 exhibits a 1-mm-thick IPMC strip with three types of input signals,

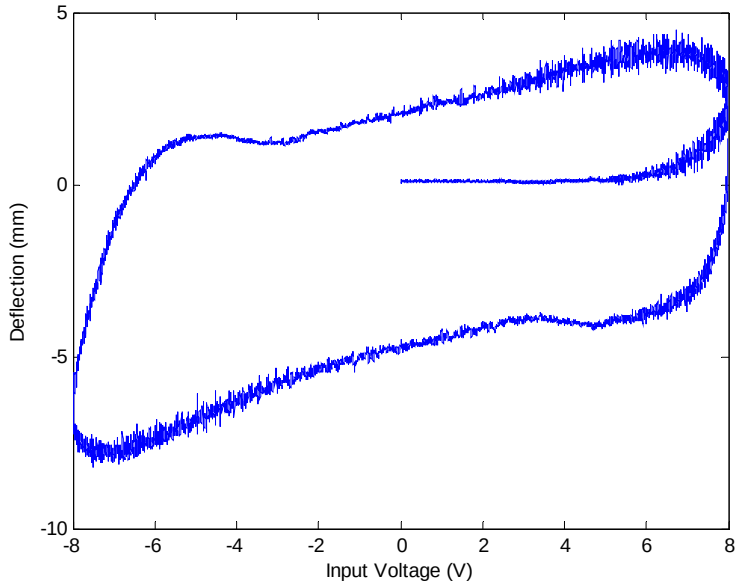

(a)

Fig. 4.24 The relationship between the output deflection and the corresponding input signal when (a) 8-V, 0.1-rad/s, (b) 8-V, 0.2-rad/s, and (c) 8-V, 0.3-rad/s sinusoidal waves were given.

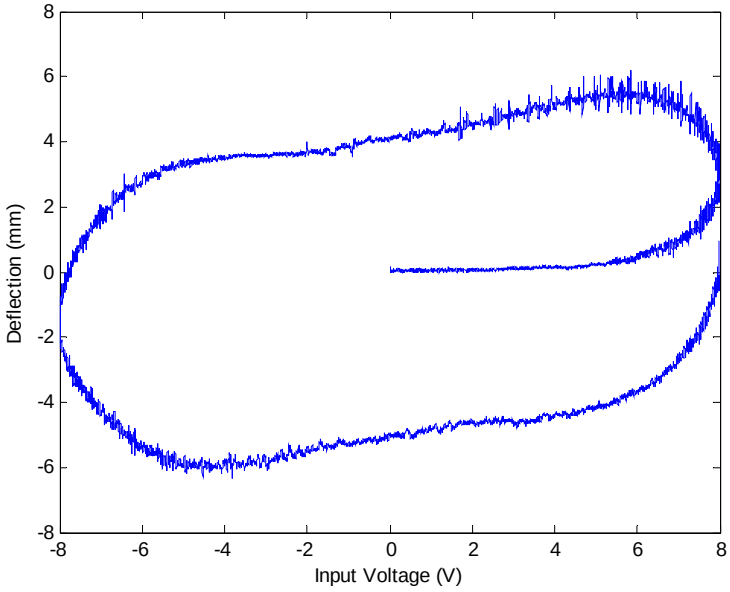

(b)

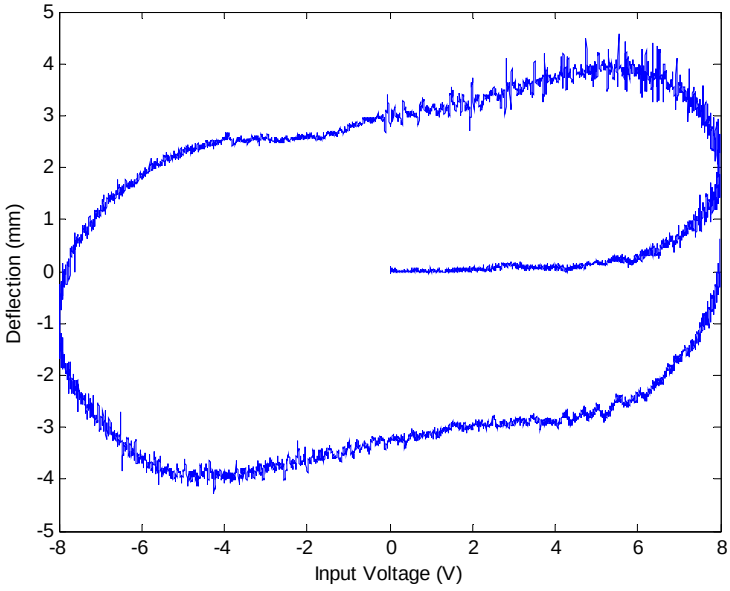

(c)

Fig. 4.24 continued.

0.1-rad/s, 0.2-rad/s, and 0.3-rad/s sinusoidal waves with an 8-V magnitude. According to the results, it is obvious that each plot had a phase lag, which became smaller as the frequency of input signals increased. That is, the area of the central elliptic became smaller. In Fig. 4.24 (a), besides the phase lag, a conspicuous nonlinear relationship between deflection and input voltage existed, and this nonlinearity caused the deflection to exhibit slow or rapid changes. In Figs. 4.24 (b) and (c), this nonlinearity did not exist anymore and the phase lag, caused by the capacitive effect, showed up. The frequencies of these input signals are 0.1 rad/s, 0.2 rad/s, and 0.3 rad/s. Compared with the results in [69], Fig. 4.24 shows a low capacitive effect because the results in [69] had apparent capacitive effects when the frequency was between 100 mHz and 50 mHz. The frequency range might change in this fundamental experiment due to the change in thickness. Therefore, according to the above results, in IPMC systems, internal current has a deeply relationship with the deflection under the same input signal. This hypothesis is applied in Chapter V in order to give an electrical model for an IPMC system.

Figs. 4.25, 4.26, and 4.27 show the capacitive effect and deviation when the frequencies of the sinusoidal input signals were in 0.1 rad/s, 0.2 rad/s, and 0.3 rad/s, respectively. In Figs. 4.25 (a), 4.26 (a), and 4.27 (a), each ellipse has a specific line style and so does the corresponding deflection in Figs. 4.25 (b), 4.26 (b), and 4.27 (b). These figures show the first four cycles so they might not exhibit the deviation conspicuously. However, it is possible to see both the nonlinear and capacitive phenomena in these three plots. According to Fig. 4.25 (b), a conspicuous nonlinear relation existed and that

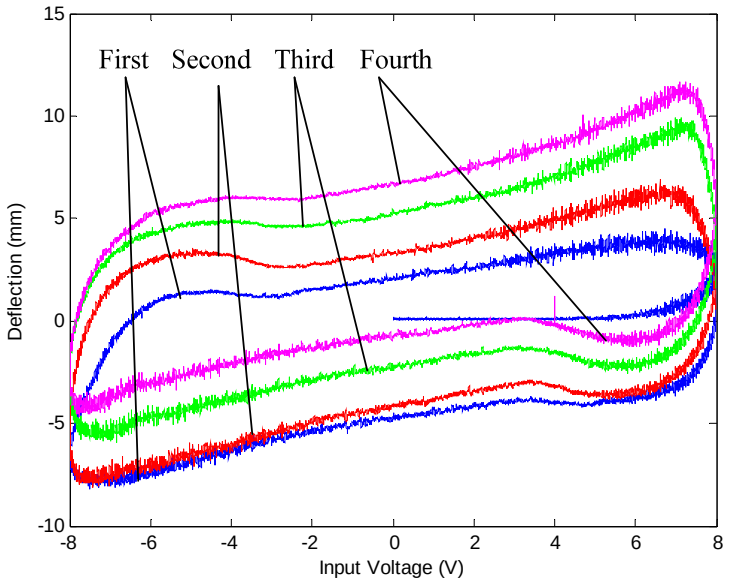

(a)

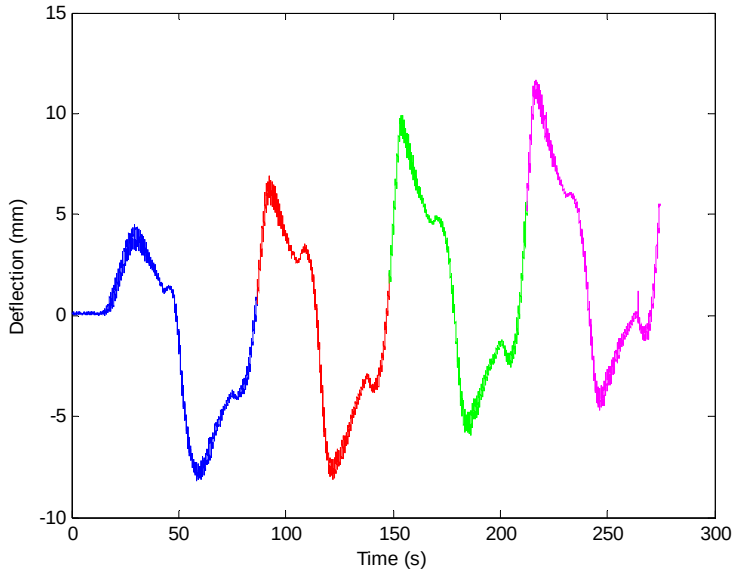

(b)

Fig. 4.25 Relationship between (a) phase-lag and (b) deviation phenomena with a 0.1-rad/s sinusoidal input signal

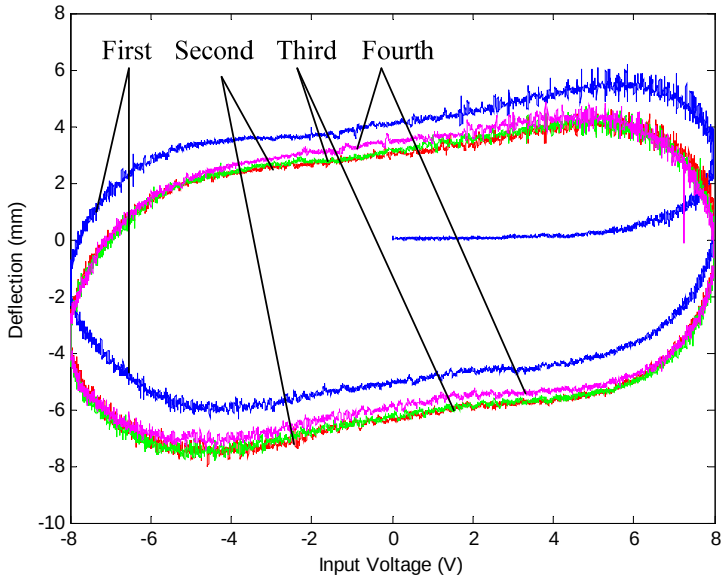

(a)

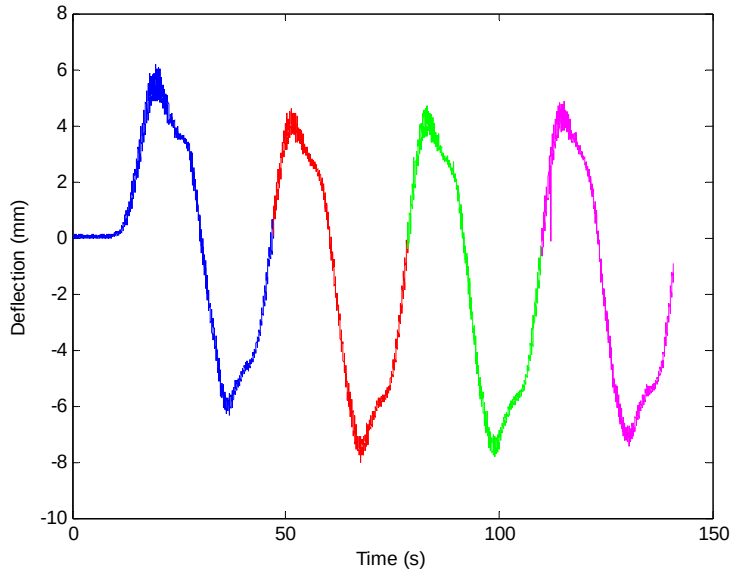

(b)

Fig. 4.26 Relationship between (a) phase-lag and (b) deviation phenomena with a 0.2-rad/s sinusoidal input signal

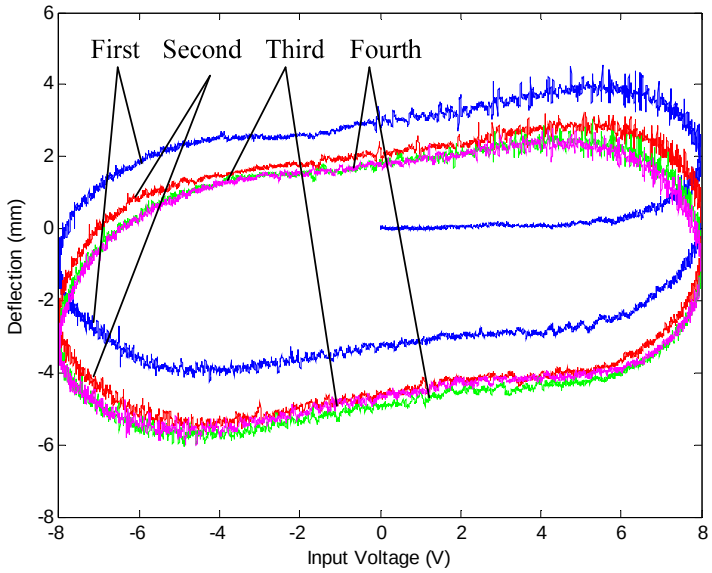

(a)

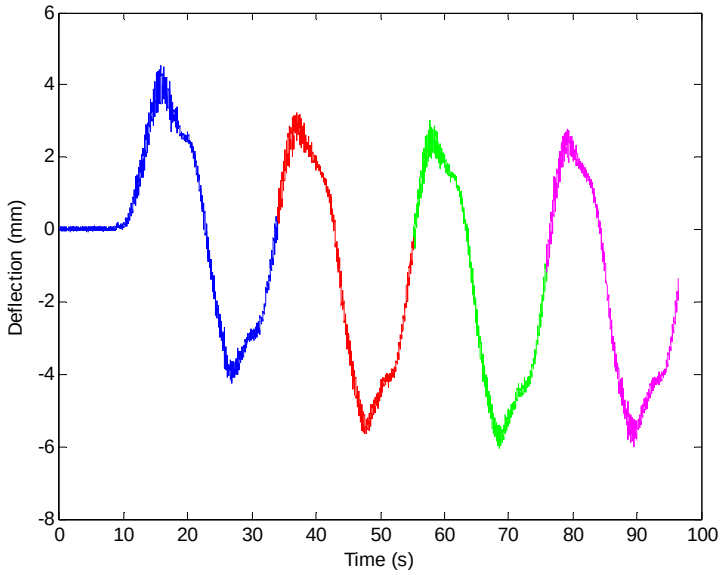

(b)

Fig. 4.27 Relationship between (a) phase-lag and (b) deviation phenomena with a 0.3-rad/s sinusoidal input signal

showed much larger than those in Figs. 4.26 (b) and 4.27 (b). Hence, these three figures show the nonlinear and deviation phenomena.

4.6 Summary

According to the experimental results given in this chapter, it is apparent that the performance of IPMC results from both internal water molecules and surface conductivity directly or indirectly. Internal water molecules must be sufficient to activate the IPMC strips, so it is better to let the robot work in an aquatic environment to both provide sufficient water and prevent surface water evaporation. Input signals can also influence the responses of IPMC strips. A large and rapid deflection without deviation is the best choice to activate the IPMC robot. After the experiment using three kinds of input signals in various frequencies, an 8-V, 0.2-rad/s square wave was chosen as the input signal for the best performance among all signals in the experiments.

In order to emphasize the importance of surface conductivity, an experiment that was used to measure the surface voltages in various spots was employed. It was found that the practical activating voltage is not exactly the same as the desired voltage due to the output impedance and surface resistance. In addition, the gap on the IPMC strip decreased the output amplitude and increased the deviation, which must be averted in order to enhance the performance of the robot.

The fundamental experiments in this chapter explain the principles and phenomena of IPMC, so they can be in support of not only selecting IPMC strips and

working environments, but also further understanding of IPMC strips in order to prevent misuse or damage. Among all, the cause of output deflection is the movement of internal water molecules. In addition, a close relationship between the internal current and the deflection was shown and explained, and this relationship is the basis of the modeling methods presented in Chapter V.

CHAPTER V

MODELING OF IPMC

IPMC has been modeled in various methods for its internal uncertainty and instability [70]. Lee *et al*. modeled IPMC strips based on an equivalent cantilever beam [71, 72]. Bufalo *et al*. tried to model IPMC system based on its mixture theory framework for mechanical actuation [73]. Tan found a dynamic model for IPMC sensors in both mechanical and electrical methods [74, 75]. Brunetto *et al*. modeled in an aquatic environment and focused on the resonant point with 80% humidity in order to exhibit sufficiently larger output deflection [76]. Bonomo *et al*. built a nonlinear electrical model for an IPMC system and made a comparison with a real system [77]. Kim *et al*. had their own electrical model by analyzing two layers of surface metallic electrodes [78]. Numerous models have been built, but only a few of them can be applied in most cases. In other words, the models fit in this case but might exhibit large error in other cases. This might result from the negligence of the influence of the surface conductivity or the distribution of internal water molecules. Because of an IPMC's structure, the internal water molecules, distribution is not only non-uniform but also LTV due to their movement. In addition, non-uniform metallic surface electrodes influence the external loading of structural modeling systems. Therefore, traditional models do not fit well without revision. In this chapter, three kinds of models, structural, mathematical, and electrical models, will be introduced and compared with to be better-fitted in real-time control and applications in the future.

5.1 Cantilever Beam with Linear Loading Distribution

A structural modeling method considers an IPMC strip a cantilever beam with loading distributions on the top surface owing to the downward bending motion it exhibits. According to the equations derived from the relationship between the dimension of the IPMC strip and the loading distribution, the deflection at each point can be predicted. In this structural model, an IPMC strip is seen as a cantilever beam with loading distribution although there is no physical external loading but internal expansion as shown in Figs. 5.1 and 5.2. With one end fixed, the other end, free end, exhibits a conspicuous bending motion as an ordinary cantilever beam. Four possible cases shown in Fig. 5.2 are taken into consideration because of the non-uniform surface conductivity, which cause the bending motion to exhibit different curvatures at each point. Therefore, it can be thought that the loading distribution does not have perfect uniformity fully on the top surface. The change of loading has a close relationship with surface conductivity, and here are four usual cases with linear decreasing in loading distribution. Figure 5.2 (a) depicts the strip shows a large bending motion by the uniform loading distribution because of perfectly uniform conductivity of surface electrodes, which is similar to the model in [71]. In practice, however, it is very difficult to reach this surface conductivity due to high cost of the surface metallic layer. Figure 5.2 (b) illustrates that the strip has a linear decreasing loading, but this strip still has good conductivity at the free end. In Fig. 5.2 (c), however, the strip has a linear decreasing loading down to zero at the free end due to the almost insulated surface resistance. Finally, Fig. 5.2 (d) indicates that the strip has higher resistance of surface electrodes so the loading decreases down to zero at one

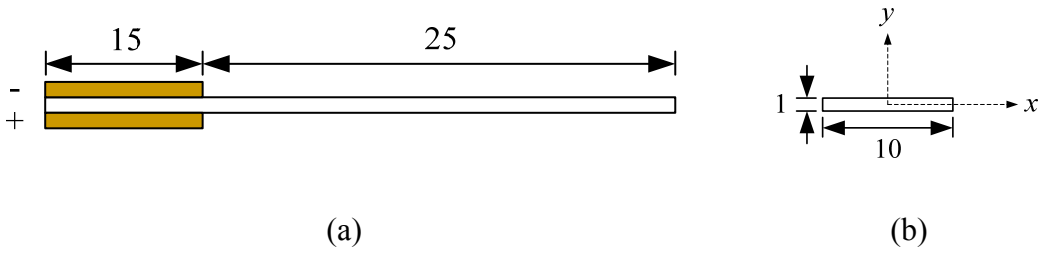

(a) (b)

Fig. 5.1 Dimension of an experimental IPMC strip (units: mm)

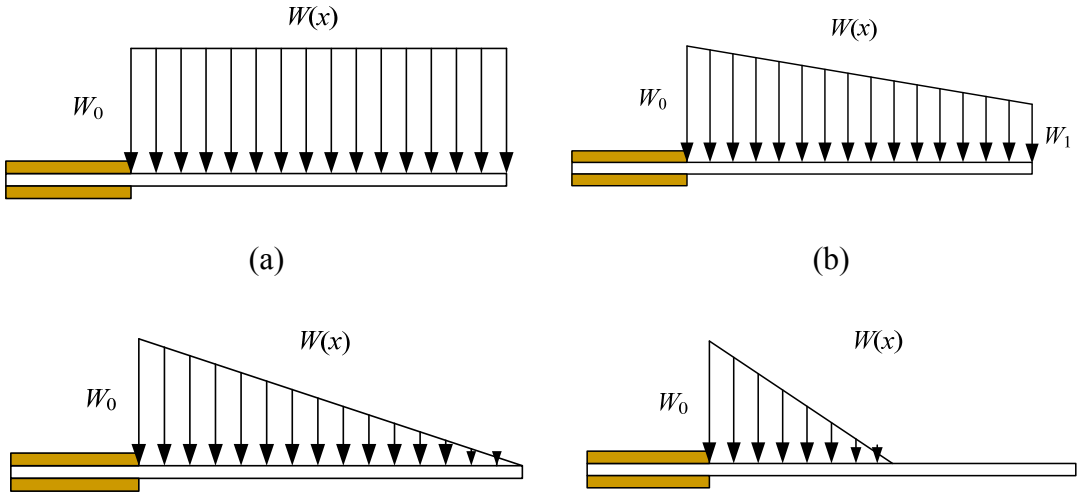

(a) (b) (c) (d)

Fig. 5.2 IPMC strips as cantilever beams under various loading distributions on the top surfaces

point (at the middle point in this case). Surface conductivity, related to the loading distribution, might be degraded in operation due to physical or chemical damages. For example, surface metallic electrodes tend to be damaged when being clipped with a tweezer, or burned by high external voltage or current. In practice, it is very challenging to prepare a well-fabricated IPMC as shown in Fig. 5.2 (a). Mostly, IPMC strips have

flawed surface, so Fig. 5.2 (b) is closer to practice. As time goes by, in around 10000 s, however, Figs. 5.2 (c) and 5.2 (d) will be more appropriate.

Figure 5.3 depicts the simulated deflections of the IPMC strip corresponding to each case in Fig. 5.2. A conspicuous discrepancy among all cases existed due to the internal current, mentioned in Section 4.4, and the distribution of internal water molecules, which can be seen as loading distribution. In Case 1, the strip exhibited a large deflection by the large and uniform distribution of water molecules on the cathode side, and the maximum deflection was as large as around 19 mm. This case, however, does not usually happen in practical experiments due to non-nuiform electrical conductivity of surface metallic electrodes. The conductivity is related to the thickness of surface metallic electrodes but tends to be non-uniform on the surface because platinum reduction is not easily controlled in fabrication. Thus, the bending motion in Case 1 may not exist in practice even in a brand-new and well-fabricated IPMC strip.

In Case 2, there is still loading distribution existing at the free end, and the deflection variation of the IPMC strip decreases with the distance from the fixed end but not down to zero, which means that the distribution of the water molecules at the free end can cause the deflection, so a linear decrease in loading force as shown in Fig. 5.2 (b) is thought to exist. In this case, the loading force at the free end is set to be half of the original force at the fixed end with a linear decrease. As the result of the simulation, this case shows a smaller deflection than Case 1 due to the decreasing surface conductivity, which causes less concentration of the internal water molecules on the cathode side, and the maximum deflection is around 10 mm as shown in Fig. 5.3.

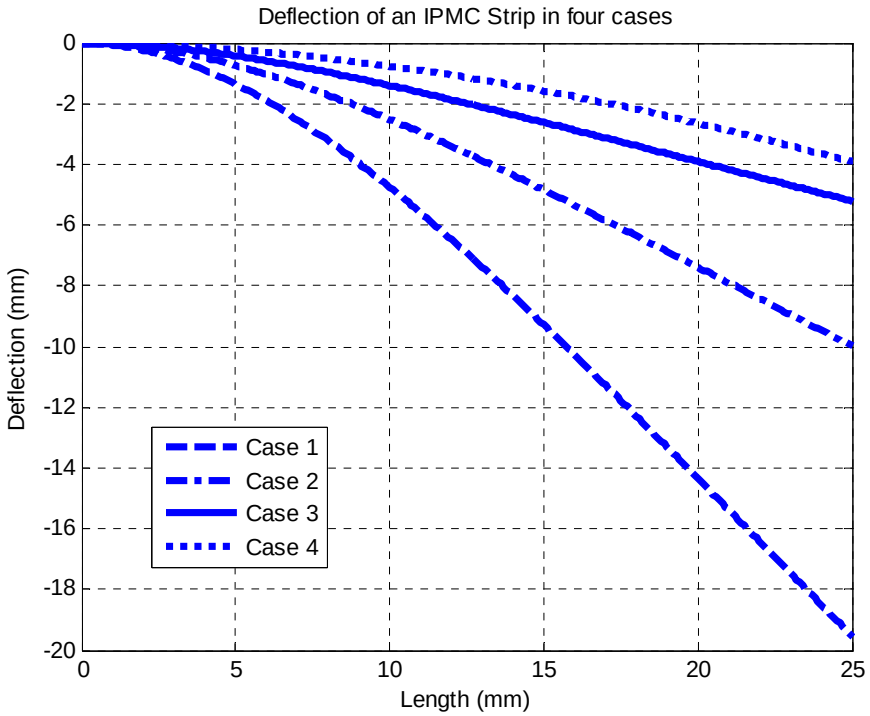

Fig. 5.3 Deflections of IPMC strips in various loading conditions

In Case 3, the loading force decreases with the distance from the fixed end linearly down to zero due to the increasing surface resistance. The distribution of internal water molecules became sparse as the distance from the fixed end increased due to the surface electric charges. It follows that the deflection must be smaller than the previous one, and the variation is also small due to the insufficient force concentration. The maximum simulated deflection is around 5 mm at the free end. In this case, the imaginary loading force is half of that in the first case, but there is a difference in maximum deflection between them. As shown in Fig. 5.3, the maximum deflection in the previous case is not twice that in this case but around 4 times.

Case 4 happens if the surface conductivity is too low to attract sufficient cations with water molecules to the cathode side from the middle of an IPMC strip. As the dotted line drawn in Fig. 5.3, the IPMC strip can be considered a cantilever beam with decreasing loading force cut off at the middle point. It follows that the deflection in this case should be the smallest due to insufficient bending force. As the thick dotted line shown in Fig. 5.3, the maximum simulated deflection is around 3.8 mm, which is less than a quarter of that in Case 1. In this case, not only the deflection but the variation rate of that is much smaller than that the previous three cases.

Fig. 5.3 depicted the simulated deflection trajectories corresponding to the four loading distributions in Fig. 5.2. Theoretically, IPMC should have an well conductive metallic surface on both sides as shown in Fig. 5.2 (a). In addition, the thickness of metallic electrodes should be both increased significantly and distributed uniformly by utilizing a great amount of platinum powders. However, metallic electrodes are easily damaged in operation. Therefore, Case 1 might not physically exist in practical operation. Cases 2, 3, and 4 usually happen in comparison with the first case and an IPMC strip changes in the sequence, Case 2, Case 3, and then Case 4 with time or operation. This phenomenon, nevertheless, often happens because the imperfectly conductive surfaces cause large power loss and deflection depending upon how conductive the surfaces are. In practical tests, for a piece of brand-new IPMC strip, the surface conductivity will become worse due to the external damages such as electrode fall-off or surface cracks, which implies that it was in Cases 2 or 3, migrating to Case 4 eventually after repetitive operation or external physical damages.

The deflection does not result from the virtual loading distribution but the expansion and contraction of internal Nafion®, so the above models might not be precise to predict the deflection. It might be better to derive a model by using physically measured output responses as to be described in Section 5.2.

5.2 System Identification with Regressive Mathematical Models

Mathematical models for IPMC systems have been used widely in various equations. Kim *et al*. and Xing *et al*. have used exponential curves to fit the results based on the corresponding step inputs by using self-designed precise controller [79−83]. After finding out appropriate parameters in their prototype exponential equations, the relationship between the the input voltage and output deflection were derived. In this case, however, the accuracy and the error are closely relevant to the protoytpe exponential equations. Some typically and prevalently used methods will be proposed in the next paragraph in order to obtain the linearized relationship between input and output of IPMC systems and predict the deflection in the specific input signal, an 8-V, 0.2-rad/s square wave in this case, for IPMC robotic applications.

System-identification methods are usually used to derive governing equations for a unknown dynamic system based on measurements in control and communication engineering [84]. With corresponding input and output deflection taken in practice, the relationship between the output deflection and the corresponding input signal can be represented in various mathematical models such as an autoregressive with exogenous

(ARX)/autoregressive moving average with exogenous (ARMAX) models, an output-error (OE) model, a Box-Jenkins (BJ) model, and a prediction-error minimization (PEM) model. Each of them has the specific structure, formula, and application and the basic architecture of all above models comes from a single-input-single-output (SISO) system with an external disturbance as shown in Fig. 5.4.

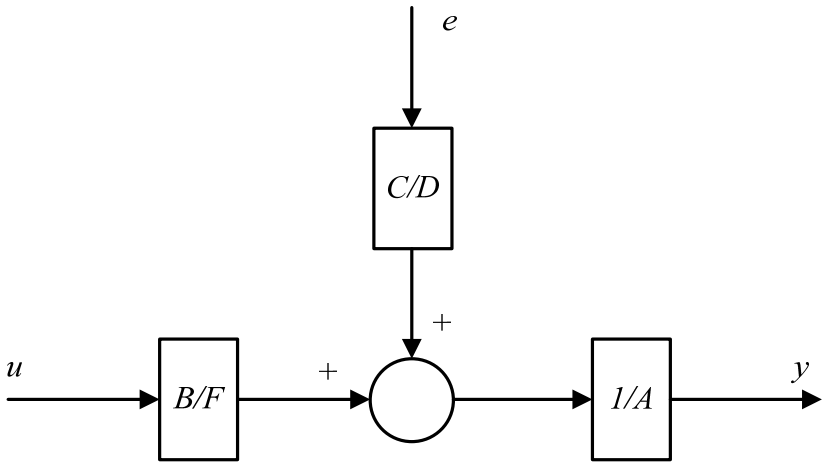

Fig. 5.4 Fundamental architecture of mathematical models using system-identification tools

Equation (5.1) is the generic architecture of this group of models based on Fig. 5.4. In this figure, y, u, and e indicate the output, input, and disturbance in a SISO system. The polynomials, $A(q)$, $B(q)$, $C(q)$, $D(q)$, and $F(q)$, indicate the coefficients of each part at each current time. The above models generate by choosing different coefficient polynomials. An 8-V, 0.2-rad/s square wave, which is provided for an aquatic robotic application, was utilized as the input signals for the control in the application. In

addition, each of them has its own DOFs, which originate from coefficient polynomials, to build an appropriate model. In this section, five typical models are used to predict the system output in a unique case, and the measured deflection is compared with the simulated deflection in these three models. Consequently, an appropriate model for an IPMC strip will be determined according to the error between them.

$$A(q)y(n) = \frac{B(q)}{F(q)}u(n-n_k) + \frac{C(q)}{D(q)}e(n) \tag{5.1}$$

$$A(q) = 1 + a_1 q^{-1} + a_2 q^{-2} + \cdots + a_{n_a} q^{-n_a}$$

$$B(q) = b_1 q^{-1} + b_2 q^{-2} + \cdots + b_{n_b} q^{-n_b}$$

$$C(q) = 1 + c_1 q^{-1} + c_2 q^{-2} + \cdots + c_{n_c} q^{-n_c}$$

$$D(q) = 1 + d_1 q^{-1} + d_2 q^{-2} + \cdots + d_{n_d} q^{-n_d}$$

$$F(q) = 1 + f_1 q^{-1} + f_2 q^{-2} + \cdots + f_{n_f} q^{-n_f}$$

where n_a is the order of $A(q)$,

n_b is the order of $B(q)$,

n_c is the order of $C(q)$,

n_d is the order of $D(q)$,

n_f is the order of $F(q)$,

n_k is the system time delay

5.2.1 ARX and ARMAX Models

For IPMC experiments, the disturbance, such as gravity, is usually ignored because it can be eliminiated easily. Only a current disturbance term instead of all accumulated ones is applied in this modeling method. In Eq. (5.2), as a consequence, the relationship between input with the current disturbance and output is emphazied and discussed as follows.

$$y(n)+a_1y(n-1)+a_2y(n-2)+\cdots+a_{n_a}y(n-n_a)$$
$$=b_1u(n-1)+b_2u(n-2)+\cdots+b_{n_b}u(n-n_b)+e(n) \tag{5.2}$$

In this case, the equation can be written as

$$A(q)y(n)=B(q)u(n)+e(n) \tag{5.3}$$

This is called an autoregressive with exogenous input (ARX) model because it has autoregressive part, $A(q)y(n)$ and exogenous input part, $B(q)u(n)$. In addition, the coefficients, $C(q)$, $D(q)$, and $F(q)$ in Eq. (5.1) are 1. An ARX model lacks adequate freedoms in describing the disturbance properties (only one term) [84], and this term is not very important for IPMC experiments. Another modeling method, an autoregressive

moving average with exogenous terms (ARMAX) model, is more precise and flexible to describe disturbance. In an ARX model, the disturbance term is taken only at the current time, $e(t)$; the disturbance term is accumluated from the selected time in an ARMAX model. For practical IPMC experiments, however, there might be no significant difference due to a negligible effect by disturbance. As an ARMAX model, the relationship between input and output is defined as follows.

$$\begin{aligned} & y(n)+a_1 y(n-1)+a_2 y(n-2)+\cdots+a_{n_a} y(n-n_a) \\ & \quad = b_1 u(n-1)+b_2 u(n-2)+\cdots+b_{n_b} u(n-n_b) \\ & \quad +e(n)+c_1 e(n-1)+c_2 e(n-2)+\cdots+c_{n_c} e(n-n_c) \end{aligned} \tag{5.4}$$

$$A(q)y(n) = B(q)u(n) + C(q)e(n) \tag{5.5}$$

By applying an ARX or an ARMAX model, the cofficients $A(q)$, $B(q)$, and $C(q)$ can be decided in Eqs. (5.2)–(5.5), and then the transfer functions for each model, $G_{ARX}(z)$ and $G_{ARMAX}(z)$, can be derived in Eqs. (5.6) and (5.7). Figures 5.5–5.6 show the comparison between the measured and simulated results by using an ARX model and an ARMAX model, respectively. In these plots, the solid line and the centerline are the physically measured deflection by the laser sensor and the simulated output according to the model. In this experiment, a 40 mm × 10 mm × 1 mm IPMC strip was tested by providing with an 8-V, 0.2-rad/s square-wave input signal, which was decided to drive

an aquatic robot and shown in the thin dashed line. It is obvious that they are not well-matched due to the deviation phenomenon discussed in Chapter IV, so the fitting rates are 71.27% and 71.16% for an ARX and an ARMAX models, respectively. The fitting rate can be obtained by typing *compare* in Matlab. Equations (5.6)–(5.7) can be obtained according to the above polynomials.

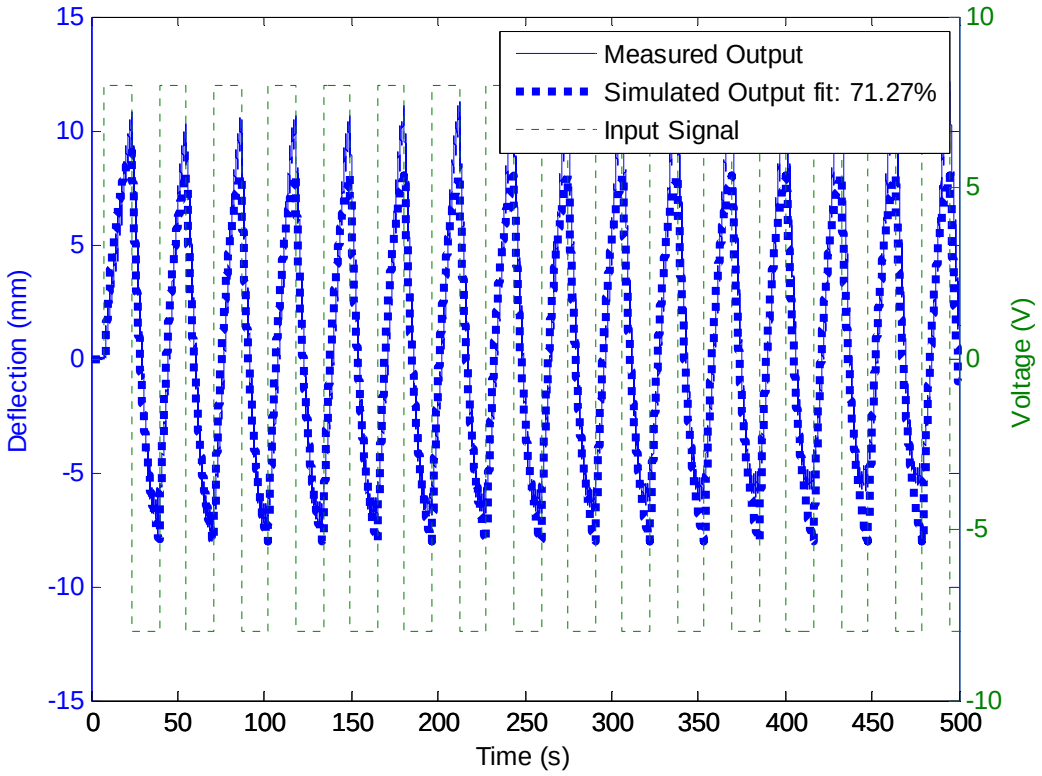

Fig. 5.5 Experimental and simulation results based on an ARX model. The measured output moves up because of deviation but the simulated output does not.

$$A(q) = 1 - 0.09561q^{-1} - 0.07897q^{-2} + 0.04122q^{-3} - 0.006026q^{-4}$$

$$B(q) = -0.0001785 + 0.002591q^{-1} - 0.0005258q^{-2} - 0.001712q^{-3}$$

$$G_{ARX}(z) = \frac{-0.0001785z^4 + 0.002591z^3 - 0.0005258z^2 - 0.001712z}{z^4 - 0.9561z^3 - 0.07897z^2 + 0.04122z - 0.006026} \tag{5.6}$$

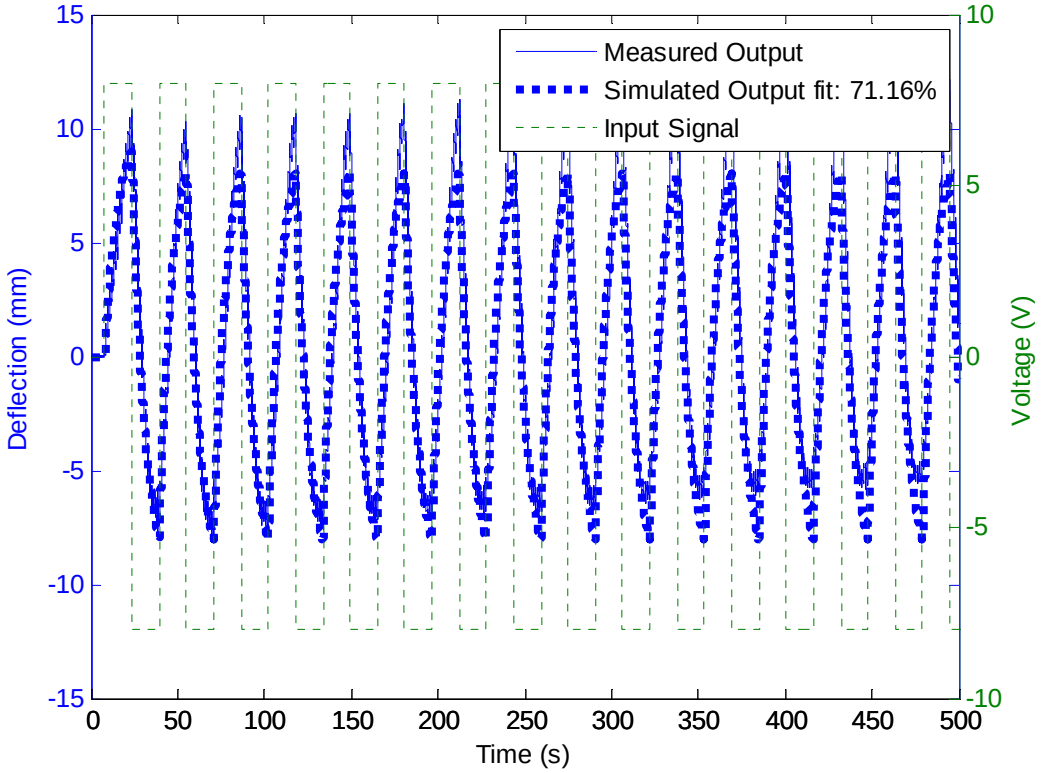

Fig. 5.6 Experimental and simulation results based on an ARMAX model. The measured output moves up because of deviation but the simulated output does not.

$$A(q) = 1 + 0.6723q^{-1} - 0.8081q^{-2} - 0.884q^{-3} + 0.02025q^{-4}$$

$$B(q) = -0.0002111 + 0.0002643q^{-1} + 0.0005727q^{-2} - 0.00001591q^{-3}$$

$$C(q) = 1 + 1.641q^{-1} + 0.868q^{-2}$$

$$G_{ARMAX}(z) = \frac{-0.0002111z^3 + 0.0002643z^2 + 0.0005727z - 0.00001591}{z^4 + 0.6723z^3 - 0.8081z^2 - 0.884z + 0.02025} \tag{5.7}$$

The fitting rates in these two models are similar to each other because the other term, disturbance, is not relevant to this application, so this term is not necessary to be taken into consideration in this IPMC experiment.

5.2.2 OE Model

In both the ARX model and the ARMAX model, a common polynomial, $A(q)$, exists in the denominators of the linearized relationship between both the input and the disturbance because $D(q)$ and $F(q)$ are both 1 in Eqs. (5.3) and (5.5) [84]. However, they may have independent denominator so the polynomials can be totally different in an output-error (OE) model. In this model, $A(q)$, $C(q)$, and $D(q)$ are defined as 1, so the only two manipulative polynomials are $B(q)$ and $F(q)$. The fundamental relationship equation is shown in Eq. (5.8), which exhibits a linear proportion between the input ($u(n)$) and the undisturbed output ($y_{un}(n)$), so the relationship can be described in detail as follows.

$$y_{un}(n) + f_1 y_{un}(n-1) + f_2 y_{un}(n-2) + \cdots + f_{n_f} y_{un}(n-n_f)$$
$$= b_1 u(n-1) + b_2 u(n-2) + \cdots + b_{n_b} u(n-n_b) \tag{5.8}$$

$$y(n) = y_{un}(n) + e(n) \tag{5.9}$$

$$y(n) = \frac{B(q)}{F(q)} u(n) + e(n) \tag{5.10}$$

The predicted output is composed of $y_{un}(n)$ and $e(n)$, which mean the undisturbed output and disturbance terms, respectively, so this model can be applied when only the current disturbance is considered and totally independent of input signals. Therefore, the transfer function seems more suitable and fit with the practical system as compared with both an ARX and an ARMAX models because of the disturbance term.

With the deflection of IPMC in an OE modeling method, the coefficients, $B(q)$ and $F(q)$, can be obtained, and then the relationship, $G_{OE}(z)$, comes out according to these two coefficients as shown in Eq. (5.11). Figure 5.7 shows the measured and simulated deflection in an OE model. It seems more fit than an ARX/ARMAX model, and the fitting rate is enhanced to 76.38%, greater than those in an ARX/ARMAX model. By using an OE model, the comparison between the measured and simulated output deflections, in the solid line and the thick dotted line, respectively, is shown in Fig. 5.7. For an OE model, however, with only two polynomials, $B(q)$ and $F(q)$, but more DOFs for this model, it appears that this OE model can be much better-matched to a practical system than an ARX/ARMAX model because in a practical IPMC system, less polynomials exist in describing the system provide more DOFs. In other words, the output deflection has less constraints of both the input and the disturbance than ARX/ARMAX models. In addition, the disturbance term in the OE model has the present term instead of all cumulative disturbances, so this model might be better

matched to a practical system that has less disturbance terms in consideration of the IPMC system.

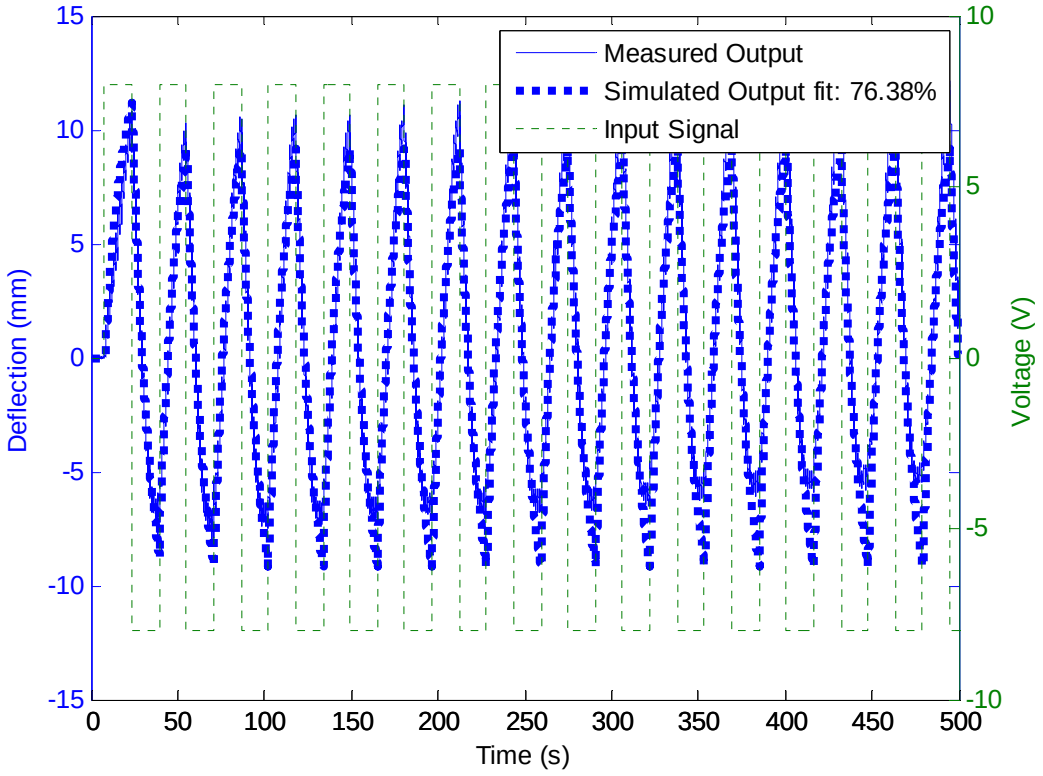

Fig. 5.7 Experimental and simulation results based on an OE model. The measured output moves up because of deviation but the simulated output does not.

$$B(q) = -0.007858 - 0.0004273q^{-1} + 0.0006506q^{-2} + 0.008431q^{-3}$$

$$F(q) = 1 + 0.5806q^{-1} - 0.03501q^{-2} - 1.021q^{-3} - 0.5242q^{-4}$$

$$G_{OE}(z) = \frac{-0.007858z^3 - 0.0004273z^2 + 0.0006506z + 0.008431}{z^4 + 0.5806z^3 - 0.03501z^2 - 1.021z - 0.5242} \tag{5.11}$$

5.2.3 BJ Model

For further natural and free modeling methods, Box-Jenkins (BJ) model is a good choice because it has four independent polynomials for the relationship between among input, disturbance, and output. Only one polynomial, $A(q)$, is the constant, 1, so BJ model has more DOFs that neither an OE model nor an ARX/ARMAX model mentioned in the previous paragraphs can reach. A BJ model is described in four polynomials, $B(q)$, $C(q)$, $D(q)$, and $F(q)$, and shown in Eq. (5.12). Each of these two terms, input and disturbance, has two independent polynomials as coefficients, so it appears that this method has sufficient DOFs to give an appropriate model for the IPMC system.

$$y(t) = \frac{B(q)}{F(q)}u(t) + \frac{C(q)}{D(q)}e(t) \tag{5.12}$$

A BJ model does not match with all practical systems completely although it has four independent polynomial coefficients to model the systems. The percentage of well-matched performance is depending on the relationship among the output, input, and disturbance. In this IPMC experiment, for example, an OE model can match better than both ARX and ARMAX models even with only two polynomials because the coefficient of the disturbance term, $e(t)$, is 1 and more similar to the practical IPMC system. Nevertheless, in a BJ model, four independent polynomials exist and stand for two

terms, $u(t)$ and $e(t)$, but this model might not be more precise or correct than the previous two models because the disturbance term was not taken into consideration in an IPMC system. After modeling by applying this model, four polynomials, and then the transfer function, $G_{BJ}(z)$, can be derived from Eq. (5.13) as shown in Fig. 5.8.

$$B(q) = -0.0001753 + 0.00263q^{-1} + 0.0002049q^{-2} - 0.002425q^{-3}$$

$$C(q) = 1 + 0.3501q^{-1} + 0.07309q^{-2} - 0.3367q^{-3} + 0.1179q^{-4}$$

$$D(q) = 1 - 0.6068q^{-1} - 0.3448q^{-2} - 0.3838q^{-3} + 0.3365q^{-4}$$

$$F(q) = 1 - 0.6115q^{-1} - 0.5154q^{-2} + 0.2521q^{-3} - 0.1251q^{-4}$$

$$G_{BJ}(z) = \frac{-0.0001753z^3 + 0.00263z^2 + 0.0002049z - 0.002425}{z^4 - 0.6115z^3 - 0.5154z^2 + 0.2521z - 0.1251} \tag{5.13}$$

Figure 5.8 shows the comparison of the output deflection from the practical experiment, and a BJ model predictor provided with an 8-V, 0.2-rad/s square-wave signal. According to the results shown in Fig. 5.8, the fitting rate reaches 76.38%, which is the same as that in an OE model although a BJ model requires two more polynomials than an OE model. Therefore, the two polynomials standing for the disturbance term cause almost no influence on the IPMC deflection. In other words, it seems that the IPMC system does not have a close relationship between the output deflection and the disturbance because two more polynomials for the disturbance term in a BJ model cannot get a conspicuous enhancement in the fitting rate. According to these four

previous models, it might enhance the fitting rate significantly to have adequate DOFs included.

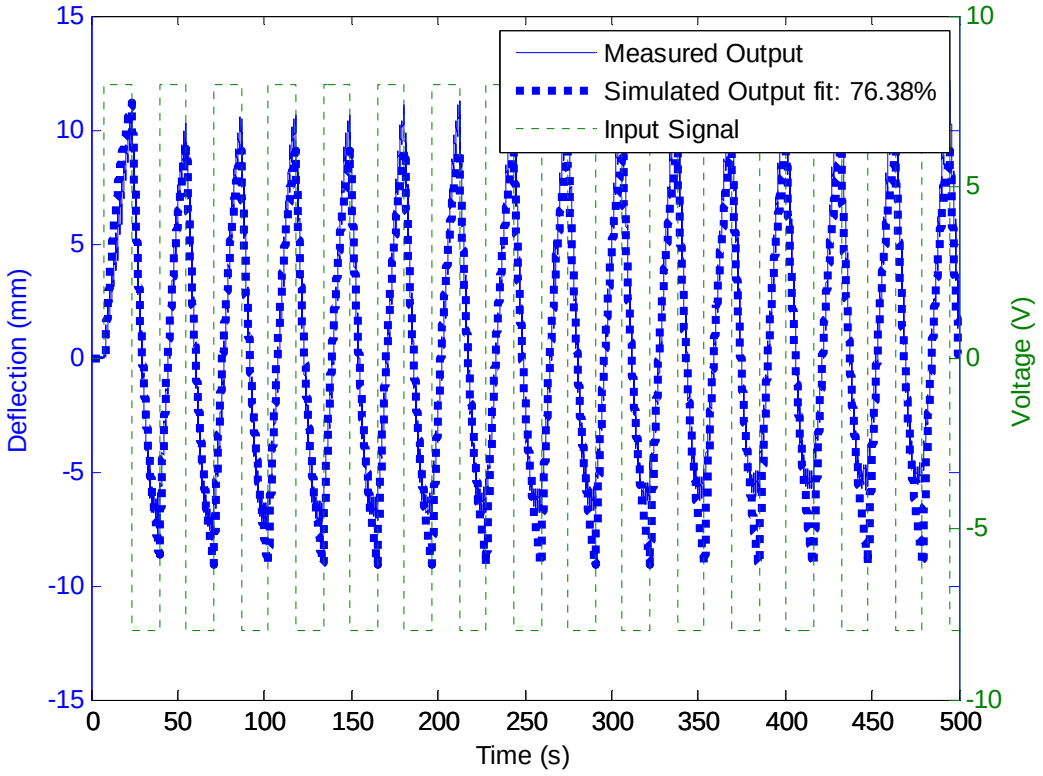

Fig. 5.8 Experimental and simulation results based on a BJ model. The measured output moves up because of deviation but the simulated output does not.

5.2.4 PEM Model

Prediction-error minimization (PEM) model, as the name implies, uses optimization to minimize the cost function [85]. This model works like an ARMAX model without a disturbance term but an error term, $e(t)$. This model can be used in both

SISO systems and multiple-input-multiple-output (MIMO) systems. A PEM modeling method can change the parameters, such as coefficient polynomials, after estimating a derived initial model to decrease the cost function [85].

A state space form has been derived based on a PEM model and shown in Eq. (5.14). All matrices can be found with the measured output deflection and the corresponding input signals. In this case, a fourth order transfer function has been chosen to compare with other models. This discrete transfer function and the comparison between its simulated output and the physically measured output are shown in Eq. (5.15) and Fig. 5.9, respectively. The simulated output has 70.08% matching with the measured output with an 8-V, 0.2-rad/s square-wave signal, the same as the previous input signals.

$$\begin{aligned} x(t+Ts) &= Ax(t) + Bu(t) + Ke(t) \\ y(t) &= Cx(t) + Du(t) + e(t) \end{aligned} \tag{5.14}$$

$$A = \begin{bmatrix} 0.99986 & -0.0016414 & 0.0040423 & 0.0022626 \\ -0.0015306 & -0.10232 & 0.4514 & 0.62704 \\ 0.000096947 & -0.027781 & -0.58704 & 1.0051 \\ -0.000054973 & -0.39388 & -0.5514 & -0.44768 \end{bmatrix}$$

$$B = \begin{bmatrix} 0.00000049412 \\ 0.0001332 \\ -0.000074562 \\ -0.000041279 \end{bmatrix}$$

$$C = \begin{bmatrix} 3776.2 & -0.74448 & -0.3334 & 0.8148 \end{bmatrix}$$

$$D = \begin{bmatrix} 0 \end{bmatrix}$$

$$K = \begin{bmatrix} 0.00025416 \\ -0.0051619 \\ 0.0013677 \\ -0.0015637 \end{bmatrix}$$

$$G_{PEM}(z) = \frac{0.001758z^3 - 0.0001489z^2 + 0.0000783z - 0.001069}{z^4 + 0.1372z^3 + 0.04551z^2 - 0.7789z - 0.4032} \tag{5.15}$$

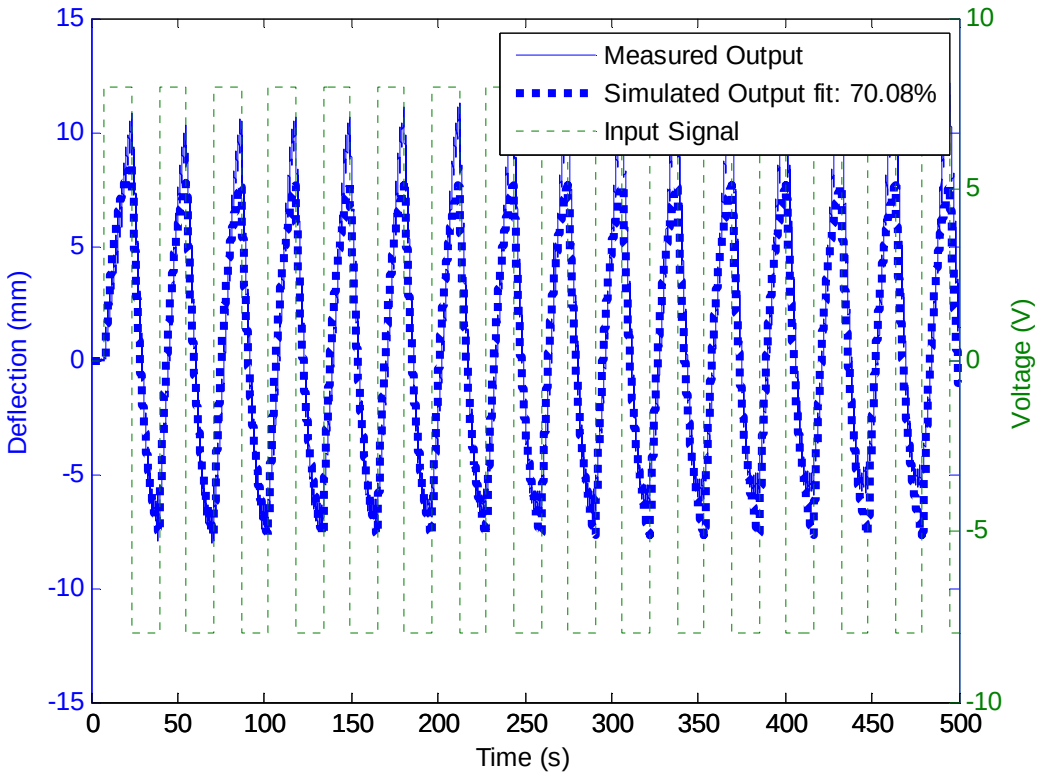

Fig. 5.9 Experimental and simulation results based on a PEM model. The measured output moves up because of deviation but the simulated output does not.

The above measured deflections, taken with a piece of IPMC strip as shown in Fig. 5.1, exhibit conspicuous deviation phenomena in Figs. 5.5–5.9. This phenomenon might decrease the capability of fitting with these models. When this deviation phenomenon begins, the unfitted parts increase due to the upward moving average line as shown in Fig. 5.10. The fitting rates are greater than 70% in each modeling method. However, all models have different transfer functions in response to various input signals. Figure 5.10 illustrates the disadvantage of the above mathematical models with some physical cases. In Figs. 5.10 (a) and (b), an 8-V, 0.1-rad/s sawtooth-wave signal and an 8-V, 0.3-rad/s sinusoidal-wave signal were applied in the system by using an ARX model and an 8-V, 0.2-rad/s square-wave input. A conspicuous difference exists in not only the amplitude of deflection but special states such as initial and speed-up states described in Chapter IV. The errors in the simulated amplitudes in Figs. 5.10 (a) and (b) are 8 mm and 2 mm, respectively. In addition, the simulated deflection exhibits no apparent difference between each of the two states in both of these two results. The other four parts in Fig. 5.10 have similar errors due to the systems with different input signals applied. The system in Figs. 5.10 (c) and (d) is an ARX model based on an 8-V, 0.2-rad/s sawtooth-wave input but generates outputs in response to an 8-V, 0.1-rad/s sinusoidal wave and an 8-V 0.3-rad/s square wave, respectively. However, in the last two parts of Fig. 5.10, the system comes from an OE model and is based on an 8-V, 0.2-rad/s square wave. The simulated output still has an error due to the different inputs utilized, an 8-V, 0.1-rad/s sawtooth wave and an 8-V, 0.3-rad/s sinusoidal wave. Therefore, the above models with high fitting rates might exhibit non-precise predicted

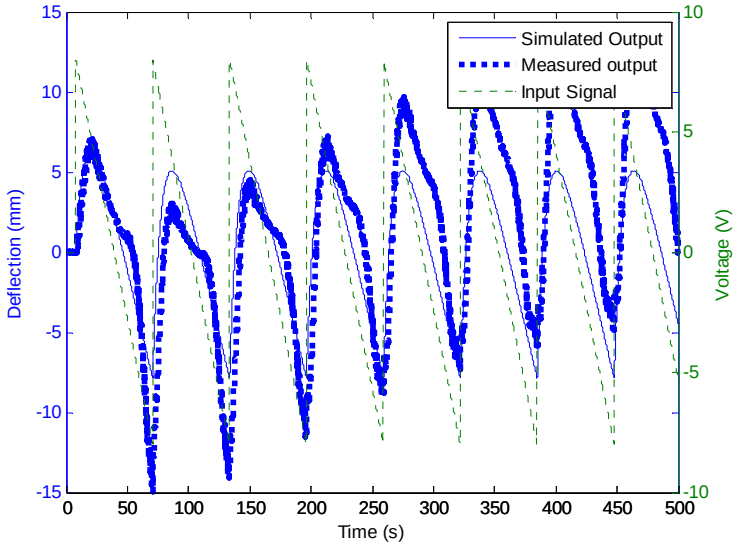

(a)

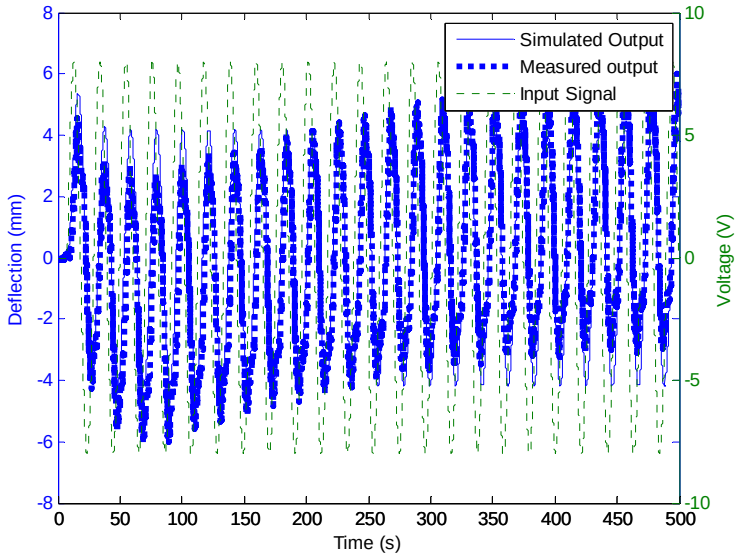

(b)

Fig. 5.10 Measured and simulated output deflection with non-corresponding inputs, (a) 0.1-rad/s sawtooth, (b) 0.3-rad/s sinusoidal, (c) 0.1-rad/s sinusoidal, (d) 0.3-rad/s square, (e) 0.1-rad/s sawtooth, and (f) 0.3-rad/s sinusoidal waves

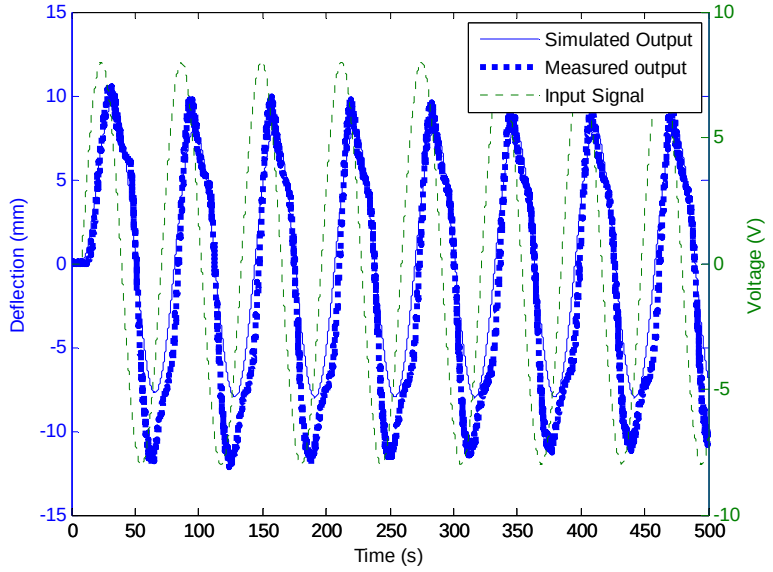

(c)

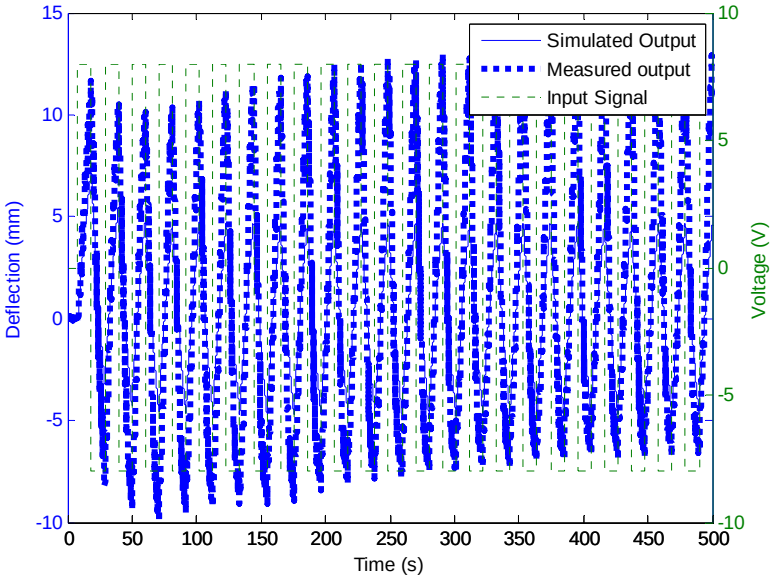

(d)

Fig. 5.10 continued.

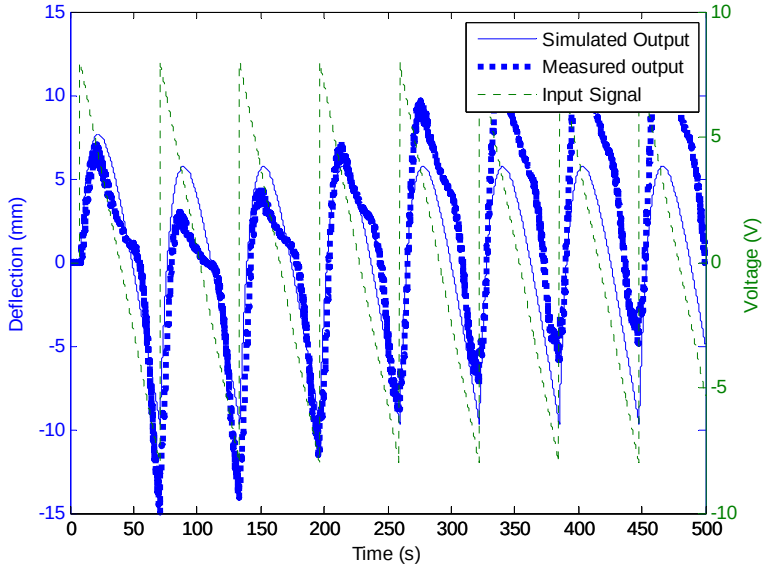

(e)

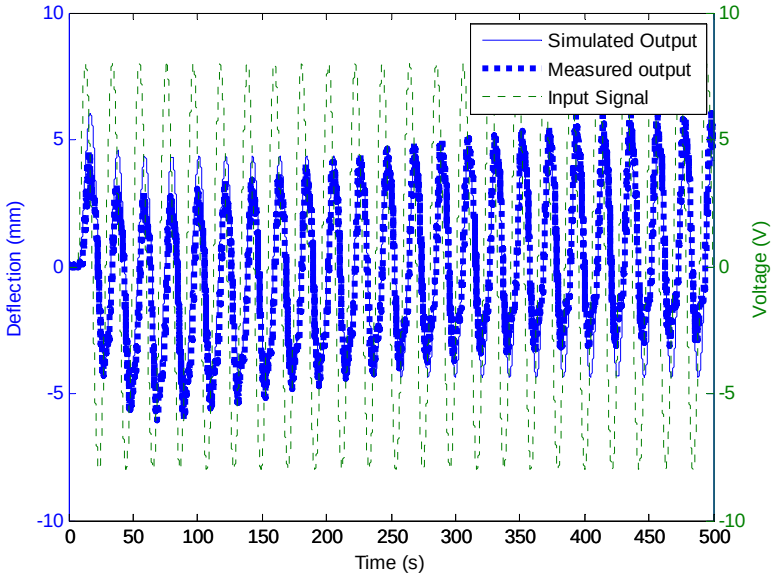

(f)

Fig. 5.10 continued.

deflection when provided with different input signals.

5.3 Electrical Modeling as a Linear Time-Variant System

An IPMC system can be seen as an electrical circuit because it exhibits output deflection, which is related to the virtual force caused by internal current in response to an external voltage. As for the internal impedances of a circuit, a model of an IPMC system consists of various linear and passive elements such as resistors, capacitors, and inductors according to the specifications [69, 75]. For example, the electrically conductive surface metallic electrodes make the surface to be full of the distribution of positive and negative charges, so it has the same property as a capacitor. The polymer base of IPMC, the Nafion® membrane, works as a resistor in this system, so Nafion® will be modeled as a group of impedances in an electrical model. Figure 5.11 illustrates the electrical model with the corresponding elements for an IPMC strip.

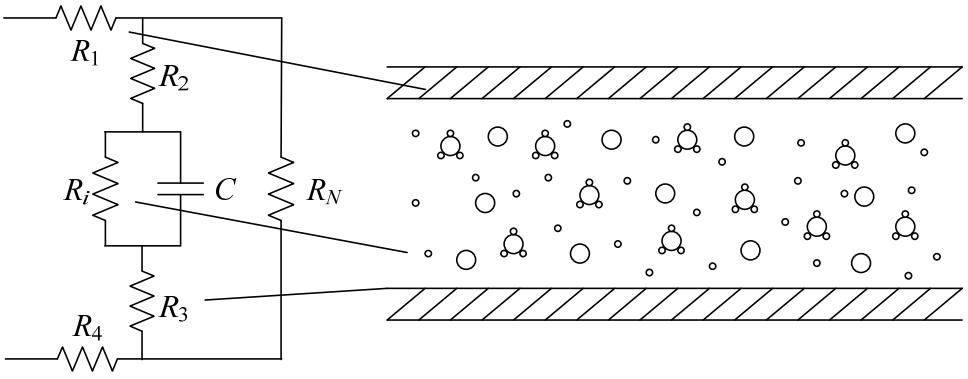

Fig. 5.11 Internal structure and the corresponding RC system

There is a directly proportional relationship between the output deflection and the internal current in an IPMC system [7, 55, 63]. According to the plots in these references, the current line appears to follow the deflection line. In addition, the relationship between the deflection and the external voltage must be obtained to predict and control the deflection. After making sure of the proportional relationship between internal current and output deflection, it is much easier to obtain the model of IPMC, which is the relationship between the input voltage and the deflection, by applying Ohm's law. Therefore, the electrical model was built and applied based on the relationship among the external voltage, the internal current, and the output deflection.

In Fig. 5.11, R_1 and R_4 are the equivalent resistors on the top and bottom surfaces, respectively, and come from the non-perfectly electrically conductive metallic surface electrodes. R_2 and R_3 indicate the equivalent resistors originating from the gap between the electrode and the Nafion® on the top and bottom surfaces, respectively, and defective reduction of platinum on the surface because it might introduce non-conducting impurities. R_i can be seen as the internal resistance, which results from the internal water molecules and impurities. The Nafion® used to fabricate IPMC is not thoroughly perfect but impure due to the internal air bubbles or dusts, which might reduce the internal electrical conductivity. In addition, R_i is variant due to the internal water-molecule concentration and distribution. This resistance would increase with a large number of internal water molecules, which cause hinders if overcrowded inside. The symbol, C, originates from the capacitor-like characteristic of IPMC because of the electrodes on the anode and cathode surfaces with the full distribution of charges. The

capacitance is closely depending upon the thickness of the IPMC. R_N, related to the current characteristics of the internal Nafion® membrane, indicates the resistance due to this membrane. The resistance of R_N would be a constant if the size and shape do not change. According to Fig. 5.11, the equivalent impedance can be derived in Eq. (5.16), which can be seen as a relationship between the external voltage and the current. In addition, there is a proportional relationship between input current and the output deflection, so the equivalent impedance can be expressed with the input voltage and the deflection as shown in Eq. (5.17). Finally, in Eq. (5.18), the relationship between input voltage and deflection of an IPMC system is derived. The constants, k_1 and k_2, indicate that there is a proportional relationship and they can be determined by experiments.

$$R_{equi} = R_1 + \{[R_2 + (R_i \,||\, C) + R_3] \,||\, R_N\} + R_4 \tag{5.16}$$

$$R = \frac{V}{I} = \frac{V}{k_1 D} \tag{5.17}$$

$$T.F. = k_2 \frac{1}{R_{equi}}$$

$$= k_2 \frac{R_i(R_2 + R_3 + R_N)Cs + (R_2 + R_i + R_3 + R_N)}{[(R_1 + R_4)(R_2 + R_3 + R_N)R_i + R_iR_N(R_2 + R_3)]Cs + [(R_1 + R_4)(R_2 + R_i + R_3 + R_N) + R_N(R_2 + R_i + R_3)]}$$

(5.18)

Figure 5.12 shows the simulation of internal current in the thick and thin IPMC strips with 8-V and 4-V step inputs, respectively. By applying both external and internal impedances, two different simulated currents are derived as shown in Figs. 5.12 (a) and (b), but they reach steady-state values eventually. A physical IPMC system shows this typical transient as the output deflection in response to a step input. A rapid and large increase shows up initially, and then it is followed by a decreasing curve toward the steady-state value slowly. For the thick IPMC, the simulation does not seem to be well-matched in practice due to the physical properties such as the stiffness. For example, it is difficult for a thick IPMC strip to exhibit an instant and uniform bending motion, so the deflection shows a slow and gradual increase up to the steady-state value in this case. On the other hand, as for a thin IPMC strip, a typical and prevalent reaction, i.e. an instant deflection followed by a slow relaxation, takes place but the actual deflection might not still be well-matched to the simulated internal current in Fig. 5.12 (b) due to some limitations that will be discussed in the next paragraphs.

A physical IPMC system is highly time-variant as modeled previously due to the internal mobile cations with water molecules. The internal properties, such as resistance, will not be kept constant because of the internal cations. Crowded cations with water molecules might enhance the internal resistance by blocking or degrading the movement of internal electrons. In addition, the surface resistance changes with the expansion or shrinking on the top and bottom surfaces when the IPMC strip bends. There are a great number of small cracks or uneven metallic coating on the surface, and they tend to reduce the conductivity due to non-uniform reduction reaction. Figure 5.13 shows some

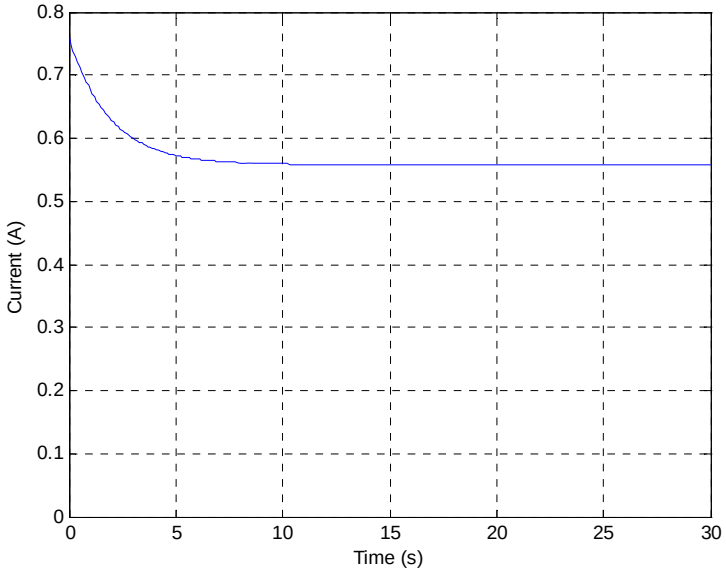

(a)

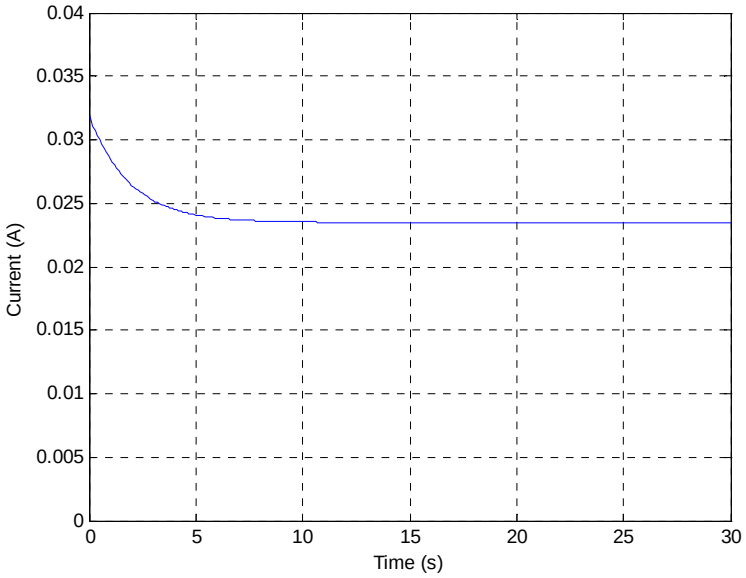

(b)

Fig. 5.12 Simulation of internal current v.s. time of (a) thick and (b) thin pieces of IPMC strips as an LTI system

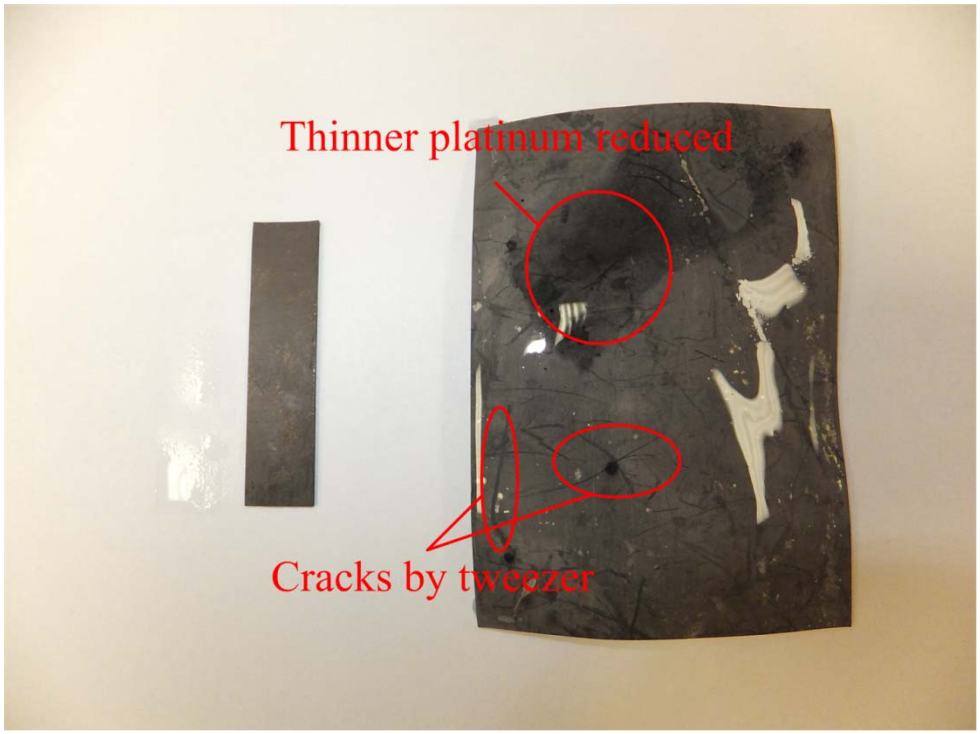

Fig. 5.13 IPMC samples with well-reduced, non-uniformly-plated, and physical cracks

typical flawed surfaces after fabrication. The left sample has uniformly reduced platinum and the surface exhibits the same brightness. On the right piece, however, besides non-uniform metallic electrodes, several cracks emerge on the surface. The darker areas exhibit low conductivity due to thinner and less metallic plating. The cracks caused by tweezers, which might be expanded with Nafion® on the anode surface significantly, also degrade the surface conductivity and the deflection in operation. Contrarily, on the opposite surface, the cracks shrink, and the surface resistance decreased gradually. Therefore, parameters such as surface and internal resistances would be time-variant in

operation. In this simulation, two LTI models for both thick and thin IPMC strips were built and simulated, but they might not be perfectly well-matched to practical systems and results shown in Chapter IV. For these reasons, an IPMC system should be treated as an LTV system, and a specific modeling method should be developed and applied. In the following case, all results will be shown based on two LTV models. With the inclusion of time-variance, the results would be closer to the practical systems.

According to Fig. 5.12, it is apparent that both results are not well-matched to these shown in Chapter IV, so now an LTV method will be applied for more precise modeling. In order to model an LTV system, the same electrical model is used, but all elements presented exponential changing in properties due to the internal cations with water molecules and structures except for the capacitance. Each element varies due to specific reasons, including physically and chemically changing characteristics. For example, if the IPMC strip is bending upward in Fig. 5.11, R_1 and R_4 will decrease and increase, respectively, because the top and bottom surfaces extend and contract, respectively. R_2 and R_3 result from the gap between the metallic electrode and the Nafion® base, so they both will increase when the strip bends upward or downward. R_i comes from the internal environment, such as the water molecules concentration, so it also increases when the strip exhibits a bending motion due to non-uniform internal water-molecule distribution. Overcrowded water molecules hinder cations movement and transmission, so the internal conductivity will be reduced instead of increased. Working environment should be also taken into consideration to choose R_i. R_N is related to the properties of Nafion®, so it does not have a conspicuous changing due to the size

that might change with temperature in operation. The last element, *C*, does not vary with time much because bending motion would not cause apparent influence on the thickness of IPMC strips. Figure 5.14 shows the simulated internal current in a thick and a thin piece of IPMC strips by using LTV electrical models. It is obvious that the internal current in the thick strip shows a gradual decrease down to the steady-state value, following the rapid rising like the previous simulation.

The thin strip, however, shows a slow and smooth decrease toward the steady-state value after the instant increase. The practical deflection is in proportion to the internal current, so the simulated deflection of the thick and thin IPMC strips can be predicted according to the simulated current in Fig. 5.14. The thin strip might exhibit a bending motion close to the simulated result, but the result curve might not show a rapid rising as shown in Fig. 5.14 (a) for the thick strip. Therefore, in practice, for a thick strip, it exhibits a slower increase toward the steady-state value instead of going with the simulated current closely and perfectly. Moreover, according to Fig. 5.14, this phenomenon happens to not only a thick but a thin IPMC strip.

TABLE 5.1 lists the values of all elements in this electrical model. By measured manually, all values can be determined to predict and simulate the output deflection of the IPMC strip in this experiment. All the values are in the initial state when applied in the time-variant method.

Equation (5.19) indicates the revision for each element in the electrical model of an IPMC system in order to improve the accuracy in a time-variant case. This revised equation originates from the movement of internal cations and water molecules, which

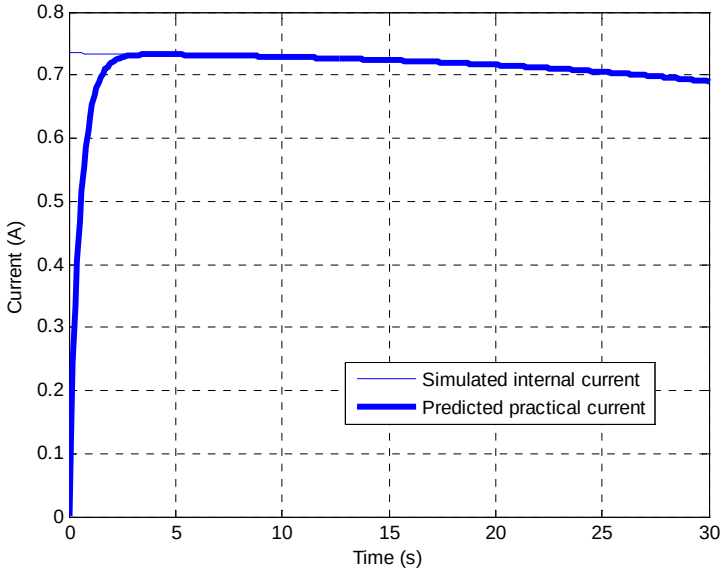

(a)

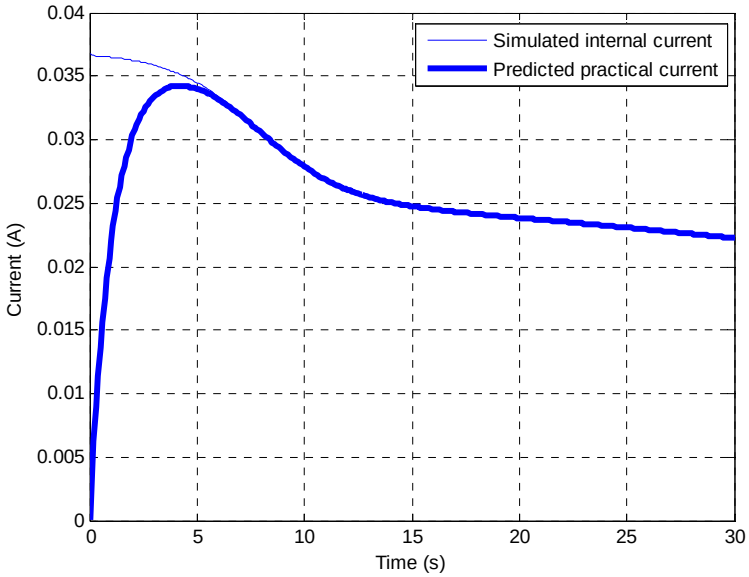

(b)

Fig. 5.14 Simulation of internal current v.s. time of (a) thick and (b) thin pieces of IPMC strips as an LTI system

TABLE 5.1 Values of all electrical elements in the electrical model given in Fig. 5.11

Element	Value	Unit	Note
R_1	5	Ω	Comes from surface resistance
R_2	2	Ω	Due to the gap between Nafion® and surface
R_3	2	Ω	Due to the gap between Nafion® and surface
R_4	5	Ω	Comes from surface resistance
R_i	0.5	Ω	Results from internal cations and water
R_N	1	Ω	Only changes with Nafion® deformation
C	1	μF	No significant change

exhibit an exponential movement toward the cathode side and stack in this side. Likely, the stacked water molecules increase the resistance exponentially. In addition, surface resistance also exhibits similar increase as the bending shows up. On the contrary, the other surface resistance exhibits exponential decrease. TABLE 5.2 lists the values of each element and constant by several trial-and-error rounds. Each element may have

TABLE 5.2 Constants in the revised equation

Element	A (Ω)	B (s)	C (unitless)
R_1, R_4	1	1	1
R_2, R_3	0.1	1	1/6
R_i	0.1	2	1
R_N	0.1	1	1

different variant constant from another due to the characteristics and the current situation such as bending speed that would influence the surface resistance significantly.

$$R(t) = R(0) + A(e^{t/B})^{C} \tag{5.19}$$

where $R(t)$ and $R(0)$ indicate the present and the initial resistances, respectively. The constants A, B, and C, originating from the characteristics of each equivalent resistor and accumulation of internal water molecules, influence the variation speed of each element.

One of the internal resistors, Ri, varies with the accumulation of cations with water molecules, so this revised equation originates from the equation of capacitor charging [86] with a minority of revision in constants. The resistor of the Nafion®, R_N, also changes with the deflection of the Nafion®. The other elements such as the surface resistors and the gap resistors also exhibit similar variation in resistance while the IPMC strip is bending. Therefore, these above resistances vary exponentially based on this revised equation.

By applying this equation, when t goes to infinity, this system becomes open-circuited like a charging capacitor because overcrowded and over stacked water molecules may hinder the movement of electrons. Without given current from an external voltage, the deflection of this thick IPMC strip may be degraded although an equivalent capacitor with low capacitance still exists and a steady voltage is given continuously. This is a typical back-relaxation phenomenon in an IPMC system. Thus, in

addition to modeling, this revised equation can be used to explain this phenomenon according to the physical characteristics.

According to Fig. 5.14, the LTV model can predict the deflection more precisely than the LTI model shown in Fig. 5.12. This time-variant method can also predict the output deflection in various situations by providing a variety of internal parameters, such as resistors. The metallic surface electrodes are used to transmit electrons and make them to be uniformly distributed on the surface in order to exhibit sufficient and uniform bending force by the surface voltage distribution. Surface resistance plays an important role because it causes great influences on the bending force and motion by attracting and repelling internal cations. However, the metallic electrodes are not so perfectly conductive that the surface voltage is weakened with the distance from the origin, copper electrodes in this case. The imperfect surface electrodes not only degrade the deflection, which influences other equivalent resistors indirectly such as internal resistance, but also consume more electrical power on the surfaces. In order to enhance the surface conductivity, IPMC has been fabricated with repetitive coating for the increase in the thickness of electrodes, and only the metals with higher conductivity, such as gold and platinum, have been listed in the options of surface electrodes [11, 56]. In addition, enhancing the surface area by roughening it with sandpapers can enhance the metallic layer on the surface [49]. In the following paragraph, the importance of surface conductivity will be explained.

Figure 5.15 shows the predicted internal current with various surface resistances for both the thick and thin IPMC strips to explain the influence of surface resistance. Six

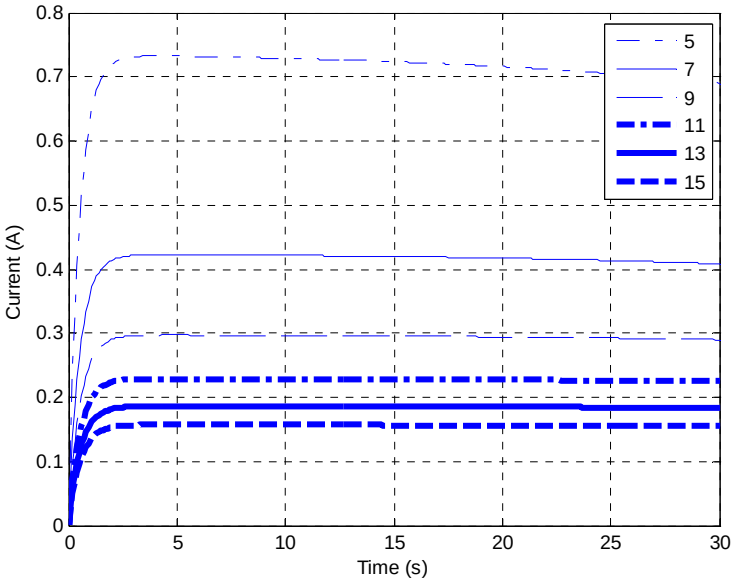

(a)

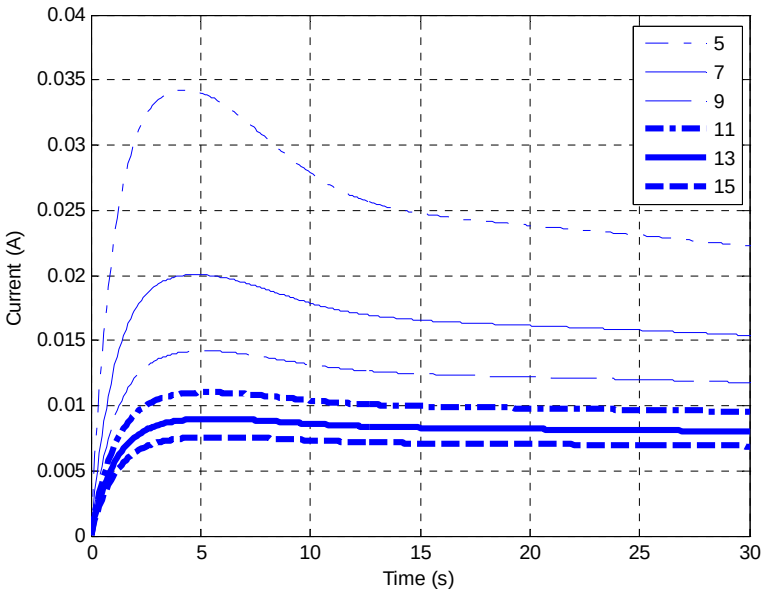

(b)

Fig. 5.15 Simulation of current with various surface conductivities of the (a) thick and (b) thin IPMC strips

groups of initial surface resistances were chosen and compared with one another. As shown in Fig. 5.15 (a), the instant rising can reach the maximum current of around 0.73 A and then goes down to 0.68 A gradually when the equivalent surface resistance is 5 Ω. The initial surface resistance increased by only 2 Ω in each case but exhibits the same rising with time. However, there is a notable difference between the two lines, so the surface resistance influences the internal current and deflection of IPMC strips significantly. The surface resistance decreases not only the maximum current but the final steady-state current, so the deflection would be degraded due to the decrease of the simulated current and the surface distributed voltage.

As for the thin IPMC strip, it also exhibits conspicuous difference between each two initial cases. It is apparent that the instant maximum current changed due to the various surface resistances. All resistances change widely and fast owing to the rapid bending motion of a thin IPMC strip. This bending motion causes an obvious decrease to the simulated internal current indirectly. In addition, all the steady-state current values also exhibit difference in each equivalent surface resistance instead of going toward a unique value. Therefore, surface conductivity improvement can enhance the internal current, related to the deflection, in both thick and thin IPMC strips by up to 2-Ω decrease. Figure 5.15 (b) shows that the predicted internal current in a thin IPMC strip with various initial surface resistances like the phenomenon happened in Fig. 5.15 (a).

According to Figs. 5.12, 5.14, and 5.15, there is no doubt that the surface resistance is one of the decisive factors to change internal current and exhibit output deflection for an IPMC strip. Output deflection will be improved significantly if the

IPMC has thicker metallic electrodes to enhance surface conductivity because the output deflection is closely related to the internal current. In addition, the maximum deflection was degraded significantly although the surface resistance increased slightly. The surface with a thick metallic electrode not only influences the surface resistance but also the internal resistances. For example, if a strip exhibits large deflection, R_2, R_3, and R_i will also increase significantly as well due to the boundary between the electrodes and surfaces, and non-uniform distribution of internal water molecules.

In practice, a well-reduced IPMC consume most power inside IPMC instead of the surface. The surface is not usually burned or damaged by high current. On the contrary, the surface with high resistance would be damaged by high current. The IPMC strip could not show large bending motion because the external power is consumed by the surface resistance instead of moving internal cations. Therefore, to prevent this vicious circle, surface metallic electrodes must be well-reduced in IPMC fabrication.

The LTV model exhibits a large difference in simulation although only 2-Ω increase is accumulated each time in the surface resistance in the previous case. As the equivalent elements of an IPMC system, R_1, R_2, R_3, R_4, R_i, R_N, and C vary with the deflection and the movement of internal water molecules instead of keeping constant, so the results as shown in Fig. 5.14 should be more precise than those in Fig. 5.12. As a consequence, this LTV method is more appropriate than the conventional model with LTI equivalent impedances.

The predicted deflection might not be consistent with the corresponding internal current in a thick IPMC strip due to structural limitation. High stiffness and more hinders,

such as overcrowded water molecules and non-mobile impurities, degrade the bending speed so that the model should be revised. This revision is derived from the dimension of the thick IPMC strip to decrease the errors caused by the structural limitation. In this case, the rise time has been extended up to 16 s based on the thickness of the experimental IPMC sample, 1 mm. Figure 5.16 depicts the comparison between the revised and measured deflections when the strips are given with a step, a sinusoidal, a square signal, and a sawtooth wave. In this figure, the response speed of the simulated deflection in a dashed line is greatly degraded but fit the actual deflection in a solid line much better than Figs. 5.12 and 5.14.

5.4 Summary and Comparison

For the structural modeling, the IPMC sample is treated as an existing cantilever beam with a force distribution on the top surface that results in the bending motion. However, the bending force comes from the movement of internal water molecules instead of physical force loading. Moreover, the force distribution might not be uniform as shown in Fig. 5.2 on the IPMC strip due to the surface conductivity. Uneven metallic coating would damage the uniformity and complicate the internal water-molecule distribution and influence the virtual force distribution indirectly as shown in Fig. 5.17. The two typical examples shown in Fig. 5.17 illustrate the strip with reduced surface conductivity due to uneven metallic electrodes or cracks, and the distribution is highly nonlinear and complex. Both provided current and deflection are not easily predicted due

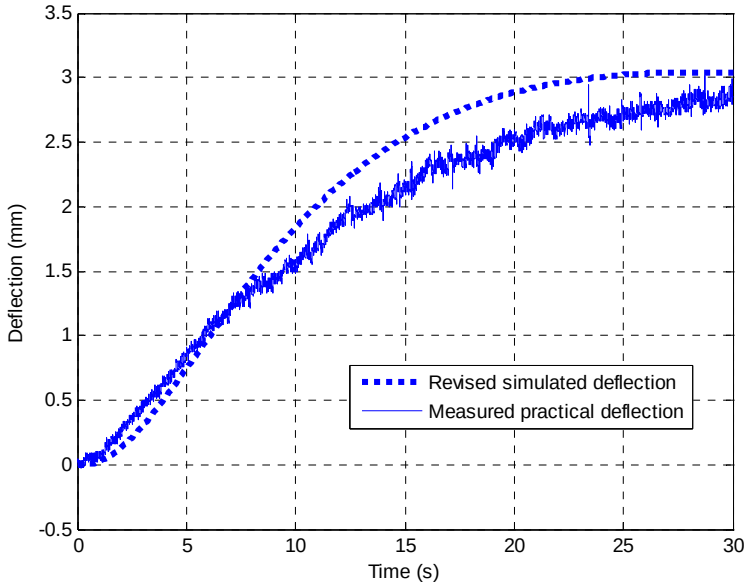

(a)

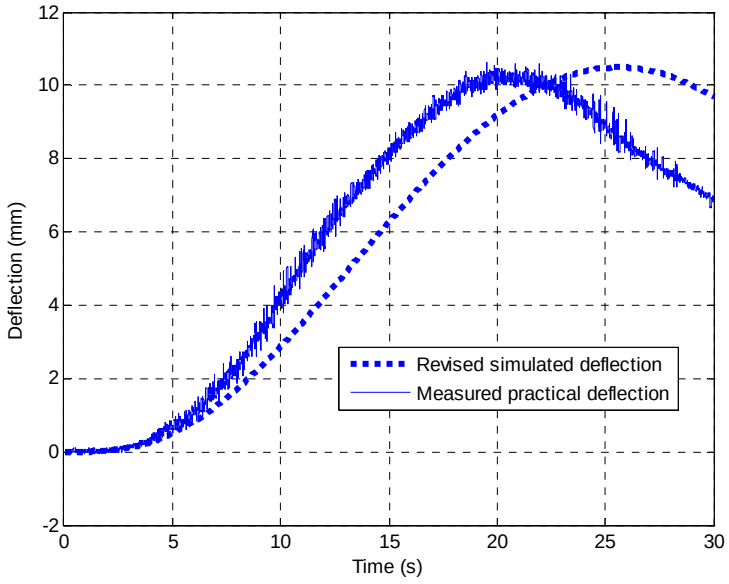

(b)

Fig. 5.16 Revised simulated deflection and measured deflection in response to (a) step, (b) sinusoidal signals, (c) square-wave, and (d) sawtooth-wave signals

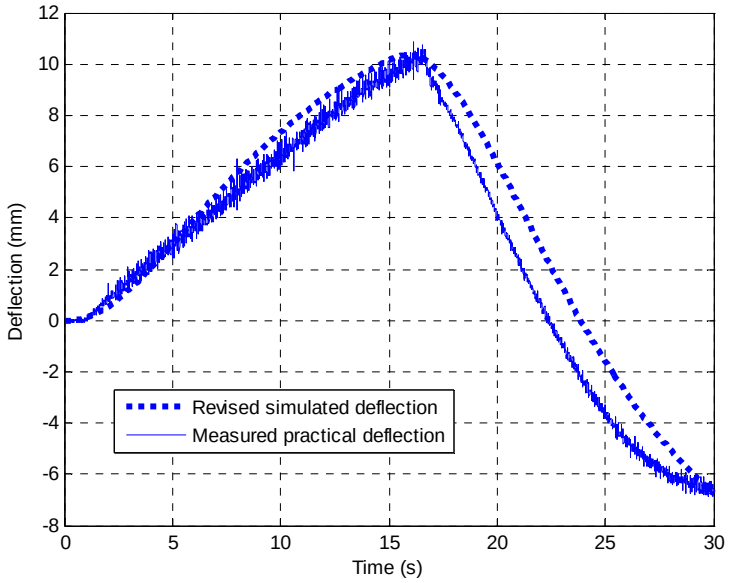

(c)

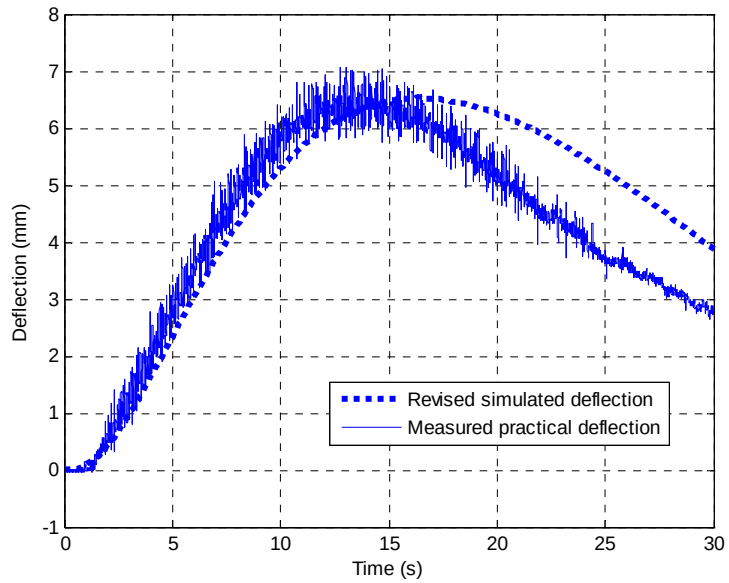

(d)

Fig. 5.16 continued.

to the complex virtual force distributions. Therefore, there might be some errors between the measured and simulated output deflection when this method is applied. In other words, this model is inappropriate because each IPMC strip has its own specific model due to various structures and thickness of metallic coating.

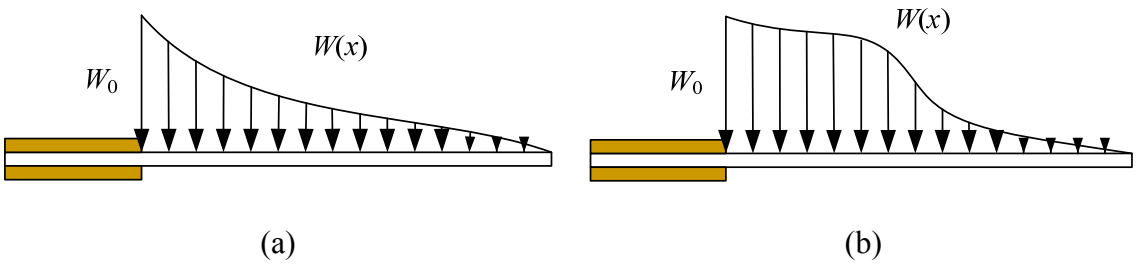

Fig. 5.17 Virtual force distribution of IPMC strips with uneven metallic coating layer

It is difficult to find an accurate transfer function of IPMC systems to predict or simulate the deflection in response to various input signals by using a structural model. A reverse-modeling method, which is used to model the system based on the output deflection and the responding input signals, would be a better fit than the conventional methods. By applying this reverse-modeling method, it is not important and relevant to explore how everything is located or distributed inside IPMC strips. A transfer function, however, can be derived according to the provided input voltage and output deflection. This modeling method looks more precise and direct, but numerous transfer functions for various input signals need to be found. In addition, the transfer functions might not be applied when provided with other signals although they exhibit high fitting rates in

response to corresponding input signals. Therefore, it takes time to find various models if various input signals are provided.

Unknown internal environment also affects to the electrical modeling because the exact internal characteristics of IPMC strips is not known. Furthermore, everything inside IPMC might be highly time-variant, which means the parameters in the transfer function varies with time in operation due to the movement of internal cations with water molecules. Therefore, it will be inaccurate to apply this electrical model with constant equivalent element values. By treating IPMC as an LTI system, the experimental results exhibit a large difference from the actual output shown in the Chapter IV. However, when employing exponential time-variant elements, the simulated results are more accurate except for the limitation due to physical structures. Therefore, this electrical modeling method with structure-based revision is the appropriate choice for IPMC systems among all models in this chapter. Nevertheless, it is not easy to simulate or predict when the IPMC is provided with complicated input signals. Furthermore, the parameter variation of all electrical elements should be determined.

TABLE 5.3 lists the comparison among all models presented in this chapter. Each model has specific benefits and weakness. All of them could be chosen depending upon working environments or given signals. IPMC is a strongly time-variant system so the LTV electrical method should be better fit than the previous two methods, and the deflection can be predicted based on the relationship between the input current and the output deflection. However, this method has not been widely applied yet due to its complicatedness.

TABLE 5.3 Comparison among all modeling methods presented in this chapter

	Structural Models	Mathematical Predictors	Electrical Models
Fundamental Concepts and Feathers	A virtual continuous loading distribution causes the bending motion	Based on various types of predictors to model according to measured outputs and responding input signals	Get simulated internal current through the equivalent model to predict output deflection
Benefits	Easily applied and considered	Spend less time finding out the system transfer function	A direct model based on the characteristics of IPMC
Weaknesses	Working principle is not the same as that of a cantilever beam	A system may have specific transfer function in various input signals	Unidentified factors still exist so the system models are not exactly perfect

CHAPTER VI

DESIGN AND IMPLEMENTATION OF AN AQUATIC IPMC-BASED ROBOT

All fabricated IPMC samples were used for the implementation of a robot based on the characteristics of IPMC, described in Chapter II, and the results of fundamental experiments, shown and listed in Chapter IV. According to the previous chapters, the dimensions of all IPMC strips have been decided, and the operational environment has been chosen as an aquatic environment. In addition, an 8-V, 0.2-rad/s square-wave signal has been selected as the activating signal since it showed high performance in Chapter IV. In this chapter, both mechanical and electrical designs will be discussed, and methods to attach wires to IPMC strips will also be described. The wire-attaching method, which is used to transmit external power, has been decided according to the benefits and weaknesses of the four choices in this chapter. Finally, the walking procedures and the corresponding input signals are illustrated in a series of figures.

---

*Part of this chapter is reprinted with permission from "Aquatic ionic-polymer-metal-composite insectile robot with multi-DOF legs," by Y.-C. Chang and W.-J. Kim, *IEEE/ASME Transactions on Mechatronics*, vol. 18, no. 2, pp. 547−555, Apr. 2013. Copyright 2013 by *IEEE/ASME Transactions on Mechatronics*, and "Design and implementation of an ionic-polymer-metal-composite aquatic biomimetic robot," by Y.-C. Chang and W.-J. Kim, in *Proceedings of ASME 2011 Dynamic Systems and Control Conference and Bath/ASME Symposium on Fluid Power and Motion Control*, Oct. 31–Nov. 2, 2011, Arlington, Virginia, USA, pp. 411−418. Copyright 2011 by DSCC.

6.1 Mechanical Design

The locomotion of biomimetic robots originates from a variety of activating structures, such as flying, crawling, and sliding by imitating insects and animals. Wood *et al*. developed a tiny flying robot with high-speed vibrating wings activated by two symmetric layers of laser-micromachined piezoceramic $PbZrTiO_3$ (PZT) [36−39]. Kingsley exhibited a well-designed and -implemented cockroach-inspired robot with agile locomotion [41]. Each structure has its specific convenience and limitation in practice. For example, flying robots can arrive arbitrarily everywhere without obstacles on the road. Nevertheless, it has to be not only as light as possible but also working with a high-frequency vibration in order to lift the body up. Furthermore, the flying trajectory is too unstable to control without rails as shown in [36]. Swimming robots are not necessary to be as light as a flying robot but the density is less than 1 g/cm^3, depending on operational environment. This class of robot is not as uncontrollable as a flying robot, and can be navigated to everywhere in an aquatic environment. The speed and space of its movement, however, is limited by the aquatic environment due to the density and viscosity of water.

The practical locomotion for IPMC walking robots will not be all of the above due to the characteristics of IPMC. A flying robot, for example, is not easy to be realized by using IPMC strips due to the requirements of both high-frequency vibration and sufficient force to lift up itself. Insects' wings need high-frequency (~100 Hz) vibration to generate the lifting force for the bodies. However, for IPMC strips, high working frequency and large force cannot be attained at the same time because they are affected

by the input signals and the thickness of the IPMC. The voltage, frequency, and pattern of input signals can change the output deflection significantly as shown in Chapter IV, and so can the thickness. In this experiment, the thickness of the IPMC strips is around 40 mil (mili-inch), which is around 1 mm and sufficient to support the body, and these IPMC strips cannot generate a sufficiently conspicuous output deflection in high frequency (around 100 Hz). Moreover, flying robots must be sufficiently light because their bodies must be lifted up by the lifting force. Nevertheless, IPMC sample is not light enough due to the basis polymer membrane and the metallic coating. For sliding motion, it needs both sufficient force and bending curvature for transverse undulation. For example, a snake swings its body on the ground in order to generate the friction to activate its body by transverse undulation when it is creeping. For this kind of locomotion, IPMC strips do not need to high-frequency operation but sufficient force and bending curvature for transverse undulation. However, it is not easy to exhibit both significant force and deflection for thick IPMC strips, so these two kinds of locomotion are not appropriate to be applied in the design of the IPMC robot.

IPMC robots have been applied in swimming robots because they just need the force from IPMC strips to navigate instead of lifting. They do not need to lift themselves up as long as the density is less than 1.0 g/cm^3. Like a fish, the only force it needs is used to activate itself unless it wants to sink or float more because swimming robots are given with buoyant force by water. For crawling motion, similar to sliding, it is working by periodic oscillation of the body. The bending curvature, however, is not necessary to be large, but the friction between the body and the ground must be sufficient to activate the

body. For example, the worm-like IPMC robot Arena *et al*. have developed exhibited a small bending in each segment but a big contribution to the movement of this robot [21].

Locomotion has its own specific limitation and weakness such as operation environment and performance as listed in TABLE 6.1. For example, flying robots have to be light to fly; swimming robots must be working in aquatic environment; sliding and crawling robots need sufficiently large friction between the ground and their own bodies

TABLE 6.1 Comparison among the robots in three operational methods [21−29, 36−46]

	Flying	Swimming	Crawling	Walking
Design requirements and limitation	Light and high-speed vibration	Work in an aquatic environment and be waterproof	Need conspicuous bending deflection to move	Stiff legs are needed for supporting the body
Advantages	Move in the air without obstacles on the ground	Weight does not destroy performance	Move on various grounds with low obstacles	Move steadily on various ground as a real insect
Disadvantages	Not easy to fly steadily	Slow movement due to the aquatic environment	Damage the body by friction	Need well-matched legs and walking procedure

to creeping on a slope. Therefore, in this research, a six-legged walking robot was designed for both its working convenience and performance.

IPMC walking robots have been implemented in various designs and structures for a while. Most of them, however, have only one DOF in each leg because thinner (less than 1 mm thickness) IPMC strips do not have sufficient force to support the bodies even keeping standing depending on the weight of robots. A two-DOF leg has been designed to prevent this problem. For the robot with two-DOF legs, each of its legs consists of a thigh and a shank, used to bend vertically and horizontally, respectively. As a human beings, the thigh and the shank operate in order to lift up the shank and move the body forward, respectively. They can be called supporters and drivers because the IPMC strips with vertical bending can support and lift up the shanks and the horizontal bending can keep driving the body forward by giving a force to the ground backward. By periodic and mutual operation of supporters and drivers, a walking robot can move smoothly and freely even in most environments or grounds instead of being limited by specific environments. Take a cockroach, a real six-legged insect, as an example, each leg has multiple DOFs and can be not only a supporter but also a driver as the design in this paragraph. A leg with various DOFs would be more convenient and effective because each leg can work independently without cooperating with all other legs. If a leg does not have both a supporter and a driver, supporters have to exhibit a well-performed cooperation with drivers in order to walk smoothly. Nevertheless, a 2-DOF leg not only needs no complicated cooperation like that, but also can be much more similar to a real insect's leg. Therefore, 2-DOF legs were selected as the final design for the six-legged

IPMC walking robot in order to imitate a real insect, and enhance the smooth of walking motion.

In the design mentioned in the previous paragraph, two pieces of IPMC strips should be attached to each other perpendicularly for both vertical and horizontal deflection. Preventing from structural deformation, a lightweight shim was used as a medium to get two strips connected to each other. Two kinds of connection have been taken into consideration as follows. One of the methods is to use a strip as a bendable joint as a connection between two main structures, such as bones, on both ends like human beings' legs. This kind of connection can imitate a real leg to exhibit good limb motion because of the similarity to human beings' or insects' legs. This connection, however, has not been widely applied in IPMC robots because the strips need both sufficient force and large bending deflection in order to activate both themselves and the structures. If the IPMC trips are thin, take 7-mil strips as an example, the instant maximal force is just around 0.9 mN with a 1.2-V step input [79−82], so it is difficult to output a conspicuous bending motion with a structural loading. Therefore, thinner strips cannot be a choice for the joints in this design due to insufficient force. On the contrarily, thicker IPMC strips can generate sufficient force to activate the structures and themselves. However, the deflection range of thicker strips is limited by the high stiffness. Furthermore, the application of IPMC strips with small deflection may enlarge the sizes of robots, so it probably increases the weight and cannot be a small biomimetic robot anymore. Consequently, it does not seem to be an appropriate connection method because IPMC strips may not exhibit a good performance on bending motion.

The other method is to connect two strips with a joint between each other, and the joint acts as not only a connector but also a fixer because the IPMC strips might bend toward unexpected direction without a fixer to confine one end. Figure 6.1 illustrates bending motion with and without a fixer attached to IPMC strips. As a connector, the joint can be flexible in size as long as it has sufficiently high stiffness to confine the IPMC strip. This method has been applied for its firmness and convenience. Take the crablike robot Ye *et al*. designed as an example, the joints used in this design might be made of thin shims or plastic membranes due to the light and thinner IPMC strips' insufficient force [87]. The joints for thin IPMC strips are not necessary to be hard and stiff because the strips cannot generate sufficient force to escape from the limitation of the fixers. In other words, they do not need stiff fixers to confine the bending motion.

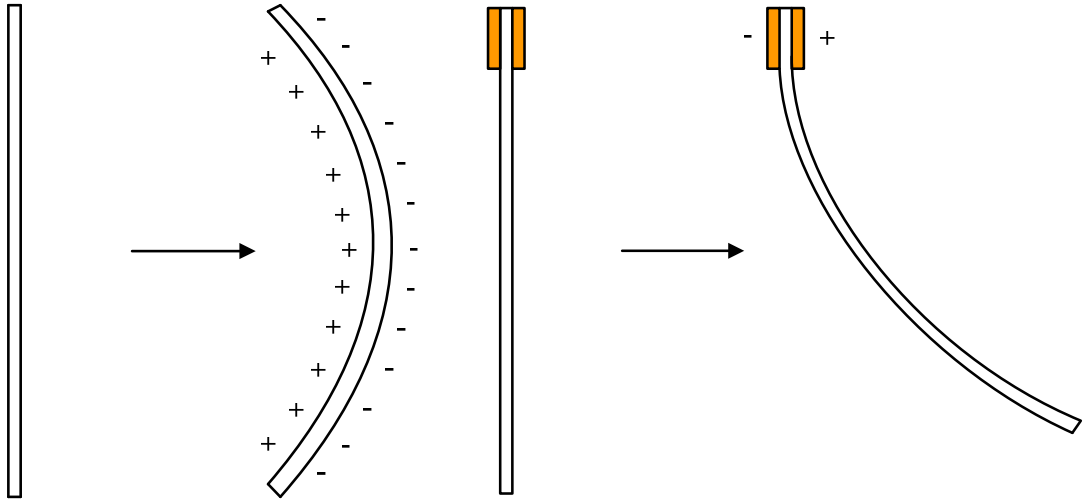

Fig. 6.1 Illustration of IPMC deflection (a) with and (b) without fixer attached

For thicker IPMC strips (around 40 mil in thickness), however, they are not supposed to be connected with light shims but hard and thick ones from being deformed by strong force. Therefore, in this experiment, the shims which were as thick as the IPMC strips were used to both connect and fix each other.

To transmit power to the robot, wiring acts as an important role between an external power supply and electrodes attached to IPMC strips. As a bridge between external power sources and IPMC strips, the wire must be both light and soft to prevent from increasing the weight and confining the motion of each strip, respectively. The ordinary wire, shown in Fig. 6.2, has been widely used to transmit current usual electrical experiments. However, with an insulated cover, this wire has high stiffness so that the motion of the IPMC robot might be confined. It seems simple to be confined by this wire for thin IPMC strips (7 mil) because they are soft and exhibit weak output bending force. Therefore, this transmission medium is not a good choice for the walking robot although thicker strips can provide stronger force.

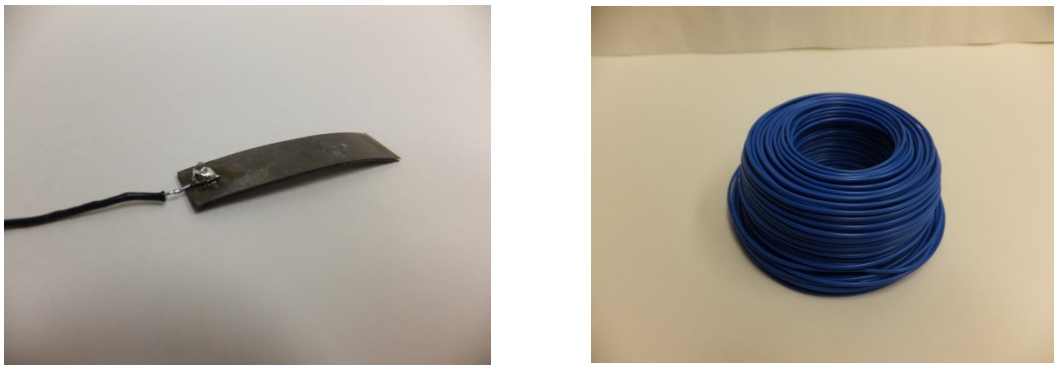

(a) (b)

Fig. 6.2 Current transmission via general wires with a layer of isolated cover

To decrease external confinement, a single build magnet wire with a layer of Polyurethane Nylon insulation, made by MWS Wires Industries, was used to transmit current to IPMC strips via copper electrodes because of low weight and softness. The magnet wire is a copper or aluminum conductor with insulation covered and mainly used to twine electromagnetic devices such as motors and transformers [75]. In order to twine devices in various sizes, wires must be provided in different diameters. In this experiment, AWG 38 single Poly Nylon magnet wires were used to prevent from confine the motion of each IPMC strip. The cross-sectional diameter of magnet wires is the decisive factor to choose the wire. However, both thin and thick wires have their own weakness in the application of the IPMC robot. The fine magnet wires would not confine the motion of the robot but tend to be broken due to short diameter and low ductility. The ordinary wires are firmer and not easily-broken, so they greatly degrade the performance and the deflection of each IPMC strip due to high stiffness. After repetitive trials and errors, the AWG 38 magnet wire could make the best connection between external power and IPMC strips among all options because of not only the sufficient firmness in structure but the maximum of current loading, which can flow at least 1 A according to preliminary testing. An IPMC strip needs around 600 mA (depending on the thickness and surface condition) to be activate when it is given with 8-V square waves. Thus, the AWG 38 magnet wire is appropriate to be used to transmitted current for IPMC strips in the robot. TABLE 6.2 lists the typical specification of the AWG 38 magnet wires. According to TABLE 6.2, the nominal cross-sectional diameter of the wires is around 0.0045 inch and the nominal resistance is around 0.6482 Ω/ft. Current

can be transmitted via low resistance and thin wires without confining the robot and large power loss during the transmission.

To transmit power to IPMC strips, wires must be attached tightly to the surface of IPMC strips. In this design, there is a medium between a wire and an IPMC strip to enhance the transmission performance and prevent the surface damage. It is difficult to attach a wire to a trip directly without any medium. This kind of materials, such as

TABLE 6.2 Characteristics of the magnet wire [88]

		38 Single Poly Nylon
Bare Diameter (Inches)	Min.	0.0039
	Nom.	0.0040
	Max.	0.0041
Diameter (Inches)	Min.	0.0042
	Nom.	0.0045
	Max.	0.0047
Resistance (Ohms Per 1000 ft at 20 ºC)	Min.	617.0
	Nom.	648.2
	Max.	681.9
Feet Per Pound		20600
Temperature Class		155 ºC
Insulation Type		Polyurethane Nylon-155

IPMC, have a layer of metal coating that tends to fall off, so most attaching methods are not feasible without damaging or destroying surface coating. In this design, four typical attaching methods have been proposed and the specialties have been listed in the following paragraphs. In order to enhance the performance of the IPMC robot, the best one should be chosen among these four attaching methods.

Figure 6.3 (a) shows a wire attached to a strip by soldering and (b) is the magnet wire. This is the most convenient and direct method because the wire is attached by the conductive solder. Solder can not only be a conductive medium to transmit current, but also attach tightly to fix wires. In addition, it is completely waterproof so it can be kept durable in deionized (DI) water. Chemical stability is another advantage of solder so it does not tend to be oxidized or rusted. Therefore, current can be transmitted from wires through solder to IPMC strips without much power loss. With high power transmission, solder is still attached to strips without falling off so this attaching method can make strips work in various environments such as in the water or air. With excellent conductivity and tight fixing, soldering can be seen as an appropriate method to attach wires to strips. Nevertheless, the high temperature during soldering might damage the surface of IPMC strips easily. The surface metallic layer will be damaged or fall off if the strip is burned by the soldering tool. Furthermore, there may be something non-conductive generating surrounding solder after soldering. This white substance is metallic oxides and degrades the conductivity extremely. Strips will be damaged if these oxides are removed physically, and both these non-conductive substances and metallic layers' falling off will degrade the performance significantly. Therefore, soldering is not

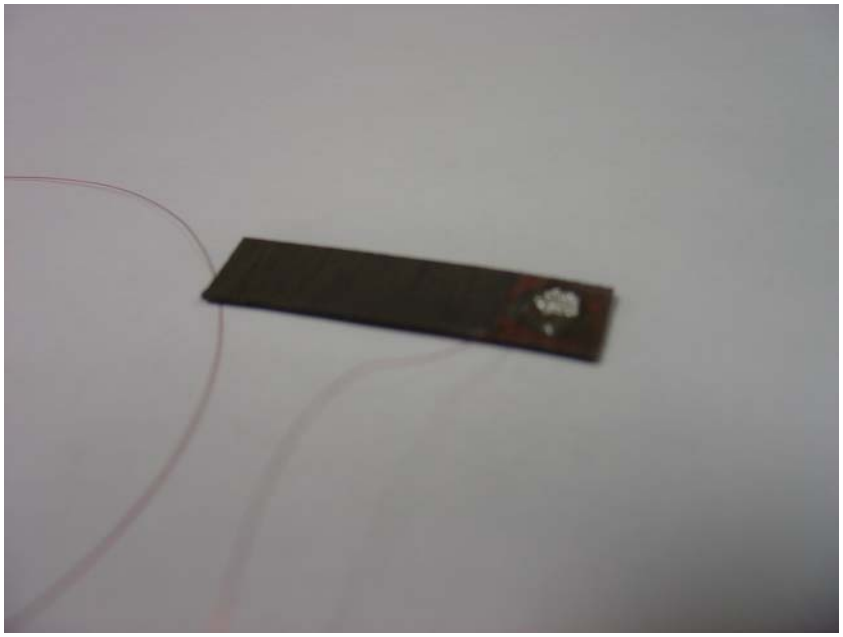

(a)

(b)

Fig. 6.3 (a) An IPMC strip transmitted current via (b) magnet wire with soldering tools

appropriate to this experiment although it has both physical and chemical stability. Fig. 6.3 (b) is the AWG 38 single Poly Nylon magnet wire used in this research.

The influence of oxidization should be taken into consideration due to the previous attaching method. Conductive glues, a good substitution for soldering, could be applied for their good conductivity, chemical stability, and practical convenience. The glue used in this research completely includes these three features. Figure 6.4 (a) shows that two wires were attached on each side of the strip by spreading the conductive epoxy (the right two bottles in Fig. 6.4 (b)) with transparency as joints to be fixed. This conductive epoxy is made by "Epoxies, Etc…" and consists of an original epoxy (the right one in Fig. 6.4 (b)), which is not conductive, and conductive silver powders (the middle one in Fig. 6.4 (b)). They must be mixed fully in 1:1 mix ratio before spreading out. With the epoxy for strong adherence and the silver powders for electrical conductivity, wires can be attached and fixed tightly to IPMC strips without destruction by high temperature or chemical reaction because the epoxy and silver powders are chemically stable and not reactive. Therefore, the high temperature caused by transmission of external power would damage neither IPMC strips nor glues anymore. In addition, this epoxy becomes hard after dried, so this is helpful to the physical stability of the entire structure of the robot. As for practical convenience, such as ordinary glues, the epoxy is needed to be spread out on IPMC surface after mixed. However, when using this epoxy, transparencies or shims should be used to press the epoxy in order to remove the internal gaps and bubbles because the internal flaws cannot transmit current but degrade the conductivity of epoxy. This epoxy seems to be perfectly appropriate for

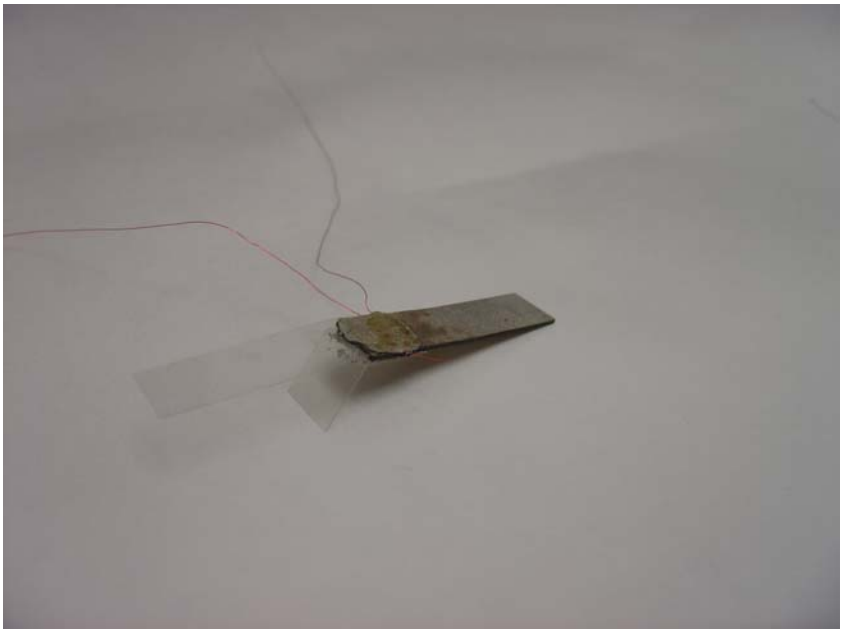

(a)

(b)

Fig. 6.4 (a) An IPMC strip with the magnet wire attached by (b) a conductive glue and an epoxy with conductive silver powders

wires attachment because of excellent conductivity, tight adherence, and chemical stability. Nevertheless, it becomes structurally damaged and non-conductive anymore after water penetrates when put in DI water. In addition, epoxy falls off easily when saturated with water. Same situation also happens to another electrically conductive glue (the left one in Fig. 6.4 (b)), which is made by Anders Products Corporation. It is much easier to be employed than the previous one because it is liquid and can be spread out for wires attaching and electrical conductivity. Besides, it needs much shorter time (around 10 minutes) to be dried than the epoxy (around 12 hours). Although this glue has better characteristics than the epoxy, a critical weakness still exists that both of them are not completely waterproof, so they cannot be used in an aquatic environment. Thus, this method is still inappropriate in the aquatic robotic application due to the weakness in the water.

In these two previous methods, the performance was degraded due to the surface metal problems caused by high temperature during soldering, and water saturation. A conductive connector, made of the core of wires, was used as a medium between wires and IPMC strips. The solder was substituted with this connector in this method. As a nice medium, this connector must be attached tightly to both surfaces and wires. The connector was bent for the wires wrapping on and fixed on strips. By going through the hole on strips, the connector could be fixed like a staple, so wires could be touched tightly by wrapping and current could be transmitted to strips. As long as the connector was well fixed, current higher than 1 A could be transmitted without high impedance (the equivalent resistance was around 3 Ω). No high temperature or chemical processes

existed in this method so it was both physically and chemically stable to provide with external power via this kind of connectors. In addition, to prevent wires from being breaking, they were covered with thin and soft membranes which would neither confine nor limit the motion of both wires and IPMC strips. Wire breaking usually happened by periodic bending due to fatigue, so there must be a soft cover on the places where bending motion usually happened, such as the place close to connectors. Figure 6.5 (a) shows an sample by using two connectors on an IPMC strip with wires wrapping. Two connectors were on different sides. It was conspicuous that the wires were covered with a layer of membrane and glue close to the connectors from broken. Figure 6.5 (b) is the connector, made of the core of wires, and it is conductive and soft for the convenience to transmit current and be mounted in various applications. This connector was fixed to a strip without using any glue or tool, so short-circuit between both surfaces should be prevented when connectors were mounted. In addition, the connector became loose very easily after repetitive bending because the connector was too small to be fixed tightly. Furthermore, in order to fix wires and strips with connectors, two holes were drilled on each strip for two connectors. Nevertheless, the physical characteristics, such as stiffness, might change due to these two holes. Also, the breaks or cracks might happen along the holes during drilling the holes. The former would affect both the output force and deflection. The latter would degrade or damage the entire strip. Therefore, this option is still not appropriate for attaching wires to IPMC strips although it does not cause any chemical reaction.

According to the previous methods to provide power by connecting wires to

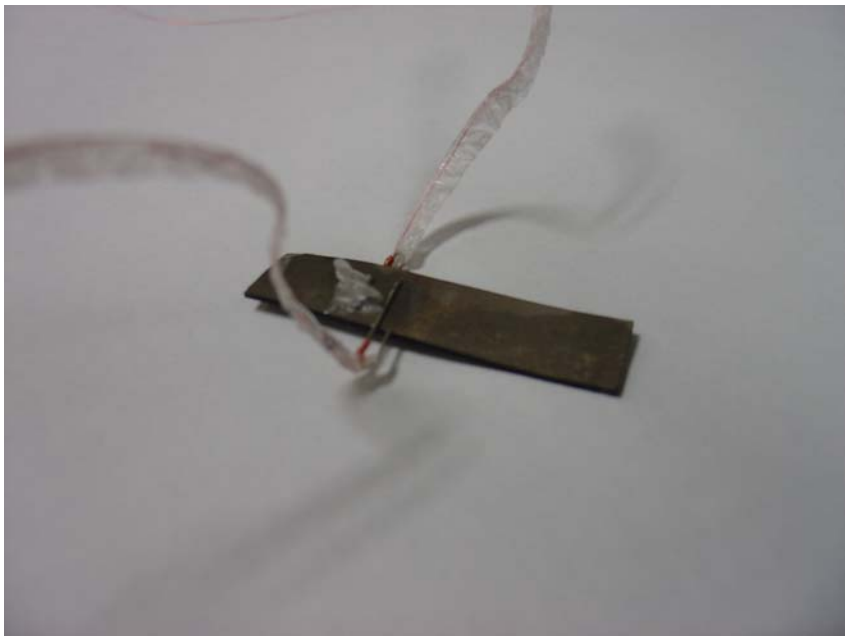

(a)

(b)

Fig. 6.5 (a) An IPMC strip with wire connection via (b) a specific connector to transmit power

IPMC strips, there should be electrically conductive metallic media, such as electrodes or connectors, which are tightly fixed with wires' connection in order to transmit current with low resistance from large power loss. In addition, it would be better if the media are chemically stable without any reaction in operation to prevent the change of characteristics. The media used in the previous cases were solder, conductive glues, and metallic connectors, respectively. However, each of them has its specific problem. For example, solder caused the existence of a non-conductive substance; the conductive glue was not fully waterproof; the metallic connectors were difficult to be fixed to IPMC strips continuously after repetitive operation. Therefore, in the last method, a metallic electrode was used for not only its large area touching IPMC strips, but both the physical and chemical stability. As the devices for testing, metallic electrodes will be used as the media to transmit current with the least power loss among the previous all methods and keep all strips stable in operation.

Figure 6.6 (a) shows two wires were connected with a strip via two copper electrodes on both sides as the media. Wires were attached to electrodes by soldering and then covered with waterproof gel, so they could be connected and fixed tightly. Electrodes were fixed to IPMC strips with shims, which could not only fix electrodes but connect two strips as a joint to work as a 2-DOF leg in this design. Copper electrodes were fixed tightly to shims with super glue. Figure 6.6 (b) shows some copper electrodes and a connector with wire attachment. Via a large area to transmit current with electrodes, IPMC strips showed better performance with less power loss. Therefore, this attaching method is much more appropriate than the previous three because of not only

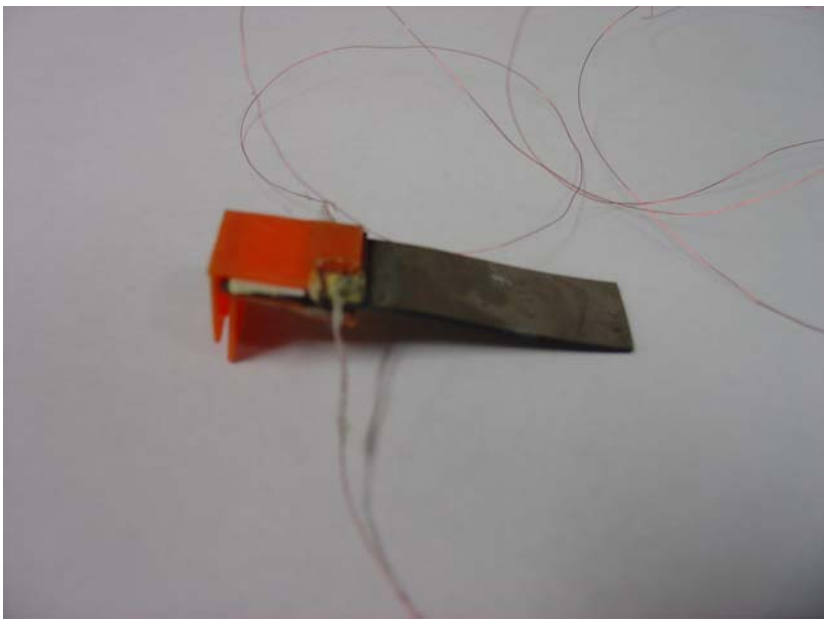

(a)

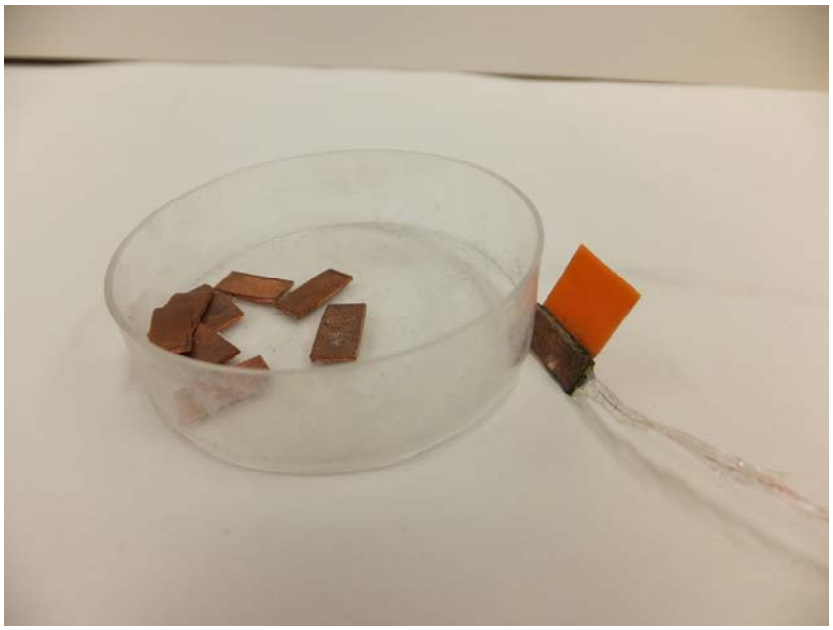

(b)

Fig. 6.6 (a) An IPMC strip with (b) a copper electrode for uniform power transmission via a magnet wire

its better attaching performance but both physical and chemical stability. This waterproof method without chemical reaction occurring presented an excellent current transmission to IPMC strips. TABLE 6.3 describes the characteristics and makes a comparison among these four wire-attaching methods.

TABLE 6.3 Comparison among four typical attaching methods

	Soldering	Conductive Epoxy	Connector	Copper Electrode
Resistance (Ω, between power and strips)	2	6	4	2
Weight (g)	1	1	0.95	1.5
Benefits	Waterproof and exhibits a tight connection	Easily-used and no damage to IPMC strips	Waterproof and no damage to IPMC strips	Waterproof with a large area for power transmission
Weakness	Non-conductive substance exists	Epoxy is not waterproof	Connectors tend to be loose	Electrodes are heavy

However, sometimes there were still small gaps between IPMC strips and electrodes due to technical problem or the softness of shims. After spreading out glue on shims, if two shims are not held sufficiently tightly, the small gaps will still exist and the performance of transmission and IPMC deflection will be degraded due to the high impedance caused by the gaps. Thus, it would be better to remove all gaps thoroughly in order to keep high power transmission and deflection performance. On the other hand, the shims were not completely hard so it might be deformed by external force. This deformation would destroy the connection between IPMC strips and electrodes. Fortunately, the IPMC strips in this experiment had no sufficiently large force to deform the shims. Moreover, the IPMC strips will be much heavier than the strips in the previous three attaching methods due to large copper electrodes. Thin (around 7 mil in thickness) IPMC strips cannot work with electrodes' loading due to insufficient force it generates. The strips in this experiment can generate sufficient force so the electrodes do not cause a problem to thick IPMC strips (40 mil in thickness). After taking the characteristics of all attaching methods, such as working duration, weight, and availability in the working environment, the last attaching method was selected as the design to provide with external voltage although it increases the weight of the entire robot greatly.

After choosing the attaching method, the structure of a 2-DOF leg was designed and shown in Fig. 6.7. All IPMC strips were cut into 40 mm × 10 mm × 1 mm. Two copper electrodes in 10 mm × 5 mm × 1 mm, attached to the strip and shims were used to provide the power via the entire area. Moreover, both the outer and the inner shims,

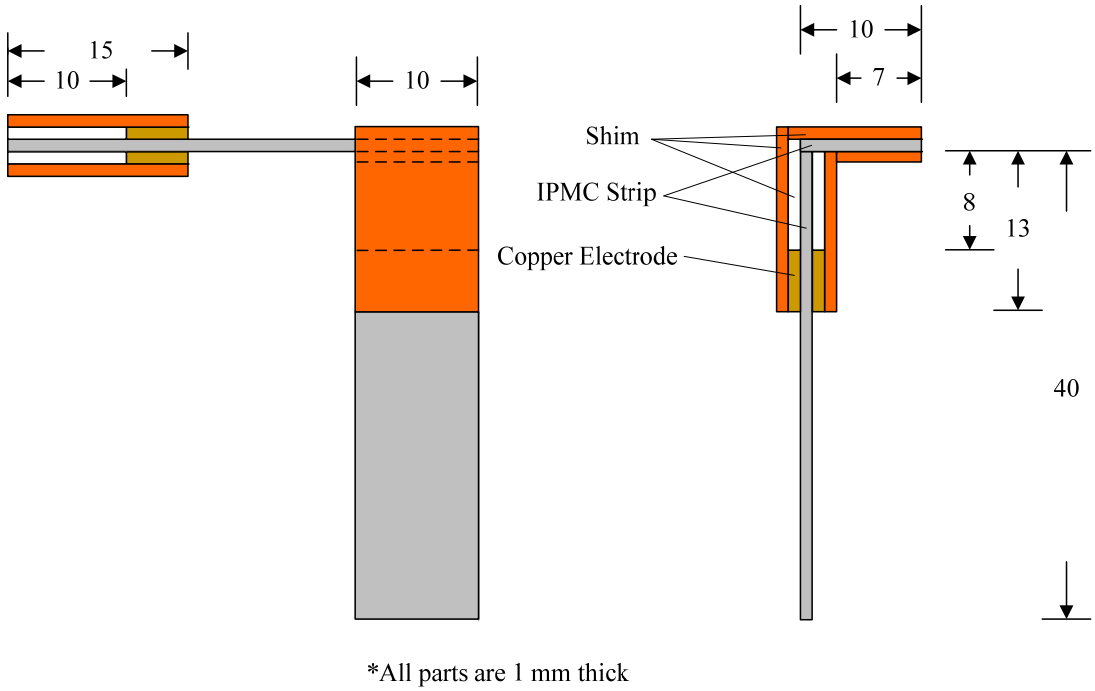

Fig. 6.7 Design of a 2-DOF leg

which were orange and white, respectively, were used to remove the gap caused by the copper electrodes, and connect two IPMC strips as a 2-DOF leg. Two layers of shims shown in Fig. 6.7 not only enhanced the stiffness of the joint but also attached everything more steadily. With tight attaching, two strips could be fixed and connected to each other, and bend toward different directions. To enhance the performance, the electrodes, shims, and strips must be attached and fixed tightly without any gap to prevent DI water's penetration, which would destroy the conductivity between the strips and the electrodes. DI water has high internal resistance (around 18.2 MΩ/cm) so it can easily degrade the performance by increasing the impedance. The resistance would be increased from 1 Ω to more than 2000 Ω although there was just a small gap which was

much less than 1 mm in distance. The performance would be degraded due to more than thousand times as high as the original resistance. As long as a tiny gap exists, the bending motion will be degraded significantly due to infiltrating DI water although the surface of IPMC strip is fully conductive. In addition, the internal current, which is seen as a virtual force and mentioned in Chapter V, decreased down to around 5 mA when the gap was filled with DI water. Therefore, it follows that the output deflection was too small to be seen.

Figure 6.8 shows the final design and the implementation of the IPMC robot, and it consists of six 2-DOF legs and a body. The width is 80 mm and the distance between two adjacent legs is 44 mm to prevent from interference because the maximum

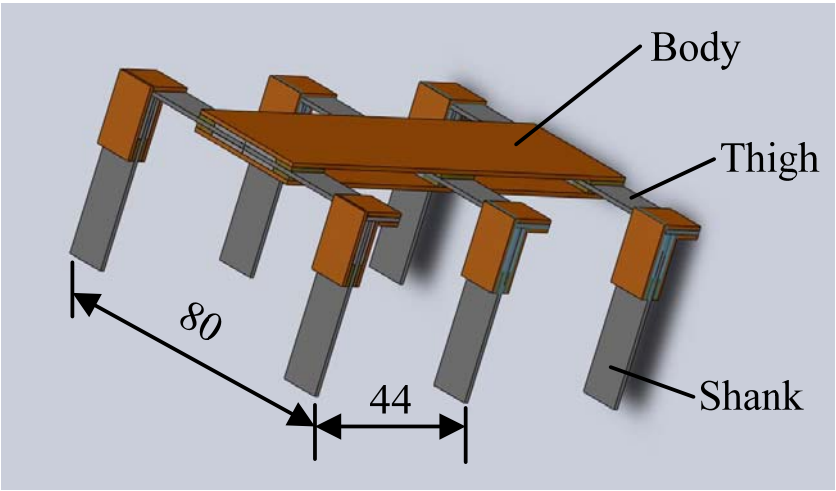

(a)

Fig. 6.8 (a) Final design of the IPMC aquatic walking robot in a fish tank (b) the implementation of the IPMC aquatic walking robot in a fish tank

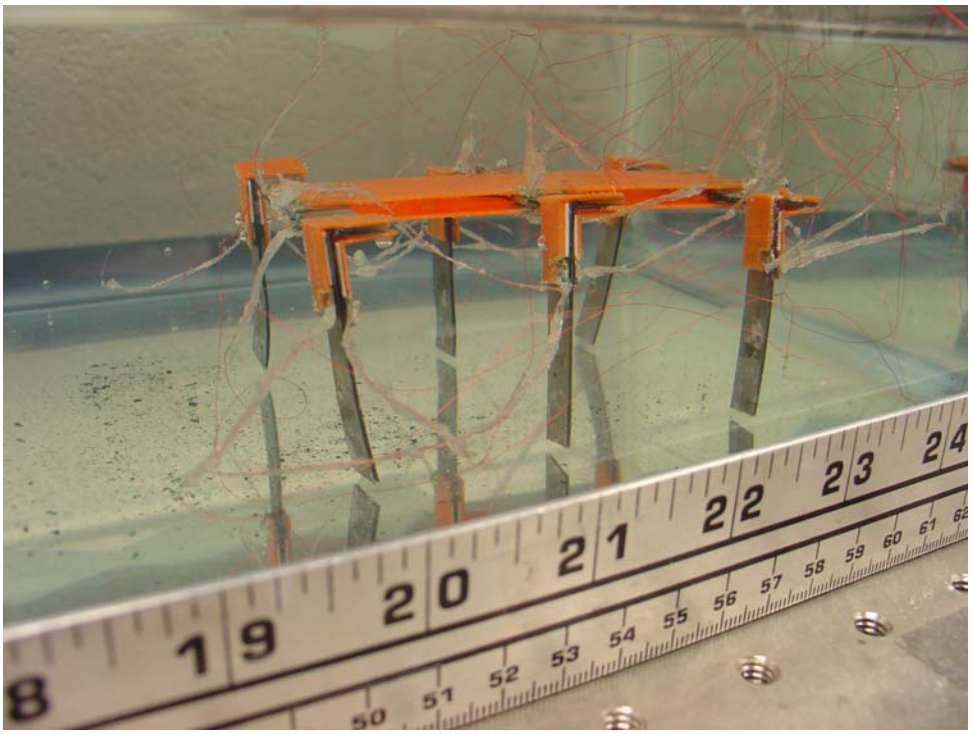

(b)

Fig. 6.8 continued.

deflection in water is less than 20 mm according to the test in Chapter IV. In addition, this distance is related to the walking procedure to be discussed in Section 6.3. According to this walking procedure, it would be more appropriate to walk in six legs instead of four or eight legs. Finally, in order to prevent body deformation, two layers of shims were mounted as the main body to enhance the stiffness, and this is why shims must be sufficiently thick for stiffness. The length of each IPMC strip should be the same, and it should be assured that all shanks must touch the ground.

6.2 Power Electronics Design

Instead of conventional 200-μm-thick IPMC strips, those used in this research required around 600 mA to be operated. The instant maximum current, around 1.5 A, occurred when the voltage changed abruptly in square waves. In order to provide high current, a voltage follower and amplifier was implemented as shown in Fig. 6.9 with an NPN (D44H8, manufactured by Fairchild Semiconductor, for Q_1 and Q_3) and a PNP (D45H8, manufactured by Fairchild Semiconductor, for Q_2) bipolar junction transistors (BJTs) [89, 90]. This circuit amplifies the current but maintains the voltage gain to be one and provides sufficiently high current by $+V_{cc}$ and $-V_{cc}$ depending on V_{in}. In addition, the upper limitation of current of these two BJTs is around 3 A, so the

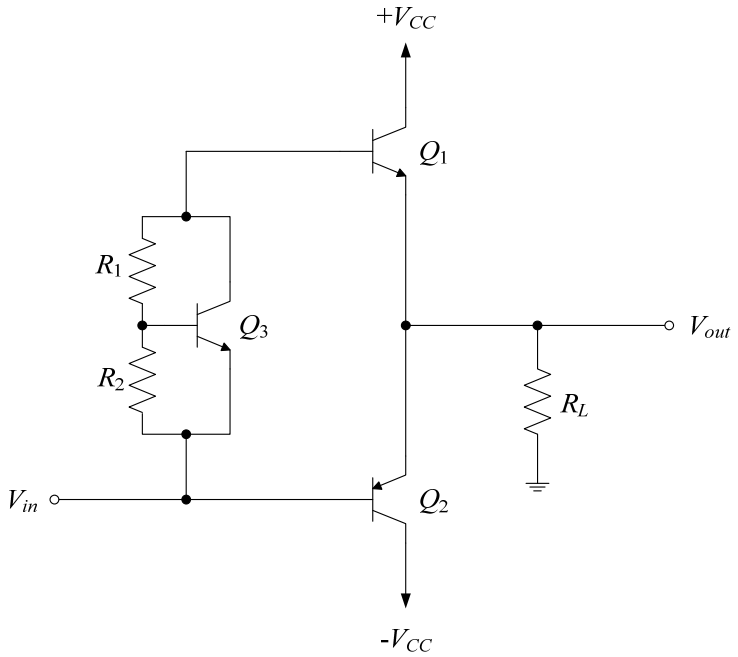

Fig. 6.9 Power-amplifier circuit

temperature increasing in each BJT did not influence the operation. Twelve of these amplifier circuits drive twelve IPMC strips individually. In Fig. 6.9, R_1 = 4.7 kΩ, R_2 = 1 kΩ, and R_L is the resistance of an IPMC strip, around 300 Ω.

6.3 Walking Procedure Design

The fundamental concept of walking locomotion is to move with at least three legs in order to keep the balance and enhance the stability in operation. Figure 6.10 illustrates this walking procedure for the IPMC robot. Taking a stride of walking motion as an example, the solid lines represent the current state, and the dashed lines, the next state, which indicates the movement of the body by Legs 1, 3, and 5. In other words, the dashed lines mean that the body moves but Legs 1, 3, and 5 still touch the original three points without movement. A solid circle and a dashed circle shown in this figure are the center of mass (CM) of the body at different moment. In order to keep the robot stable in

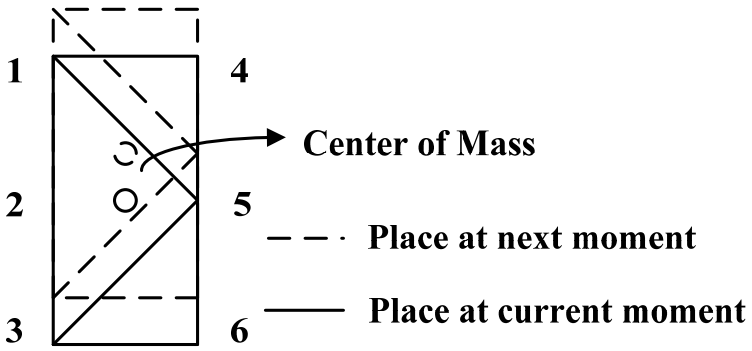

Fig. 6.10 Fundamental concept of walking procedure for IPMC robot

operation, the dashed CM should be located in the area of the solid triangle made by Legs 1, 3, and 5. The same situation happens when the robot is walking with the other three legs. In this way, the distance of each stride should be designed and limited according to the maximum output deflection of an IPMC strip. In addition, the triangle should be sufficiently large for the movement of CM. In this design, the robot reached the maximal stride and the fastest speed.

In this research, two options of walking procedures will be discussed. According to the illustration in Fig. 6.11, the IPMC robot walks by each three legs touching on the same plane to keep the balance. In Fig. 6.11, a typical walking procedure is illustrated in detail and the main concept comes from the stable triangle made by three legs. In Fig. 6.11 (a), a stable robot stood with all six legs. In Fig. 6.11 (b), Legs 1, 3, and 5 lifted up for the preparation for making a stride. Legs 2, 4, and 6, however, did not move at all to keep the body stable. Then, the shanks of Legs 1, 3, and 5 bent forward as shown in Fig. 6.11 (c). At the same time, the shanks of Legs 2, 4, and 6 bent backward to move the body. This stride could reach 10 mm according to the output deflection in Chapter IV. After starting to make a stride, the next step was to change the supporting points from Legs 2, 4, and 6 to Legs 1, 3, and 5. This progress, shown in Fig. 6.11 (d), consisted of two motions. The first one is to let Legs 1, 3, and 5 touch the ground, and second one is to lift up Legs 2, 4, and 6 for the next stride. In order to move the body, the shanks of Legs 1, 3, and 5 bent backward like Legs 2, 4, and 6 in Fig. 6.11 (c). In addition, the shanks of Legs 2, 4, and 6 bent forward to make another step as shown in Fig. 6.11 (e). In the last figure, Fig. 6.11 (f), Legs 1, 3, and 5, and Legs 2, 4, and 6 lifted up and bent

downward, respectively, to complete a full cycle. By repetitive and mutually cooperative motion of each strip, the robot walked steadily without rail or track. In addition, this robot was not confined by. Thus, an IPMC robot walked in an aquatic environment by using six 2-DOF legs with their collaboration. The simulated signals came from the Simulink® block diagram shown in Fig. 6.12, and Fig. 6.13 shows the corresponding

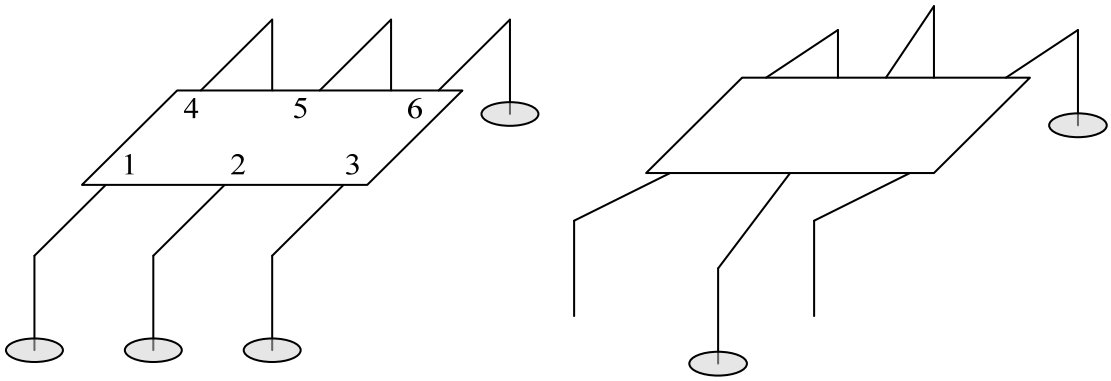

(a) (b)

Fig. 6.11 Locomotion of the IPMC robot in the first procedure. The legs with the shaded ovals touch the floor. (a) Initial state, (b) the thighs of Legs 1, 3, and 5 lifted up, and the thighs of Legs 2, 4, and 6 bent downward, (c) the shanks of Legs 1, 3, and 5 bent forward, and the shanks of Legs 2, 4, and 6 bent backward to move the body forward, (d) the thighs of Legs 1, 3, and 5 bent downward to take over the supporting points right after the thighs of Legs, 2, 4, and 6 lifted up, (e) the shanks of Legs 1, 3, and 5 bent backward to move the body forward and the shanks of Legs 2, 4, and 6 bent forward, (f) the thighs of Legs 1, 3, and 5 bent downward to take over the supporting points right after the thighs of Legs 2, 4, and 6 lifted up

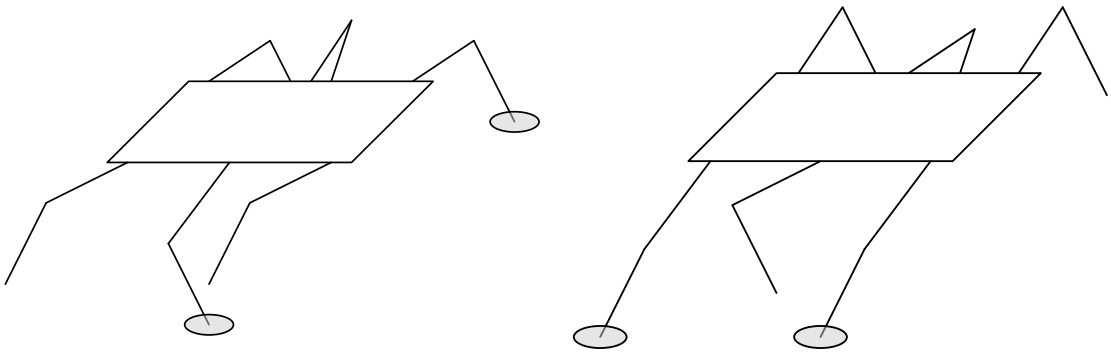

(c) (d)

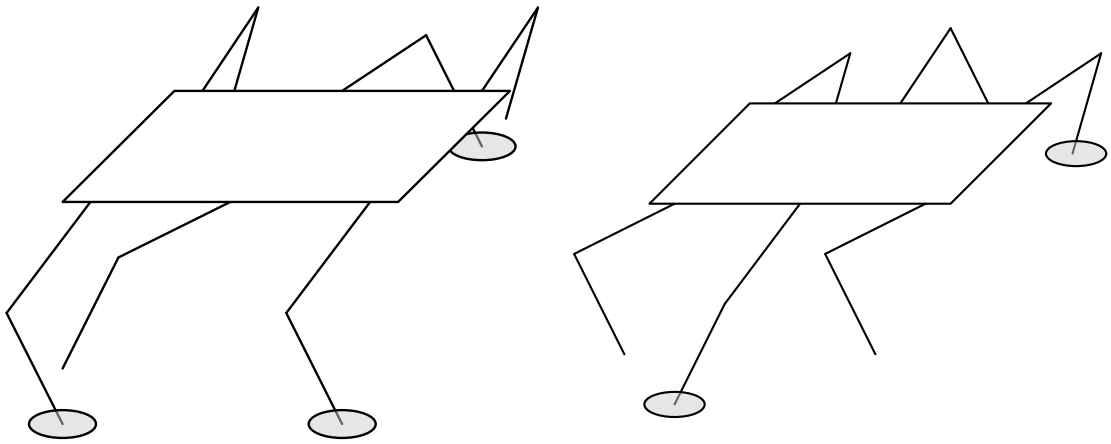

(e) (f)

Fig. 6.11 continued.

input signals in each state for this IPMC robot.

In Figs. 6.13 and 6.16, LU (Left Upper), RU (Right Upper), LL (Left Lower), and RL (Right Lower) mean the thighs of Legs 1, 3, and 5, the thighs of Legs 2, 4, and 6, the shanks of Legs 1, 3, and 5, and the shanks of Legs 2, 4, and 6, respectively. In this walking procedure, two triangles, made of each three legs, keep the balance by touching

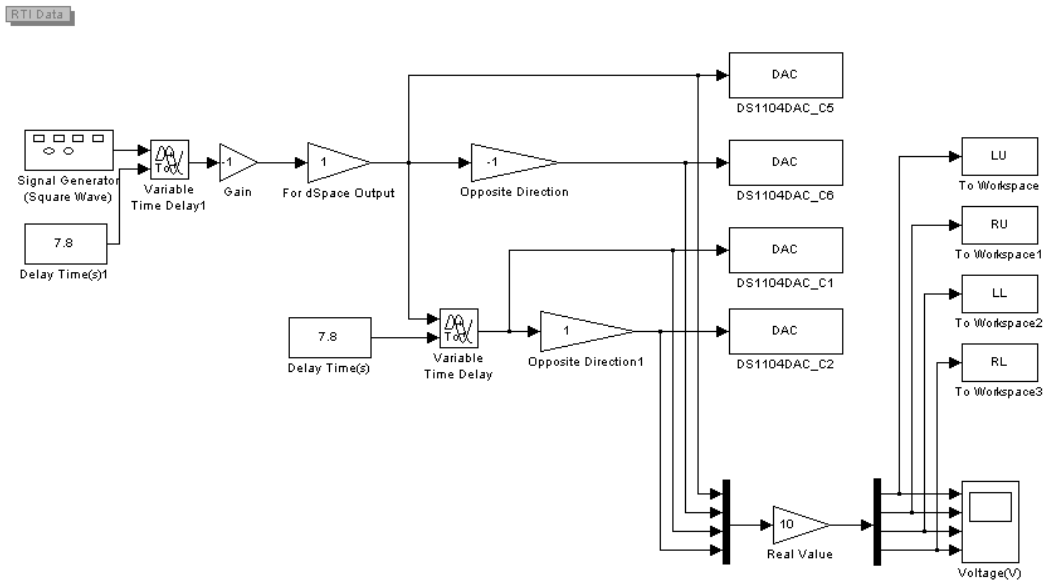

Fig. 6.12 Block diagram of the input signals for the first procedure

the ground. Theoretically, the robot could keep moving steadily for the two symmetric triangles in both sizes and shapes. Nevertheless, a discontinuous motion, existed between Fig. 6.11 (c) and Fig. 6.11 (d), might destroy the smoothness of the entire walking progress. When Legs 1, 3, and 5 lifted up and Legs 2, 4, and 6 bent down to take over the plane, it might cause unstable oscillation due to not exactly same plane where the two triangles were located. This phenomenon might not only affect the stability of the robot in operation but degrade the smooth of walking locomotion. In order to exchange the supporting points more smoothly, the other walking procedure has been proposed in Fig. 6.14. The walking procedure illustrated in Fig. 6.14 used similar concept and method to move the body. Figure 6.14 (a) shows the initial status. In Fig. 6.14 (b), like the previous procedure, Legs 1, 3, and 5 lifted up, and then the shanks of

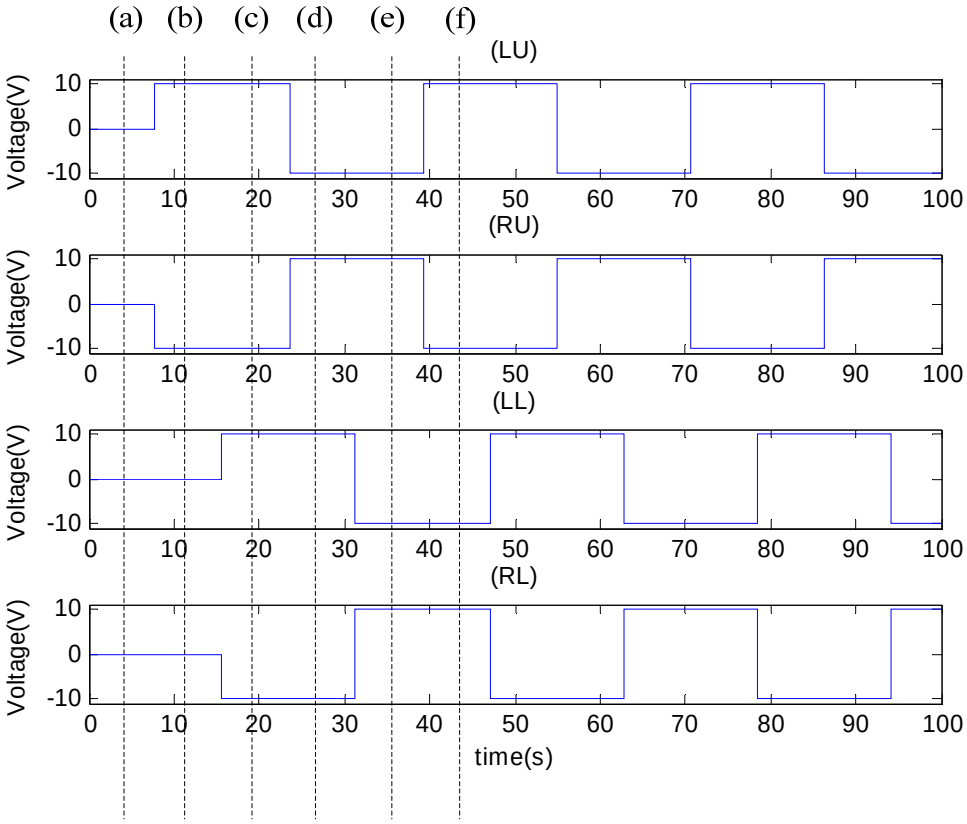

Fig. 6.13 Input signals corresponding to each state in Fig. 6.11

them bent forward as shown in Fig. 6.14 (c). Then, Legs 1, 3, and 5 bent downward with keeping the shanks bending forward to make a stride. However, Legs 2, 4, and 6 had not worked at all yet to keep the balance as shown in Fig. 6.14 (d). At this moment, all legs touched the ground. In Fig. 6.14 (e), Legs 2, 4, and 6 lifted up after Legs 1, 3, and 5 touched the ground smoothly as supporting points. In Fig. 6.14 (f), the shanks of Legs 1, 3, and 5, and Legs 2, 4, and 6 bent forward and backward, respectively, in order to move the body forward. Then, with keeping Legs 1, 3, and 5 stopped, Legs 2, 4, and 6 bent downward to make all six legs to be supporting points on the ground simultaneously as

shown in Fig. 6.14 (g). At this moment, all six legs touched the ground together again for the steady walking motion. Finally, Legs 1, 3, and 5 lifted up and then Legs 2, 4, and 6

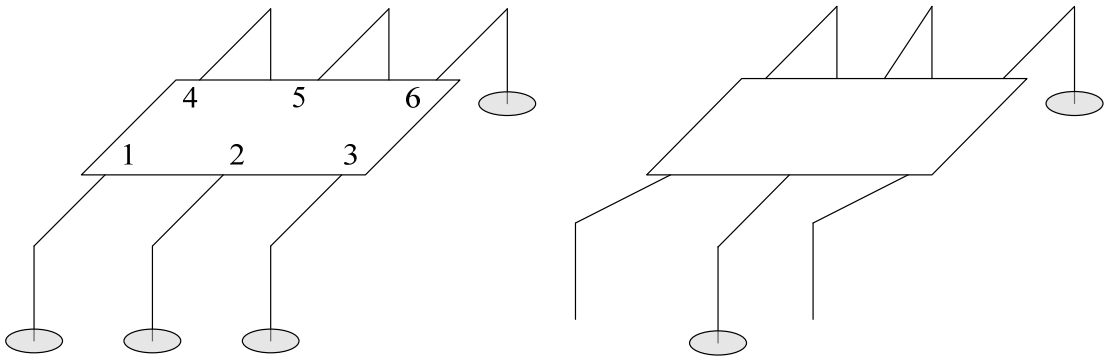

(a) (b)

Fig. 6.14 Locomotion of the IPMC robot in the second procedure. The legs with the shaded ovals touch the floor. (a) Initial state, (b) the thighs of Legs 1, 3, and 5 lifted up, (c) the shanks of Legs 1, 3, and 5 bent forward, (d) the thighs of Legs 1, 3, and 5 bent downward to touch the ground with Legs 2, 4, and 6. At this time, all legs touched the ground to keep the balance and prevent from the discontinuity happening in Procedure 1. Legs 2, 4, and 6 had not bent at all by this state. (e) The shanks of Legs 1, 3, and 5 bent backward to move the body forward and the thighs of Legs 2, 4, and 6 lifted up, (f) the shanks of Legs 1, 3, and 5 kept bending and the shanks of Legs 2, 4, and 6 bent forward, (g) Legs 1, 3, and 5 did not change and the thighs of Legs 2, 4, and 6 bent downward to touch the ground. At this time, all legs touched the ground again. (h) The thighs of Legs 1, 3, and 5 lifted up and the shanks of Legs 2, 4, and 6 bent backward.

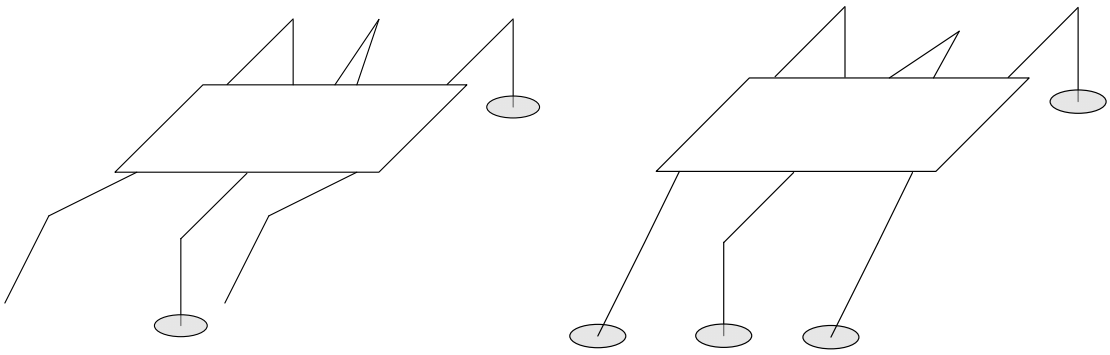

(c) (d)

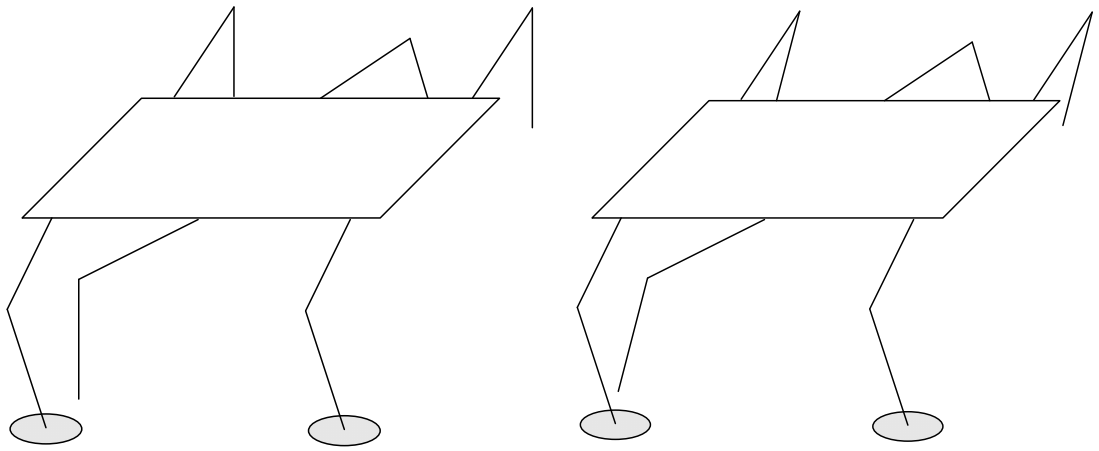

(e) (f)

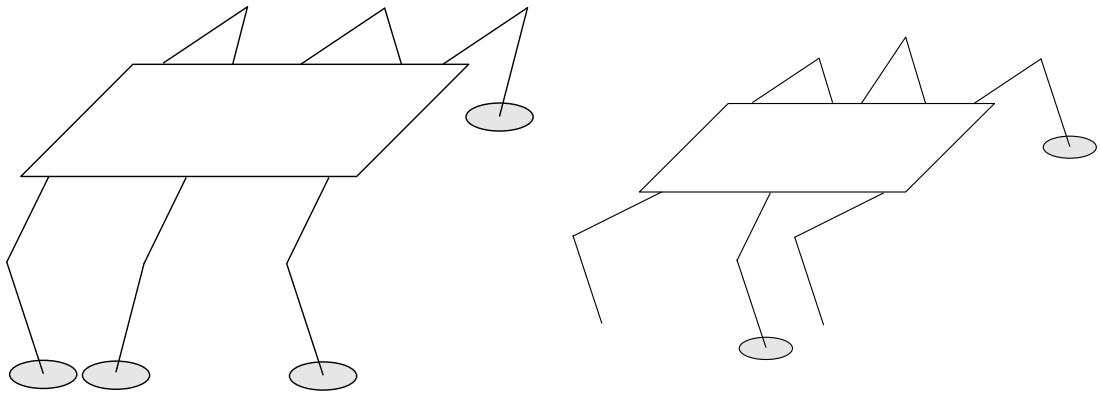

(g) (h)

Fig. 6.14 continued.

moved the body forward as shown in Fig. 6.14 (h). The disadvantage in the previous procedure was solved by using all six legs to transfer supporting points, so the discontinuity was eliminated theoretically. In this way, the robot could walk more smoothly and exhibit continuous walking motion. Figure 6.15 is the block diagram of the simulated input signals for this walking procedure. Figure 6.16 shows the input signals for four sets of legs corresponding to each moment in Fig. 6.14. Four independent signal sources were used to offer for four sets of legs in different phases. Figure 6.17 is the graphic user interface (GUI). Users can not only get the real-time information but also change the internal parameters because of the RTI function in order to meet a fully bidirectional communication between the users and the system.

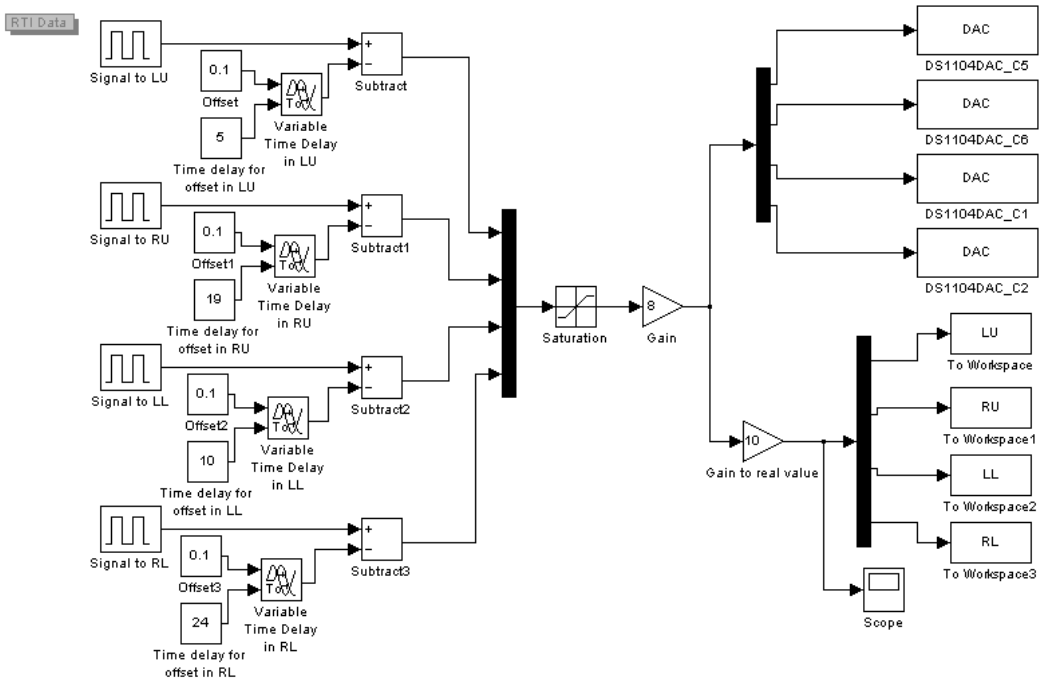

Fig. 6.15 Block diagram of the input signals for the second procedure

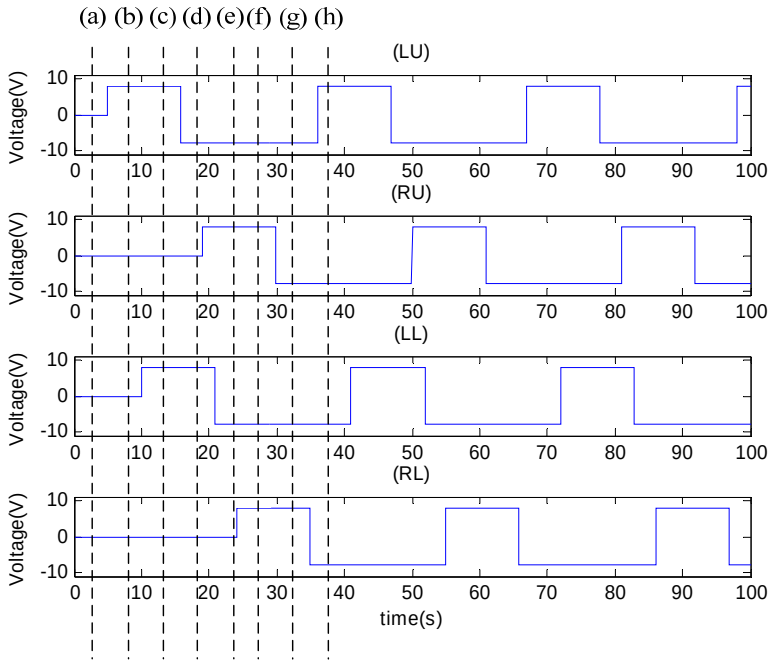

Fig. 6.16 Input signals corresponding to each state in Fig. 6.14

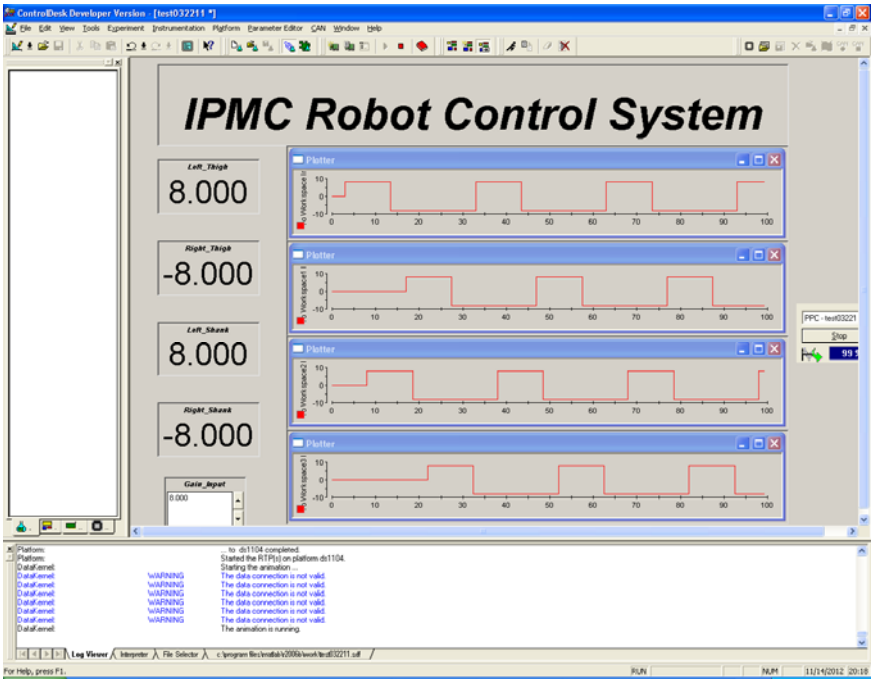

Fig. 6.17 Graphic user interface with ControlDesk

6.4 Walking Testing Results

According to the fundamental testing of the IPMC properties in Chapter IV, the working environment and input signal have been decided, and then an aquatic robot was constructed and implemented as shown in Fig. 6.8. It was as light as 39 g with the dimension of 102 mm × 80 mm × 43 mm. The previous two walking procedures were employed in the testing and results are shown in Figs. 6.18–6.19 in sequential figures. This robot did not exhibit conspicuous motion in each state due to slow and small deflection of IPMC strips, so two similar walking motion occurred by both of the two procedures. However, an apparent discontinuity existed between Figs. 6.18 (c) and 6.18 (d), and that degraded the stability of the robot. In Fig. 6.19, this discontinuity decreased significantly for the smooth and continuous input signals. Although the discontinuity was not eliminated completely, the robot demonstrated steady walking motion and the average speed in water could reach up to 0.5 mm/s with 0.2-rad/s square-wave driving signal, which could cause larger deflection than step input by abrupt change between wave crests and troughs. The robot walked smoothly and steadily because each of the three legs works as a tripod for the stability as illustrated in Fig. 6.14. A short discontinuity as mentioned above happened when supporting points were changed. In addition, the aquatic environment and the friction between the ground and the IPMC strips also affected the performance of the IPMC robot. For example, the speed would change if water is flowing or other surfaces instead of glass are used as the ground. Each IPMC strip exhibited non-identical deflection due to various surface conditions, such as conductivities and shapes. In this research, however, all strips were selected according to

the deflection testing in order to let all legs could make almost the same stride at the same speed. The bubbles caused by water electrolysis were generated continuously in operation but did not affect the robot's locomotion significantly. Besides, the effect of wires could be ignored due to the sufficient force generated by the fabricated thick IPMC strips.

This robot contains 12 pieces of IPMC strips, and each of them needs around 600 mA on average, when provided with 8-V square waves as the input signals. The average power consumption is around 4 W per strip. In addition, our robot costs only around $300 for the platinum powders and Nafion®. For one robot, around 1 g of platinum powder was used as the surface electrodes.

Figures 6.18–6.19 illustrate the locomotion of the IPMC robot in each state by employing both procedures, respectively. In actual testing, not all IPMC strips exhibited conspicuous deflection as anticipated as shown in Figs 6.11 and 6.14 because water might infiltrate into the gap between IPMC strips and copper electrodes. However, the robot in both figures exhibited smooth locomotion except for the discontinuity in the first procedure. This disadvantage caused not only the oscillation but also backward movement. It might not be conspicuously shown in Fig. 6.18 due to the thickness of IPMC strips. In Fig. 6.19, the second procedure was employed in order to degrade this phenomenon by providing four individual input signals for each set of legs with specific time delay. The discontinuity has been degraded significantly instead of being eliminated completely due to non-perfectly rapid reaction. The walking performance has been enhanced significantly for the more smooth and continuous locomotion.

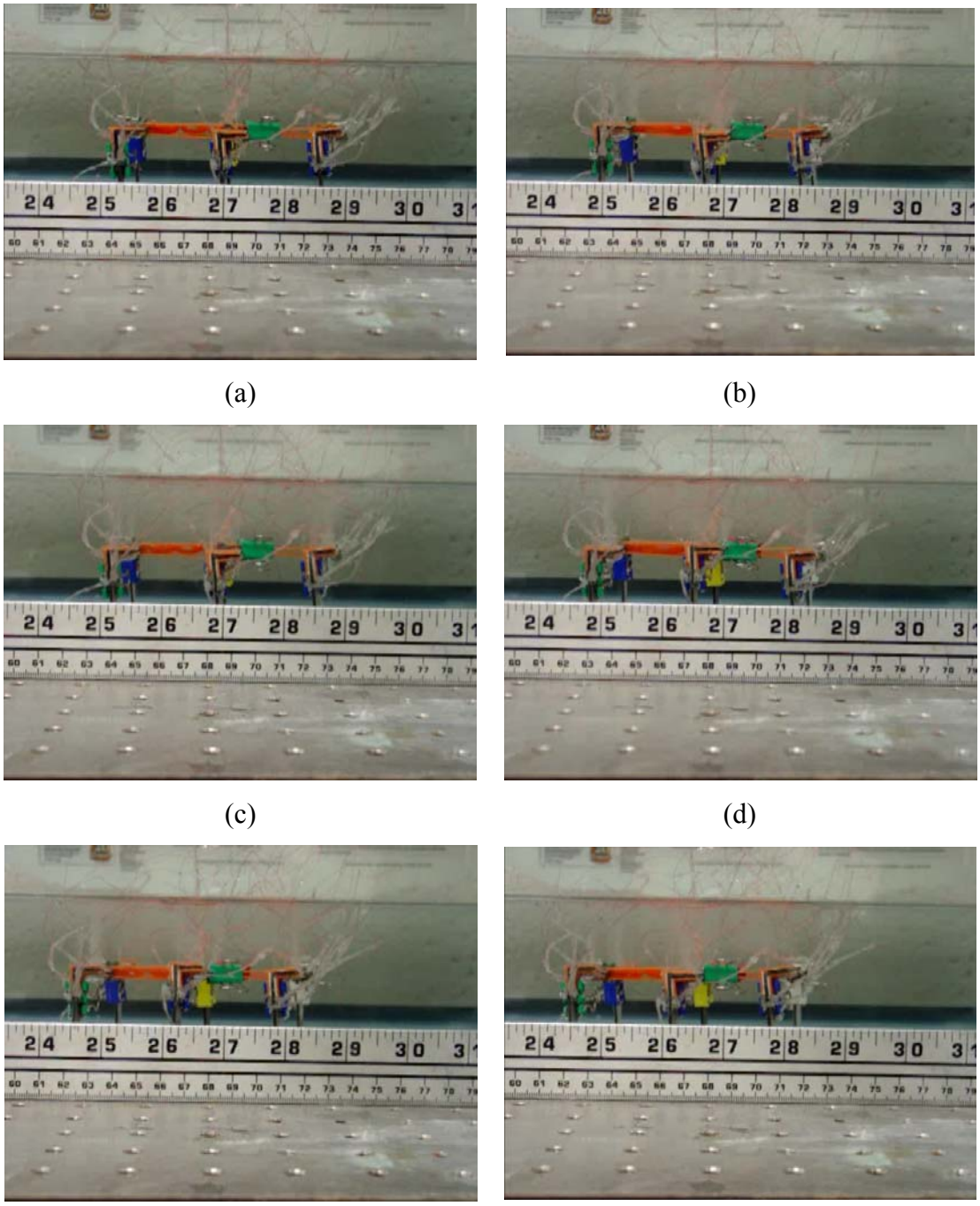

(a) (b)

(c) (d)

(e) (f)

Fig. 6.18 Practical aquatic walking testing in sequential pictures by applying the first procedure

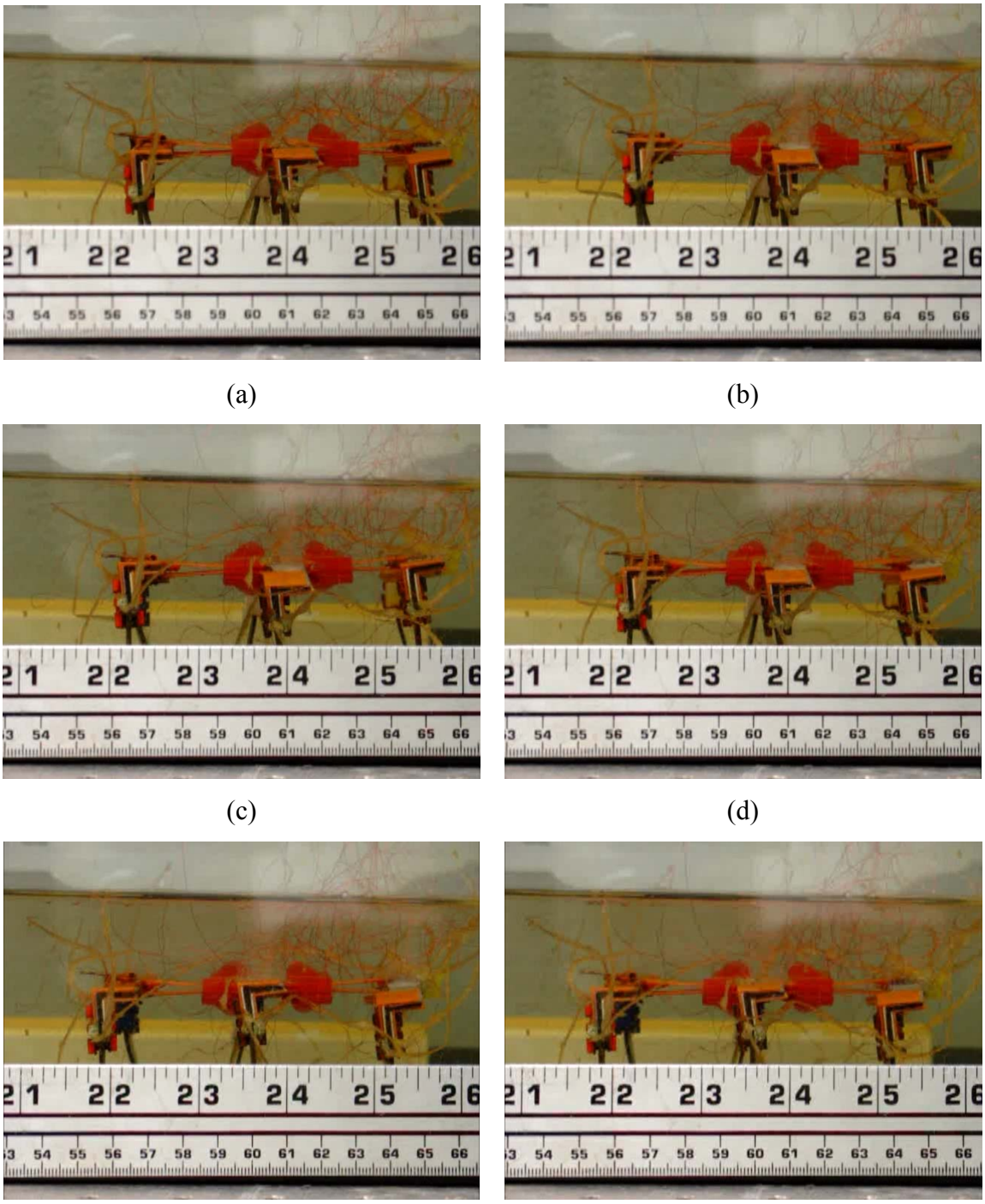

(a) (b)

(c) (d)

(e) (f)

Fig. 6.19 Practical aquatic walking testing in sequential pictures by applying

The second procedure

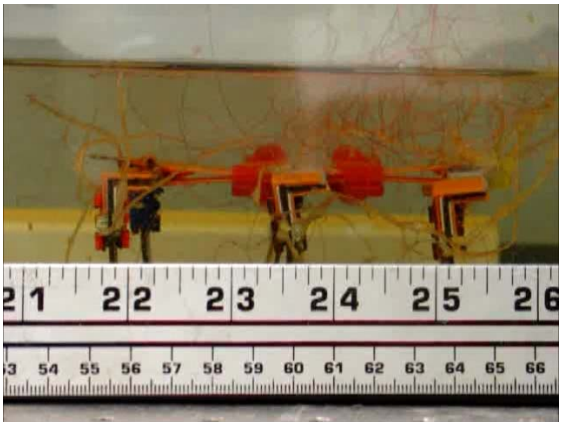

(g)

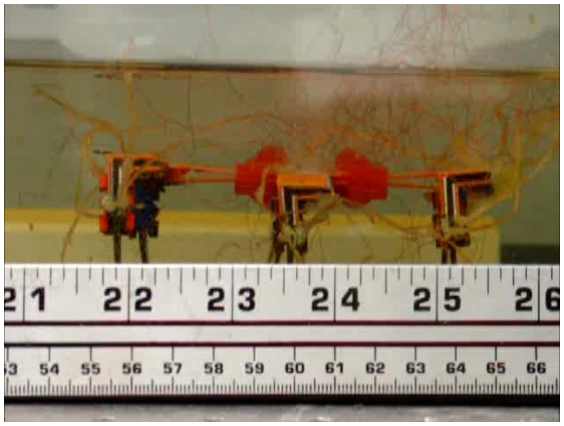

(h)

Fig. 6.19 continued.

CHAPTER VII

CONCLUSIONS

AND FUTURE WORK

The IPMC-based aquatic robot, including material fabrication, structure design methodology, implementation, and practical operation was described and explained in the previous chapters. The current performance, such as the speed, duration, power consumption has much room for improvement by further discussion and research. For example, a well-designed leg with thickly-plated IPMC strips might exhibit both better arc-like bending and stronger output force simultaneously. Sufficient force and fast movement are the decisive factors of insectile robots in various applications. Except for the limitations due to the characteristics of IPMC, performance could be improved by various better designs and fabrication processes.

7.1 Conclusions

An aquatic walking robot has been designed and implemented in this research. Based on various experiments and tests, such as the effects of surface water concentration and aquatic environment, IPMC strips and their design methodologies for this robot were developed. Nafion® is the basis membrane of IPMC, so where and how water molecules move is the key aspect of deflection. The fabricated IPMC strips were 1-mm thick in order to sustain and drive the body. These thick IPMC strips could not

bend without relatively high driving current, so a power amplifier circuit was designed for each strip to provide required current. This circuit consists of a voltage follower and a current amplifier which can generate the current in need and maintain a unity voltage gain.

This IPMC robot has six 2-DOF legs in order to imitate a real-life insect closely. For this robot, a supporter and a driver are combined into a 2-DOF leg, which consists of a thigh and a shank, in order to replace conventional 1-DOF legs. The twelve IPMC strips were grouped into four sets, and their motions were choreographed for smooth locomotion. Each set of three shanks simultaneously touching on the ground in a tripod-fashion can keep the balance and stability. In addition, all 2-DOF legs can make a stride independently instead of two sets of 1-DOF legs. The driving signals provide the power for the four sets of IPMC strips, the thighs and the shanks of each set of the three legs. With these driving signals, all legs of this robot can make a stride to walk in water and keep the stability at the same time.

Finally, this IPMC walking robot with a microcontroller, power circuits, and sensors can operate stand-alone instead of being tethered to a personal computer. In addition, robots may have more precise and steady performance with better-designed controllers [91]. Therefore, an IPMC-based robot can be used in seabed engineering and exploration because water pressure causes nothing to the deflection of IPMC. In addition, IPMC robots would be better than other underwater robots because of the availability in various shapes and sizes for specific applications and environments.

7.2 Future Work

IPMC robots could work better significantly by other methodologies such as the following ways.

(1) IPMC fabrication improvement. According to Chapter II, the performance, including the bending deflection and output force, is relevant to the thickness and the surface metallic electrode coating. The Nafion® membrane was roughened with sandpapers to enlarge the distribution area for metallic electrodes plating. Therefore, performance of IPMC can be improved by a larger coating surface area. In addition, the thickness of the entire strip could vary instead of keeping constant in order to provide sufficient force and deflection. Figure 7.1 proposes two examples of an IPMC strip shank with varying thickness or designs. The thickness close to

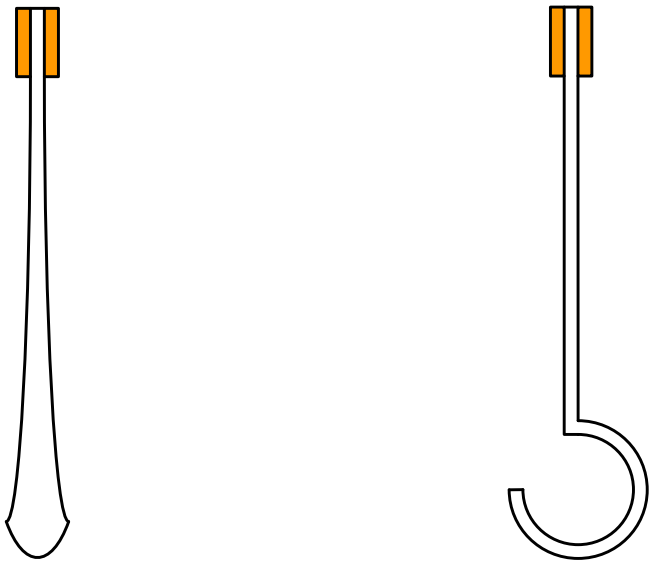

(a) (b)

Fig. 7.1 Side view of various designs of shanks for IPMC walking robots

electrodes is still thin but the lower part is stiffer. All the improved designs are used to keep the stiffness and enhance the bending deflection.

(2) Extension of IPMC operation duration. Internal water molecules are essential for IPMC operation, so the applications of IPMC is either working in an aquatic environment or keeping the concentration of internal water molecules. In addition to surface water, however, internal water will decrease when IPMC is works in air. Some researchers coated a thin layer of waterproof membrane to prevent the evaporation of both surface and internal water molecules [92, 93]. This thin membrane might degrade the performance due to its own stiffness, so the applications of IPMC could be significantly enlarged instead of keeping the internal water molecules if both soft and waterproof membranes can be coated on IPMC strips.

(3) Better robot hardware design. In this research, two IPMC strips were exactly perpendicular to each other in each leg. A real insect, such a cockroach, has six compound legs and each leg has dexterous designs to provide agile locomotion. The design in this research is the first generation and proved that IPMC is an appropriate choice for walking robot. A next-generation robot could be designed to apply more dexterous locomotion for legs in order to imitate a real-life insect as shown in Fig. 7.1. Therefore, it is unnecessary for the IPMC strips in a leg to be perfectly perpendicular to each other. In addition, each leg might have more than two DOFs like a real cockroach.

REFERENCES

[1] K. J. Kim and S. Tadokoro (eds.), *Electroactive Polymers for Robotic Applications: Artificial Muscles and Sensors*, Baker & Taylor Books New York, NY, 2007.

[2] Material property data. Available: http://www.matweb.com/index.aspx (2013).

[3] K. Oguro, Y. Kawami, and H. Takenaka, "An actuator element of polyelectrolyte gel membrane-electrode composite," (in Japanese), *Bulletin of the Government Industrial Research Institute*, *Osa*ka, vol. 43, no. 1, pp. 21−24, Mar. 1992.

[4] K. Sadeghipour, R. Salomon, and S. Neogi, "Development of a novel electrochemically active membrane and 'smart' material based vibration sensor/damper," *Smart Materials and Structures*, vol. 2, no. 1, pp. 172−179, Jun. 1992.

[5] M. Shahinpoor, "Conceptual design, kinematics and dynamics of swimming robotic structures using ionic polymeric gel muscles," *Smart Materials and Structures*, vol. 1, no. 1, pp. 91−94, Mar. 1992.

[6] DuPont™, "General information on Nafion® membrane for electrolysis," DuPont Corporation, Fayetteville, NC, Apr. 1999.

[7] S. Nemat-Nasser and Y. Wu, "Tailoring actuation of ionic polymer-metal composites through cation combination," in *Proceedings of SPIE*, vol. 5051, pp. 245−253, Jul. 2003.

[8] DuPont™, "DuPontTM Nafion® PFSA membranes NE-1135, N-115, N-117, NE-1110," DuPont Corporation, Fayetteville, NC, 2005.

[9] T. Kobayashi and M. Omiya, "A study on properties of ionic polymer metal composite," *Advanced Materials Research*, vols. 143−144, pp. 394−398, Oct. 2010.

[10] W. Kaal and S. Herold, "Electroactive polymer actuators in dynamic application," *IEEE/ASME Transaction on Mechatronics*, vol. 16, no. 1, pp. 24−32, Feb. 2011.

[11] Y. Nakabo, K. Takagi, T. Mukai, H. Yoshida, and K. Asaka, "Bending response of an artificial muscle in high-pressure water environments," in *Proceedings of SPIE, Smart Structures and Materials*, vol. 5759, pp. 388−395, Mar. 2005.

[12] E. Mbemmo, Z. Chen, S. Shatara, and X. Tan, "Modeling of biomimetic robotic fish propelled by an ionic polymer-metal composite actuator," in *Proceedings of 2008 IEEE International Conference on Robotics and Automation*, Pasadena, CA, May 2008, pp. 689−694.

[13] Z. Chen, S. Shatara, and X. Tan, "Modeling of biomimetic robotic fish propelled by an ionic polymer-metal composite caudal fin," *IEEE/ASME Transaction on Mechatronics*, vol. 15, no. 3, pp. 448−459, Jun. 2010.

[14] X. Tan, D. Kim, N. Usher, D. Laboy, J. Jackson, A. Kapetanovic, J. Rapai, B. Sabadus, and X. Zhou, "An autonomous robotic fish for mobile sensing," in *Proceedings of the 2006 IEEE/RSJ International Conference on Intelligent Robots and Systems*, Beijing, China, Oct. 2006, pp. 5424−5429.

[15] X. Ye, B. Gao, S. Guo, and L. Wang, "Development of ICPF actuated underwater microrobots," *International Journal of Automation and Computing*, vol. 3, no. 4, pp. 382−391, Oct. 2006.

[16] S. Guo, Y. Ge, L. Li, and S. Liu, "Underwater swimming micro robot using IPMC

actuator," in *Proceedings of the 2006 IEEE International Conference on Mechatronics and Automation*, Luoyang, China, Jun. 2006, pp. 249−254.

[17] S. Guo, T. Fukuda, and K. Asaka, "A new type of fish-like underwater microrobot," *IEEE/ASME Transactions on Mechatronics*, vol. 8, no. 1, pp. 136−141, Mar. 2003.

[18] S. Xu, B. Liu, and L. Hao, "A small remote operated robotic fish actuated by IPMC," in *Proceedings of the 2008 IEEE International Conference on Robotics and Biomimetics*, Bangkok, Thailand, Feb. 2009, pp. 1152−1156.

[19] Y. Yang, X. Ye, and S. Guo, "A new type of jellyfish-like microrobot," in *Proceedings of the 2007 IEEE International Conference on Integration Technology*, Shenzhen, China, Mar. 2007, pp. 673−678.

[20] S. Guo, L. Shi, X. Ye, and L. Li, "A new jellyfish type of underwater microrobot," in *Proceedings of the 2007 IEEE International Conference on Mechatronics and Automation*, Harbin, China, Aug. 5−8, 2007, pp. 509−514.

[21] P. Arena, C. Bonomo, L. Fortuna, M. Frasca, and S. Graziani, "Design and control of an IPMC wormlike robot," *IEEE Transactions on Systems, Man, and Cybernetics, Part B: Cybernetics*, vol. 36, no. 5, pp. 1044−1052, Oct. 2006.

[22] K. Takagi, M. Yamamura, Z. W. Luo, M. Onishi, S. Hirano, K. Asaka, and Y. Hayakawa, "Development of a rajiform swimming robot using ionic polymer artificial muscles," in *Proceedings of the 2006 IEEE/RSJ International Conference on Intelligent Robots and Systems*, Beijing, China, Oct. 9−15, 2006, pp. 1861−1866.

[23] S. Guo, L. Shi, and K. Asaka, "IPMC actuator-based an underwater microrobot

with 8 legs," in *Proceedings of 2008 IEEE International Conference on Mechatronics and Automation*, Takamatsu, Japan, Aug. 5−8, 2008, pp. 551−556.

[24] S. Guo, L. Shi, and K. Asaka, "IPMC actuator-sensor based a biomimetic underwater microrobot with 8 legs," in *Proceedings of the IEEE International Conference on Automation and Logistics*, Qingdao, China, Sep. 1−3, 2008, pp. 2495−2500.

[25] W. Zhang, S. Guo, and K. Asaka, "Development of an underwater biomimetic microrobot with compact structure and flexible locomotion," *Microsystem Technologies*, vol. 13, nos. 8−10, pp. 883−890, May 2007.

[26] W. Zhang, S. Guo, and K. Asaka, "A tripodic biomimetic underwater microrobots utilizing ICPF actuators," in *Proceedings of the 2006 IEEE/RSJ International Conference on Intelligent Robots and Systems*, Beijing, China, Oct. 9−15, 2006, pp. 2418−2423.

[27] W. Zhang, S. Guo, and K. Asaka, "Developments of two novel types of underwater crawling microrobots," in *Proceedings of the IEEE International Conference on Mechatronics and Automation*, Niagara Falls, Canada, Jul. 2005, pp. 1884−1889.

[28] W. Zhang, S. Guo, and K. Asaka, "Design and experimental results of a tripodic biomimetic microrobot with 5 DOFs," in *Proceedings of the 6th World Congress on Intelligent Control and Automation*, Dalian, China, Jun. 21−23, 2006, pp. 8378−8382.

[29] W. Zhang, S. Guo, and Kinji Asaka, "Development and analysis an underwater biomimetic microrobot," in *Proceedings of the 2006 IEEE International*

Conference on Information Acquisition, Weihai, Shandong, China, Aug. 20−23, 2006, pp. 212−217.

[30] Z. Chen, T. I. Um, and H. Bart-Smith, "Ionic polymer-metal composite enabled robotic manta ray," in *Proceedings of SPIE*, *Electroactive Polymer Actuators and Devices* (*EAPAD*) *2011*, vol. 7976, pp. 797637-1−797637-12, Mar. 2011.

[31] W.-S. Chu, K.-T. Lee, S.-H. Song, M.-W. Han, J.-Y. Lee, H.-S. Kim, M.-S. Kim, Y.-J. Park, K.-J. Cho, and S.-H. Ahn, "Review of biomimetic underwater robots using smart actuators," *International Journal of Precision Engineering and Manufacturing*, vol. 13, no. 7, pp. 1281−1292, Jul. 2012.

[32] N. Tomita, K. Takagi, and K. Asaka, "Development of a quadruped soft robot with fully IPMC body," *SICE Annual Conference 2011*, Waseda University, Tokyo, Japan, Sep. 13−18, 2011, pp. 1687−1690.

[33] K. Yun and W.-J. Kim, "System identification and microposition control of ionic polymer metal composite for three-finger gripper manipulation," *Journal of Systems and Control Engineering*, vol. 220, no. 7, pp. 539−551, May 2006.

[34] K. Yun and W.-J. Kim, "Microscale position control of an electroactive polymer using an anti-windup scheme," *Smart Materials and Structures*, vol. 15, no. 4, pp. 924−930, Mar. 2006.

[35] K. Yun, "A novel three-finger IPMC gripper for microscale applications," Ph.D. dissertation, Department of Mechanical Engineering, Texas A&M University, College Station, TX, 2006.

[36] R. J. Wood, "The first takeoff of a biologically inspired at-scale robotic insect,"

IEEE/ASME Transactions on Mechatronics, vol. 24, no. 2, pp. 341−347, Apr. 2008.

[37] R. Sahai, K. C. Galloway, and R. J. Wood, "Elastic element integration for improved flapping-wing micro air vehicle performance," *IEEE Transaction on Robotics*, to be published.

[38] R. J. Wood, S. Avadhanula, R. Sahai, E. Steltz, and R. S. Fearing, "Microrobot Design Using Fiber Reinforced Composites," *Journal of Mechanical Design*, vol. 130, no. 5, pp. 052304-1−052304-11, May 2008.

[39] P. -E J. Duhamel, N. O. Perez-Arancibia, G. L. Barrows, and R. J. Wood, "Biologically inspired optical-flow sensing for altitude control of flapping-wing microrobots," *IEEE/ASME Transactions on Mechatronics*, vol. 18, no. 2, pp. 556−568, Apr. 2013.

[40] C. D. Onal, R. J. Wood, and D. Rus, "An origami-inspired approach to worm robots," *IEEE/ASME Transactions on Mechatronics*, vol. 18, no. 2, pp. 430−438, Apr. 2013.

[41] D. A. Kingsley, "A cockroach inspired robot with artificial muscles," Ph.D. dissertation, Department of Mechanical and Aerospace Engineering, Case Western Reserve University, Cleveland, OH, 2005.

[42] J. Currie, M. Beckerleg, and J. Collins, "Software evolution of a hexapod robot walking gait," in *Proceedings of the 15th International Conference on Mechatronics and Machine Vision in Practice*, Auckland, New-Zealand, Dec. 24, 2008, pp. 305−310.

[43] W. Guo, M. Zhong, M. Li, and Y. Li, "Design of a six legged wall-climbing robot,"

in *Proceedings of the IEEE Conference on Advanced Robotics and Its Social Impacts*, Taipei, Taiwan, Aug. 23−25, 2008, pp. 1−4.

[44] AQUA project homepage, a project and implementation of various underwater robots, Available: http://www.aquarobot.net:8080/AQUA/index_html (2013).

[45] A. Mathis, J. Russell, T. Moore, J. Cohen, B. Satterfield, N. Kohut, X.-Y. Fu, and R. S. Fearing, "Autonomous navigation of a 5 gram crawling millirobot in a complex environment," in *Proceeding of the 15th International Conference on Climbing and Walking Robots and the Support Technologies for Mobile Machines*, DeKalb, IL, *Adaptive Mobile Robotics*, *Section 3: Autonomous Robots*, Jul. 23−26, 2012, pp. 121−128.

[46] K. K. Leang, Y. Shan, S. Song, and K. J. Kim, "Integrated sensing for IPMC actuators using strain gages for underwater applications," *IEEE/ASME Transaction on Mechatronics*, vol. 17, no. 2, pp. 345−355, Apr. 2012.

[47] Environment Robot Inc., Available: http://www.environmental-robots.com (2013)

[48] Y. Shan, "Fabrication and integrated feedforward and feedback control of ionic polymer-metal composite actuators," M.S. thesis, Department of Mechanical Engineering, Virginia Commonwealth University, Richmond, VA, 2008.

[49] N. Jin, B. Wang, K. Bian, Q. Chen, and K. Xiong, "Performance of ionic polymer-metal composite (IPMC) with different surface roughening methods," *Frontier Mechanical Engineering in China*, vol. 4, no. 4, pp. 430−435, Dec. 2009.

[50] S. Saher, S. Moon, S. J. Kim, H. J. Kim, and Y. H. Kim, "O_2 plasma treatment for ionic polymer metal nano composite (IPMNC) actuator," *Sensors and Actuators B*:

Chemical, vol. 147, no. 1, pp. 170−179, May 2010.

[51] S. J. Kim, I. T. Lee, and Y. H. Kim, "Performance enhancement of IPMC actuator by plasma surface treatment," *Smart Materials and Structures*, vol. 16, no. 1, pp. N6−N11, Jan. 2007.

[52] B. Stoimenov, J. Rossiter, and T. Mukai, "Anisotropic surface roughness enhances the bending response of ionic polymer-metal composite (IPMC) artificial muscles," in *Proceedings of SPIE*, *Smart Materials IV*, vol. 6413, pp. 641302-1−641302-10, Dec. 2006.

[53] B. Stoimenov, J. Rossiter, and T. Mukai, "Frequency response of anisotropic ionic polymer metal composites (IPMC) transducers," in *Proceedings of SPIE*, *Electroactive Polymer Actuators and Devices* (*EAPAD*) *2008*, vol. 6927, pp. 69270K-1−69270K-9, Apr. 2008.

[54] S. J. Lee, M. J. Han, S. J. Kim, J. Y. Jho, H. Y. Lee, and Y. H. Kim, "A new fabrication method for IPMC actuators and application to artificial fingers," *Smart Materials and Structures*, vol. 15, no. 5, pp. 1217−1224, Oct. 2006.

[55] S. Nemat-Nasser, and Y. Wu, "Comparative experimental study of ionic polymer-metal composites with different backbone ionomers and in various cation forms," *Journal of Applied Physics*, vol. 93, no. 9, pp. 5255−5267, May 2003.

[56] M. Bennett, "Manufacture and characterization of ionic polymer transducers employing non-precious metal electrodes," M.S. thesis, Department of Mechanical Engineering, Virginia Polytechnic Institute and State University, Blackburg, VA, 2002.

[57] L. Dai, Y. Zhang, H. Zhou, L. Li, and H. Duan, "Preparation of a new ionic polymer-metal composite," in *Proceedings of the 2nd IEEE International Conference on Nano/Micro Engineered and Molecular System*, Bangkok, Thailand, Jan. 16−19, 2007, pp. 50−54.

[58] DuPont™, "General information on Nafion® membrane for electrolysis," DuPont Corporation, Fayetteville, NC, 1999.

[59] DuPont™, "DuPont™ Nafion® PFSA membranes NE-1135, N-115, N-117, NE-1110," DuPont Corporation, Fayetteville, NC, 2005.

[60] R. Lumia and M. Shahinpoor, "IPMC microgripper research and development," *Journal of Physics*: *Conference Series*, vol. 127, no. 1, pp. 1− 8, Oct. 2008.

[61] T. Ganley, D. L. S. Hung, G. Zhu, and X. Tan, "Modeling and inverse compensation of temperature-dependent ionic polymer–metal composite sensor dynamics," *IEEE/ASME Transaction on Mechatronics*, vol. 16, no. 1, pp. 80−89, Feb. 2011.

[62] dSPACE, Available: http://www.dspace.com/en/inc/home.cfm (2013).

[63] S. Nemat-Nasser and Y. Wu, "Tailoring the actuation of ionic polymer–metal composites," *Smart Materials and Structures*, vol. 15, no. 4, pp. 909−923, Aug. 2006.

[64] S. Nemat-Nasser and S. Zamani, "Modeling of electrochemomechanical response of ionic polymer-metal composites with various solvents," *Journal of Applied Physics,* vol. 100, no. 6, pp. 064310-1−064310-18, Sep. 2006.

[65] Y.-C. Chang and W.-J. Kim, "Aquatic ionic-polymer-metal-composite insectile

robot with multi-DOF legs," *IEEE/ASME Transactions on Mechatronics*, vol. 18, no. 2, pp. 547−555, Apr. 2013.

[66] Y.-C. Chang and W.-J. Kim, "Design and implementation of an ionic-polymer-metal-composite aquatic biomimetic robot," in *Proceedings of ASME 2011 Dynamic Systems and Control Conference and Bath/ASME Symposium on Fluid Power and Motion Control*, Oct. 31–Nov. 2, 2011, Arlington, Virginia, USA, pp. 411−418.

[67] B. Stoimenov, J. Rossiter, and T. Mukai, "Manufacturing of ionic polymer-metal composites (IPMCs) that can actuate into complex curves," in *Proceedings of SPIE*, *Electroactive Polymer Actuators and Devices* (*EAPAD*) 2007, vol. 6524, pp. 65240T-1−65240T-11, Apr. 2007.

[68] J. Rossiter, B. Stoimenov, and T. Mukai, "A linear actuator from a single ionic polymer-metal composite (IPMC) strip," in *Proceedings of SPIE*, *Electroactive Polymer Actuators and Devices* (*EAPAD*) 2007, vol. 6524, pp. 65241B-1−65241B-11, Apr. 2007.

[69] C. Bonomo, L. Fortuna, P. Giannone, and S. Graziani, "A circuit to model the electrical behavior of an ionic polymer-metal composite," *IEEE Transactions on Circuits and Systems-I: Regular Papers*, vol. 53, no. 2, pp. 338−350, Feb. 2006.

[70] A. J. McDaid, "Modelling and control of IPMC actuators for biomedical robotics applications," Ph.D. dissertation, Department of Mechanical Engineering, the University of Auckland, Auckland, New Zealand, 2011.

[71] S. Lee, H. C. Park, and K. J. Kim, "Equivalent modeling for ionic polymer-metal

composite actuators based on beam theories," *Smart Materials and Structures*, vol. 14, no. 6, pp. 1363−1368, Dec. 2005.

[72] S. Lee, K. J. Kim, and I.-S. Park, "Modeling and experiment of a muscle-like linear actuator using an ionic polymer-metal composite and its actuation characteristics," *Smart Materials and Structures*, vol. 16, no. 3, pp. 583−588, Jun. 2007.

[73] G. D. Bufalo, L. Placidi, and M. Porfiri, "A mixture theory framework for modeling the mechanical actuation of ionic polymer metal composites," *Smart Materials and Structures*, vol. 17, no. 4, pp. 1−14, Aug. 2008.

[74] Z. Chen, X. Tan, A. Will, and C. Ziel, "A dynamic model for ionic polymer-metal composite sensors," *Smart Materials and Structures*, vol. 16, no. 4, pp. 1477−1488, Aug. 2007.

[75] Z. Chen and X. Tan, "A control-oriented and physics-based model for ionic polymer-metal composite actuators," *IEEE/ASME Transactions on Mechatronics*, vol. 13, no. 5, pp. 519−529, Oct. 2008.

[76] P. Brunetto, L. Fortuna, P. Giannone, S. Graziani, and F. Pagano, "A resonant vibrating tactile probe for biomedical applications based on IPMC," *IEEE Transactions on Instrumentation and Measurement*, vol. 59, no. 5, pp. 1453−1462, May 2010.

[77] C. Bonomo, L Fortuna, P Giannone, S Graziani, and S Strazzeri, "A nonlinear model for ionic polymer metal composites as actuators," *Smart Materials and Structures*, vol. 16, no. 1, pp. 1−12, Feb. 2007.

[78] S. J. Kim, S.-M. Kim, K. J. Kim, and Y. H. Kim, "An electrode model for ionic

polymer-metal composites," *Smart Materials and Structures*, vol. 16, no. 6, pp. 2286−2295, Dec. 2007.

[79] N. D. Bhat and W.-J. Kim, "Precision force and position control of ionic polymer–metal composite," *Journal of Systems and Control Engineering*, vol. 218, no. 6, 421−432, Sep. 2004.

[80] N. D. Bhat and W.-J. Kim, "System identification and control of ionic polymer metal composite," in *Proceedings of the 10th SPIE Symposium on Smart Materials and Structures*, Mar. 2003, vol. 5049, pp. 526−535.

[81] N. D. Bhat, "Modeling and precision control of ionic polymer metal composite," M.S. thesis, Department of Mechanical Engineering, Texas A&M University, College Station, TX, 2003.

[82] N. D. Bhat and W.-J. Kim, "Precision position control of ionic polymer metal composite," in *Proceedings of the 2004 American Control Conference*, Boston Massachusetts, Jun. 30−Jul. 2, 2004, pp. 740−745.

[83] H.-L. Xing, J.-H. Jeon, K. C. Park, and I.-K. Oh, "Active disturbance rejection control for precise position tracking of ionic polymer–metal composite actuators," *IEEE/ASME Transactions on Mechatronics*, vol. 18, no. 1, pp. 86−95, Feb. 2013.

[84] L. Ljung, *System Identification: Theory for the User*, 2nd Edition, Prentice Hall, Upper Saddle River, NJ, 1999.

[85] MatLab product help for "PEM," a system identification tool for dynamic system modeling, Available: http://www.mathworks.com/help/ident/ref/pem.html (2013)

[86] A. Agarwal and J. H. Lang, *Foundations of analog and digital electronic circuits*. Morgan Kaufmann Publishers, San Mateo, CA, 2005.

[87] X. Ye, B. Gao, S. Guo, W. Feng, and K. Wang, "A novel underwater crablike microrobot," in *Proceedings of the 2006 IEEE International Conference on Mechatronics and Automation*, Luoyang, China, Jun. 25−28, 2006, pp. 272−277.

[88] MWS Wires Industries, Available: http://www.mwswire.com (2013).

[89] D44H8 datasheet, STMicroelectronics, Oct. 2009, Available: http://www.st.com

[90] D45H8 datasheet, STMicroelectronics, Oct. 2009, Available: http://www.st.com

[91] A. Shariati, A. Meghdari, and P. Shariati, "Intelligent control of an IPMC actuated manipulator using emotional learning based controller," in *Proceedings of SPIE, Metamaterials: Fundamentals and Applications*, vol. 7029, pp. 70291J-1−70291J-11, Sep. 2008.

[92] S. J. Kim, I. T. Lee, H.-Y. Lee, and Y. H. Kim, "Performance improvement of an ionic polymer-metal composite actuator by parylene thin film coating," *Smart Materials and Structures*, vol. 15, no. 6, pp. 1540−1546, Sep. 2006.

[93] S. J. Kim, M. S. Kim, S. R. Shin, I. Y. Kim, S. I Kim, S. H. Lee, T. S. Lee, and G. M. Spinks, "Enhancement of the electromechanical behavior of IPMCs based on chitosan/polyaniline ion exchange membranes fabricated by freeze-drying," *Smart Materials and Structures*, vol. 14, no. 5, pp. 889−894, Sep. 2005.

APPENDIX A

SIMULINK® BLOCK DIAGRAM

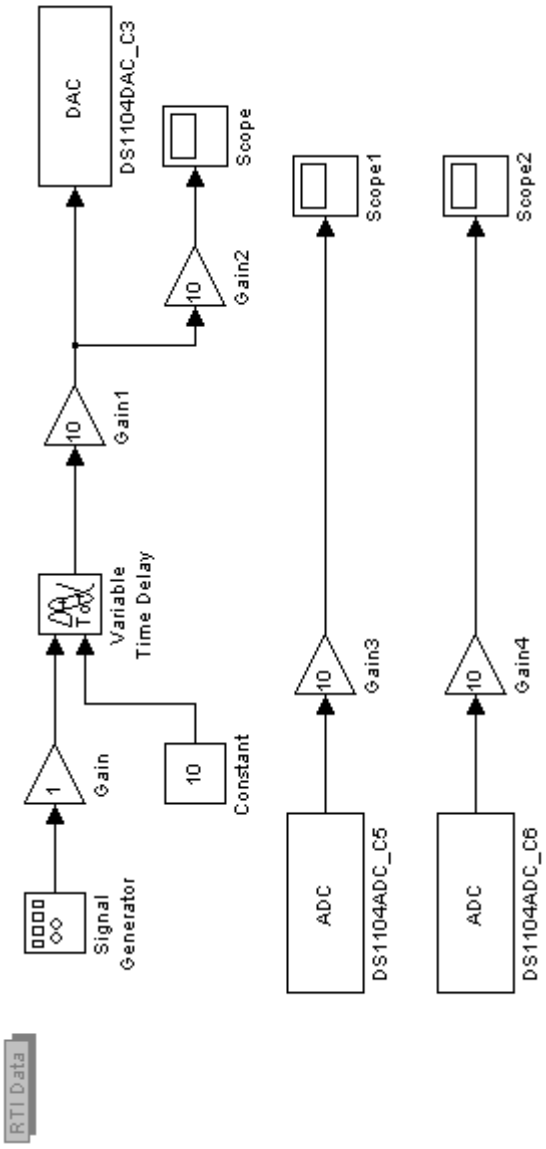

Fig. A.1 Voltage measuring at two spots on an IPMC strip

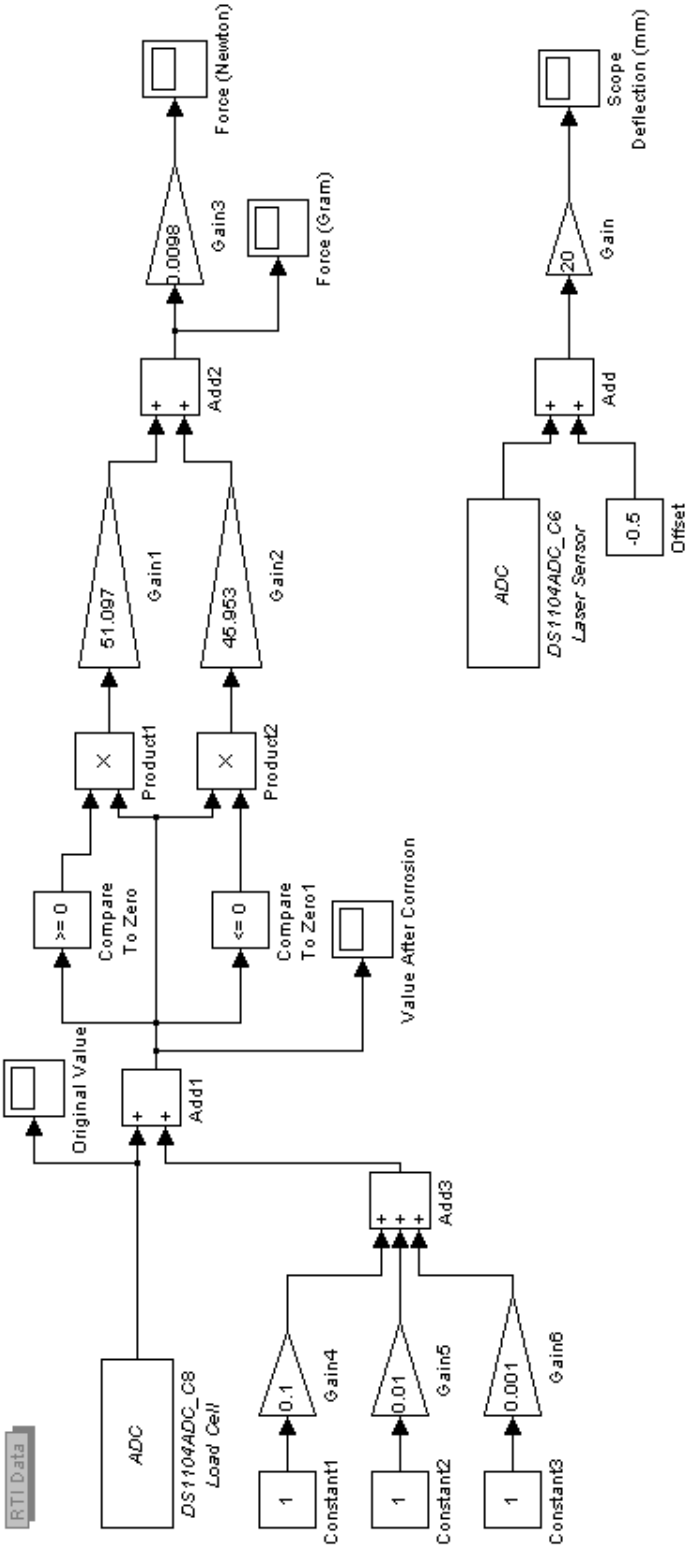

Fig. A.2 IPMC measuring system

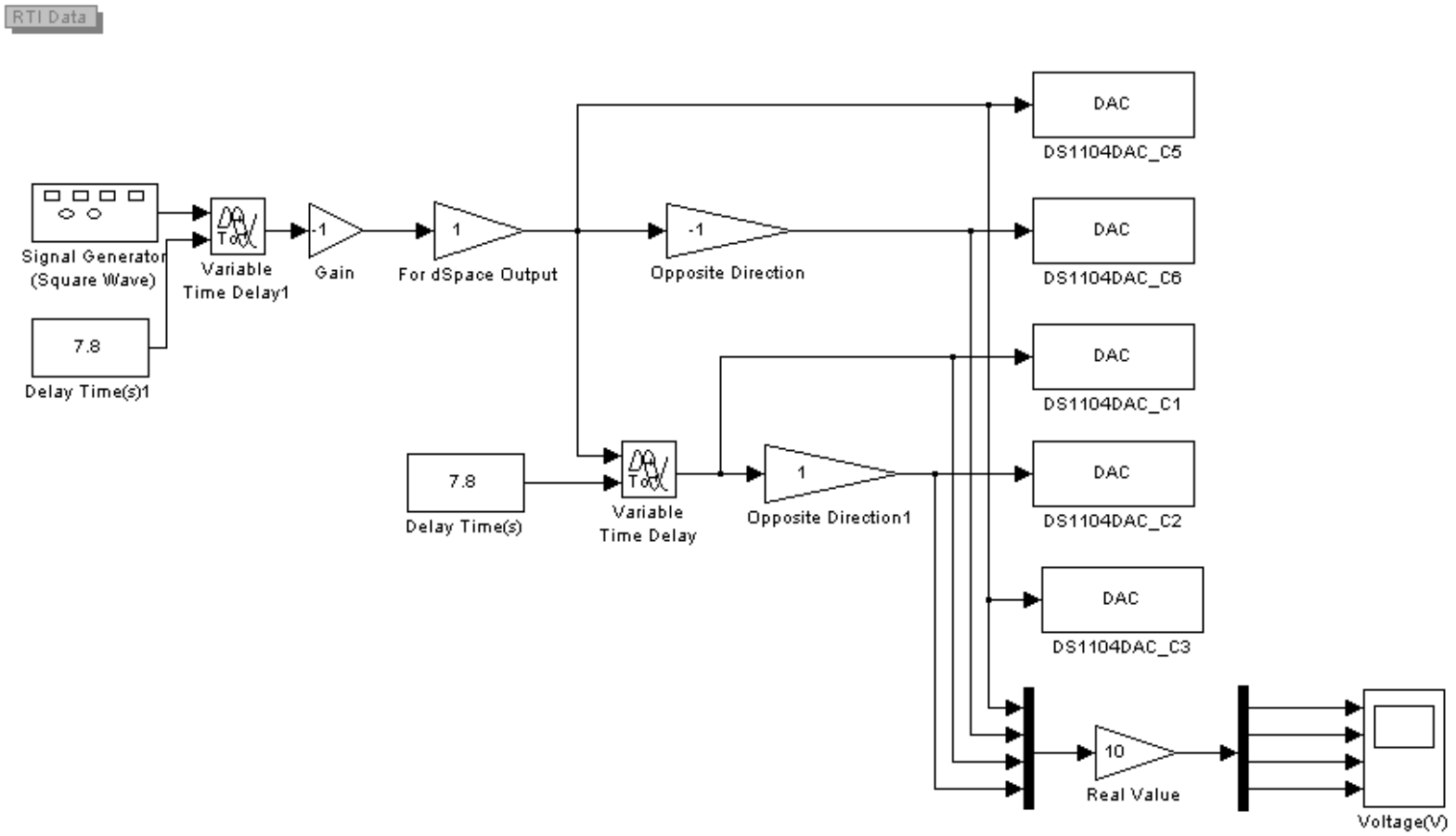

Fig. A.3 IPMC robot walking in the first procedure

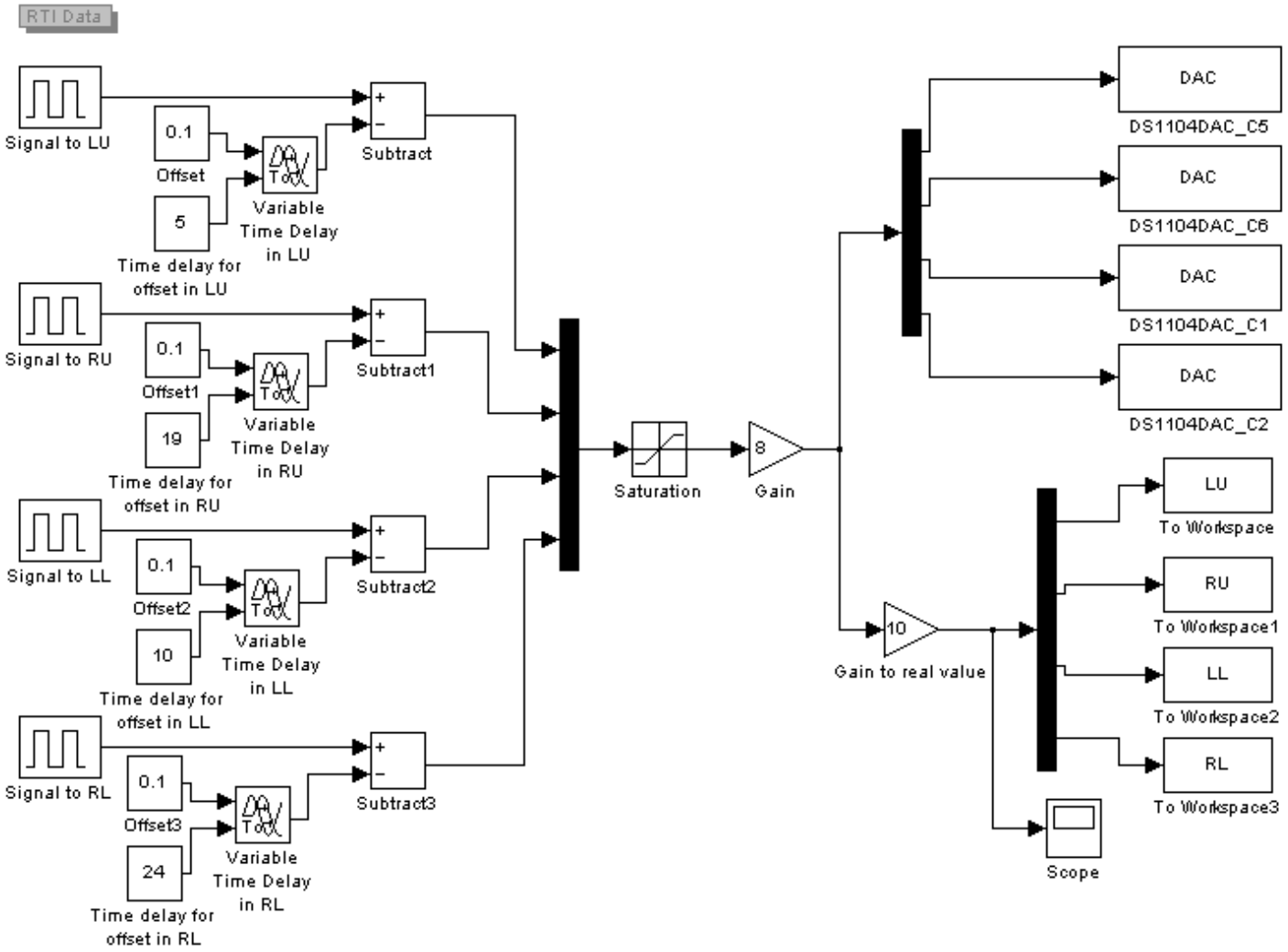

Fig. A.4 IPMC robot walking in the second procedure

APPENDIX B

MATLAB® CODE

```
%%%%%%%%%%%%%%%%%%%%%%%%%%%%%%%%%%%%%%%%%%%%%%%%%%%%%%%%%%%%%%%%%%%%%%%%
% This code includes all Matlab plots in Chapter IV                          %
% Import all data before running this code                                   %
%%%%%%%%%%%%%%%%%%%%%%%%%%%%%%%%%%%%%%%%%%%%%%%%%%%%%%%%%%%%%%%%%%%%%%%%
clc;

t = 0:0.001:500;

figure(1)  % Fig. 4.2

plot(t,t_2_112510.Y(1,1).Data, 'LineStyle', '-')
hold on

xlabel('Time (s)')
ylabel('Deflection (mm)')

ylim([-3 18])

figure(2)  % Fig. 4.4

plot(t,t_2_1_112510.Y(1,1).Data, 'LineStyle', '-')
hold on
```

```
xlabel('Time (s)')

ylabel('Deflection (mm)')


ylim([-3 15])


figure(3)  % Fig. 4.7 (a)


plot(t,t_4_3_112510.Y(1,1).Data, 'LineStyle', '-')

hold on


xlabel('Time (s)')

ylabel('Deflection (mm)')


ylim([-2 28])


figure(4)  % Fig. 4.7 (b)


plot(t,t_4_2_112510.Y(1,1).Data, 'LineStyle', '-')

hold on


xlabel('Time (s)')

ylabel('Deflection (mm)')
```

```
ylim([-2 28])

figure(5)  % Fig. 4.7 (c)

plot(t,t_4_5_112510.Y(1,1).Data, 'LineStyle', '-')
hold on

xlabel('Time (s)')
ylabel('Deflection (mm)')

ylim([-2 28])

figure(6)  % Fig. 4.7 (d)

plot(t,t_4_10_10_112510.Y(1,1).Data, 'LineStyle', '-')
hold on

xlabel('Time (s)')
ylabel('Deflection (mm)')

ylim([-1 6])
```

```
figure(7)  % Fig. 4.8 (a)

% Draw a plot with two y-axes
[A1, A2, A3] = plotyy(t,saw01122010_5.Y(1,1).Data,t,saw01122010_5.Y(1,2).Data *
0.8,'plot');

set (A3, 'Linestyle', ':')
% Label x-axis
xlabel('Time (s)')

% Set the tick spacing of left y-axis
set(A1(1), 'yTick', [-15:5:15])
% Set the limitation of left y-axis
set(A1(1), 'ylim', [-15 15])

% Set the tick spacing of right y-axis
set(A1(2), 'yTick', [-10:5:10])
% Set the limitation of right y-axis
set(A1(2), 'ylim', [-10 10])

% Label left y-axis
set(get(A1(1),'Ylabel'),'String','Deflection (mm)')
```

```
% Label right y-axis
set(get(A1(2),'Ylabel'),'String','Voltage (V)')

figure(8)  % Fig. 4.8 (b)

[B1, B2, B3] = plotyy(t,saw02122010_5.Y(1,1).Data,t,saw02122010_5.Y(1,2).Data *
0.8,'plot');

set (B3, 'Linestyle', ':')
xlabel('Time (s)')

% Set the tick spacing of left y-axis
set(B1(1), 'yTick', [-10:5:10])
% Set the limitation of left y-axis
set(B1(1), 'ylim', [-10 10])

% Set the tick spacing of right y-axis
set(B1(2), 'yTick', [-10:5:10])
% Set the limitation of right y-axis
set(B1(2), 'ylim', [-10 10])

% Label left y-axis
```

```
set(get(B1(1),'Ylabel'),'String','Deflection (mm)')
% Label right y-axis
set(get(B1(2),'Ylabel'),'String','Voltage (V)')

figure(9)  % Fig. 4.8 (c)

[C1, C2, C3] = plotyy(t,saw03122010_5.Y(1,1).Data,t,saw03122010_5.Y(1,2).Data *
0.8,'plot');

set (C3, 'Linestyle', ':')
xlabel('Time (s)')

% Set the tick spacing of left y-axis
set(C1(1), 'yTick', [-8:2:8])
% Set the limitation of left y-axis
set(C1(1), 'ylim', [-8 8])

% Set the tick spacing of right y-axis
set(C1(2), 'yTick', [-10:5:10])
% Set the limitation of right y-axis
set(C1(2), 'ylim', [-10 10])
```

```
% Label left y-axis
set(get(C1(1),'Ylabel'),'String','Deflection (mm)')
% Label right y-axis
set(get(C1(2),'Ylabel'),'String','Voltage (V)')

figure(10)  % Fig. 4.9 (a)

[D1, D2, D3] = plotyy(t,sin01122010_5.Y(1,1).Data,t,sin01122010_5.Y(1,2).Data *
0.8,'plot');

set (D3, 'Linestyle', ':')
xlabel('Time (s)')

% Set the tick spacing of left y-axis
set(D1(1), 'yTick', [-15:5:15])
% Set the limitation of left y-axis
set(D1(1), 'ylim', [-15 15])

% Set the tick spacing of right y-axis
set(D1(2), 'yTick', [-10:5:10])
% Set the limitation of right y-axis
set(D1(2), 'ylim', [-10 10])
```

```
% Label left y-axis
set(get(D1(1),'Ylabel'),'String','Deflection (mm)')
% Label right y-axis
set(get(D1(2),'Ylabel'),'String','Voltage (V)')

figure(11)  % Fig. 4.9 (b)

[E1, E2, E3] = plotyy(t,sin02122010_5.Y(1,1).Data,t,sin02122010_5.Y(1,2).Data *
0.8,'plot');

set (E3, 'Linestyle', ':')
xlabel('Time (s)')

% Set the tick spacing of left y-axis
set(E1(1), 'yTick', [-10:5:10])
% Set the limitation of left y-axis
set(E1(1), 'ylim', [-10 10])

% Set the tick spacing of right y-axis
set(E1(2), 'yTick', [-10:5:10])
% Set the limitation of right y-axis
set(E1(2), 'ylim', [-10 10])
```

```
% Label left y-axis
set(get(E1(1),'Ylabel'),'String','Deflection (mm)')
% Label right y-axis
set(get(E1(2),'Ylabel'),'String','Voltage (V)')

figure(12)  % Fig. 4.9 (c)

[F1, F2, F3] = plotyy(t,sin03122010_5.Y(1,1).Data,t,sin03122010_5.Y(1,2).Data *
0.8,'plot');

set (F3, 'Linestyle', ':')
xlabel('Time (s)')

% Set the tick spacing of left y-axis
set(F1(1), 'yTick', [-8:2:8])
% Set the limitation of left y-axis
set(F1(1), 'ylim', [-8 8])

% Set the tick spacing of right y-axis
set(F1(2), 'yTick', [-10:5:10])
% Set the limitation of right y-axis
set(F1(2), 'ylim', [-10 10])
```

```
% Label left y-axis
set(get(F1(1),'Ylabel'),'String','Deflection (mm)')
% Label right y-axis
set(get(F1(2),'Ylabel'),'String','Voltage (V)')

figure(13)  % Fig. 4.10 (a)

[G1, G2, G3] = plotyy(t,squ01122010_5.Y(1,1).Data,t,squ01122010_5.Y(1,2).Data *
0.8,'plot');

set (G3, 'Linestyle', ':')
xlabel('Time (s)')

% Set the tick spacing of left y-axis
set(G1(1), 'yTick', [-20:5:20])
% Set the limitation of left y-axis
set(G1(1), 'ylim', [-20 20])

% Set the tick spacing of right y-axis
set(G1(2), 'yTick', [-10:5:10])
% Set the limitation of right y-axis
set(G1(2), 'ylim', [-10 10])
```

```
% Label left y-axis
set(get(G1(1),'Ylabel'),'String','Deflection (mm)')
% Label right y-axis
set(get(G1(2),'Ylabel'),'String','Voltage (V)')

figure(14)  % Fig. 4.10 (b)

[H1, H2, H3] = plotyy(t,squ02122010_7.Y(1,1).Data,t,squ02122010_7.Y(1,2).Data *
0.8,'plot');

set (H3, 'Linestyle', ':')
xlabel('Time (s)')

% Set the tick spacing of left y-axis
set(H1(1), 'yTick', [-15:5:15])
% Set the limitation of left y-axis
set(H1(1), 'ylim', [-15 15])

% Set the tick spacing of right y-axis
set(H1(2), 'yTick', [-10:5:10])
% Set the limitation of right y-axis
set(H1(2), 'ylim', [-10 10])
```

```
% Label left y-axis
set(get(H1(1),'Ylabel'),'String','Deflection (mm)')
% Label right y-axis
set(get(H1(2),'Ylabel'),'String','Voltage (V)')

figure(15)  % Fig. 4.10 (c)

[I1, I2, I3] = plotyy(t,squ03122010_5.Y(1,1).Data,t,squ03122010_5.Y(1,2).Data *
0.8,'plot');

set (I3, 'Linestyle', ':')
xlabel('Time(s)')

% Set the tick spacing of left y-axis
set(I1(1), 'yTick', [-15:5:15])
% Set the limitation of left y-axis
set(I1(1), 'ylim', [-15 15])

% Set the tick spacing of right y-axis
set(I1(2), 'yTick', [-10:5:10])
% Set the limitation of right y-axis
set(I1(2), 'ylim', [-10 10])
```

```
% Label left y-axis
set(get(I1(1),'Ylabel'),'String','Deflection (mm)')
% Label right y-axis
set(get(I1(2),'Ylabel'),'String','Voltage (V)')

figure(16)  % Fig. 4.11 (b)

plot(t,squ02010111_6v.Y(1,1).Data, 'LineStyle', '-')
hold on

xlabel('Time (s)')
ylabel('Deflection (mm)')

figure(17)  % Fig. 4.12 (b)

plot(t,squ02010111_6v_back.Y(1,1).Data, 'LineStyle', '-')
hold on

xlabel('Time (s)')
ylabel('Deflection (mm)')

figure(18)  % Fig. 4.13 (b)
```

```
plot(t,squ02010211__6v.Y(1,1).Data, 'LineStyle', '-')
hold on

xlabel('Time (s)')
ylabel('Deflection (mm)')

figure(19)  % Fig. 4.14

plot(t,squ02122710_1v.Y(1,1).Data, '-r')
hold on

plot(t,squ02122710_2v.Y(1,1).Data, '-g')
hold on

plot(t,squ02122710_3v.Y(1,1).Data, '-b')
hold on

plot(t,squ02122710_4v.Y(1,1).Data, '-y')
hold on

plot(t,squ02122710_5v.Y(1,1).Data, '-c')
hold on
```

```
plot(t,squ02122710_6v.Y(1,1).Data, '-m')
hold on

xlabel('Time (s)')
ylabel('Deflection (mm)')
legend('1V', '2V', '3V', '4V', '5V', '6V')

figure(20)  % Fig. 4.16 (a)

plot(t,0.8 * tri_saw02012011_1.Y(1,1).Data, ':')
hold on

plot(t,tri_saw02012011_1.Y(1,2).Data, '-')
hold on

plot(t,tri_saw02012011_1.Y(1,3).Data, '-.')
hold on

xlabel('Time (s)')
ylabel('Voltage (V)')
legend('Vin', 'Vout1', 'Vout2')
ylim([-12 12])
```

```
figure(21)  % Fig. 4.16 (b)

plot(t,0.8 * tri_sin02012011_1.Y(1,1).Data, ':')
hold on

plot(t,tri_sin02012011_1.Y(1,2).Data, '-')
hold on

plot(t,tri_sin02012011_1.Y(1,3).Data, '-.')
hold on

xlabel('Time (s)')
ylabel('Voltage (V)')
legend('Vin', 'Vout1', 'Vout2')
ylim([-12 12])

figure(22)  % Fig. 4.16 (c)

plot(t,0.8 * tri_squ02012011_1.Y(1,1).Data, ':')
hold on

plot(t,tri_squ02012011_1.Y(1,2).Data, '-')
```

```
hold on

plot(t,tri_squ02012011_1.Y(1,3).Data, '-.')
hold on

xlabel('Time (s)')
ylabel('Voltage (V)')
legend('Vin', 'Vout1', 'Vout2')
ylim([-12 12])

figure(23)  % Fig. 4.20 (a)

plot(t,saw_uncut02122710_1.Y(1,1).Data, 'LineStyle', '-')
hold on

xlabel('Time (s)')
ylabel('Deflection (mm)')

figure(24)  % Fig. 4.20 (b)

plot(t,saw_cut02122710_1.Y(1,1).Data, 'LineStyle', '-')
hold on
```

```
xlabel('Time (s)')
ylabel('Deflection (mm)')

figure(25)  % Fig. 4.21 (a)

plot(t,sin_uncut02122710_1.Y(1,1).Data, 'LineStyle', '-')
hold on

xlabel('Time (s)')
ylabel('Deflection (mm)')

figure(26)  % Fig. 4.21 (b)

plot(t,sin_cut02122710_1.Y(1,1).Data, 'LineStyle', '-')
hold on

xlabel('Time (s)')
ylabel('Deflection (mm)')

figure(27)  % Fig. 4.22 (a)

plot(t,squ_uncut02122710_1.Y(1,1).Data, 'LineStyle', '-')
```

```
hold on

xlabel('Time (s)')
ylabel('Deflection (mm)')

figure(28)  % Fig. 4.22 (b)

plot(t,squ_cut02010511_3.Y(1,1).Data, 'LineStyle', '-')
hold on

xlabel('Time (s)')
ylabel('Deflection (mm)')

figure(29)  % Fig. 4.23

plot(t,squ_cut02010511_4.Y(1,1).Data, 'LineStyle', '-')
hold on

xlabel('Time (s)')
ylabel('Deflection (mm)')

figure(30)  % Fig. 4.24 (a)
```

```
x11 = sin01122010_6.Y(1,2).Data(1,1:86564) * 0.8;

y11 = sin01122010_6.Y(1,1).Data(1,1:86564);


plot(x11,y11)


xlabel('Input Voltage (V)')

ylabel('Deflection (mm)')


figure(31)  % Fig. 4.24 (b)


x21 = sin02122010_5.Y(1,2).Data(1,1:47119) * 0.8;

y21 = sin02122010_5.Y(1,1).Data(1,1:47119);


plot(x21,y21)


xlabel('Input Voltage (V)')

ylabel('Deflection (mm)')


figure(32)  % Fig. 4.24 (c)


x31 = sin03122010_5.Y(1,2).Data(1,1:34029) * 0.8;

y31 = sin03122010_5.Y(1,1).Data(1,1:34029);
```

```
plot(x31,y31)

xlabel('Input Voltage (V)')
ylabel('Deflection (mm)')

figure(33)  % Fig. 4.25 (a)

x11 = sin01122010_6.Y(1,2).Data(1,1:86564) * 0.8;
y11 = sin01122010_6.Y(1,1).Data(1,1:86564);

plot(x11,y11,'Color','blue')

hold on

x12 = sin01122010_6.Y(1,2).Data(1,86565:148428) * 0.8;
y12 = sin01122010_6.Y(1,1).Data(1,86565:148428);

plot(x12,y12,'Color','red')

hold on

x13 = sin01122010_6.Y(1,2).Data(1,148429:212428) * 0.8;
```

```
y13 = sin01122010_6.Y(1,1).Data(1,148429:212428);

plot(x13,y13,'Color','green')

hold on

x14 = sin01122010_6.Y(1,2).Data(1,212429:274428) * 0.8;
y14 = sin01122010_6.Y(1,1).Data(1,212429:274428);

plot(x14,y14,'Color','magenta')

xlabel('Input Voltage (V)')
ylabel('Deflection (mm)')
% legend('1st','2nd','3rd','4th')

figure(34)  % Fig. 4.25 (b)

t11 = 0.001:0.001:86.564;
t12 = 86.565:0.001:148.428;
t13 = 148.429:0.001:212.428;
t14 = 212.429:0.001:274.428;
```

```
plot(t11,y11,'Color','blue')

hold on


plot(t12,y12,'Color','red')

hold on


plot(t13,y13,'Color','green')

hold on


plot(t14,y14,'Color','magenta')


xlabel('Time (s)')

ylabel('Deflection (mm)')


figure(35)  % Fig. 4.26 (a)


x21 = sin02122010_5.Y(1,2).Data(1,1:47119) * 0.8;

y21 = sin02122010_5.Y(1,1).Data(1,1:47119);


plot(x21,y21,'Color','blue')


hold on
```

```
x22 = sin02122010_5.Y(1,2).Data(1,47120:78564) * 0.8;
y22 = sin02122010_5.Y(1,1).Data(1,47120:78564);

plot(x22,y22,'Color','red')

hold on

x23 = sin02122010_5.Y(1,2).Data(1,78565:109928) * 0.8;
y23 = sin02122010_5.Y(1,1).Data(1,78565:109928);

plot(x23,y23,'Color','green')

hold on

x24 = sin02122010_5.Y(1,2).Data(1,109929:140928) * 0.8;
y24 = sin02122010_5.Y(1,1).Data(1,109929:140928);

plot(x24,y24,'Color','magenta')

xlabel('Input Voltage (V)')
ylabel('Deflection (mm)')
% legend('1st','2nd','3rd','4th')
```

```
figure(36)  % Fig. 4.26 (b)

t21 = 0.001:0.001:47.119;
t22 = 47.120:0.001:78.564;
t23 = 78.565:0.001:109.928;
t24 = 109.929:0.001:140.928;

plot(t21,y21,'Color','blue')
hold on

plot(t22,y22,'Color','red')
hold on

plot(t23,y23,'Color','green')
hold on

plot(t24,y24,'Color','magenta')

xlabel('Time (s)')
ylabel('Deflection (mm)')

figure(37)  % Fig. 4.27 (a)
```

```
x31 = sin03122010_5.Y(1,2).Data(1,1:34029) * 0.8;

y31 = sin03122010_5.Y(1,1).Data(1,1:34029);


plot(x31,y31,'Color','blue')


hold on


x32 = sin03122010_5.Y(1,2).Data(1,34030:55264) * 0.8;

y32 = sin03122010_5.Y(1,1).Data(1,34030:55264);


plot(x32,y32,'Color','red')


hold on


x33 = sin03122010_5.Y(1,2).Data(1,55265:75928) * 0.8;

y33 = sin03122010_5.Y(1,1).Data(1,55265:75928);


plot(x33,y33,'Color','green')


hold on


x34 = sin03122010_5.Y(1,2).Data(1,75929:96528) * 0.8;
```

```
y34 = sin03122010_5.Y(1,1).Data(1,75929:96528);

plot(x34,y34,'Color','magenta')

xlabel('Input Voltage (V)')
ylabel('Deflection (mm)')
% legend('1st','2nd','3rd','4th')

figure(38)  % Fig. 4.27 (b)

t31 = 0.001:0.001:34.029;
t32 = 34.030:0.001:55.264;
t33 = 55.265:0.001:75.928;
t34 = 75.929:0.001:96.528;

plot(t31,y31,'Color','blue')
hold on

plot(t32,y32,'Color','red')
hold on

plot(t33,y33,'Color','green')
```

```
hold on

plot(t34,y34,'Color','magenta')

xlabel('Time (s)')
ylabel('Deflection (mm)')



%%%%%%%%%%%%%%%%%%%%%%%%%%%%%%%%%%%%%%%%%%%%%%%%%%%%%%%%%%%%%%%%%%%%%%%%%%%%
% This code includes all Matlab plots in Chapter V                              %
% Import all data before running this code                                      %
% Run the Simulink file, Chapter5.mdl, first                                    %
%%%%%%%%%%%%%%%%%%%%%%%%%%%%%%%%%%%%%%%%%%%%%%%%%%%%%%%%%%%%%%%%%%%%%%%%%%%%
clc;

% Set all parameters of the IPMC strip structural model
i = 1;
E = 90;
I = 0.833;
L = 25;
w0 = 0.03;
w1 = 0.01;
```

```
% Obtain the corresponding input and output deflection for figure (7) to
% figure (28)
a11 = saw01122010_5.Y(1,1).Data;
a12 = 0.8 * saw01122010_5.Y(1,2).Data;
a21 = saw02122010_5.Y(1,1).Data;
a22 = 0.8 * saw02122010_5.Y(1,2).Data;
a31 = saw03122010_5.Y(1,1).Data;
a32 = 0.8 * saw03122010_5.Y(1,2).Data;
a41 = sin01122010_5.Y(1,1).Data;
a42 = 0.8 * sin01122010_5.Y(1,2).Data;
a51 = sin02122010_5.Y(1,1).Data;
a52 = 0.8 * sin02122010_5.Y(1,2).Data;
a61 = sin03122010_5.Y(1,1).Data;
a62 = 0.8 * sin03122010_5.Y(1,2).Data;
a71 = squ01122010_5.Y(1,1).Data;
a72 = 0.8 * squ01122010_5.Y(1,2).Data;
a81 = squ02122010_7.Y(1,1).Data;
a82 = 0.8 * squ02122010_7.Y(1,2).Data;
a91 = squ03122010_5.Y(1,1).Data;
a92 = 0.8 * squ03122010_5.Y(1,2).Data;

a1_input = a12';
```

```
a1_output = a11';

a2_input = a22';

a2_output = a21';

a3_input = a32';

a3_output = a31';

a4_input = a42';

a4_output = a41';

a5_input = a52';

a5_output = a51';

a6_input = a62';

a6_output = a61';

a7_input = a72';

a7_output = a71';

a8_input = a82';

a8_output = a81';

a9_input = a92';

a9_output = a91';


% Set time period for the mathematic models

t1 = 0:0.001:500;


% Record the points of IPMC strips with the length in each condition
```

```
for x = 0:0.1:25
   f1(1,i) = -1 / (E * I) * ((1 / 120) * (w0 - w1) / L * x ^ 5 - 1 / 24 * w0 * x ^ 4 + L / 12 *
(w0 + w1) * x ^ 3);
   f2(1,i) = 1 / (E * I) * (-1 / 24 * w0 * x ^ 4 + L / 6 * w0 * x ^ 3 - w0 * L ^ 2 / 4 * x ^ 2);
   f3(1,i) = 1 / (E * I) * ((1 / 120) * (w0 - w1) / L * x ^ 5 - 1 / 24 * w0 * x ^ 4 + L / 12 *
(w0 + w1) * x ^ 3 - (w0 + 2 * w1) * L ^ 2 / 12 * x ^ 2);
   f4(1,i) = 1 / (E * I) * ((1 / 120) * w0 / L * x ^ 5 - 1 / 24 * w0 * x ^ 4 + L / 12 * w0 * x
^ 3 - w0 * L ^ 2 / 12 * x ^ 2);
   f5(1,i) = 1 / (E * I) * ((1 / 60) * w0 / L * x ^ 5 - 1 / 24 * w0 * x ^ 4 + L / 24 * w0 * x ^
3 - w0 * L ^ 2 / 24 * x ^ 2);
   i = i + 1;
end

figure(1)  % Not included

x = 0:0.1:25;
plot(x,f1)
hold on

title('Deflection of an IPMC Strip')
xlabel('Length (mm)')
ylabel('Deflection (mm)')
```

```
figure(2)  % Not included

x = 0:0.1:25;
plot(x,f2)
hold on

title('Deflection of an IPMC Strip -- Situation 1')
xlabel('Length (mm)')
ylabel('Deflection (mm)')

figure(3)  % Not included

x = 0:0.1:25;
plot(x,f3)
hold on

title('Deflection of an IPMC Strip -- Situation 2')
xlabel('Length (mm)')
ylabel('Deflection (mm)')

figure(4)  % Not included
```

```
x = 0:0.1:25;
plot(x,f4)
hold on

title('Deflection of an IPMC Strip -- Situation 3')
xlabel('Length (mm)')
ylabel('Deflection (mm)')

figure(5)  % Not included

x = 0:0.1:25;
plot(x,f5)
hold on

title('Deflection of an IPMC Strip -- Situation 4')
xlabel('Length (mm)')
ylabel('Deflection (mm)')

figure(6)  % Fig. 5.3
x = 0:0.1:25;
plot(x,f2,'Linestyle','--','LineWidth',3)
hold on
```

```
x = 0:0.1:25;
plot(x,f3,'Linestyle','-.','LineWidth',3)
hold on

x = 0:0.1:25;
plot(x,f4,'Linestyle','-','LineWidth',3)
hold on

x = 0:0.1:25;
plot(x,f5,'Linestyle',':','LineWidth',3)
hold on

legend('Case 1','Case 2','Case 3','Case 4')
title('Deflection of an IPMC Strip in four cases')
xlabel('Length (mm)')
ylabel('Deflection (mm)')
grid on

% Read input and output
a1_data = iddata(a1_output,a1_input,0.001);
a2_data = iddata(a2_output,a2_input,0.001);
a3_data = iddata(a3_output,a3_input,0.001);
```

```
a4_data = iddata(a4_output,a4_input,0.001);

a5_data = iddata(a5_output,a5_input,0.001);

a6_data = iddata(a6_output,a6_input,0.001);

a7_data = iddata(a7_output,a7_input,0.001);

a8_data = iddata(a8_output,a8_input,0.001);

a9_data = iddata(a9_output,a9_input,0.001);


% Percentage of fit can be found by typing "compare(a8_data,a8_m)"


% Using ARX modeling method to model

a1_m = arx(a1_data,[4 4 0]);

a2_m = arx(a2_data,[4 4 0]);

a3_m = arx(a3_data,[4 4 0]);

a4_m = arx(a4_data,[4 4 0]);

a5_m = arx(a5_data,[4 4 0]);

a6_m = arx(a6_data,[4 4 0]);

a7_m = arx(a7_data,[4 4 0]);

a8_m = arx(a8_data,[4 4 0]);

a9_m = arx(a9_data,[4 4 0]);


% Get the transfer function

a1_sys = tf(a1_m,'measured');
```

```
a2_sys = tf(a2_m,'measured');

a3_sys = tf(a3_m,'measured');

a4_sys = tf(a4_m,'measured');

a5_sys = tf(a5_m,'measured');

a6_sys = tf(a6_m,'measured');

a7_sys = tf(a7_m,'measured');

a8_sys = tf(a8_m,'measured');

a9_sys = tf(a9_m,'measured');


% Simulated Output

a1_oplot = lsim(a1_sys,a1_input,t1);

a2_oplot = lsim(a2_sys,a2_input,t1);

a3_oplot = lsim(a3_sys,a3_input,t1);

a4_oplot = lsim(a4_sys,a4_input,t1);

a5_oplot = lsim(a5_sys,a5_input,t1);

a6_oplot = lsim(a6_sys,a6_input,t1);

a7_oplot = lsim(a7_sys,a7_input,t1);

a8_oplot = lsim(a8_sys,a8_input,t1);

a9_oplot = lsim(a9_sys,a9_input,t1);


figure(7)  % Fig. 5.5
```

```
[A1,A2,A3] = plotyy(t1,a8_output,t1,a8_input,'plot');
% Set the pattern of the lines
set(A2,'LineStyle','-','LineWidth',1)
set(A3,'LineStyle',':','LineWidth',1)
hold on

plot(t1,a8_oplot,'Linestyle',':','LineWidth',3)

legend('Measured Output','Simulated Output fit: 71.27%','Input Signal')
xlabel('Time (s)')

% Set the tick spacing of left y-axis
set(A1(1), 'yTick', [-15:5:15])
% Set the limitation of left y-axis
set(A1(1), 'ylim', [-15 15])

% Set the tick spacing of right y-axis
set(A1(2), 'yTick', [-10:5:10])
% Set the limitation of right y-axis
set(A1(2), 'ylim', [-10 10])

% Label left y-axis
```

```
set(get(A1(1),'Ylabel'),'String','Deflection (mm)')
% Label right y-axis
set(get(A1(2),'Ylabel'),'String','Voltage (V)')

figure(8)  % Not included in content

% Draw the root locus
rlocus(a8_sys)

figure(9)  % Not included in content

% Draw the Bode plot
bode(a8_sys)
margin(a8_sys)

% Using ARMAX modeling method to model
b1_m = armax(a1_data,[4 4 2 0]);
b2_m = armax(a2_data,[4 4 2 0]);
b3_m = armax(a3_data,[4 4 2 0]);
b4_m = armax(a4_data,[4 4 2 0]);
b5_m = armax(a5_data,[4 4 2 0]);
b6_m = armax(a6_data,[4 4 2 0]);
```

```
b7_m = armax(a7_data,[4 4 2 0]);

b8_m = armax(a8_data,[4 4 2 0]);

b9_m = armax(a9_data,[4 4 2 0]);


% Get the transfer function

b1_sys = tf(b1_m,'measured');

b2_sys = tf(b2_m,'measured');

b3_sys = tf(b3_m,'measured');

b4_sys = tf(b4_m,'measured');

b5_sys = tf(b5_m,'measured');

b6_sys = tf(b6_m,'measured');

b7_sys = tf(b7_m,'measured');

b8_sys = tf(b8_m,'measured');

b9_sys = tf(b9_m,'measured');


% Simulate output

b1_oplot = lsim(b1_sys,a1_input,t1);

b2_oplot = lsim(b2_sys,a2_input,t1);

b3_oplot = lsim(b3_sys,a3_input,t1);

b4_oplot = lsim(b4_sys,a4_input,t1);

b5_oplot = lsim(b5_sys,a5_input,t1);

b6_oplot = lsim(b6_sys,a6_input,t1);
```

```
b7_oplot = lsim(b7_sys,a7_input,t1);

b8_oplot = lsim(b8_sys,a8_input,t1);

b9_oplot = lsim(b9_sys,a9_input,t1);


figure(10)  % Fig. 5.6


[B1,B2,B3] = plotyy(t1,a8_output,t1,a8_input,'plot');

% Set the pattern of the lines

set(B2,'LineStyle','-','LineWidth',1)

set(B3,'LineStyle',':','LineWidth',1)

hold on


plot(t1,b8_oplot,'Linestyle',':','LineWidth',3)


legend('Measured Output','Simulated Output fit: 71.16%','Input Signal')

xlabel('Time (s)')


% Set the tick spacing of left y-axis

set(B1(1), 'yTick', [-15:5:15])

% Set the limitation of left y-axis

set(B1(1), 'ylim', [-15 15])
```

```
% Set the tick spacing of right y-axis
set(B1(2), 'yTick', [-10:5:10])
% Set the limitation of right y-axis
set(B1(2), 'ylim', [-10 10])

% Label left y-axis
set(get(B1(1),'Ylabel'),'String','Deflection (mm)')
% Label right y-axis
set(get(B1(2),'Ylabel'),'String','Voltage (V)')

figure(11)  % Not included in content

rlocus(b8_sys)

figure(12)  % Not included in content

bode(b8_sys)
margin(b8_sys)

% Using Output-error (OE) modeling method to model
c1_m = oe(a1_data,[4,4,1]);
c2_m = oe(a2_data,[4,4,1]);
```

```
c3_m = oe(a3_data,[4,4,1]);

c4_m = oe(a4_data,[4,4,1]);

c5_m = oe(a5_data,[4,4,1]);

c6_m = oe(a6_data,[4,4,1]);

c7_m = oe(a7_data,[4,4,1]);

c8_m = oe(a8_data,[4,4,1]);

c9_m = oe(a9_data,[4,4,1]);


% Get transfer function

c1_sys = tf(c1_m,'measured');

c2_sys = tf(c2_m,'measured');

c3_sys = tf(c3_m,'measured');

c4_sys = tf(c4_m,'measured');

c5_sys = tf(c5_m,'measured');

c6_sys = tf(c6_m,'measured');

c7_sys = tf(c7_m,'measured');

c8_sys = tf(c8_m,'measured');

c9_sys = tf(c9_m,'measured');


% Simulate output

c1_oplot = lsim(c1_sys,a1_input,t1);

c2_oplot = lsim(c2_sys,a2_input,t1);
```

```
c3_oplot = lsim(c3_sys,a3_input,t1);

c4_oplot = lsim(c4_sys,a4_input,t1);

c5_oplot = lsim(c5_sys,a5_input,t1);

c6_oplot = lsim(c6_sys,a6_input,t1);

c7_oplot = lsim(c7_sys,a7_input,t1);

c8_oplot = lsim(c8_sys,a8_input,t1);

c9_oplot = lsim(c9_sys,a9_input,t1);


figure(13)  % Fig. 5.7


[C1,C2,C3] = plotyy(t1,a8_output,t1,a8_input,'plot');

% Set the pattern of the lines

set(C2,'LineStyle','-','LineWidth',1)

set(C3,'LineStyle',':','LineWidth',1)

hold on


plot(t1,c8_oplot,'Linestyle',':','LineWidth',3)


legend('Measured Output','Simulated Output fit: 76.38%','Input Signal')

xlabel('Time (s)')


% Set the tick spacing of left y-axis
```

```
set(C1(1), 'yTick', [-15:5:15])
% Set the limitation of left y-axis
set(C1(1), 'ylim', [-15 15])

% Set the tick spacing of right y-axis
set(C1(2), 'yTick', [-10:5:10])
% Set the limitation of right y-axis
set(C1(2), 'ylim', [-10 10])

% Label left y-axis
set(get(C1(1),'Ylabel'),'String','Deflection (mm)')
% Label right y-axis
set(get(C1(2),'Ylabel'),'String','Voltage (V)')

figure(14)  % Not included in content

rlocus(c8_sys)

figure(15)  % Not included in content

bode(c8_sys)
margin(c8_sys)
```

```
% Using Box-Jenkins (BJ) modeling method to model
d1_m = bj(a1_data,[4 4 4 4 0]);
d2_m = bj(a2_data,[4 4 4 4 0]);
d3_m = bj(a3_data,[4 4 4 4 0]);
d4_m = bj(a4_data,[4 4 4 4 0]);
d5_m = bj(a5_data,[4 4 4 4 0]);
d6_m = bj(a6_data,[4 4 4 4 0]);
d7_m = bj(a7_data,[4 4 4 4 0]);
d8_m = bj(a8_data,[4 4 4 4 0]);
d9_m = bj(a9_data,[4 4 4 4 0]);

% Get transfer function
d1_sys = tf(d1_m,'measured');
d2_sys = tf(d2_m,'measured');
d3_sys = tf(d3_m,'measured');
d4_sys = tf(d4_m,'measured');
d5_sys = tf(d5_m,'measured');
d6_sys = tf(d6_m,'measured');
d7_sys = tf(d7_m,'measured');
d8_sys = tf(d8_m,'measured');
d9_sys = tf(d9_m,'measured');
```

```
% Simulate output
d1_oplot = lsim(d1_sys,a1_input,t1);
d2_oplot = lsim(d2_sys,a2_input,t1);
d3_oplot = lsim(d3_sys,a3_input,t1);
d4_oplot = lsim(d4_sys,a4_input,t1);
d5_oplot = lsim(d5_sys,a5_input,t1);
d6_oplot = lsim(d6_sys,a6_input,t1);
d7_oplot = lsim(d7_sys,a7_input,t1);
d8_oplot = lsim(d8_sys,a8_input,t1);
d9_oplot = lsim(d9_sys,a9_input,t1);

figure(16)  % Fig. 5.8

[D1, D2, D3] = plotyy(t1,a8_output,t1,a8_input,'plot');
% Set the pattern of the lines
set(D2,'LineStyle','-','LineWidth',1)
set(D3,'LineStyle',':','LineWidth',1)
hold on

plot(t1,d8_oplot,'Linestyle',':','LineWidth',3)

legend('Measured Output','Simulated Output fit: 76.38%','Input Signal')
```

```
xlabel('Time (s)')

% Set the tick spacing of left y-axis
set(D1(1), 'yTick', [-15:5:15])
% Set the limitation of left y-axis
set(D1(1), 'ylim', [-15 15])

% Set the tick spacing of right y-axis
set(D1(2), 'yTick', [-10:5:10])
% Set the limitation of right y-axis
set(D1(2), 'ylim', [-10 10])

% Label left y-axis
set(get(D1(1),'Ylabel'),'String','Deflection (mm)')
% Label right y-axis
set(get(D1(2),'Ylabel'),'String','Voltage (V)')

figure(17)  % Not included in content

rlocus(d8_sys)

figure(18)
```

```
bode(d8_sys)

margin(d8_sys)


% Using PEM modeling method to model

e1_m = pem(a1_data,4);

e2_m = pem(a2_data,4);

e3_m = pem(a3_data,4);

e4_m = pem(a4_data,4);

e5_m = pem(a5_data,4);

e6_m = pem(a6_data,4);

e7_m = pem(a7_data,4);

e8_m = pem(a8_data,4);

e9_m = pem(a9_data,4);


% Get transfer function

e1_sys = tf(e1_m,'measured');

e2_sys = tf(e2_m,'measured');

e3_sys = tf(e3_m,'measured');

e4_sys = tf(e4_m,'measured');

e5_sys = tf(e5_m,'measured');

e6_sys = tf(e6_m,'measured');

e7_sys = tf(e7_m,'measured');
```

```
e8_sys = tf(e8_m,'measured');

e9_sys = tf(e9_m,'measured');


% Simulate output

e1_oplot = lsim(e1_sys,a1_input,t1);

e2_oplot = lsim(e2_sys,a2_input,t1);

e3_oplot = lsim(e3_sys,a3_input,t1);

e4_oplot = lsim(e4_sys,a4_input,t1);

e5_oplot = lsim(e5_sys,a5_input,t1);

e6_oplot = lsim(e6_sys,a6_input,t1);

e7_oplot = lsim(e7_sys,a7_input,t1);

e8_oplot = lsim(e8_sys,a8_input,t1);

e9_oplot = lsim(e9_sys,a9_input,t1);


figure(19)  % Fig. 5.9


[E1,E2,E3] = plotyy(t1,a8_output,t1,a8_input,'plot');

% Set the pattern of the lines

set(E2,'LineStyle','-','LineWidth',1)

set(E3,'LineStyle',':','LineWidth',1)

hold on
```

```
plot(t1,e8_oplot,'Linestyle',':','LineWidth',3)

legend('Measured Output','Simulated Output fit: 70.08%','Input Signal')
xlabel('Time (s)')

% Set the tick spacing of left y-axis
set(E1(1), 'yTick', [-15:5:15])
% Set the limitation of left y-axis
set(E1(1), 'ylim', [-15 15])

% Set the tick spacing of right y-axis
set(E1(2), 'yTick', [-10:5:10])
% Set the limitation of right y-axis
set(E1(2), 'ylim', [-10 10])

% Label left y-axis
set(get(E1(1),'Ylabel'),'String','Deflection (mm)')
% Label right y-axis
set(get(E1(2),'Ylabel'),'String','Voltage (V)')

figure(20)  % Not included in content
```

```
rlocus(e8_sys)

figure(21)  % Not included in content

bode(e8_sys)
margin(e8_sys)

% Simulate output by applying different input
a81_oplot = lsim(a8_sys,a1_input,t1);
a86_oplot = lsim(a8_sys,a6_input,t1);
a24_oplot = lsim(a2_sys,a4_input,t1);
a29_oplot = lsim(a2_sys,a9_input,t1);
c81_oplot = lsim(c8_sys,a1_input,t1);
c86_oplot = lsim(c8_sys,a6_input,t1);

figure(22)  % Fig. 5.10 (a)

[F1,F2,F3] = plotyy(t1,a81_oplot,t1,a1_input,'plot');
% Set the pattern of the lines
set(F2,'LineStyle','-','LineWidth',1)
set(F3,'LineStyle',':','LineWidth',1)
hold on
```

```
plot(t1,a1_output,'Linestyle',':','LineWidth',3);

legend('Simulated Output','Measured output','Input Signal')
xlabel('Time (s)')

% Set the tick spacing of left y-axis
set(F1(1), 'yTick', [-15:5:15])
% Set the limitation of left y-axis
set(F1(1), 'ylim', [-15 15])

% Set the tick spacing of right y-axis
set(F1(2), 'yTick', [-10:5:10])
% Set the limitation of right y-axis
set(F1(2), 'ylim', [-10 10])

% Label left y-axis
set(get(F1(1),'Ylabel'),'String','Deflection (mm)')
% Label right y-axis
set(get(F1(2),'Ylabel'),'String','Voltage (V)')

figure(23)  % Fig. 5.10 (b)
```

```
[G1,G2,G3] = plotyy(t1,a86_oplot,t1,a6_input, 'plot');
% Set the pattern of the lines
set(G2,'LineStyle','-','LineWidth',1)
set(G3,'LineStyle',':','LineWidth',1)
hold on

plot(t1,a6_output,'Linestyle',':','LineWidth',3);

legend('Simulated Output','Measured output','Input Signal')
xlabel('Time (s)')

% Set the tick spacing of left y-axis
set(G1(1), 'yTick', [-8:2:8])
% Set the limitation of left y-axis
set(G1(1), 'ylim', [-8 8])

% Set the tick spacing of right y-axis
set(G1(2), 'yTick', [-10:5:10])
% Set the limitation of right y-axis
set(G1(2), 'ylim', [-10 10])

% Label left y-axis
```

```
set(get(G1(1),'Ylabel'),'String','Deflection (mm)')
% Label right y-axis
set(get(G1(2),'Ylabel'),'String','Voltage (V)')

figure(24)  % Fig. 5.10 (c)

[H1,H2,H3] = plotyy(t1,a24_oplot,t1,a4_input,'plot');
% Set the pattern of the lines
set(H2,'LineStyle','-','LineWidth',1)
set(H3,'LineStyle',':','LineWidth',1)
hold on

plot(t1,a4_output,'Linestyle',':','LineWidth',3);

legend('Simulated Output','Measured output','Input Signal')
xlabel('Time (s)')

% Set the tick spacing of left y-axis
set(H1(1), 'yTick', [-15:5:15])
% Set the limitation of left y-axis
set(H1(1), 'ylim', [-15 15])
```

```
% Set the tick spacing of right y-axis
set(H1(2), 'yTick', [-10:5:10])
% Set the limitation of right y-axis
set(H1(2), 'ylim', [-10 10])

% Label left y-axis
set(get(H1(1),'Ylabel'),'String','Deflection (mm)')
% Label right y-axis
set(get(H1(2),'Ylabel'),'String','Voltage (V)')

figure(25)  % Fig. 5.10 (d)

[I1,I2,I3] = plotyy(t1,a29_oplot,t1,a9_input,'plot');
% Set the pattern of the lines
set(I2,'LineStyle','-','LineWidth',1)
set(I3,'LineStyle',':','LineWidth',1)
hold on

plot(t1,a9_output,'Linestyle',':','LineWidth',3);

legend('Simulated Output','Measured output','Input Signal')
xlabel('Time (s)')
```

```
% Set the tick spacing of left y-axis
set(I1(1), 'yTick', [-10:5:15])
% Set the limitation of left y-axis
set(I1(1), 'ylim', [-10 15])

% Set the tick spacing of right y-axis
set(I1(2), 'yTick', [-10:5:10])
% Set the limitation of right y-axis
set(I1(2), 'ylim', [-10 10])

% Label left y-axis
set(get(I1(1),'Ylabel'),'String','Deflection (mm)')
% Label right y-axis
set(get(I1(2),'Ylabel'),'String','Voltage (V)')

figure(26)  % Fig. 5.10 (e)

[J1,J2,J3] = plotyy(t1,c81_oplot,t1,a1_input, 'plot');
% Set the pattern of the lines
set(J2,'LineStyle','-','LineWidth',1)
set(J3,'LineStyle',':','LineWidth',1)
hold on
```

```
plot(t1,a1_output,'Linestyle',':','LineWidth',3);

legend('Simulated Output','Measured output','Input Signal')
xlabel('Time (s)')

% Set the tick spacing of left y-axis
set(J1(1), 'yTick', [-15:5:15])
% Set the limitation of left y-axis
set(J1(1), 'ylim', [-15 15])

% Set the tick spacing of right y-axis
set(J1(2), 'yTick', [-10:5:10])
% Set the limitation of right y-axis
set(J1(2), 'ylim', [-10 10])

% Label left y-axis
set(get(J1(1),'Ylabel'),'String','Deflection (mm)')
% Label right y-axis
set(get(J1(2),'Ylabel'),'String','Voltage (V)')

figure(27)  % Fig. 5.10 (f)
```

```
[K1,K2,K3] = plotyy(t1,c86_oplot,t1,a6_input, 'plot');
% Set the pattern of the lines
set(K2,'LineStyle','-','LineWidth',1)
set(K3,'LineStyle',':','LineWidth',1)
hold on

plot(t1,a6_output,'Linestyle',':','LineWidth',3);

legend('Simulated Output','Measured output','Input Signal')
xlabel('Time (s)')

% Set the tick spacing of left y-axis
set(K1(1), 'yTick', [-10:5:10])
% Set the limitation of left y-axis
set(K1(1), 'ylim', [-10 10])

% Set the tick spacing of right y-axis
set(K1(2), 'yTick', [-10:5:10])
% Set the limitation of right y-axis
set(K1(2), 'ylim', [-10 10])

% Label left y-axis
```

```
set(get(K1(1),'Ylabel'),'String','Deflection (mm)')
% Label right y-axis
set(get(K1(2),'Ylabel'),'String','Voltage (V)')



% The following code is to model an IPMC system by using electrical method
% The value of the capacitor affects the time duration of high current
% the values of other resistors determine the maximum internal current

R11_1 = 14;
R12_1 = 2;
R13_1 = 20;
R14_1 = 2;
R15_1 = 40;
R16_1 = 14;
C1_1 = 0.0001;

R11_2 = 14;
R12_2 = 2;
R13_2 = 50;
R14_2 = 2;
R15_2 = 20;
```

```
R16_2 = 14;

C1_2 = 0.1;

% Set time period for the electrical models

t2 = 0:0.1:30;

i = 1;

sys1_1 = tf([R13_1 * (R12_1 + R14_1 + R15_1) * C1_1 (R12_1 + R13_1 + R14_1 +
R15_1)], [((R11_1 + R16_1) * R13_1 * (R12_1 + R14_1 + R15_1) + R13_1 * R15_1 *
(R12_1 + R14_1)) * C1_1 (R11_1 + R16_1) * (R12_1 + R13_1 + R14_1 + R15_1) +
R15_1 * (R12_1 + R13_1 + R14_1)]);
sys1_2 = tf([R13_2 * (R12_2 + R14_2 + R15_2) * C1_2 (R12_2 + R13_2 + R14_2 +
R15_2)], [((R11_2 + R16_2) * R13_2 * (R12_2 + R14_2 + R15_2) + R13_2 * R15_2 *
(R12_2 + R14_2)) * C1_2 (R11_2 + R16_2) * (R12_2 + R13_2 + R14_2 + R15_2) +
R15_2 * (R12_2 + R13_2 + R14_2)]);

figure(28)  % Fig. 5.12 (a)

test1_1 = 24 * step(sys1_1, 1);

plot(t2, test1_1(1:301,1));
```

```
xlabel('Time (s)')

ylabel('Current (A)')

xlim([0 30]);

ylim([0 0.8]);


grid on;


figure(29)  % Fig. 5.12 (b)


test1_2 = 1 * step(sys1_2, 1000);


plot(t2, test1_2(1:301,1));


xlabel('Time (s)')

ylabel('Current (A)')

xlim([0 30]);

ylim([0 0.04]);

grid on;


figure(30)  % Combine Figs. (28) and (29)


test1_1 = 24 * step(sys1_1, 1);
```

```
plot(t2,test1_1(1:301,1),'Linestyle','-');

hold on

test1_2 = 1 * step(sys1_2, 1000);
plot(t2,test1_2(1:301,1),'Linestyle','-.');

legend('Thick IPMC','Thin IPMC')
xlabel('Time (s)')
ylabel('Current (A)')
xlim([0 30]);
ylim([0 0.8]);

grid on;

% Build the second model to compare the simulated and practical internal
% current
R21_1 = 0;
R22_1 = 0;
R23_1 = 0;
R24_1 = 0;
R25_1 = 0;
```

```
R26_1 = 0;

C2_1 = 0.000001;


R21_2 = 5;

R22_2 = 2;

R23_2 = 0.5;

R24_2 = 2;

R25_2 = 1;

R26_2 = 5;

C2_2 = 0.001;

i = 1;


for j = 0:0.1:30

    R21_1(1,i) = 5 + 1 * exp(-t2(1,i)) ^ (1/4);

    R22_1(1,i) = 2 + 0.1 * exp(-t2(1,i)) ^ (1/4);

    R23_1(1,i) = 0.5 + 0.1 * exp(t2(1,i)/2) ^ (1/6);

    R24_1(1,i) = 2 - 0.1 * exp(-t2(1,i)) ^ (1/4);

    R25_1(1,i) = 1 + 0.1 * exp(t2(1,i)/2) ^ (1/6);

    R26_1(1,i) = 5 - 1 * exp(-t2(1,i)) ^ (1/4);

    sys2_1(1,i) = tf([R23_1(1,i) * (R22_1(1,i) + R24_1(1,i) + R25_1(1,i)) * C2_1
(R22_1(1,i) + R23_1(1,i) + R24_1(1,i) + R25_1(1,i))], [((R21_1(1,i) + R26_1(1,i)) *
R23_1(1,i) * (R22_1(1,i) + R24_1(1,i) + R25_1(1,i)) + R23_1(1,i) * R25_1(1,i) *
```

```
(R22_1(1,i) + R24_1(1,i))) * C2_1 (R21_1(1,i) + R26_1(1,i)) * (R22_1(1,i) + R23_1(1,i)
+ R24_1(1,i) + R25_1(1,i)) + R25_1(1,i) * (R22_1(1,i) + R23_1(1,i) + R24_1(1,i))]);
    test2_1(:,i) = 8 * step(sys2_1(1,i),t2);
    TT_1(i,1) = test2_1(i,i);
    i = i + 1;
end

i = 1;

for j = 0:0.1:30
    R21_2(1,i) = 5 + 2 * exp(-t2(1,i)) ^ (1/1);
    R22_2(1,i) = 2 + 1 * exp(-t2(1,i)) ^ (1/1);
    R23_2(1,i) = 0.5 + 1 * exp(t2(1,i)/4) ^ (1/6);
    R24_2(1,i) = 2 - 1 * exp(-t2(1,i)) ^ (1/1);
    R25_2(1,i) = 1 + 0.1 * exp(t2(1,i)) ^ (1/2);
    R26_2(1,i) = 5 - 2 * exp(-t2(1,i)) ^ (1/1);
    sys2_2(1,i) = tf([R23_2(1,i) * (R22_2(1,i) + R24_2(1,i) + R25_2(1,i)) * C2_2
(R22_2(1,i) + R23_2(1,i) + R24_2(1,i) + R25_2(1,i))], [((R21_2(1,i) + R26_2(1,i)) *
R23_2(1,i) * (R22_2(1,i) + R24_2(1,i) + R25_2(1,i)) + R23_2(1,i) * R25_2(1,i) *
(R22_2(1,i) + R24_2(1,i))) * C2_2 (R21_2(1,i) + R26_2(1,i)) * (R22_2(1,i) + R23_2(1,i)
+ R24_2(1,i) + R25_2(1,i)) + R25_2(1,i) * (R22_2(1,i) + R23_2(1,i) + R24_2(1,i))]);
    test2_2(:,i) = 0.4 * step(sys2_2(1,i),t2);
```

```
    TT_2(i,1) = test2_2(i,i);
    i = i + 1;
end

i = 1;

% Generate a sinusoidal and a square wave to make a response for this model
[u1,ttt] = gensig('sin',65,30,0.1);
[u2,ttt] = gensig('square',30,30,0.1);
u2 = (u2 - 0.5) * (-16);

for j = 0:0.1:30
    R21_1(1,i) = 5 + 1 * exp(-t2(1,i)) ^ (1/1);
    R22_1(1,i) = 2 + 0.1 * exp(-t2(1,i)) ^ (1/1);
    R23_1(1,i) = 0.5 + 0.1 * exp(t2(1,i)/2) ^ (1/6);
    R24_1(1,i) = 2 - 0.1 * exp(-t2(1,i)) ^ (1/1);
    R25_1(1,i) = 1 + 0.1 * exp(t2(1,i)/2) ^ (1/6);
    R26_1(1,i) = 5 - 1 * exp(-t2(1,i)) ^ (1/1);
    sys2_3(1,i) = tf([R23_1(1,i) * (R22_1(1,i) + R24_1(1,i) + R25_1(1,i)) * C2_1
(R22_1(1,i) + R23_1(1,i) + R24_1(1,i) + R25_1(1,i))], [(R21_1(1,i) + R26_1(1,i)) *
R23_1(1,i) * (R22_1(1,i) + R24_1(1,i) + R25_1(1,i)) + R23_1(1,i) * R25_1(1,i) *
```

```
(R22_1(1,i) + R24_1(1,i)) * C2_1 (R21_1(1,i) + R26_1(1,i)) * (R22_1(1,i) + R23_1(1,i)
+ R24_1(1,i) + R25_1(1,i)) + R25_1(1,i) * (R22_1(1,i) + R23_1(1,i) + R24_1(1,i))]);
    test2_3(:,i) = 8 * step(sys2_3(1,i),t2);
    TT_3(i,1) = test2_3(i,i);
    sys2_5(1,i) = sys2_3(1,i) * tf([0.04],[1 0.4 0.04]);
    sys2_6(1,i) = sys2_3(1,i) * tf([0.04],[1 0.4 0.04]);
    sys2_7(1,i) = sys2_3(1,i) * tf([0.04],[1 0.4 0.04]);
    sys2_8(1,i) = sys2_3(1,i) * tf([0.04],[1 0.4 0.04]);
    test2_5(:,i) = 36 * step(sys2_5(1,i),t2);
    test2_6(:,i) = 145 * lsim(sys2_6(1,i),u1,t2);
    test2_7(:,i) = 18 * lsim(sys2_7(1,i),u2,t2);
    test2_8(:,i) = 15 * lsim(sys2_8(1,i),u3,t2);
    TT_5(i,1) = test2_5(i,i);
    TT_6(i,1) = test2_6(i,i);
    TT_7(i,1) = test2_7(i,i);
    TT_8(i,1) = test2_8(i,i);
    i = i + 1;
end

i = 1;

for j = 0:0.1:30
```

```
    R21_2(1,i) = 5 + 2 * exp(-t2(1,i)) ^ (1/1);
    R22_2(1,i) = 2 + 1 * exp(-t2(1,i)) ^ (1/1);
    R23_2(1,i) = 0.5 + 1 * exp(t2(1,i)/4) ^ (1/6);
    R24_2(1,i) = 2 - 1 * exp(-t2(1,i)) ^ (1/1);
    R25_2(1,i) = 1 + 0.1 * exp(t2(1,i)) ^ (1/2);
    R26_2(1,i) = 5 - 2 * exp(-t2(1,i)) ^ (1/1);
    sys2_4(1,i) = tf([R23_2(1,i) * (R22_2(1,i) + R24_2(1,i) + R25_2(1,i)) * C2_2
(R22_2(1,i) + R23_2(1,i) + R24_2(1,i) + R25_2(1,i))], [(R21_2(1,i) + R26_2(1,i)) *
R23_2(1,i) * (R22_2(1,i) + R24_2(1,i) + R25_2(1,i)) + R23_2(1,i) * R25_2(1,i) *
(R22_2(1,i) + R24_2(1,i)) * C2_2 (R21_2(1,i) + R26_2(1,i)) * (R22_2(1,i) + R23_2(1,i)
+ R24_2(1,i) + R25_2(1,i)) + R25_2(1,i) * (R22_2(1,i) + R23_2(1,i) + R24_2(1,i))]);
    test2_4(:,i) = 0.4 * step(sys2_4(1,i),t2);
    TT_4(i,1) = test2_4(i,i);
    i = i + 1;
end

figure(31)  % Not included in content

title('Value Changes of the Elements in a Thick IPMC Strip')

subplot(3,2,1)
plot(t2,R21_1);
```

```
title('Value of R1')
xlabel('Time (s)')
ylabel('Resistance (Ohm)')
grid on;

subplot(3,2,2)
plot(t2,R22_1);

title('Value of R2')
xlabel('Time (s)')
ylabel('Resistance (Ohm)')
grid on;

subplot(3,2,3)
plot(t2,R23_1);

title('Value of R3')
xlabel('Time (s)')
ylabel('Resistance (Ohm)')
grid on;

subplot(3,2,4)
```

```
plot(t2,R24_1);

title('Value of R4')
xlabel('Time (s)')
ylabel('Resistance (Ohm)')
grid on;

subplot(3,2,5)
plot(t2,R25_1);

title('Value of R5')
xlabel('Time (s)')
ylabel('Resistance (Ohm)')
grid on;

subplot(3,2,6)
plot(t2,R26_1);

title('Value of R6')
xlabel('Time (s)')
ylabel('Resistance (Ohm)')
grid on;
```

```
figure(32)  % Fig. 5.14 (a)

plot(t2,TT_1,'Linestyle','-');
hold on;

plot(t2,TT_3,'Linestyle','-','LineWidth',3);

legend('Simulated internal current','Predicted practical current');
xlabel('Time (s)')
ylabel('Current (A)')
ylim([0 0.8]);
grid on;

figure(33)  % Comparison among all simulation methods of a thick IPMC strip

test1_1 = 24 * step(sys1_1, 1);
plot(t2,test1_1(1:301,1),'Linestyle','-');
hold on;

plot(t2,TT_1,'Linestyle',':','LineWidth',3);
hold on;
```

```
plot(t2,TT_3,'Linestyle','-','LineWidth',3);

legend('Simulated internal current (Time-invariant)','Simulated internal current (Time-
variant)','Predicted practical current');
xlabel('Time (s)')
ylabel('Current (A)')
ylim([0 0.8]);
grid on;

figure(34)  % Not included in content

title('Value Changes of the Elements in a Thin IPMC Strip')

subplot(3,2,1)
plot(t2,R21_2);

title('Value of R1')
xlabel('Time (s)')
ylabel('Resistance (Ohm)')
grid on;

subplot(3,2,2)
```

```
plot(t2,R22_2);

title('Value of R2')
xlabel('Time (s)')
ylabel('Resistance (Ohm)')
grid on;

subplot(3,2,3)
plot(t2,R23_2);

title('Value of R3')
xlabel('Time (s)')
ylabel('Resistance (Ohm)')
grid on;

subplot(3,2,4)
plot(t2,R24_2);

title('Value of R4')
xlabel('Time (s)')
ylabel('Resistance (Ohm)')
grid on;
```

```
subplot(3,2,5)

plot(t2,R25_2);


title('Value of R5')

xlabel('Time (s)')

ylabel('Resistance (Ohm)')

grid on;


subplot(3,2,6)

plot(t2,R26_2);


title('Value of R6')

xlabel('Time (s)')

ylabel('Resistance (Ohm)')

grid on;


figure(35)  % Comparison among all simulation methods of a thin IPMC strip


test1_2 = 1 * step(sys1_2, 1000);

plot(t2,test1_2(1:301,1),'Linestyle','-');

hold on;
```

```
plot(t2,TT_2,'Linestyle',':');
hold on;

plot(t2,TT_4,'Linestyle','-','LineWidth',3);

legend('Simulated internal current (Time-invariant)','Simulated internal current (Time-
variant)','Predicted practical current');
xlabel('Time (s)')
ylabel('Current (A)')
xlim([0 30]);
ylim([0 0.04]);
grid on;

figure(36)  % Fig. 5.14 (b)

plot(t2,TT_2,'Linestyle','-');
hold on;

plot(t2,TT_4,'Linestyle','-','LineWidth',3);

legend('Simulated internal current','Predicted practical current');
xlabel('Time (s)')
```

```
ylabel('Current (A)')
ylim([0 0.04]);
grid on;

figure(37)  % Combine Figs. (32 and (36)

plot(t2,TT_1,'Linestyle','-');
hold on;

plot(t2,TT_3,'Linestyle','--');
hold on;

plot(t2,TT_2,'Linestyle',':');
hold on;

plot(t2,TT_4,'Linestyle','-.');
hold on;

legend('Simulated internal current (Thick)','Predicted practical current
(Thick)','Simulated internal current (Thin)','Predicted practical current (Thin)');
xlabel('Time (s)')
ylabel('Current (A)')
```

```
ylim([0 0.8]);
grid on;

% Build the third model for surface condition comparison
R31_1 = 0;
R32_1 = 0;
R33_1 = 0;
R34_1 = 0;
R35_1 = 0;
R36_1 = 0;
C3_1 = 0.000001;

R31_2 = 0;
R32_2 = 0;
R33_2 = 0;
R34_2 = 0;
R35_2 = 0;
R36_2 = 0;
C3_2 = 0.00001;

i = 1;
```

```
for x = 0:2:10
   i = 1;
  for j = 0:0.1:30
     R31_1(1,i) = 5 + 2 * x + 1 * exp(-t2(1,i)) ^ (1/1);
     R32_1(1,i) = 2 + 0.1 * exp(-t2(1,i)) ^ (1/1);
     R33_1(1,i) = 0.5 + 0.1 * exp(t2(1,i)/2) ^ (1/6);
     R34_1(1,i) = 2 - 0.1 * exp(-t2(1,i)) ^ (1/1);
     R35_1(1,i) = 1 + 0.1 * exp(t2(1,i)/2) ^ (1/6);
     R36_1(1,i) = 5 + 2 * x - 1 * exp(-t2(1,i)) ^ (1/1);
     sys3_1(1,i) = tf([R33_1(1,i) * (R32_1(1,i) + R34_1(1,i) + R35_1(1,i)) * C3_1
(R32_1(1,i) + R33_1(1,i) + R34_1(1,i) + R35_1(1,i))], [((R31_1(1,i) + R36_1(1,i)) *
R33_1(1,i) * (R32_1(1,i) + R34_1(1,i) + R35_1(1,i)) + R33_1(1,i) * R35_1(1,i) *
(R32_1(1,i) + R34_1(1,i))) * C3_1 (R31_1(1,i) + R36_1(1,i)) * (R32_1(1,i) + R33_1(1,i)
+ R34_1(1,i) + R35_1(1,i)) + R35_1(1,i) * (R32_1(1,i) + R33_1(1,i) + R34_1(1,i))]);
     test3_1(:,i) = 8 * step(sys3_1(1,i),t2);
     TT3_1(i,x / 2 + 1) = test3_1(i,i);
     i = i + 1;
  end

  i = 1;

  for j = 0:0.1:30
```

```
    R31_2(1,i) = 5 + 2 * x + 2 * exp(-t2(1,i)) ^ (1/1);
    R32_2(1,i) = 2 + 1 * exp(-t2(1,i)) ^ (1/1);
    R33_2(1,i) = 0.5 + 1 * exp(t2(1,i)/4) ^ (1/6);
    R34_2(1,i) = 2 - 1 * exp(-t2(1,i)) ^ (1/1);
    R35_2(1,i) = 1 + 0.1 * exp(t2(1,i)) ^ (1/2);
    R36_2(1,i) = 5 + 2 * x - 2 * exp(-t2(1,i)) ^ (1/1);
    sys3_2(1,i) = tf([R33_2(1,i) * (R32_2(1,i) + R34_2(1,i) + R35_2(1,i)) * C3_2
(R32_2(1,i) + R33_2(1,i) + R34_2(1,i) + R35_2(1,i))], [((R31_2(1,i) + R36_2(1,i)) *
R33_2(1,i) * (R32_2(1,i) + R34_2(1,i) + R35_2(1,i)) + R33_2(1,i) * R35_2(1,i) *
(R32_2(1,i) + R34_2(1,i))) * C3_2 (R31_2(1,i) + R36_2(1,i)) * (R32_2(1,i) + R33_2(1,i)
+ R34_2(1,i) + R35_2(1,i)) + R35_2(1,i) * (R32_2(1,i) + R33_2(1,i) + R34_2(1,i))]);
    test3_2(:,i) = 0.4 * step(sys3_2(1,i),t2);
    TT3_2(i,x / 2 + 1) = test3_2(i,i);
    i = i + 1;
  end

  i = 1;

  for j = 0:0.1:30
    R31_1(1,i) = 5 + 2 * x + 1 * exp(-t2(1,i)) ^ (1/4);
    R32_1(1,i) = 2 + 0.1 * exp(-t2(1,i)) ^ (1/4);
    R33_1(1,i) = 0.5 + 0.1 * exp(t2(1,i)/2) ^ (1/6);
```

```
    R34_1(1,i) = 2 - 0.1 * exp(-t2(1,i)) ^ (1/4);
    R35_1(1,i) = 1 + 0.1 * exp(t2(1,i)/2) ^ (1/6);
    R36_1(1,i) = 5 + 2 * x - 1 * exp(-t2(1,i)) ^ (1/4);
    sys3_3(1,i) = tf([R33_1(1,i) * (R32_1(1,i) + R34_1(1,i) + R35_1(1,i)) * C3_1
(R32_1(1,i) + R33_1(1,i) + R34_1(1,i) + R35_1(1,i))], [(R31_1(1,i) + R36_1(1,i)) *
R33_1(1,i) * (R32_1(1,i) + R34_1(1,i) + R35_1(1,i)) + R33_1(1,i) * R35_1(1,i) *
(R32_1(1,i) + R34_1(1,i)) * C3_1 (R31_1(1,i) + R36_1(1,i)) * (R32_1(1,i) + R33_1(1,i)
+ R34_1(1,i) + R35_1(1,i)) + R35_1(1,i) * (R32_1(1,i) + R33_1(1,i) + R34_1(1,i))]);
    test3_3(:,i) = 8 * step(sys3_3(1,i),t2);
    TT3_3(i,x / 2 + 1) = test3_3(i,i);
    i = i + 1;
  end

  i = 1;

  for j = 0:0.1:30
    R31_2(1,i) = 5 + 2 * x + 2 * exp(-t2(1,i)) ^ (1/1);
    R32_2(1,i) = 2 + 1 * exp(-t2(1,i)) ^ (1/1);
    R33_2(1,i) = 0.5 + 1 * exp(t2(1,i)/4) ^ (1/6);
    R34_2(1,i) = 2 - 1 * exp(-t2(1,i)) ^ (1/1);
    R35_2(1,i) = 1 + 0.1 * exp(t2(1,i)) ^ (1/2);
    R36_2(1,i) = 5 + 2 * x - 2 * exp(-t2(1,i)) ^ (1/1);
```

```
      sys3_4(1,i) = tf([R33_2(1,i) * (R32_2(1,i) + R34_2(1,i) + R35_2(1,i)) * C3_2
(R32_2(1,i) + R33_2(1,i) + R34_2(1,i) + R35_2(1,i))], [(R31_2(1,i) + R36_2(1,i)) *
R33_2(1,i) * (R32_2(1,i) + R34_2(1,i) + R35_2(1,i)) + R33_2(1,i) * R35_2(1,i) *
(R32_2(1,i) + R34_2(1,i)) * C3_2 (R31_2(1,i) + R36_2(1,i)) * (R32_2(1,i) + R33_2(1,i)
+ R34_2(1,i) + R35_2(1,i)) + R35_2(1,i) * (R32_2(1,i) + R33_2(1,i) + R34_2(1,i))]);
      test3_4(:,i) = 0.4 * step(sys3_4(1,i),t2);
      TT3_4(i,x / 2 + 1) = test3_4(i,i);
      i = i + 1;
  end
end

figure(38)  % Fig. 5.15 (a)

plot(t2,TT3_1(:,1),'Linestyle','-','LineWidth',1);
hold on

plot(t2,TT3_1(:,2),'Linestyle','--','LineWidth',1);
hold on

plot(t2,TT3_1(:,3),'Linestyle',':','LineWidth',1);
hold on
```

```
plot(t2,TT3_1(:,4),'Linestyle','-.','LineWidth',1);
hold on

plot(t2,TT3_1(:,5),'Linestyle','-','LineWidth',3);
hold on

plot(t2,TT3_1(:,6),'Linestyle','--','LineWidth',3);
hold on

legend('5','7','9','11','13','15')
xlabel('Time (s)')
ylabel('Current (A)')
ylim([0 0.8]);
grid on;

figure(39)  % Fig. 5.15 (b)

plot(t2,TT3_2(:,1),'Linestyle','-','LineWidth',1);
hold on

plot(t2,TT3_2(:,2),'Linestyle','--','LineWidth',1);
hold on
```

```
plot(t2,TT3_2(:,3),'Linestyle',':','LineWidth',1);
hold on

plot(t2,TT3_2(:,4),'Linestyle','-.','LineWidth',1);
hold on

plot(t2,TT3_2(:,5),'Linestyle','-','LineWidth',3);
hold on

plot(t2,TT3_2(:,6),'Linestyle','--','LineWidth',3);
hold on

legend('5','7','9','11','13','15')
xlabel('Time (s)')
ylabel('Current (A)')
ylim([0 0.04]);
grid on;

figure(40)  % Not included in content

plot(t2,TT3_3(:,1),'Linestyle','-.','LineWidth',1);
hold on
```

```
plot(t2,TT3_3(:,2),'Linestyle','-','LineWidth',1);
hold on

plot(t2,TT3_3(:,3),'Linestyle','--','LineWidth',1);
hold on

plot(t2,TT3_3(:,4),'Linestyle','-.','LineWidth',3);
hold on

plot(t2,TT3_3(:,5),'Linestyle','-','LineWidth',3);
hold on

plot(t2,TT3_3(:,6),'Linestyle','--','LineWidth',3);
hold on

legend('5','7','9','11','13','15')
xlabel('Time (s)')
ylabel('Current (A)')
ylim([0 0.8]);
grid on;

figure(41)  % Not included in content
```

```
plot(t2,TT3_4(:,1),'Linestyle','-.','LineWidth',1);
hold on

plot(t2,TT3_4(:,2),'Linestyle','-','LineWidth',1);
hold on

plot(t2,TT3_4(:,3),'Linestyle','--','LineWidth',1);
hold on

plot(t2,TT3_4(:,4),'Linestyle','-.','LineWidth',3);
hold on

plot(t2,TT3_4(:,5),'Linestyle','-','LineWidth',3);
hold on

plot(t2,TT3_4(:,6),'Linestyle','--','LineWidth',3);
hold on

legend('5','7','9','11','13','15')
xlabel('Time (s)')
ylabel('Current (A)')
ylim([0 0.04]);
```

```
grid on;

t3 = 0:0.001:30;

figure(42)  % Fig. 4.7 (d), not included in Chaper V

plot(t3,0.235 * t_4_10_10_112510.Y(1,1).Data(1,10001:40001), 'LineStyle', '-')
hold on

xlabel('Time (s)')
ylabel('Deflection (mm)')

ylim([0 0.8])
grid on

figure(43)  % Comparison among all simulation methods of a thick IPMC strip

test1_1 = 24 * step(sys1_1, 1);

plot(t2,test1_1(1:301,1),'Linestyle','-');
hold on;
```

```
plot(t2,TT_1,'Linestyle','--');
hold on;

plot(t2,TT_3,'Linestyle',':');
hold on;

plot(t3,0.235 * t_4_10_10_112510.Y(1,1).Data(1,10001:40001), 'LineStyle', '-')

legend('Simulated internal current (Time-invariant)','Simulated internal current (Time-
variant)','Predicted practical current','Measured practical deflection');
xlabel('Time (s)')
ylabel('Current (A)')
ylim([0 0.8]);
grid on;

figure(44)  % Fig. 5.16 (a)

plot(t2,TT_5,'LineStyle',':','LineWidth',3)
hold on
plot(t3,t_4_10_10_112510.Y(1,1).Data(1,10001:40001),'LineStyle', '-')

legend('Revised simulated deflection','Measured practical deflection');
```

```
xlabel('Time (s)')

ylabel('Deflection (mm)')

grid on;


figure(45)  % Fig. 5.16 (b)


plot(t2,TT_6,'LineStyle',':','LineWidth',3);

hold on


plot(t3,sin01122010_5.Y(1,1).Data(1,10001:40001),'LineStyle', '-')


legend('Revised simulated deflection','Measured practical deflection')

xlabel('Time (s)')

ylabel('Deflection (mm)')

grid on;


figure(46)  % Not included

[L1, L2, L3] = plotyy(t2,TT_6,t2,8 * u1,'plot');


hold on

plot(t3,sin01122010_5.Y(1,1).Data(1,10001:40001),'LineStyle',':')
```

```
legend('Revised simulated Output','Measured practical deflection','Input signal')
xlabel('Time (s)')

% Set the tick spacing of left y-axis
set(L1(1), 'yTick', [-5:5:15])
% Set the limitation of left y-axis
set(L1(1), 'ylim', [-5 15])

% Set the tick spacing of right y-axis
set(L1(2), 'yTick', [-5:5:15])
% Set the limitation of right y-axis
set(L1(2), 'ylim', [-5 15])

% Label left y-axis
set(get(L1(1),'Ylabel'),'String','Deflection (mm)')
% Label right y-axis
set(get(L1(2),'Ylabel'),'String','Voltage (V)')

grid on;

figure(47)  % Fig. 5.16 (c)
```

```
plot(t2,TT_7,'LineStyle',':','LineWidth',3);
hold on

plot(t3,squ02122010_7.Y(1,1).Data(1,7001:37001),'LineStyle', '-');

legend('Revised simulated deflection','Measured practical deflection')
xlabel('Time (s)')
ylabel('Deflection (mm)')
grid on;

figure(48)  % Not included
[M1, M2, M3] = plotyy(t2,TT_7,t2,u2,'plot');

hold on
plot(t3,squ02122010_7.Y(1,1).Data(1,7001:37001),'LineStyle',':')

legend('Revised simulated Output','Measured practical deflection','Input signal')
xlabel('Time (s)')

% Set the tick spacing of left y-axis
set(M1(1), 'yTick', [-10:5:15])
% Set the limitation of left y-axis
```

```
set(M1(1), 'ylim', [-10 15])

% Set the tick spacing of right y-axis
set(M1(2), 'yTick', [-10:5:15])
% Set the limitation of right y-axis
set(M1(2), 'ylim', [-10 15])

% Label left y-axis
set(get(M1(1),'Ylabel'),'String','Deflection (mm)')
% Label right y-axis
set(get(M1(2),'Ylabel'),'String','Voltage (V)')

grid on;

figure(49)  % Fig. 5.16 (d)

plot(t2,TT_8,'LineStyle',':','LineWidth',3)
hold on

plot(t3,saw01122010_5.Y(1,1).Data(1,7001:37001),'LineStyle', '-');

legend('Revised simulated deflection','Measured practical deflection')
```

```
xlabel('Time (s)')
ylabel('Deflection (mm)')
grid on;

figure(50)  % Not included
[N1, N2, N3] = plotyy(t2,TT_8,t2,u3,'plot');

hold on
plot(t3,saw01122010_5.Y(1,1).Data(1,7001:37001),'LineStyle',':')

legend('Revised simulated Output','Measured practical deflection','Input signal')
xlabel('Time (s)')

% Set the tick spacing of left y-axis
set(N1(1), 'yTick', [-5:5:10])
% Set the limitation of left y-axis
set(N1(1), 'ylim', [-5 10])

% Set the tick spacing of right y-axis
set(N1(2), 'yTick', [-5:5:10])
% Set the limitation of right y-axis
set(N1(2), 'ylim', [-5 10])
```

```
% Label left y-axis
set(get(N1(1),'Ylabel'),'String','Deflection (mm)')
% Label right y-axis
set(get(N1(2),'Ylabel'),'String','Voltage (V)')

grid on;
```